UNIVERSITY OF SOUTHAMPTON

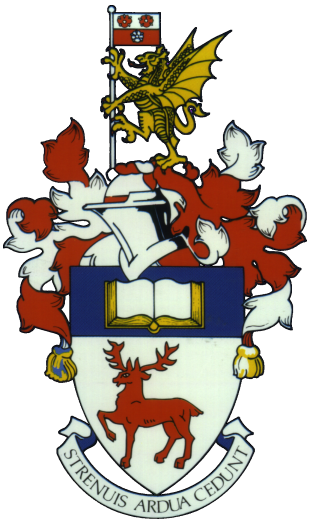


# Cluster-based Model for Calcium Excitations from Coupled IP3R Channels

by

Svitlana Braichenko

A thesis submitted for the degree of
Doctor of Philosophy

in the
Faculty of Engineering and Physical Sciences
Computational Engineering and Design

February 2020

UNIVERSITY OF SOUTHAMPTON
FACULTY OF ENGINEERING AND PHYSICAL SCIENCES
AERONAUTICS, ASTRONAUTICS AND COMPUTATIONAL ENGINEERING

Doctor of Philosophy

# CLUSTER-BASED MODEL FOR CALCIUM EXCITATIONS FROM COUPLED IP3R CHANNELS

by Svitlana Braichenko

## ABSTRACT

Clusters of $IP_3$ receptor channels in the membranes of the endoplasmic reticulum (ER) of many non-excitable cells release calcium ions in a cooperative manner giving rise to dynamical patterns such as puffs, waves and oscillations that occur on various spatial and temporal scales. We introduce a minimal yet descriptive reaction-diffusion model of $IP_3$ receptors for a saturating concentration of $IP_3$ using a principled reduction of a detailed Markov chain description of individual channels. A dynamical systems analysis reveals the possibility of excitable, bistable and oscillatory dynamics of this model that correspond to three types of observed patterns of calcium release – puffs, waves and spikes respectively. We explain the emergence of these patterns via a bifurcation analysis of a coupled two-cluster model, compute the phase diagram and quantify the speed of the waves and period of oscillations in terms of system parameters. Further, we extend our approach to a stochastic reaction-diffusion model with the $IP_3$ dependent randomly distributed clusters of channels. Our model reveals how the main characteristics of the activity of clusters, namely inter-puff intervals (IPIs), depend on the $IP_3$ loads. Furthermore, by performing a correlation analysis of $[Ca^{2+}]$ traces at the neighbouring clusters, we obtain the principal characteristics of the membrane which define the possibility of $Ca^{2+}$ wave initiation and propagation. Using given approach, we aim to link the local properties of $IP_3R$ channels and clusters, such as channel type or coupling between channels, with the global patterns which may emerge from these channels, e. g. spikes, waves or oscillations. We study the effect of cooperative behaviour of the $IP_3$ clusters found by Taufiq-Ur-Rahman et al. [2009] and also introduce insight into the clustering of the channels using the Ising-like approach.

# Contents

# List of Figures

# List of Tables

**Page**

# Nomenclature

| | |
|---|---|
| $c$ | concentration of $Ca^{2+}$ in cytosol |
| $p$ | concentration of $IP_3$ in cytosol |
| $a_i$ | first-order transition rate constant |
| $b_i$ | second-order transition rate constant |
| $d_i$ | dissociation constant $d_i = \frac{b_i}{a_i}$ |
| $S_{ijk}$ | the fraction of $IP_3R$ subunits in state $ijk$ according to the DYK model |
| $\mu$ | a probability of $IP_3$ binding |
| $C^{\mathrm{up}}(c,p)$ | an effective $IP_3$ binding rate from compound state $y$ corresponding to the lower plane of DYK cube towards $1-y$ state corresponding to upper plane of the DYK cube |
| $C^{\mathrm{up}}_{\mathrm{ch}}(c,p)$ | a combined rate for 4 subsequent $IP_3$ bindings governed by $C^{\mathrm{up}}(c,p)$ |
| $C^{\mathrm{down}}(c)$ | an effective $IP_3$ unbinding rate between compound states $y$ and $1-y$ |
| $c_s$ | $Ca^{2+}$ concentration at the opened channels |
| $c_d$ | $Ca^{2+}$ 'coupling' concentration at the closed channels |
| $c$ | $Ca^{2+}$ cytosolic concentration |
| $c_0$ | $Ca^{2+}$ rest concentration |
| $N$ | a number of activatable (all four subunits have $IP_3$ bound) $IP_3R$ channels in a cluster |
| $N_{\mathrm{tot}}$ | a total number of channels in a cluster |
| $a$ | a fraction of channels residing in an open state |
| $z$ | a fraction of channels residing in a rest state |
| $g$ | a fraction of channels residing in a closed state with both $Ca^{2+}$ activating and inhibiting bond |
| $h'$ | a fraction of channels residing in a closed state with an inhibiting bond |
| $h$ | a fraction of channels residing in a compound closed state comprising two inhibitory states $g$ and $h'$ |
| $k_a^{\pm}$ | transition rates towards and from channel state $a$ |
| $k_i^{+}$ | transition rate towards $h$ |
| $k_{1,2}$ | transition rates from $h$ |
| $g_0$ | the fraction of $g$ relative to $h$ |
| $\epsilon$ | the parameter which characterises the sharpness of step between none active channels and one active channel |
| $\lambda$ | the equilibration rate |
| $\lambda_{1,2}$ | the eigenvalues of Jacobian at a fixed point |
| $a_j$ | a fraction of channels residing in an open state within the $j^{th}$ cluster |
| $h_j$ | a fraction of channels residing in a closed state within the $j^{th}$cluster |
| $c_j$ | cytosolic $Ca^{2+}$ concentration within the $j^{th}$ cluster |
| $k_{a_j}^{\pm}$ | transition rate coefficients towards and from $a_j$ |
| $k_{1j,2j}$ | transition rate coefficients from $h_j$ |
| $D$ | the diffusion constant |
| $J_{kl}$ | the coupling flux between $k^{th}$ and $l^{th}$ cluster |
| $\ell$ | a distance between neighbouring clusters |
| $dx$ | a step in space chosen for numerical integration |
| $dt$ | a step in time chosen for numerical integration |

| | |
|---|---|
| $a(r,t)$ | a distribution of opened channels within the simulation domain |
| $h(r,t)$ | a distribution of inhibited channels within the simulation domain |
| $c(r,t)$ | a distribution of $Ca^{2+}$ concentration within the simulation domain |
| $H(x)$ | Heaviside function |
| $r_{\mathrm{cl}}$ | a cluster radius |
| $P_p$ | pump strength |
| $K_p$ | pump dissociation constant |
| $P_l$ | leak amplitude |
| $A$ | amplitude of a stochastic noise term |
| $\mathrm{d}W$ | Wiener increments generated from a normal $(0,1)$ Gaussian distribution |
| $k_{ij}$ | correlation coefficient of $[Ca^{2+}]$ traces between the pairs of neighbouring clusters averaged over certain timespan |
| $P_{\mathrm{act}}$ | the steady-state open probability of activation of a single $IP_3R$ subunit |
| $P_{\mathrm{open}}$ | the steady-state open probability of activation of an $IP_3R$ channel calculated from the probability of the activation of at least 3 subunits |
| $\sigma_j$ | state of a channel in the Ising $IP_3$ model (active/inactive) |
| $S_i$ | state of a channel in the Ising $IP_3$ model (open/closed) |
| $\tilde{h}$ | an scaled external field applied to a cluster composed of the effects of $[Ca^{2+}]$ and $[IP_3]$ |
| $\tilde{J}$ | a scaled coupling constant between channels in a cluster |
| $H(\{S_i\})$ | the Hamiltonian of the $IP_3R$ cluster with state $\{S_i\}$ |
| $Z$ | the partition function of the $IP_3R$ cluster |
| $P_{\mathrm{o}}^N$ | the average steady-state open probability of a cluster containing $N$ channels |
| $m$ | the average state of a cluster (mean-field variable) |

# Glossary

***Xenopus* oocyte** female cell involved in fertilisation and reproduction widely used in embryological research found mostly in *Xenopus laevis* frogs native to Africa [Xen, 2019]. 1–3, 5, 6, 11, 43, 55, 84, 91, 115

**axon** a long cylindrical tube which extends from each neurone and electrical signals propagate along its outer membrane, about 50 to 70 $\mathring{A}$ [Murray, 2000]. 14, 15

**buffer** the functional protein which binds to $Ca^{2+}$ and regulates its ability to diffuse. There are several types of buffers such as immobile (EGTA) and mobile (BAPTA), etc. 2, 5, 46

**$Ca^{2+}$ blip** an event of a $Ca^{2+}$ release from a single $IP_3R$ channel. 3, 4, 7, 31, 32, 115

**$Ca^{2+}$ oscillation** (or $Ca^{2+}$ clock) oscillatory local or global $Ca^{2+}$ releases [Cheng and Lederer, 2008]. 3, 5, 6, 8, 10, 12, 19, 24, 35, 57, 61, 67

**$Ca^{2+}$ puff** an event of a $Ca^{2+}$ release from a cluster of $IP_3R$ channels. 1, 3–7, 10, 13, 24, 32, 65, 75, 76, 94, 98, 99, 115

**$Ca^{2+}$ spike** global $Ca^{2+}$ transient $Ca^{2+}$ release from the array of clusters localised by excessive concentrations of buffers in experiments [Cheng and Lederer, 2008]. 3, 5, 7, 65, 70

**$Ca^{2+}$ wave** a regenerative $Ca^{2+}$ release which travels across coupled clusters [Cheng and Lederer, 2008]. 3–8, 10, 12, 13, 32, 33, 45, 49, 50, 65, 70, 77

**cluster** (or $Ca^{2+}$ release unit) a group of tightly packed channels, either RyRs or $IP_3Rs$ or a mixture, in the $Ca^{2+}$ store membrane where $Ca^{2+}$ release may occur [Cheng and Lederer, 2008]. 2–8, 11, 13, 14, 24, 27, 31–33, 36, 37, 45, 47–50, 55, 57, 59

**cytosol** the fluid portion of the cell, excluding nucleus, organelles and other solids [Sadava et al., 2011]. 1, 2

**DT40 cell** the cell line derived from chicken B widely used in gene experiments [Winding and Berchtold, 2001]. 82, 84, 91, 99

**ER** (endoplasmic reticulum) a system of membranous tubes and flattened sacs found in the cytoplasm of eukaryotes [Sadava et al., 2011]. It is an organelle which stores the substantial part of the intracellular $Ca^{2+}$ concentration. 1, 2, 5, 6, 8, 13, 19, 21, 31, 60, 61, 64, 66, 67, 81

**$IP_3$** inositol 1,4,5-trisphosphate receptor is an intracellular second messenger derived from membrane phospholipids [Sadava et al., 2011]. 2, 4, 6, 8, 28, 61, 65

**$IP_3R$ channel** inositol 1,4,5-trisphosphate receptor channel is $Ca^{2+}$ channel activated by $IP_3$. 2, 4–6, 8, 10, 13, 28, 32, 50, 61, 101, 102, 115, 117

**Purkinje cell of the cerebellum** large neuron cells discovered in the cortex of brain cerebellum. This cell line is named after its explorer Czech physiologist Jan Evangelista Purkinje [Martone, 2015]. 84

**SH-SY5Y neuroblastoma cell** human-derived cell line cloned from cells taken from the patient with neuroblastoma. 1, 6

# Acronyms

**CICR** $Ca^{2+}$-induced $Ca^{2+}$ release. 18, 31

**CLE** Chemical Langevin Equation. 73, 74

**IPI** inter-puff interval. 71, 75–77, 81, 95, 97, 98

**ISI** inter-spike interval. 77

**SDE** Stochastic Differential Equation. 70

# Declaration of Authorship

---

I, Svitlana Braichenko, declare that this thesis entitled 'Cluster-based Model for Calcium Excitations from Coupled IP3R Channels' and the work presented in the thesis are my own, and have been generated by me as the result of my own original research.

I confirm that:

- This work was done wholly or mainly while in candidature for a research degree at this University;
- Where any part of this thesis has previously been submitted for a degree or any other qualification at this University or any other institution, this has been clearly stated;
- Where I have consulted the published work of others, this is always clearly attributed;
- Where I have quoted from the work of others, the source is always given. With the exception of such quotations, this thesis is entirely my own work;
- I have acknowledged all main sources of help;
- Where the thesis is based on work done by myself jointly with others, I have made clear exactly what was done by others and what I have contributed myself;
- Parts of this work have been published:

Signed:

Date:

Part of this work has been published in Journals:

- **S. Braichenko**, A. Bhaskar, and S. Dasmahapatra. Phenomenological cluster-based model of $Ca^{2+}$ waves and oscillations for inositol 1,4,5-trisphosphate receptor ($IP_3R$) channels. Physical Review E, 98(3):032413, sep 2018. ISSN 2470-0045. doi:10.1103/PhysRevE.98.032413.
- **S. Braichenko**, A. Bhaskar, and S. Dasmahapatra. Dynamics of $Ca^{2+}$ puff termination failure in IP3R channels (manuscript under preparation to be submitted to Chaos).
- **S. Braichenko**, A. Bhaskar, and S. Dasmahapatra. Ising model incorporates the clustering of IP3R channels (manuscript under preparation to be submitted to Physical Review Letters).

And also in conferences:

- **S. Braichenko**, A. Bhaskar, and S. Dasmahapatra, The reduced approach to the stochastic modelling of cooperative $Ca^{2+}$ release through $IP_3R$ channels yields the global characteristics of the cell regulation, Poster presented at: Physics of Cells: From Biochemical to Mechanical; 2018 September 3-7; Harrogate, UK.
- **S. Braichenko**, A. Bhaskar, and S. Dasmahapatra, The Simplified Approach to Spatio-temporal Arrangements of Stochastic $Ca^{2+}$ Signals Triggered by $IP_3$ Release, Poster and flash presented at: Open Calcium Conference; 2018 July 12; Milton Keynes, UK.
- **S. Braichenko**, A. Bhaskar, and S. Dasmahapatra, The spatial arrangements of stochastic $Ca^{2+}$ signals triggered by $IP_3$ release, Oral presentation at: MiLS meeting on Spatial cell signalling; 2018 May 30; Nottingham, UK.
- **S. Braichenko**, A. Bhaskar, and S. Dasmahapatra, The spatial arrangements of stochastic $Ca^{2+}$ signals triggered by $IP_3$ release, Poster presented at: 3rd European Calcium Channel Conference; 2018 May 9-12; Alpbach, Austria.
- **S. Braichenko**, A. Bhaskar, and S. Dasmahapatra, Calcium release dynamics in clusters of $IP_3$ channels, Poster presented at: EMBO Workshop: Dynamics of living cells; 2017 Sep 25-29; Cargese, France.

# Acknowledgements

This project was supervised by Dr. Srinandan Dasmahapatra and Prof. Atul Bhaskar, whose guidance and support throughout this Ph.D. have been very valuable.

The Ph.D. was funded by Erasmus Mundus ACTIVE grant $2013-2523/001-001$ and a Research Studentship from the Faculty of Engineering and the Environment, University of Southampton.

The author acknowledges the use of the IRIDIS High-Performance Computing Facility, and associated support services at the University of Southampton, in the completion of this work.

Last but not least, the author would like to thank Andrii Iakovliev for significant support in preparing the materials and the manuscript.

# Chapter 1

# Introduction

Calcium is a ubiquitous signalling agent in the human body. 'Almost everything we do is controlled by $Ca^{2+}$ – how we move, how our heart beats and how our brain stores information' [Berridge et al., 1998]. Most of the calcium is encapsulated in teeth and bones whereas only 1% of total concentration exists in the ionic form as $Ca^{2+}$ and is involved in cell regulation. $Ca^{2+}$ regulates various cellular processes in many types of cells. For example, $Ca^{2+}$ signalling is probably best studied during fertilisation in immature *Xenopus* oocytes. This cell type is most suitable for experimental purposes [Callamaras et al., 1998, Marchant et al., 1999, Parker and Ivorra, 1990, Shuai et al., 2006] because of their large size. Another example of well-studied $Ca^{2+}$ signals is SH-SY5Y neuroblastoma cells [Dickinson and Parker, 2013, Dickinson et al., 2012, Smith et al., 2009, Wiltgen et al., 2014]. Those cells are smaller and harder to study but they are of particular interest in medical studies. Laboratory engineered cell line DT40 is created particularly for patch-clamp experiments [Taufiq-Ur-Rahman et al., 2009]. There are many more cell types studied experimentally; however, the focus of the present thesis lies on those highlighted above. $Ca^{2+}$ also performs regulation during muscle contraction, heartbeat & contraction, immune response, brain function, etc. [Berridge, 2012, Mikoshiba, 2007]. The mechanism of such regulation is very complex and varies for different cell types.

Despite the complicated nature of $Ca^{2+}$ regulation, there is a universal scheme of $Ca^{2+}$ signalling [Berridge et al., 2000]. Most of the cytosolic $Ca^{2+}$ is released by various stimuli from intracellular storage of $Ca^{2+}$. For $Ca^{2+}$ storage within the cell, here we consider the endoplasmic reticulum (ER) as shown in Figure 1.1 where the different stages of the calcium signalling schema are indicated. Stage one is the stimulus – it can be either intracellular or extracellular, and it can have either electrical or chemical nature. At the next stage of the scheme, $Ca^{2+}$ is released from ER through the specific channels. At the third stage, most of the cytosolic $Ca^{2+}$ is anchored by functional proteins called buffers and does not participate in the cell activity. The rest of $Ca^{2+}$ remains free and participates in the cellular processes at stage four such as fertilisation, cell growth and death, heartbeat, etc. At the final stage, when the regulation is performed, $Ca^{2+}$ is released by buffers and pumped from the cytoplasmic space (cytosol) back to the ER.

The focus of our study is on the modelling of $Ca^{2+}$ released from the ER membrane (i.e. stage two in Figure 1.1). Often $Ca^{2+}$ released from channels forms curious spatio-temporal patterns within the membrane (e.g. $Ca^{2+}$ puffs, spikes, waves and oscillations). These patterns serve for different physiological purposes. Analysis of the hierarchy of the releases and connections between them is important to understand the very basics of cellular functions. Curiously, only

up to 1% of $Ca^{2+}$ is involved in signalling while up to 99% of cytosolic $Ca^{2+}$ is bound to buffers – they generally play a role of anchors attracting and retaining $Ca^{2+}$. In such a way, buffers often regulate cytosolic $Ca^{2+}$ concentrations and the ability of calcium ions to diffuse, thus, indirectly affecting the patterns formed by $Ca^{2+}$ in signalling. There are several kinds of buffers: mobile and immobile, reviewed by Rüdiger [2014b].

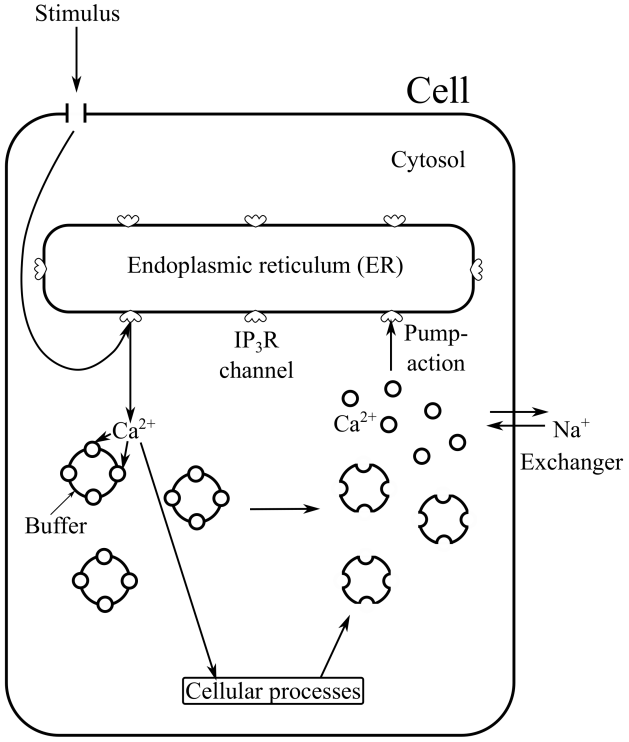


FIGURE 1.1: The scheme of $Ca^{2+}$ signalling. The stimulus triggers $Ca^{2+}$ release from $IP_3R$ channels in the plasmatic membrane of the ER. Thereafter, most of the $Ca^{2+}$ released is bound to buffers, whereas a small proportion regulates various cellular processes. After regulation, $Ca^{2+}$ leaves buffers. Finally, it is removed from the cytosol by various exchangers and pumps.

While many types of $Ca^{2+}$ release channels are implicated in these processes, in this thesis we are concerned with the dynamics of $Ca^{2+}$ released into the cytosol from inositol 1,4,5-triphosphate receptor ($IP_3R$) channels that are triggered by inositol trisphosphate, further in the text abbreviated as $IP_3$, being secondary messenger molecules [Mikoshiba, 2007]. $IP_3R$ channels are usually present in non-excitable cells and are mainly localised in the endoplasmic reticulum (ER) membrane where they are believed to form tight clusters to enable $Ca^{2+}$ signalling [Mak and Foskett, 1997]. Experimental observations by Taufiq-Ur-Rahman et al. [2009] and Smith et al. [2014] suggest that the distribution of clusters varies by cell type. For example, SH-SY5Y neuroblastoma cells contain around 4 to 6 channels per each cluster (a few contain up to 10 channels), HeLa cell clusters, on average, contain 2 to 3 channels and *Xenopus* oocyte clusters contain around 20 channels each [Dickinson et al., 2012]. However, theoretical and experimental investigations concerning processes involved in the formation of clusters, as well as the mechanisms by which they regulate $Ca^{2+}$ signalling are poorly understood, which is a subject of ongoing research.

$IP_3R$ channels are expressed in three subforms which are connected to various types of $Ca^{2+}$ release dynamics [Hernandez et al., 2007, Iino, 2000, Mataragka and Taylor, 2018]. In this thesis, we are mostly concerned with $IP_3R$-1 and $IP_3R$-3 subforms due to the fact that the steady-state behaviour of $Ca^{2+}$ releases connected to these subforms are studied more extensively by the experimentalists [Mak et al., 1998, Taufiq-Ur-Rahman et al., 2009].

$Ca^{2+}$ signalling events corresponding to release from $Ca^{2+}$ channels [Berridge, 2012] constitute a multiscale hierarchy consisting of three distinct types of events taking place at different spatial and temporal scales involving individual channels, clusters of channels and groups of channel clusters. The events occurring at the smallest scale ($\sim 10\,\text{nm}$ and $\sim 10\,\text{ms}$) are called $Ca^{2+}$ blips (Figure 1.2 (a)). They are the building blocks of signals on larger scales. Blips occur when $Ca^{2+}$ is released from a single channel into the cytosol. Coordinated $Ca^{2+}$ release from a cluster of channels – a collection of co-occurring $Ca^{2+}$ blips – is called a $Ca^{2+}$ puff (Figure 1.2 (b)) and appears at the second level of the hierarchy ($\sim 100\,\text{nm}$ and $\sim 100\,\text{ms}$). This cooperation between signalling events is regulated by $Ca^{2+}$ in a concentration-dependent feedback mechanism. Low $Ca^{2+}$ concentrations (maximum activity for $200 - 500$ nM) diffuse around the cytosol and cause the further release from neighbouring channels, whereas $Ca^{2+}$ in high cytosolic concentrations inhibits further $Ca^{2+}$ release. This feedback mechanism is called $Ca^{2+}$ induced $Ca^{2+}$ release (CICR). The final level in the hierarchy ($\sim 1\,\mu\text{m}$ and $\sim 1\,\text{s}$) is associated with $Ca^{2+}$ spikes, $Ca^{2+}$ waves and $Ca^{2+}$ oscillations (Figure 1.2 (c)). The term $Ca^{2+}$ oscillations is rarely mentioned nowadays, as $Ca^{2+}$ releases are believed to be stochastic, mostly non-periodic [Skupin et al., 2008] and composed of sequences of $Ca^{2+}$ spikes. We use term oscillations in this thesis to address nearly periodic releases specifically observed in several cell types, e. g. *Xenopus* oocytes [Marchant and Parker, 2001]. $Ca^{2+}$ spikes correspond to global transient releases from a group of clusters. $Ca^{2+}$ waves are formed as sequential releases travelling from excited clusters to neighbouring ones. $Ca^{2+}$ oscillations are repetitive $Ca^{2+}$ spikes or $Ca^{2+}$ waves. All the events on the highest hierarchical level that we consider ($Ca^{2+}$ spikes, waves, oscillations) consist of the coordinated release of $Ca^{2+}$ puffs from a group of clusters.

$Ca^{2+}$ oscillations are experimentally observed in various types of cells [Berridge, 2007]. Many models associate the occurrence of $Ca^{2+}$ oscillations with $IP_3$ regulation [Berridge, 2007, De Young and Keizer, 1992, Li and Rinzel, 1994, Politi et al., 2006, Smedler and Uhlén, 2014]. Some studies connect the emergence of $Ca^{2+}$ oscillations with the oscillating level of $IP_3$ triggered by binding to various enzymes, such as PLC (phospholipase C) or $IP_3$ kinase [Berridge, 2007, De Young and Keizer, 1992, Li and Rinzel, 1994, Politi et al., 2006]. Please see Figure 1.3 for more detailed $IP_3$ production pathway. Others report that $Ca^{2+}$ oscillations may occur even if the $IP_3$ concentration is non-oscillatory [Berridge, 2007, Braichenko et al., 2018]. Various studies explain oscillatory $Ca^{2+}$ behaviour as a sequence of stochastic $Ca^{2+}$ spikes [Falcke, 2003a, Skupin et al., 2008, Thurley et al., 2011]. Apart from $Ca^{2+}$ oscillations and $Ca^{2+}$ spikes propagating wavefronts have also been much studied. These are implicated, for instance, in the fertilization of *Xenopus* oocytes, and are generated when a sperm cell makes contact with a *Xenopus* oocyte.

In this thesis, we introduce a modelling approach capable of capturing the spatial and temporal dynamics of $Ca^{2+}$ puffs, waves and oscillations that build upon qualitative insights from dynamical systems theory as applied to a reduced order model, which involves only a few variables. A well-known example of such reduction is that studied by Li and Rinzel [1994], Rüdiger [2014a],

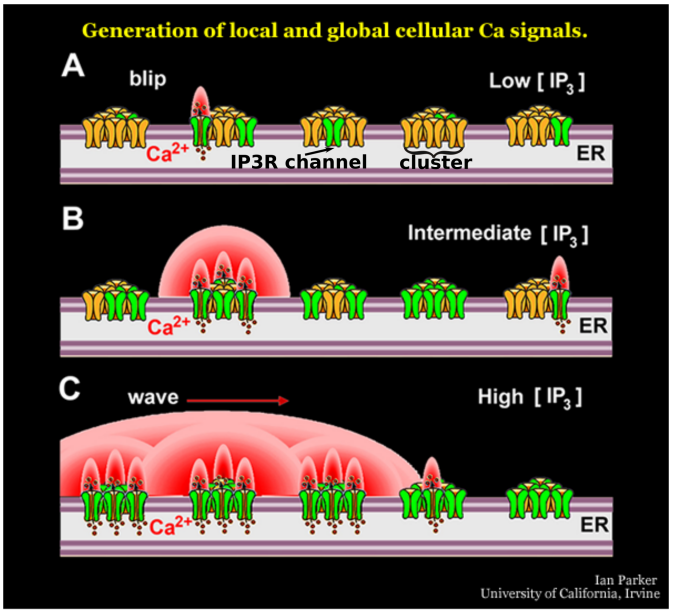


FIGURE 1.2: The $Ca^{2+}$ signalling events. (a) The smallest $Ca^{2+}$ release event called $Ca^{2+}$ blip prevails under low loads of $IP_3$ concentration. (b) $Ca^{2+}$ puff occurs as a $Ca^{2+}$ release from a cluster of $IP_3R$ channels. (c) At high $[IP_3]$, $Ca^{2+}$ release typically travels as a $Ca^{2+}$ wave. (Adapted from Parker [2014])

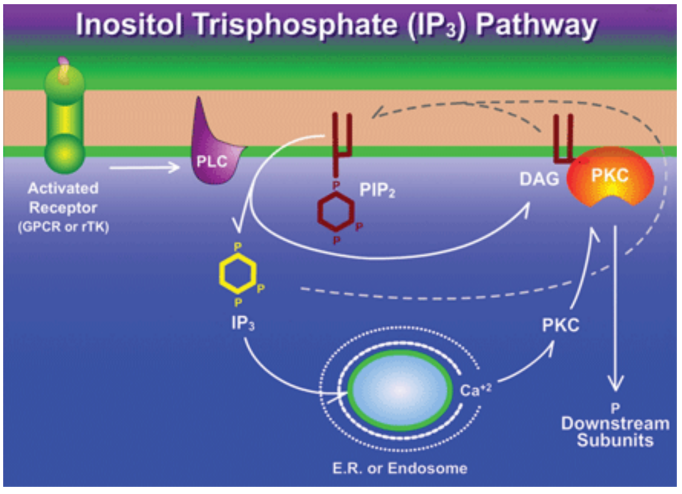


FIGURE 1.3: $IP_3$ production pathway. $IP_3$ is produced after external signal reaches G-protein (GPCR), enabling PLC to produce $IP_3$ kinase ($PIP_2$) [Thatcher, 2010].

which is in turn obtained from De Young and Keizer [1992]. First, we assume the $IP_3$ concentration to be sustained at a high enough level so that it increases the probability of occurrence of $Ca^{2+}$ waves and oscillations. Such an approach is an extension of the $Ca^{2+}$ puff excitability model in a single cluster proposed by Rüdiger [2014a]. The model we propose here is of a deterministic reaction-diffusion type, where diffusion of $Ca^{2+}$ between clusters of channels smooths the $Ca^{2+}$ release from individual activated clusters modelled by reaction dynamics. Here we study the dependence of the velocity and period of waves and oscillations on the diffusion coefficient, equilibration rate and a number of channels in each cluster.

Further, we extend our approach considering the realistic dynamics of $Ca^{2+}$ release and various levels of $[IP_3]$. We propose a stochastic modelling of $[Ca^{2+}]$ released from the channels in a two-dimensional domain in the ER membrane containing a random distribution of channels. We aim to link the local characteristics of $IP_3R$ channels and clusters, such as the numbers of channels in clusters and the characteristics of individual channels, with the statistics of global $Ca^{2+}$ spikes and waves. From the stochastic behaviour of $Ca^{2+}$ releases from a single cluster obtained from our model we gain an insight into the nature of $Ca^{2+}$ signal production by comparing the statistics of puffs with various computational and experimental findings [Dickinson et al., 2012, Rückl et al., 2015, Taufiq-Ur-Rahman et al., 2009, Wiltgen et al., 2014].

## 1.1 Motivation

$Ca^{2+}$ waves and oscillations perform the regulation of various vital functions in biological organisms. Thus, it is a crucial challenge nowadays to understand how $Ca^{2+}$ operates because disorders in $Ca^{2+}$ regulation could cause multiple diseases. For example, neurodegenerative disorders are linked with dysfunction of $IP_3R$ channels in neurones e.g. Huntington's disease, spinocerebellar ataxia and Alzheimer disease [Fedorenko et al., 2014]. Also, disruption in $Ca/IP_3$ pathway might cause asthma, atrial arrhythmias, autism spectrum disorder, cancer, epilepsy, etc. [Berridge, 2016]. While we are concerned with different kinds of cells in this thesis, our study aims to develop a general approach to $Ca^{2+}$ dynamics which contributed to the fundamental understanding of $Ca^{2+}$ signalling.

The present study is focused on building a new understanding of the dynamical properties of $Ca^{2+}$ releases within a membrane – $Ca^{2+}$ puffs, $Ca^{2+}$ spikes, $Ca^{2+}$ waves and $Ca^{2+}$ oscillations. A $Ca^{2+}$ wave is a kind of a chemical wave regulating processes in a variety of cells. Information is often transmitted as a pulse of increased $Ca^{2+}$ concentration travelling through the cytoplasm. Experimental evidence of $Ca^{2+}$ waves exist in medaka eggs [Ridgway et al., 1977], *Xenopus* oocytes [Lechleiter et al., 1991, Wiseman et al., 2018], hepatocytes [Nathanson et al., 1994], articular chondrocytes [Dandrea and Vittur, 1995], cardiac myocytes [Nivala et al., 2012] etc. A $Ca^{2+}$ spike is normally described as a $Ca^{2+}$ release event triggered from a bunch of clusters which is confined in space (normally by the action of buffers), and its main regulatory function is in encoding the sequences which trigger further protein cascades [Cheng and Lederer, 2008, Thurley et al., 2014]. $Ca^{2+}$ oscillations (repetitive $Ca^{2+}$ waves or spikes) are also experimentally observed in cells such as immature oocytes during fertilisation, liver cells, smooth muscle cells, astrocytes, etc. [Berridge, 2007]. The sequences of spikes or waves, sometimes called wave trains, are versatile and not necessarily periodic. They are believed to be involved in various regulatory functions in living cells [Thurley et al., 2014]. $Ca^{2+}$ puffs were observed in many cell types e.g. *Xenopus laevis* oocytes [Parker and Ivorra, 1990], HeLa cells [Bootman and Berridge, 1996], human neuroblastoma cells [Dickinson et al., 2012, Smith et al., 2009]. It is generally believed that both $Ca^{2+}$ waves and $Ca^{2+}$ oscillations are formed from lower hierarchical structures $Ca^{2+}$ puffs. However, under some physiological conditions, $Ca^{2+}$ puffs have a separate regulation value [Berridge et al., 1998, Nakamura et al., 2012]. Simple computational models capable of simulating different types of behaviour such as $Ca^{2+}$ puffs, waves and oscillations, and characterising them qualitatively and qualitatively in time and space are extremely important for a good understanding of the underlying processes.

Motivated by a wealth of observations and measurements of $Ca^{2+}$ concentration under different experimental circumstances, here we aim to develop a model that would schematically represent the actual physiology of the $Ca^{2+}$ pattern formation. In Figure 1.4 we present a typical fluorescent traces of $Ca^{2+}$ signals for two cell types as an example of such experimental evidence previously reported. Figure 1.4 (a) and (b) represent the classical experiments performed by Marchant et al. [1999] on *Xenopus* oocytes. They observe $Ca^{2+}$ puff shown in Figure 1.4 (a) without prior $IP_3$ photorelease. Figure 1.4 (b) depicts a $Ca^{2+}$ wave triggered by $IP_3$ release from a cage by photolysis. Typically, the velocities of such waves vary considerably. For example, on the surfaces of *Xenopus* eggs, it is about $10\,\mu$m/s. However, for other cell types, it may reach up to $100\,\mu$m/s. Another distinctive example of experimental studies concerns the observation of $Ca^{2+}$ oscillations. Generally, $Ca^{2+}$ oscillations occur either spontaneously, or in response to stimulation. Observations of testosterone-induced $Ca^{2+}$ oscillations in SH-SY5Y neuroblastoma cells, as reported by Estrada et al. [2006] is shown in Figure 1.4 (c). The amplitude, shape, and period of such oscillations are highly variable and depend on the type of cell. The periods may vary from around one to hundreds of seconds.

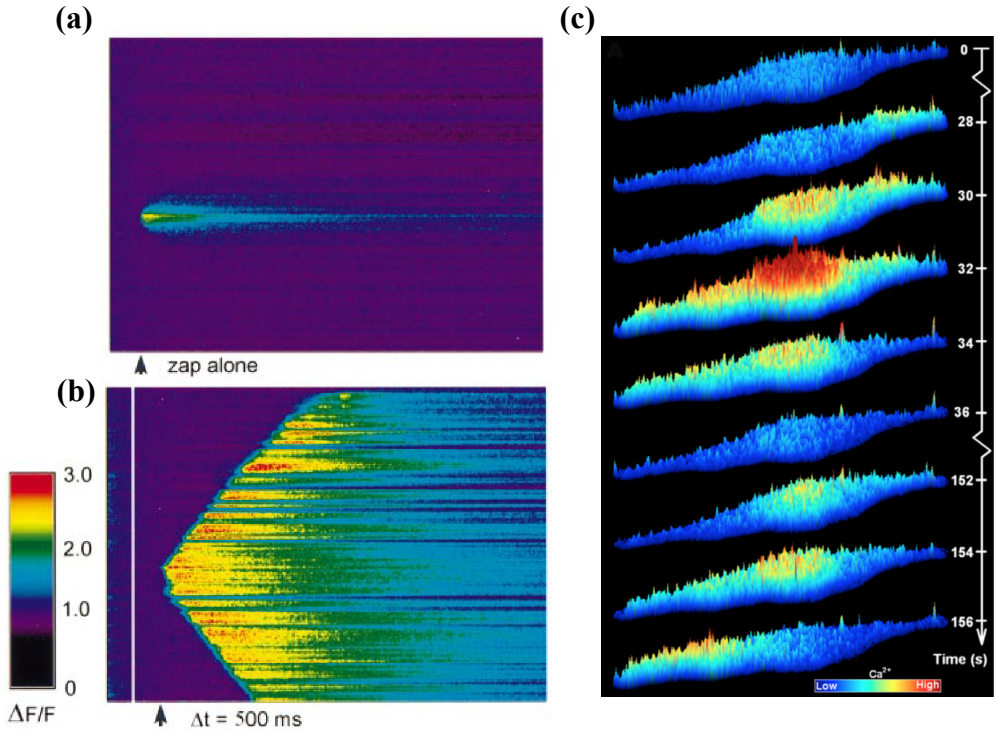


FIGURE 1.4: The experimental observations of the $Ca^{2+}$ puff without $IP_3$ photorelease (a) and $Ca^{2+}$ wave triggered by photolysis flashes (b) in *Xenopus* oocytes (adapted from Marchant et al. [1999]). (c) The observations of $Ca^{2+}$ oscillations in SH-SY5Y neuroblastoma cells (adapted from Estrada et al. [2006]).

The dynamical system analysis is further applied here to the non-homogeneous reaction-diffusion equations developed for the group of $IP_3R$ channel clusters in the ER membrane of a typical cell. Using this approach, we hope to be able to qualitatively represent the $Ca^{2+}$ release processes in clusters in the ER membrane and to give a deeper understanding of the mechanisms underlying the interaction between clusters. It is widely believed that the interaction between clusters is governed by $Ca^{2+}$ diffusion. The other important component of $Ca^{2+}$ modelling is taking account for the stochastic nature of $Ca^{2+}$ release events. The approach that combines stochastic

and deterministic modelling is very common nowadays [Rüdiger et al., 2007, 2010a] and will be employed further in this research. Broadly speaking, it is often assumed that there are two major reasons for the occurrence of $Ca^{2+}$ spikes, waves and oscillations. We consider the domain of a membrane which represents the cluster of channels in an unexcited state. It is generally known that random $Ca^{2+}$ blips occur continuously throughout this domain. The first possible reason for the global $Ca^{2+}$ signals to occur is that extracellular $Ca^{2+}$ released by an external stimulus enters the domain and prompts excitation of sequences of clusters leading to a large-scale release event. The second reason is that the random behaviour of $Ca^{2+}$ blips can cooperate in such a way that spontaneous large-scale events occur. Because of these, $Ca^{2+}$ puffs can occur solely or in groups leading to $Ca^{2+}$ waves and oscillations. We are interested in developing a model capable of showing the emergence of such behaviour using reduced approaches. It helps in our understanding the formation of $Ca^{2+}$ signals and the influence of the various conditions in the cell and membrane on the $Ca^{2+}$ dynamics.

## 1.2 Aims and Research objectives

In this thesis, we aim to build a simple model using a reduced modelling approach, which allows us to study the general tendencies in a complex nature of $Ca^{2+}$ signalling. Then we aim to extend this model accounting for more detailed dynamics according to the nature of $Ca^{2+}$ blips, puffs, spikes, waves and oscillations. We aim to address the unresolved questions in $Ca^{2+}$ signalling such as how channels are assembled into clusters and how the particular arrangements affect the generation of $Ca^{2+}$ signals. The general aims of the present work and the specific objectives are enumerated below.

**Aims:**

- To understand the generic principles of the transmission of signalling within a cell via $Ca^{2+}$ excitations.
- To distil the essential factors out of highly complex physicochemical behaviour in the spirit of minimalism, and to incorporate them in a model of $Ca^{2+}$ signalling.
- To determine how the parameters governing the mechanisms of $Ca^{2+}$ signalling affect the local and global patterns performing various regulation functions.

**Objectives:**

- To study the emergence of $Ca^{2+}$ puffs and oscillations in an isolated cluster with a simplified model of $Ca^{2+}$ signalling.
- To study the spatial aspects of the emergence of $Ca^{2+}$ waves and oscillations with a reaction-diffusion framework comprising an extended modelling approach of a chain of coupled clusters and a one-dimensional membrane.
- To study the emergence of $Ca^{2+}$ signals with a realistic two-dimensional stochastic approach accounting for $IP_3$ variability.

- To explain a rich set of experimentally observed $Ca^{2+}$ dynamics phenomena theoretically.
- To study the connections between $IP_3R$ channels forming a cluster with a modified Ising model.

Following the aims and objectives, further, we present the layout of the thesis.

## 1.3 The layout of the thesis

An introduction to the $Ca^{2+}$ dynamics and the motivation for the present work were briefly discussed in the current chapter. The relevant literature reviewed in Chapter 2. Further, we extend the discussion to the model developed in the current study in Chapters 3 and 4. We present a detailed study of the three-state-model [Rüdiger, 2014a] of a single cluster of $IP_3R$ channel channels in Chapter 3 adjusting the model to different measurements. Then we formulate the spatial extension of the cluster-based model proposed in Chapter 4. In Section 4.2 the oscillatory $Ca^{2+}$ behaviour in the discrete chain of coupled clusters is studied. Then, in Section 4.3 we model the emergence of $Ca^{2+}$ waves and $Ca^{2+}$ oscillations in the finite one-dimensional domain of the ER. Further, we include $IP_3$ dependence and extend the model to two spatial dimensions with random positioning of clusters in Chapter 5. We introduce the stochasticity into $IP_3$-dependent dynamical model in Chapter 6. In Chapter 7, we define the major triggers of $Ca^{2+}$ behaviour and incorporate them into the stochastic model capable of explaining various experimental observations. Chapter 8 contains the modelling of a cluster of coupled channels using the mean-field Ising approach. Finally, Chapter 9 contains conclusions and suggestions for future research.

# Chapter 2

# Background and Literature Review

Understanding the nature of $Ca^{2+}$ signalling is a crucial scientific challenge. An important aspect of this is the capability of modelling the processes as informed by laboratory experiments. The significant rise in the recent interest in the phenomenological and detailed modelling of complex biological systems is due to the current development of experimental capabilities and computational techniques at a multiplicity of scales. Hence, new disciplines such as computational biology, biophysics, mathematical physiology etc. have recently grown in a highly interdisciplinary way. The main interest of these disciplines is the study of neuronal networks, cell regulation and cell signalling. A reasonably significant part of studies in these disciplines concerns $Ca^{2+}$ modelling. The research in the calcium signalling domain has come into play in the last thirty-forty years. Although many individual components of $Ca^{2+}$ signalling pathway have been studied in detail, the general picture of $Ca^{2+}$ dynamics is currently at a stage of development and requires further study.

In this chapter, we aim to briefly cover some of the most important models from the literature relevant to the present study. Since our analysis and computations in the subsequent chapters are based on some of these models we describe them in greater detail. These models include the kinetic gating model proposed by De Young and Keizer [1992] and its several simplifications made in Li and Rinzel [1994], and Rüdiger [2014a].

## 2.1 Modelling of calcium dynamics

The modelling proposed in this thesis shares certain features (e.g., excitability, activation-inhibition and reaction-diffusion) with several well-known models in different branches of mathematical biology. Mathematical modelling in biology originated from genetics and neuroscience. Perhaps the most prominent among the studies of excitability in neuronal networks for electrical action potential propagation through axon is the model proposed by Hodgkin and Huxley [1952]. A simplification of this model by FitzHugh [1961], Nagumo et al. [1962] became one of the best-studied models of excitable systems. It has served as a basis for a plethora of new approaches in mathematical biology – FitzHugh-Nagumo type models [Guckenheimer and Kuehn, 2009, Jones, 1984, Lindner et al., 2004]. The original FitzHugh-Nagumo is explained in detail further here.

Another direction in mathematical biology can be attributed to having started from a classical work by Fisher [1937] who introduced reaction-diffusion type modelling which yielded a travelling wave solution corresponding to the spatial spread of a particular gene in biological populations. Similarly, a reaction-diffusion model was proposed by Turing [1952] to study the morphogenesis of patterns in mammals using activator-inhibitor-based description.

In the present thesis, we study the excitability in $Ca^{2+}$ signalling. We start with an activator-inhibitor model of $Ca^{2+}$ dynamics [Rüdiger et al., 2010b] which exhibits excitability similarly to FitzHugh-Nagumo type models. We introduce in the tradition of Fisher [1937] and Turing [1952], a reaction-diffusion dynamics into this model to study the formation of patterns in $Ca^{2+}$ signalling.

At this point, we discuss the body of published literature concerned with $Ca^{2+}$ dynamics. Typically, $Ca^{2+}$ waves and $Ca^{2+}$ oscillations are studied deterministically (extensively reviewed by [Falcke, 2003b]). Hence, $Ca^{2+}$ wave models use phenomenological approaches with a smooth wave-front propagating at constant velocity composed of the cooperative $Ca^{2+}$ puffs. Deterministic models focused on $Ca^{2+}$ dynamics at the intracellular level are tabulated in Table 2.1. These models are mostly described in terms of reaction-diffusion partial differential equations of $Ca^{2+}$ fluxes which are reviewed in detail by Falcke [2004]. For example, Kupferman et al. [1997] developed a simple model of $Ca^{2+}$ wave propagation. The wave velocity was found by matching a piecewise linear analytical solution with boundary conditions at the interfaces of the membrane. The limitation of this study is the oversimplification of the wave propagation phenomena as the non-linear interactions play crucial roles in the front initiation. Another phenomenological and deterministic approach for $Ca^{2+}$ wave modelling has been employed by Duffy et al. [1998] who added layers of complexity associated with the non-linear activation and buffering of $Ca^{2+}$. They obtained realistic dynamics of wave propagation. Although quite innovative at the time, this approach is limited by the choice of non-linear terms, which do not address the detailed nature of $Ca^{2+}$ release channels as the building blocks of $Ca^{2+}$ signalling at smaller scales of structural hierarchy within cells.

There is an alternative approach to the modelling of $Ca^{2+}$ dynamics. It is based on the deterministic gating models developed for single-channel activity. In the simplest case, an $IP_3R$ channel can be regarded as a two-state system with random transitions between the opened and the closed states. The dynamics of such systems is described in terms of mean fractions of the channels in the corresponding state calculated according to the bulk volumes. The gating in channels is described by open probability and it can be dependent on various environmental conditions, such as changes in chemical concentrations, temperature etc. The gating properties of a single channel can be obtained from patch-clamp measurements [Neher and Sakmann, 1976]. The key ideas behind the gating-based modelling are presented by De Young and Keizer [1992] (further referred as DYK model). This model is also included as the deterministic model in Table 2.1. It plays a crucial role in the current research, and, is discussed in greater detail in Section 2.3. In parallel, an alternative gating model based on a three-subunit structure was developed by Atri et al. [1993]. They studied the propagation of the planar, circular and spiral $Ca^{2+}$ waves and the emergence of $Ca^{2+}$ oscillations. Similarly to DYK, the authors incorporated $Ca^{2+}$ activation and inhibition of $IP_3R$. Within a similar framework, Jafri and Keizer [1995] studied the influence of buffering on wave propagation. While all these studies are used extensively as the basis for $Ca^{2+}$ modelling, the clustering of $IP_3R$ channels has been observed much later [Mak and Foskett,

1997]. Thus, these studies are built on the assumption of well-mixing subunits in the membrane having not enough flexibility to capture all the variety of phenomena observed.

Most of the former models are based on the assumption that $Ca^{2+}$ release channels have a homogeneous distribution in the cytoplasm. However, experimental findings suggest that channels are grouped into clusters in the membrane [Mak and Foskett, 1997, Smith et al., 2009]. The diameters of these clusters ($\sim 500$ nm in *Xenopus* oocytes) are much smaller compared to distances between them ($\sim 3\,\mu$m in *Xenopus* oocytes [Rüdiger, 2014b]). This problem was taken into account by Sneyd and Sherratt [1997] in the spatially discrete model. This study includes the calculation of the upper limit of a cluster spacing allowing for wave propagation. Wave velocity in *Xenopus* oocyte was modelled by Dupont and Goldbeter [1993] with much lower diffusion coefficient compared to the discrete two-pool model of cardiac myocytes [Dupont and Goldbeter, 1994]. The investigation of spatial discreteness was summarised in the fire-diffuse-fire model proposed by Dawson et al. [1999]. The saltatory (burst-like) and continuous mechanisms of the wave propagation were revealed in this study for certain limiting cases. The timescales for the decay of $Ca^{2+}$ profiles at the single cluster were estimated by Thul and Falcke [2004b] and the optimal cluster sizes for effective transmission of oscillations within the cell were studied by Shuai and Jung [2003b].

TABLE 2.1: Stochastic and deterministic $Ca^{2+}$ models on the different spatial levels.

| **Model type** / **Spatial level** | **Deterministic models** | **Stochastic/hybrid models** |
|---|---|---|
| Isolated channel | - | Rüdiger et al. [2007]<br>Shuai et al. [2008]<br>Siekmann et al. [2012] |
| Cluster of channels | - | Shuai et al. [2006]<br>Rüdiger et al. [2010b]<br>Ullah et al. [2012]<br>Cao et al. [2013]<br>Rüdiger [2014a] |
| Intracellular level | De Young and Keizer [1992]<br>Atri et al. [1993]<br>Dupont and Goldbeter [1993, 1994]<br>Li and Rinzel [1994]<br>Jafri and Keizer [1995]<br>Thul and Falcke [2004b]<br>Kupferman et al. [1997]<br>Sneyd and Sherratt [1997]<br>Duffy et al. [1998]<br>Dawson et al. [1999]<br>Thul et al. [2009]<br>Cao et al. [2014]<br>Dickinson et al. [2016]<br>Sneyd et al. [2017]<br>Han et al. [2017]<br>Braichenko et al. [2018] | Keizer and Smith [1998]<br>Shuai and Jung [2003b]<br>Falcke [2003a]<br>Coombes and Timofeeva [2003]<br>Thul and Falcke [2004a, 2006]<br>Skupin et al. [2008]<br>Calabrese et al. [2010]<br>Thurley et al. [2011, 2012]<br>Thul et al. [2012]<br>Weinberg and Smith [2014]<br>Rückl et al. [2015]<br>Rückl and Rüdiger [2016]<br>Cao et al. [2017]<br>Falcke et al. [2018] |

According to experimental findings by Bootman et al. [1997], even global events of $Ca^{2+}$ releases can be formed from elementary events by chance. Therefore, $Ca^{2+}$ dynamics should be described

in detail using stochastic methods. Even $Ca^{2+}$ waves and oscillations in cells which are not negligible can be formed of random cooperative openings [Schmidle, 2008]. The stochastic nature of $Ca^{2+}$ signalling was first considered by Keizer and Smith [1998] in their model for a saltatory propagation of $Ca^{2+}$ waves in cardiac myocytes (the stochastic model in Table 2.1). Employing a reaction-diffusion approach, they extended the simplified two-variable model by Li and Rinzel [1994] derived from DYK. The work by Falcke [2003a] was devoted to the stochastic modelling of $Ca^{2+}$ oscillations. Thereafter, Calabrese et al. [2010], Coombes and Timofeeva [2003] adapted fire-diffuse-fire model for an inhomogeneous distribution of channels with stochastic openings.

As reviewed by Dupont et al. [2016], with the development of experimental techniques for single-channel activity measurements [Ionescu et al., 2007], a separate branch of $Ca^{2+}$ modelling emerged [Siekmann et al., 2012, Ullah et al., 2012]. These models are obtained by directly fitting to the single-channel data measured from the channels at the nuclear envelope. They feature several modes of $Ca^{2+}$ signalling known as park mode (mostly resting $IP_3R$ channel) and drive mode (active $IP_3R$ channel releasing $Ca^{2+}$ most of the time). The transitions between the modes might be complex and nonlinear; and may also vary for different cell types as well as the number of modes. In most of published literature, there are 2 [Cao et al., 2014, 2017, Falcke et al., 2018, Han et al., 2017, Siekmann et al., 2012] or 3 [Ionescu et al., 2007, Ullah et al., 2012] modes in $IP_3R$ channels.

Most of the standard $Ca^{2+}$ models are highly complex. They may contain from two to thousands of variables [Rüdiger, 2014b]. With the discovery of spatial inhomogeneity [Smith et al., 2009] the complexity grows even more rapidly. Our approach is to decompose the $Ca^{2+}$ dynamics into easily manageable modules, which capture the various experimental and theoretical findings and compose a phenomenological model that can reproduce the variety of phenomena observed.

There have been several attempts to reduce the complexity of $Ca^{2+}$ modelling. The most successful ones incorporate a reduction of the number of variables within a hybrid stochastic-deterministic approach. However, this technique, in combination with reaction-diffusion modelling at the whole-cell level, is still computationally too expensive – the hybrid models in Table 2.1. Moreover, cellular geometry appears important to $Ca^{2+}$ dynamics and makes the modelling task even more complicated [Sneyd et al., 2017]. In the simplest models, the membrane is assumed to be an idealised flat plane, the channel openings are represented by source terms for $Ca^{2+}$ chemical species (Figure 2.1 (a)). This approach is relevant for studying the properties of $Ca^{2+}$ signals qualitatively, thus, we use this approach in our model. There are also studies Shuai et al. [2006] which consider channels to be distributed in the cytosolic voxels (Figure 2.1 (b)) to incorporate the effects of signalling in three dimensions. We believe that the two-dimensional modelling is sufficient for the task at hand, i.e. to bring out the essentials of the physicochemical behaviour without the ambition to mimic every detail, so we will not consider the three-dimensional case due to it being over-complicated for conceptualisation.

To summarise all the studies reviewed, we conclude that there are some fundamental deterministic models [De Young and Keizer, 1992, Duffy et al., 1998] which can describe $Ca^{2+}$ waves and some types of oscillations. There are also many stochastic and hybrid models [Cao et al., 2013, Rüdiger et al., 2007, Shuai et al., 2008, Skupin et al., 2008, Thul and Falcke, 2006, Thurley et al., 2011] at a single spatial scale of structural hierarchy, as well as several multi-scale ones [Thul et al., 2012, Ullah et al., 2012]. In addition to these, there are some fundamental

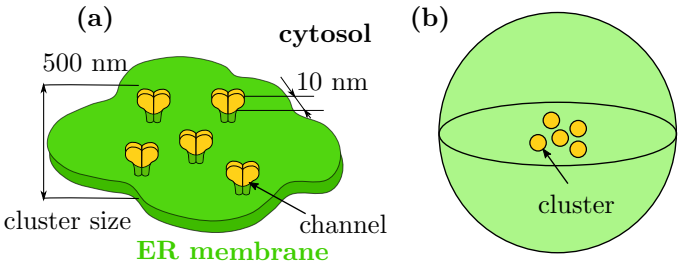


FIGURE 2.1: Different ER membrane geometry in modelling concepts. (a) The green surface represents the membrane with the channels forming clusters [Rüdiger, 2014b]. (b) Bulk distributed channels in a spherical domain [Thurley et al., 2012].

stochastic models of $Ca^{2+}$ releases from $IP_3R$ channels developed by Falcke [2003a], Keizer and Smith [1998].

The focus of the current research is motivated by the following: on the one hand, deterministic models are generally simple models and are not able to reproduce a variety of spontaneous phenomena experimentally observed in living cells. On the other hand, most of stochastic and hybrid models tend to be so complicated that it becomes extremely challenging to distil any understanding of the underlying physical and biological mechanisms because of a multiplicity of parameters simultaneously controlling the response.

The current research focuses on combining the deterministic and stochastic properties of $Ca^{2+}$ waves and oscillations occurring in the ER membrane containing multiple clustered channels. Unlike previously considered deterministic models [Dawson et al., 1999, Sneyd and Sherratt, 1997, Thul et al., 2009], our approach here gives a clearer mechanistic insight into the link between single-channel properties and the features at higher levels in the spatial hierarchy. This is achieved by a dynamical systems analysis of the reduced version of the DYK [De Young and Keizer, 1992] model proposed by Rüdiger [2014a]. Our model allows us to understand different dynamical regimes at the single-cluster level and relate these properties to larger spatial scales. This reveals the dependence of $Ca^{2+}$ wave and oscillatory response on the parameters of channels and clusters, including their inhibition and termination. We also build on the results of a detailed hybrid stochastic-deterministic single-cluster study by Rückl et al. [2015] and its extension on a grid of clusters [Rückl and Rüdiger, 2016] which shows different durations of $Ca^{2+}$ release events depending on the $IP_3$ level.

We introduce a deterministic spatial model of $Ca^{2+}$ puffs, waves and oscillations building upon qualitative insights from dynamical systems theory applied to a lumped parameter model of $IP_3R$ channel subunits [De Young and Keizer, 1992], reduced to a few variables [Li and Rinzel, 1994, Rüdiger, 2014a] integrated into channels and heterogeneous clusters of channels [Rückl et al., 2015]. We assume the $IP_3$ concentration to be sustained at a high level so that it increases the probability of the occurrence of $Ca^{2+}$ waves and oscillations, extending the observation of excitability of channel clusters in [Rüdiger, 2014a]. Note, that $Ca^{2+}$ signalling is a complex stochastic problem. However, at first, we build an expository device – a simplified deterministic model – to investigate various principal types of behaviour, which serves as the foundation for the stochastic analysis introduced next. Further, we account for the variability of $[IP_3]$ levels by including $IP_3$ unbinding. The extended model also gives insight into the number of activatable channels. According to the most recent experimental studies four subunits must bind $IP_3$ to

enable a channel activation [Alzayady et al., 2016]. Unlike models by [Rückl and Rüdiger, 2016, Rückl et al., 2015], who uses the assumption that at least 3 subunits in a channel must bind $IP_3$ to became activatable, our model is matched with the current experimental data requiring all 4 subunits to bind [$IP_3$] [Alzayady et al., 2016]. The model proposed here is of a reaction-diffusion type. The diffusion of $Ca^{2+}$ between clusters of channels smooths the $Ca^{2+}$ release from individual activated clusters modelled by reaction dynamics [Braichenko et al., 2018]. We also study the dependence of the velocity and period of waves, spikes and oscillations on the diffusion coefficient, equilibration rate and a number of channels in each cluster.

Aiming to validate the model against experimental results, we propose an $IP_3$ extension of the model within deterministic and stochastic frameworks. We consider realistic timescales for $IP_3$ dynamics [Dickinson et al., 2016] to explain the termination of $Ca^{2+}$ oscillations. Our model shows realistic inter-puff intervals and is suitable for studying the spatial effects of $Ca^{2+}$ releases.

Finally, we study the effect of anti-cooperation between $IP_3$ channels induced by $IP_3$ binding according to Taufiq-Ur-Rahman et al. [2009]. We adapt our cluster-based model to the data and study the $Ca^{2+}$ release in deterministic and stochastic setup incorporating coupling effects. The modelling results display great consistency with the experimental data provided by [Dickinson et al., 2012, Wiltgen et al., 2014]. In the following sections, a host of models are discussed upon which we develop our analyses and computations in the subsequent chapters.

## 2.2 Hodgkin and Huxley model and its simplification by FitzHugh and Nagumo

To introduce the excitability and dynamical system analysis, we cover two classical excitable models of neuronal electrical activity in this section. For further details please refer to Keener and Sneyd [2008] or Murray [2000].

The Hodgkin-Huxley model [Hodgkin and Huxley, 1952] was developed to show the propagation of electrical impulse throughout the nerve axon of a squid. The impulses arise because the membrane is permeable to potassium ($K^+$) ions and sodium ($Na^+$) ions. There is an equilibrium transmembrane potential of $V_{\text{eq}} = -70$ mV in the rest state, which can be altered due to the ions passing through the membrane. Thus, the current is given by

$$I(t) = C\frac{\mathrm{d}V}{\mathrm{d}t} + I_i, \tag{2.1}$$

where the first term is the contribution from the change in transmembrane potential $V$ within a structure of capacitance $C$, the second term $I_i$ corresponds to the current due to the individual passing of ions through the membrane. The individual currents are obtained from the experiments by Hodgkin and Huxley [1952] and comprise the total ion current

$$I_i = I_{Na} + I_K + I_L = g_{Na}m^3h(V - V_{Na}) + g_K n^4(V - V_K) + g_L(V - V_L), \tag{2.2}$$

where $I_{Na}$ is sodium current, $I_K$ is potassium current, $I_L$ is a leak current (includes all other types of ions); $g_{Na}m^3h$, $g_K n^4$, and $g_L$ are corresponding conductances found in the experiment [Hodgkin and Huxley, 1952]; $V_{Na}$, $V_K$, and $V_L$ are constant equilibrium potentials. The

gating variables $m$, $n$, and $h$ (change in the range between 0 and 1) were derived from the respective conductances to agree with the experimental data. Their kinetics is governed by the following first-order differential equations

$$\frac{\mathrm{d}m}{\mathrm{d}t} = \alpha_m(\tilde{V})(1-m) - \beta_m(\tilde{V})m, \tag{2.3}$$

$$\frac{\mathrm{d}n}{\mathrm{d}t} = \alpha_n(\tilde{V})(1-n) - \beta_n(\tilde{V})n, \tag{2.4}$$

$$\frac{\mathrm{d}h}{\mathrm{d}t} = \alpha_h(\tilde{V})(1-h) - \beta_h(\tilde{V})h, \tag{2.5}$$

where $n$ – potassium activation, $m$ – sodium activation, $h$ – sodium inactivation, $\tilde{V} = V - V_{\mathrm{eq}}$. Transition rate functions $\alpha(V)$ and $\beta(V)$ are obtained by matching the solutions of Equations (2.3)–(2.5) to the experimental data (for details please see Keener and Sneyd [2008]):

$$\alpha_m = 0.1\frac{25-\tilde{V}}{\exp\left(\frac{25-\tilde{V}}{10}\right)-1}, \tag{2.6}$$

$$\beta_m = 4\exp\left(\frac{-\tilde{V}}{18}\right), \tag{2.7}$$

$$\alpha_h = 0.07\exp\left(\frac{-\tilde{V}}{20}\right), \tag{2.8}$$

$$\beta_h = \frac{1}{\exp\left(\frac{30-\tilde{V}}{10}\right)+1}, \tag{2.9}$$

$$\alpha_n = 0.01\,\frac{10-\tilde{V}}{\exp\left(\frac{10-\tilde{V}}{10}\right)-1}, \tag{2.10}$$

$$\beta_m = 0.125\exp\left(\frac{-\tilde{V}}{80}\right), \tag{2.11}$$

where the constants $g_{Na} = 120$, $g_K = 36$ and $g_L = 30$.

Under the conditions of some external current $I_a$ applied to the axon from (2.1) considering (2.2) we obtain

$$C\frac{\mathrm{d}\tilde{V}}{\mathrm{d}t} = -g_{Na}m^3h(\tilde{V}-\tilde{V}_{Na}) - g_Kn^4(\tilde{V}-\tilde{V}_K) - g_L(\tilde{V}-\tilde{V}_L) + I_a, \tag{2.12}$$

written in terms of variable $\tilde{V} = V - V_{\mathrm{eq}}$ to simplify the formulation of Equations (2.3)–(2.11) retaining Equation (2.2) unchanged since $V_{\mathrm{eq}}$ is constant and $\mathrm{d}V/\,\mathrm{d}t = \mathrm{d}\tilde{V}/\,\mathrm{d}t$. Here $\tilde{V}_{Na} = V_{Na} - V_{\mathrm{eq}}$, $\tilde{V}_K = V_K - V_{\mathrm{eq}}$, $\tilde{V}_L = V_L - V_{\mathrm{eq}}$.

The system (2.3)–(2.5) together with Equation (2.12) forms the Hodgkin-Huxley model which is capable of showing different kinds of behaviour characteristic to nerve regulation. The dynamical analysis of the full 4-variable system is a challenging task, thus FitzHugh and Nagumo [FitzHugh, 1961, Nagumo et al., 1962] reduced it to capture the key features of the model. The reduction is based on the difference in the timescales for $m$, $n$, and $h$ variables. As $m$ changes much faster than $n$ and $h$, the authors considered $\mathrm{d}m/\,\mathrm{d}t = 0$ in Equation (2.3). They also observed that the substitution $h = h_0$, where $h_0$ is constant, does not change the behaviour significantly. The

implication of the assumptions made above results in the FitzHugh-Nagumo model

$$\frac{\mathrm{d}v}{\mathrm{d}t} = f(v) - w + I_a, \tag{2.13}$$

$$\frac{\mathrm{d}w}{\mathrm{d}t} = bv - \gamma w, \tag{2.14}$$

$$\tag{2.15}$$

where $v = V/V_1$ corresponds to the dimensionless membrane potential ($V_1$ is the largest stable solution of equation $\mathrm{d}V/\,\mathrm{d}t = -F(V)$). $F(V)$ and its dimensionless version $f(v) = v(a-v)(v-1)$ leads to a shape of the travelling electrical pulse; $0 < a < 1$, $b$, and $\gamma$ are positive constants which are parameters of the model; $w$ is an effective variable derived from $m$, $n$, and $h$; $t$ here and after in this section referred as dimensionless time variable. For non-dimensionalisation and the detailed expressions of dimensionless variables please see Keener and Sneyd [2008]. We do not provide them here to avoid distraction.

Equations (2.14), (2.15) can be studied by analysing the nullclines and fixed points of the system on the phase plane $(v, w)$. Nullclines are the lines on the phase plane for which one of the variables is time-independent. For example, the curve $w = f(v)$ in Figure 2.2 is $v$-nullcline. This nullcline is obtained by setting $\mathrm{d}v/\,\mathrm{d}t = 0$ in Equation (2.14). Similarly, the straight line $w = bv/\gamma$ is the $w$-nullcline. The steady states are characterised by the special points, known as the fixed points of the system (2.14), (2.15) obtained from solving the equations under the conditions of steady-state, i.e. $\mathrm{d}v/\,\mathrm{d}t = 0$, $\mathrm{d}w/\,\mathrm{d}t = 0$. These points are the points of intersection of the nullclines. The stability of these points can be determined by calculating the eigenvalues of the Jacobian at each point (see Strogatz [2014]). For example, the system has one stable fixed point at the origin $(0, 0)$ as shown in Figure 2.2. This means that at normal conditions, the system rests at this point. Also after perturbing the system, it returns to the fixed point after waiting for long enough. The phase portrait in Figure 2.2 (a) is an example of an excitable steady

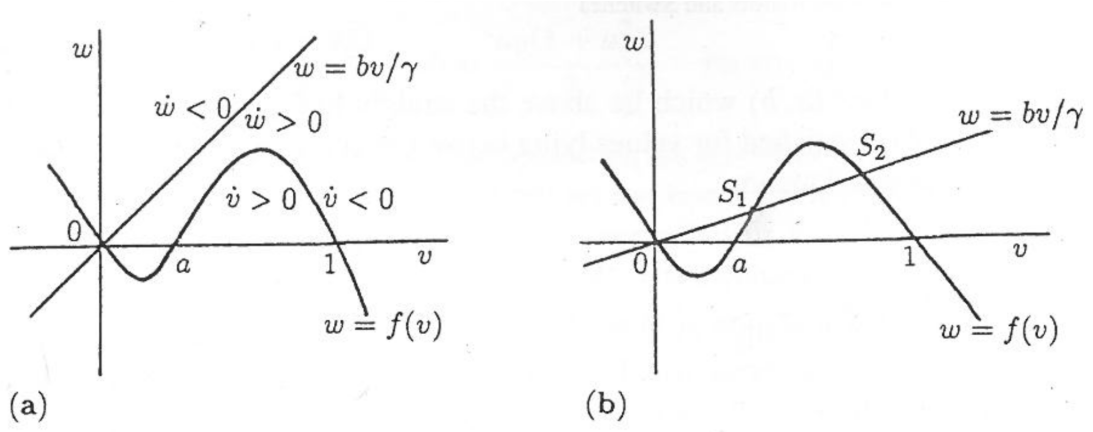


FIGURE 2.2: The nullclines in the phase plane for the FitHhugh-Nagumo model in the case of $I_a = 0$. (a) The example of the stable but excitable state. (b) The case with two stable states $(0, 0)$ and $S_2$ and one unstable $S_1$ obtained from (a) by changing parameters $a$, $b$ and $\gamma$ (adapted from Murray [2000]).

state. The actual mechanism of excitability is depicted in Figure 2.3. If a small perturbation drives the system away from the state $(0, 0)$, the system follows a small trajectory (for example $P$). Otherwise, if the perturbation is large to push the system to cross the unstable branch

and reach point $A$ then the system follows a large trajectory (for example, $ABCDO$). The evolution of dynamical variables $v$ and $w$ in time for large trajectory $ABCDO$ is shown in Figure 2.3 (b). The excitability is the key feature of the Hodgkin-Huxley model illustrated

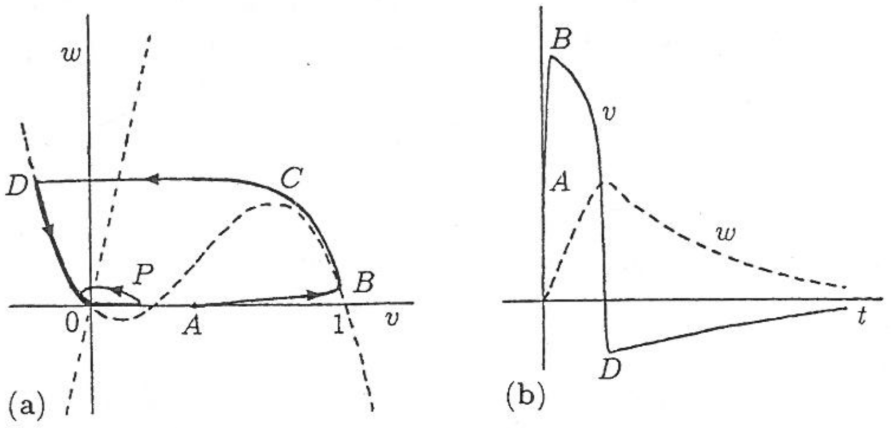


FIGURE 2.3: The excitability in the FitzHugh-Nagumo model for $I_a = 0$, $a = 0.25$, and $b = \gamma = 2 \times 10^{-3}$. (a) The small perturbation applied at the fixed point $(0, 0)$ drives short trajectory denoted $P$, while the large perturbation from $(0, 0)$ to $A$ gives long trajectory along the stable branches of the nullclines denoted $ABCDO$. (b) The trajectory $ABCDO$ in the phase diagram (a) interpreted as functions $v(t)$, $w(t)$ (adapted from Murray [2000]).

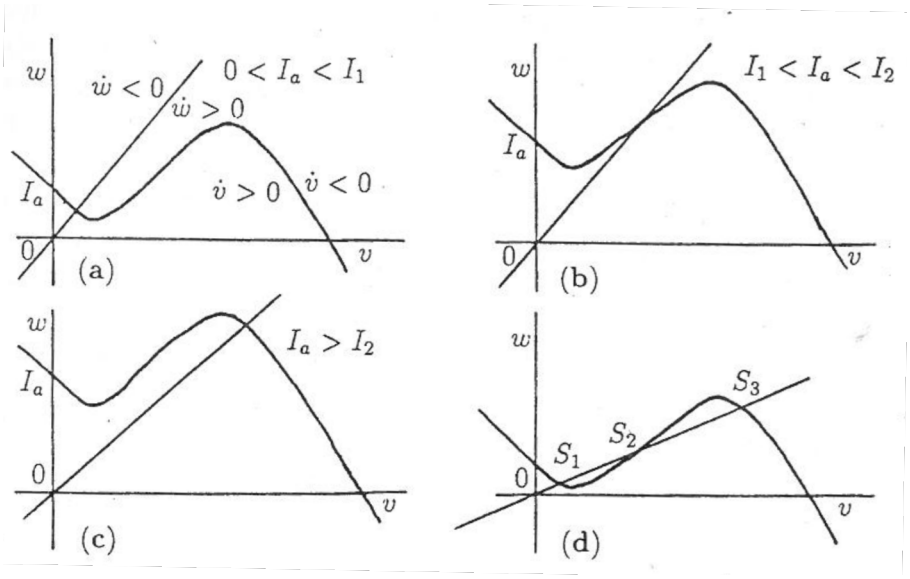


FIGURE 2.4: The nullclines for the FitzHugh-Nagumo model with different applied currents $I_a$. Plot (a) and (c) characterise excitable behaviour with stable fixed points. Plot (b) is for unstable and limit cycle periodic solutions. In the case (d) the fixed points $S_1$ and $S_3$ are stable while $S_2$ is unstable (adapted from [Murray, 2000]).

explicitly using the FitzHugh-Nagumo model. By varying the parameters $a$, $b$ and $\gamma$, one can switch the qualitative behaviour of the system from being excitable (Figure 2.2 (a)) to becoming bistable (Figure 2.2 (b)). The existence of two stable fixed points $(0, 0)$ and $S_2$ is an indicator of bistability.

Figure 2.4 illustrates the variety of phase portraits for different levels of the applied current $I_a$. Interestingly, through varying $I_a$ in a window $(I_1, I_2)$ shown in Figure 2.4 (b) the fixed point may

be unstable and the stable limit cycles are possible. The phase portrait depicted in Figure 2.4 (d) is similar to the one shown in Figure 2.2 (b).

Returning to $Ca^{2+}$ dynamics, the idea of the simplification of the general DYK model [De Young and Keizer, 1992] and deriving the FitzHugh-Nagumo-like excitable approach was adopted first by Li and Rinzel [1994] and then by Rüdiger [2014a]. The following three sections are devoted to the derivation of those models.

## 2.3 De Young and Keizer model of calcium oscillations

The DYK model [De Young and Keizer, 1992] is one of the first models which successfully accounts for key empirical findings of $IP_3R$ channels. In the original model, the channel consists of three subunits reflecting the conductance levels experimentally observed by Bezprozvanny et al. [1991], Watras et al. [1991]. In the more recent models, e. g. by Rückl et al. [2015], Rüdiger [2014a], each channel consists of four subunits, at least three of which need to be activated for channel opening. Each subunit has 3 binary state variables $S_{ijk} \in \{0, 1\}$, corresponding to 3 binding sites – for $IP_3$, activating $Ca^{2+}$ and inhibiting $Ca^{2+}$ – with a state transition diagram shown in Figure 2.5 and described in its caption. The fraction of subunits in a given state ($S_{ijk}$) is represented by the variable $x_{ijk}$, such that they sum up to unity, i.e. $\sum_{i=0}^{1}\sum_{j=0}^{1}\sum_{k=0}^{1} x_{i,j,k} = 1$. The presence of $IP_3$ at each channel enhances $Ca^{2+}$ release, while calcium either amplifies or inhibits further $Ca^{2+}$ release (called calcium-induced calcium release, $Ca^{2+}$-induced $Ca^{2+}$ release (CICR)).

The dynamics of the states depicted in the scheme shown in Figure 2.5 can be written as a set of differential equations. For example, the fraction of subunits in active state $S_{110}$, denoted $x_{110}$, is governed by the equation

$$\frac{\mathrm{d}x_{110}}{\mathrm{d}t} = -(V_1 + V_2 + V_3), \tag{2.16}$$

where

$$V_1 = b_5 x_{110} - a_5 c x_{100}, \tag{2.17}$$

$$V_2 = a_2 c x_{110} - b_2 x_{111}, \tag{2.18}$$

$$V_3 = b_1 x_{110} - a_1 p x_{010}. \tag{2.19}$$

Similar first-order equations describing the dynamics of other state variables $x_{ijk}$, formulated in terms of fractions of seven subunit states gives a full model of a subunit activation (there are eight subunits, but *only seven* of them are independent because the fractions of channels in corresponding states must add up to unity, i.e. $\sum_{i,j,k=0,1} x_{ijk} = 1$).

Returning to $IP_3R$ channel, all three subunits must be in state $S_{110}$ for the channel to be open. $Ca^{2+}$ released from opened channels spreads within the surroundings and triggers other channels to open. The steady-state open probability for a channel to open is calculated from the seven equations of type (2.16) under steady-state condition $\mathrm{d}x_{ijk}/\mathrm{d}t = 0$, where $i, j, k = 0, 1$. The

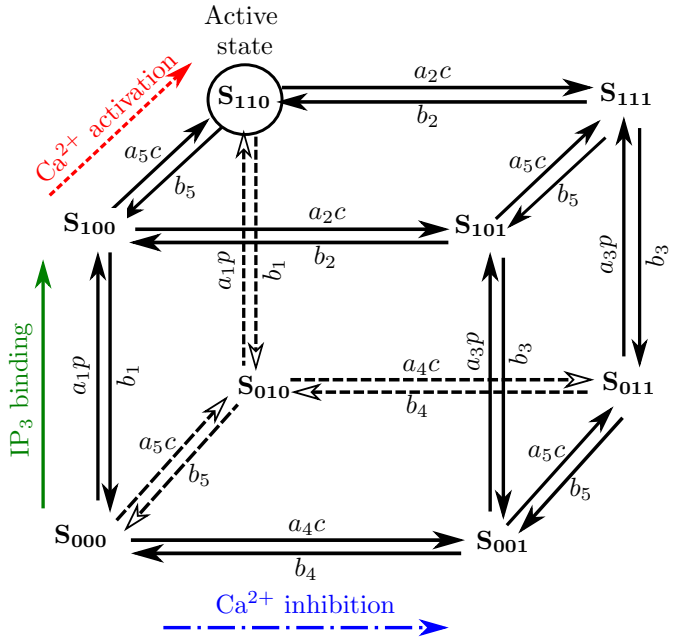


FIGURE 2.5: Schematic diagram of the DYK eight-state gating model of the activation of a single subunit of an $IP_3R$ channel; the eight corners of the schematic will be referred as the DYK cube [De Young and Keizer, 1992]. Each vertex of the cube directly corresponds to a specific state of a subunit labelled with $S_{ijk}$, where $i$ corresponds to the $IP_3$ activating site, $j$ to the $Ca^{2+}$ activating site and $k$ to the $Ca^{2+}$ inhibiting site. Each binding site can be either unbound $(i, j, k = 0)$, or bound $(i, j, k = 1)$. The green arrow indicates binding (unbinding) of $IP_3$ to the binding site while the red dashed and blue dot-dashed arrows correspond to $Ca^{2+}$ activating and inhibiting transitions respectively. The transitions between the states are governed by the second-order ($a_l p$ or $a_l c$, where $p = [IP_3]$, $c = [Ca^{2+}]$), and the first-order ($b_l$) rate constants, where $l = \overline{1,5}$) [De Young and Keizer, 1992]).

equilibrium open probability for a channel is

$$P^e_{\text{open}} = (x^e_{110})^3 = \left[\frac{cpd_2}{(cp + pd_2 + d_1d_2 + cd_3)(c + d_5)}\right]^3, \tag{2.20}$$

where $d_i = b_i/a_i$, $i = \overline{1,5}$. The distributions of the open probability are depicted for several values $[IP_3]$ in Figure 2.6. The parameters used by De Young and Keizer are obtained by fitting the distribution (2.20) to the experimental data by Watras et al. [1991] and are given in Table 2.2. The cytosolic $[Ca^{2+}]$ is defined through the $Ca^{2+}$ fluxes between the cytosolic volume and the ER volume

$$\frac{\mathrm{d}c}{\mathrm{d}t} = J_{\text{act}} + J_{\text{leak}} + J_{\text{pump}} = c_1(\nu_1 P^e_{\text{open}} + \nu_2)(c_{\text{ER}} - c) - \frac{\nu_3 c^2}{c^2 + k_3^2}, \tag{2.21}$$

where the first term characterises the outward $Ca^{2+}$ from ER into the cytosol. It is composed of $Ca^{2+}$ activation and leak fluxes, denoted by $J_{\text{act}}$ and $J_{\text{leak}}$, respectively. The third term in this equation is the inward flux, denoted by $J_{\text{pump}}$, which is pumping up $[Ca^{2+}]$ from the cytosol back into ER. All the parameters used here are defined in Table 2.2 and their values presented there too. The bifurcation diagram obtained from equation (2.21) is presented in Figure 2.7. It shows the existence of stable periodic orbits in a certain range of $[Ca^{2+}]$ and $[IP_3]$. These periodic solutions are proposed to explain the occurrence of $Ca^{2+}$ oscillations. These results are in agreement with some experimental data, but this model is not adequate to explain the whole

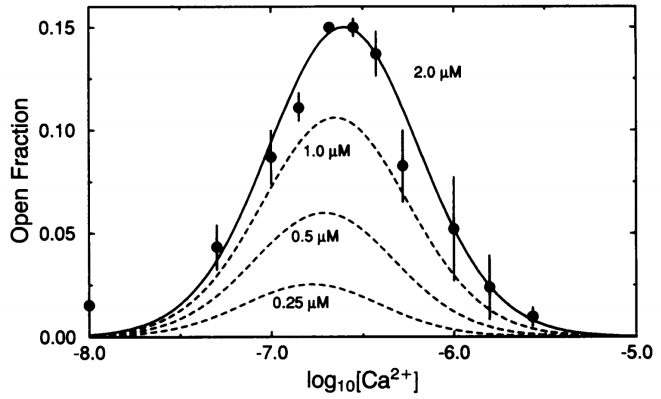


FIGURE 2.6: The open probability of $IP_3R$ channel (solid line) fitted to data by Bezprozvanny et al. [1991] for $p = 2\,\mu$M (black dots with error bars). Also, prediction of open probability profiles is plotted for $p = 1.0$, 0.5, and $0.25\,\mu$M (dashed lines) (adapted from De Young and Keizer [1992]).

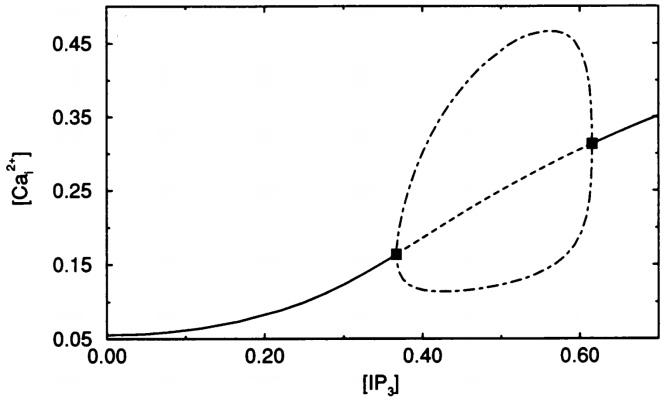


FIGURE 2.7: Bifurcation diagram obtained from DYK model for $Ca^{2+}$ and $IP_3$ concentrations. The solid line indicates steady states, the dashed line indicates unstable steady states, the dotted-dashed line indicates stable periodic orbits (adapted from De Young and Keizer [1992]).

range of oscillations observed. The application of the DYK model in its general form to spatially distributed channels is too complicated even for a couple of channels. Hence, multiple attempts at reducing its complexity have been made in the last few decades. A simplification proposed by Li and Rinzel [1994] is discussed in the next section.

## 2.4 Li and Rinzel simplification of DYK

The DYK model assumes that all 4-subunit channels are "well-mixed" in the membrane and dispenses with spatial effects such as clustering. The application of the DYK model for a channel in its general form, to a clustered spatial distribution of channels on the ER membrane, is hindered by the complexity of its state space. Most of the reductions of DYK share the common feature of $IP_3$-dependent activation and CICR. For example, Li and Rinzel [1994] proposed to dispense fast and slow binding processes in the DYK model. From Table 2.2 it is noticeable that transition rates $a_{1,3,5}$ and $b_{1,3,5}$ are reasonably larger than $a_{2,4}$ and $b_{2,4}$, respectively. Thus,

TABLE 2.2: Parameters used in DYK model De Young and Keizer [1992], where $d_i = b_i/a_i$.

| Parameter | Value | Short description |
|---|---|---|
| $a_1$ | 400 $(\mu\mathrm{M}\cdot\mathrm{s})^{-1}$ | $IP_3$ binding rate |
| $b_1$ | 52 $\mathrm{s}^{-1}$ | $IP_3$ unbinding rate |
| $d_1$ | 0.13 $\mu$M | $IP_3$ dissociation constant |
| $a_2$ | 0.2 $(\mu\mathrm{M}\cdot\mathrm{s})^{-1}$ | $Ca^{2+}$ inhibition binding rate |
| $b_2$ | 0.21 $\mathrm{s}^{-1}$ | $Ca^{2+}$ inhibition unbinding rate |
| $d_2$ | 1.05 $\mu$M | $Ca^{2+}$ inhibition dissociation constant |
| $a_3$ | 400 $(\mu\mathrm{M}\cdot\mathrm{s})^{-1}$ | $IP_3$ binding rate |
| $b_3$ | 377.36 $\mathrm{s}^{-1}$ | $IP_3$ unbinding rate |
| $d_3$ | 943.4 nM | $IP_3$ dissociation constant |
| $a_4$ | 0.2 $(\mu\mathrm{M}\cdot\mathrm{s})^{-1}$ | $Ca^{2+}$ inhibition binding rate |
| $b_4$ | 0.029 $\mathrm{s}^{-1}$ | $Ca^{2+}$ inhibition unbinding rate |
| $d_4$ | 144.5 nM | $Ca^{2+}$ inhibition dissociation constant |
| $a_5$ | 20 $(\mu\mathrm{M}\cdot\mathrm{s})^{-1}$ | $Ca^{2+}$ activation binding rate |
| $b_5$ | 1.65 $\mathrm{s}^{-1}$ | $Ca^{2+}$ activation unbinding rate |
| $d_5$ | 82.34 nM | $Ca^{2+}$ activation dissociation constant |
| $c_0$ | 2.0 $\mu$M | Total $[Ca^{2+}]$ in cytosolic volume |
| $c_1$ | 0.85 | The ratio of ER and cytosolic volumes |
| $\nu_1$ | 6 $\mathrm{s}^{-1}$ | Maximum $Ca^{2+}$ flux from $IP_3R$ channel |
| $\nu_2$ | 0.11 $\mathrm{s}^{-1}$ | $Ca^{2+}$ leak constant |
| $\nu_3$ | 0.9 $(\mu\mathrm{M}\cdot\mathrm{s})^{-1}$ | Maximum $Ca^{2+}$ uptake |
| $k_3$ | 0.1 $\mu$M | $Ca^{2+}$ pump activation constant |

the receptor states can be arranged into two groups: group I contains the states with unbound inhibiting $Ca^{2+}$ ($S_{000}$, $S_{010}$, $S_{100}$, and $S_{110}$), and the rest of the states form group II ($S_{001}$, $S_{011}$, $S_{101}$, and $S_{111}$). Taking into account the fast rate of $IP_3$ binding and $Ca^{2+}$ activation binding, the transitions within each group can be considered as quasistationary. However, we need to account for slow switching between group I and group II.

The kinetics governing the right-hand side plane of the DYK cube depicted in Figure 2.8 corresponding to the group I are described by the following set of differential equations

$$\frac{\mathrm{d}x_{000}}{\mathrm{d}t} = -x_{000}(a_1 p + a_4 c + a_5 c) + x_{100} b_1 + x_{001} b_4 + x_{010} b_5, \tag{2.22}$$

$$\frac{\mathrm{d}x_{100}}{\mathrm{d}t} = -x_{100}(b_1 + a_2 c + a_5 c) + x_{000} a_1 p + x_{101} b_2 + x_{110} b_5, \tag{2.23}$$

$$\frac{\mathrm{d}x_{010}}{\mathrm{d}t} = -x_{010}(a_1 p + a_4 c + b_5) + x_{110} b_1 + x_{011} b_4 + x_{000} a_5 c, \tag{2.24}$$

where the fractions sum to unity

$$x_{110} + x_{100} + x_{000} + x_{010} + y = 1, \tag{2.25}$$

where the dynamical variable $y$ represents the sum of the fractions of states on the left-hand side of the DYK as $y = x_{001} + x_{011} + x_{111} + x_{101}$. Note, that the fractions of subunits in states $S_{ijk}$ are denoted as $x_{ijk}$. Equations (2.22)–(2.24) in a quasi-steady-state approximation ($\mathrm{d}x_{000}/\,\mathrm{d}t = 0$, $\mathrm{d}x_{100}/\,\mathrm{d}t = 0$, $\mathrm{d}x_{010}/\,\mathrm{d}t = 0$) and through setting the fast terms proportional to $a_4 c$, $b_4$, $a_2 c$, $b_2$

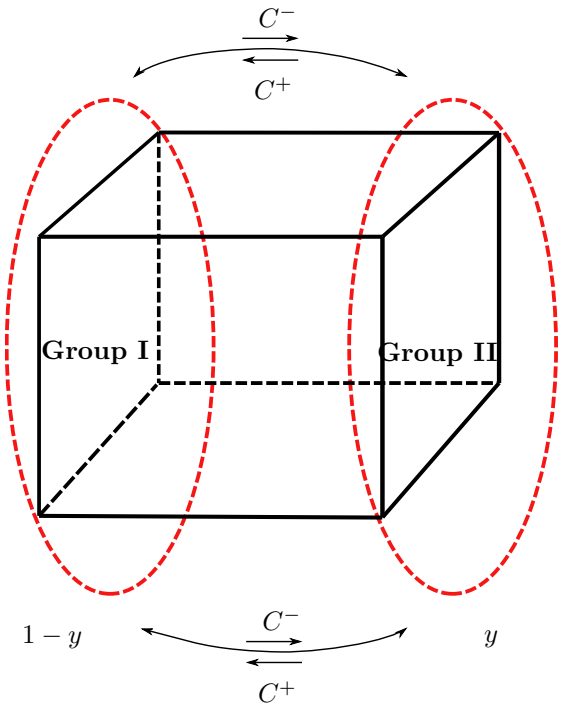


FIGURE 2.8: The simplification of the DYK model proposed by Li and Rinzel [1994]. The fractions of binding states are separated into two groups presented by compound ratio $y$ for the group I and $1-y$ for group II. The transition rates between those two groups are $C^+$ and $C^-$ (reproduced from Li and Rinzel [1994]).

to zero with some rearrangements become

$$x_{000}(a_1 p + a_5 c) = x_{100} b_1 + x_{010} b_5, \tag{2.26}$$

$$x_{001}(b_1 + a_5 c) = x_{000} a_1 p + x_{110} b_5, \tag{2.27}$$

$$x_{010}(a_1 p + b_5) = x_{110} b_1 + x_{000} a_5 c. \tag{2.28}$$

Solving Equations (2.27)–(2.28) together with constraint (2.25) gives expressions for the steady-state values for each subunit state in group I

$$x_{000} = \frac{d_1 d_5 (1-y)}{(p+d_1)(c+d_5)}, \tag{2.29}$$

$$x_{100} = \frac{d_5 p (1-y)}{(p+d_1)(c+d_5)}, \tag{2.30}$$

$$x_{010} = \frac{d_1 c (1-y)}{(p+d_1)(c+d_5)}, \tag{2.31}$$

$$x_{110} = \frac{pc(1-y)}{(p+d_1)(c+d_5)}, \tag{2.32}$$

where $d_i = b_i/a_i$.

Similarly, for group II we obtain the steady-state values as

$$x_{001} = \frac{d_3 d_5 y}{(p+d_3)(c+d_5)}, \tag{2.33}$$

$$x_{101} = \frac{d_5 p y}{(p+d_3)(c+d_5)}, \tag{2.34}$$

$$x_{011} = \frac{d_3 c}{(p+d_3)(c+d_5)}, \tag{2.35}$$

$$x_{111} = \frac{pc}{(p+d_3)(c+d_5)}. \tag{2.36}$$

The slow dynamics is presented by transitions

$$K^- = a_4 c(x_{000} + x_{010}) + a_2 c(x_{100} + x_{110}) = \frac{(b_4 d_1 d_2 + b_2 d_4 p)c(1-y)}{d_2 d_4 (p+d_1)}, \tag{2.37}$$

$$K^+ = b_4(x_{001} + x_{011}) + b_2(x_{101} + x_{111}) = \frac{(b_2 p + b_4 d_3)\, y}{p+d_3}. \tag{2.38}$$

The dynamics of compound state $y$ is governed by

$$\frac{\mathrm{d}y}{\mathrm{d}t} = \left(\frac{(b_2 p d_4 + b_4 d_2 d_1)c}{d_2 d_4 (p+d_1)}\right)(1-y) - \left(\frac{b_2 d_3 + b_4 p}{p+d_3}\right) y, \tag{2.39}$$

where the slow transition rates are obtained from steady-state equations for the group I (2.30)–(2.32) and group II (2.34)–(2.36).

The above can be expressed in a compact form for $h = (1-y)$, and we obtain the dynamical equation similar to the Hodgkin and Huxley model (2.4)–(2.4)

$$\tau_h(c,p)\frac{\mathrm{d}h}{\mathrm{d}t} = h_\infty(c,p) - h, \tag{2.40}$$

where the first term comprises the corresponding $\alpha$ and $\beta$ terms

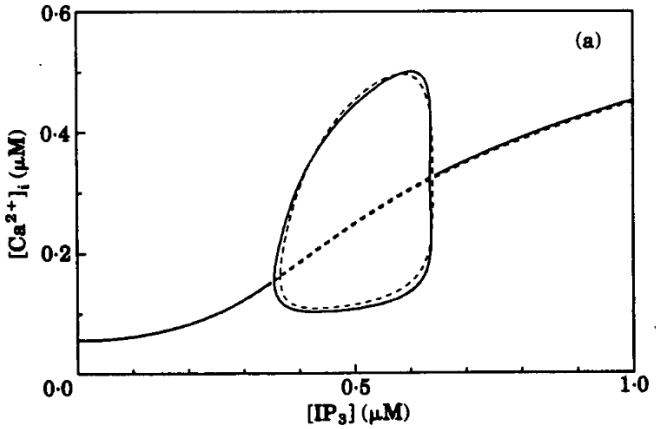


FIGURE 2.9: The comparison of bifurcation diagram obtained from the Li-Rinzel model (solid lines) and the DYK model (dotted lines) similarly to Figure 2.7 (adapted from Li and Rinzel [1994]).

$$h_\infty(c,p) = \frac{\beta(p)}{\alpha(c,p)+\beta(p)}, \tau_h = \frac{1}{\alpha(c,p)+\beta(p)}, \tag{2.41}$$

where, unlike Hodgkin-Huxley rates which were estimated on a purely empirical basis, the Li-Rinzel transition rates are obtained from the simplified DYK dynamics in Section 2.4

$$\alpha(c,p) = \frac{(b_2 p d_4 + b_4 d_2 d_1)c}{d_2 d_4 (p+d_1)}, \beta(p) = \frac{b_2 d_3 + b_4 p}{p+d_3}. \tag{2.42}$$

Considering that $P^e_{\text{open}} = (x_{110})^3$, where $x_{110}$ is (2.32), Equations (2.40), (2.21) form the Li-Rinzel two-variable model. It is capable of showing the $Ca^{2+}$ oscillations almost in the same range as the DYK model (Figure 2.9).

## 2.5 Cluster-based model as a simplification of DYK

Here we discuss a three-state model developed for a cluster of $IP_3R$ channels proposed by Rüdiger [2014a]. In the present thesis, we provide the derivation of this model using a reduction of the number of possible states in the DYK model (a schematic representation of such simplification is shown in Figure 2.10 and Figure 2.12). This model exhibits excitability of $Ca^{2+}$ puffs similarly to the FitzHugh-Nagumo model mentioned in Section 2.2. Considering that our cluster-based spatial model is developed employing the features of the Rüdiger's model, we further discuss his reasoning in details.

Rüdiger [2014a] proposed the following assumptions to simplify the DYK model. Firstly, they assume that $[IP_3]$ is so high within the cytosol that most of the $IP_3$ sites are considered to be saturated. This means that the rate of transitions according to the blue arrow in Figure 2.12 (a) is high. Therefore, we are left with the upper plane of the cube (shown in Figure 2.12 (b)) which prevails in defining the dynamics of a subunit. In such a way, the total number of variables in the DYK model is significantly reduced.

This assumption is not sufficiently studied in Rüdiger [2014a], thus, here we perform the derivation in detail. Such reduction is obtained from the simplification made similar to that presented by Li and Rinzel in Section 2.4. Similarly, we present the two groups of subunits represented by the upper and lower planes of the DYK cube shown in Figure 2.8. Mathematically, the kinetics governing the upper plane of the DYK cube is formulated as the next set of differential equations

$$\frac{\mathrm{d}x_{110}}{\mathrm{d}t} = -x_{110}(b_1 + a_2 c + b_5) + x_{010} a_1 p + x_{111} b_2 + x_{100} a_5 c, \tag{2.43}$$

$$\frac{\mathrm{d}x_{100}}{\mathrm{d}t} = -x_{100}(b_1 + a_2 c + a_5 c) + x_{000} a_1 p + x_{101} b_2 + x_{110} b_5, \tag{2.44}$$

$$\frac{\mathrm{d}x_{101}}{\mathrm{d}t} = -x_{101}(b_2 + a_2 c + a_5 c) + x_{100} a_2 c + x_{001} a_3 p + x_{111} b_5, \tag{2.45}$$

where $x_{110} + x_{100} + x_{101} + x_{111} = 1 - y$, $y = x_{000} + x_{001} + x_{011} + x_{010}$.

In the case of high $[IP_3]$ concentration, the $IP_3$ binding sites are saturated. Therefore, we can apply the condition of detailed balance between upper and lower planes of the DYK cube: $a_i p x_{0jk} = b_i x_{1jk}$ for four sets of $i$, $j$ and $k$ such as $i = 1$, $j = 0, 1$, $k = 0$ and $j = 3$, $j = 0, 1$, $k = 1$. From these conditions we derive

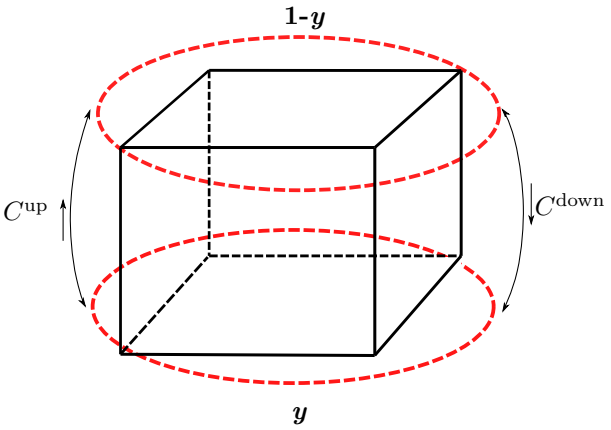


FIGURE 2.10: The simplification of the DYK model in the case of high [IP$_3$]. The fractions of binding states are separated into two groups presented by lower plane represented by compound ratio $y$ and upper $1-y$ plane of the DYK cube. The transition rates between those two groups are $C^{\text{down}}$ and $C^{\text{up}}$.

$$x_{000} = \frac{x_{100}b_1}{a_1 p}, \tag{2.46}$$

$$x_{010} = \frac{x_{110}b_1}{a_1 p}, \tag{2.47}$$

$$x_{001} = \frac{x_{101}b_3}{a_3 p}, \tag{2.48}$$

$$x_{011} = \frac{x_{111}b_3}{a_3 p}. \tag{2.49}$$

We substitute equations (2.46)–(2.49) into the system (2.43)–(2.45). The resulting four-state-model is

$$\frac{\mathrm{d}x_{110}}{\mathrm{d}t} = -x_{110}(a_2 c + b_5) + x_{111}b_2 + x_{100}a_5 c, \tag{2.50}$$

$$\frac{\mathrm{d}x_{100}}{\mathrm{d}t} = -x_{100}(a_2 c + a_5 c) + x_{101}b_2 + x_{110}b_5, \tag{2.51}$$

$$\frac{\mathrm{d}x_{101}}{\mathrm{d}t} = -x_{101}(b_2 + a_5 c) + x_{100}a_2 c + x_{111}b_5, \tag{2.52}$$

where $x_{110} + x_{100} + x_{101} + x_{111} = 1 - y$ due to conservation of probability, $y = x_{010} + x_{000} + x_{001} + x_{011}$.

Similarly to the approach of Li and Rinzel, we separate the upper and lower planes of the DYK cube. Consider the lower plane of the DYK cube in a steady state. Thus we obtain

$$x_{000} = \frac{d_5 d_4 y}{(c + d_5)(c + d_4)}, \tag{2.53}$$

$$x_{001} = \frac{d_5 c y}{(c + d_5)(c + d_4)}, \tag{2.54}$$

$$x_{010} = \frac{d_4 c y}{(c + d_5)(c + d_4)}, \tag{2.55}$$

$$x_{011} = \frac{c^2 y}{(c + d_5)(c + d_4)}, \tag{2.56}$$

where $d_i = b_i/a_i$.

Analogously, the upper plane is in a steady-state for fractions $x_{ijk}$ given by:

$$x_{100} = \frac{d_5 d_2 (1-y)}{(c+d_5)(c+d_2)}, \tag{2.57}$$

$$x_{101} = \frac{d_5 c (1-y)}{(c+d_5)(c+d_2)}, \tag{2.58}$$

$$x_{110} = \frac{d_2 c (1-y)}{(c+d_5)(c+d_2)}, \tag{2.59}$$

$$x_{111} = \frac{c^2 (1-y)}{(c+d_5)(c+d_2)}. \tag{2.60}$$

The transition rates between these two groups are obtained from steady-state equations from upper (2.54)–(2.56) to lower (2.58)–(2.60) planes and reversely

$$K^{\text{down}} = b_1(x_{100}+x_{110}) + b_3(x_{101}+x_{111}) = C^{\text{down}}(1-y), \tag{2.61}$$

$$K^{\text{up}} = a_1 p(x_{000}+x_{010}) + a_3 p(x_{001}+x_{011}) = C^{\text{up}} y, \tag{2.62}$$

where

$$C^{\text{down}} = \frac{b_3 c + b_1 d_2}{c+d_2}, \tag{2.63}$$

$$C^{\text{up}} = \frac{(a_3 c + a_1 d_4)p}{c+d_4}. \tag{2.64}$$

Thus, the probability of a subunit being in the upper square of the DYK cube is

$$\mu = \frac{k}{k+1}, \tag{2.65}$$

where $k = C^{\text{up}}(p)/C^{\text{down}}$. Notably, $\mu \to 1$ when $p \to \infty$. It means that with an increase of $[\text{IP}_3]$ the probability of the subunit being in the lower plane of the DYK cube tends to zero. Thus, we can reduce the dynamics by considering the transitions between subunit states only in the upper plane of the DYK cube.

The transitions between the upper and lower planes of the cube are governed by the dynamics of the compound state $y$ in the following manner

$$\frac{\mathrm{d}y}{\mathrm{d}t} = C^{\text{down}}(1-y) - C^{\text{up}} y. \tag{2.66}$$

The solution of equation (2.66) is straightforward

$$y(t) = A e^{-(C^{\text{down}}+C^{\text{up}})t} + \frac{C^{\text{down}}}{C^{\text{down}}+C^{\text{up}}}. \tag{2.67}$$

It follows that the equilibrium solution for the system is

$$y_{eq} = \frac{C^{\text{down}}}{C^{\text{down}}+C^{\text{up}}} = \frac{(b_3 c + b_1 d_2)(c+d_4)}{(a_1 d_4 + a_3 c)(c+d_2)p + (b_1 d_2 + b_3 c)(c+d_4)} \overset{p \gg 1}{\sim} \frac{1}{p}, \tag{2.68}$$

in the case of $IP_3$ saturation, we consider $p = [IP_3]$ to be very high. Taking that into account and assuming that waiting time is long enough $t \gg 1/(C^{\text{down}} + C^{\text{up}})$ we obtain $y \to 0$. The dependence of waiting times on the $[IP_3]$ is shown in Figure 2.11. Where $t_1$, $t_2$ and $t_3$ are the times required for $y$ to reach certain low level ($y \approx 0.01$) under $[IP_3]$ of $0.5\,\mu$M, $1\,\mu$M and $10\,\mu$M, respectively. Considering all assumptions made before, we further operate with the three-variable system taking into account that $x_{110} + x_{100} + x_{101} + x_{111} = 1$. Thereafter, we extend

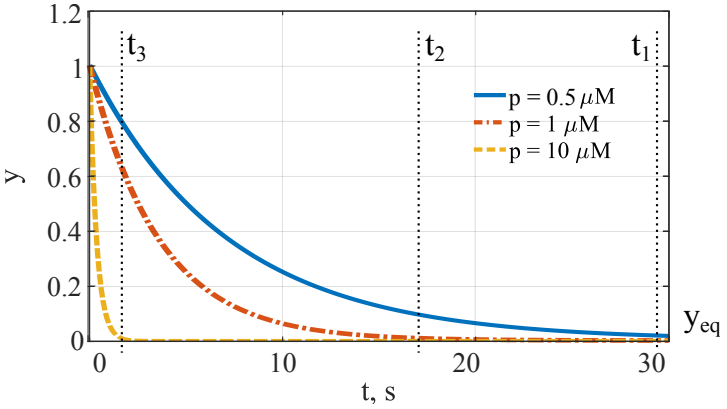


FIGURE 2.11: The equilibration of compound state $y$ to small value $y_{eq}$ for $[IP_3] = 0.5\,\mu$M (blue solid line), $[IP_3] = 1\,\mu$M (red dot-dashed line), and $[IP_3] = 10\,\mu$M (yellow dashed line). The equilibration times denoted $t_1$, $t_2$, and $t_3$ are shown with vertical dashed lines decreases with the rise in $[IP_3]$ ($t_1 \gg t_2 \gg t_3$). The curves obtained for $A = 1$, $c = 0.025\,\mu$M, here we use DYK rates proposed in Rückl et al. [2015].

our discussion from terms of subunits to channels. At the level of channels, we obtain the four-state model of each subunit (Figure 2.12 (c)). Rüdiger [2014a] proposed a model of a cluster of channels, where $a$ is a fraction of channels in an open state (corresponds to $x_{110}$ for subunit), $z$ is a fraction of channels in a rest state (corresponds to $x_{100}$ for subunit), $h'$ is a fraction of channels in a closed state with bound $IP_3$ and $Ca^{2+}$ inhibiting sites (corresponds to $x_{101}$ for subunit), $g$ is a fraction of channels in a closed state with all three sites are bound (corresponds to $x_{111}$ for subunit). Considering previous arguments the system (2.50)–(2.52) transforms to

$$\frac{da}{dt} = k_a^+ cz - k_a^- a + k_i^- g - k_i^+ c_s a, \tag{2.69}$$

$$\frac{dg}{dt} = k_a^+ ch' - k_a^- g - k_i^- g + k_i^+ c_s a, \tag{2.70}$$

$$\frac{dh'}{dt} = k_a^- g - k_a^+ ch' + k_i^+ cz - k_i^- h', \tag{2.71}$$

where $z = 1 - a - g - h'$.

The kinetics of these variables is governed by rates $k_a^\pm$, $k_i^\pm$ and concentrations $c$ and $c_s$, where $c_s$ is cytosolic $[Ca^{2+}]$ at opened channel (Figure 2.13 (b)). In this model, we adopt the assumption of separating two scales for the $Ca^{2+}$ concentration at the cluster [Rüdiger et al., 2010a]. Immediately after the release $[Ca^{2+}]$ reaches concentrations of hundreds of $\mu$M, while after the milliseconds it equilibrates to the cytosolic levels of tens of nM. This effect may be accommodated in the effective reaction kinetics shown in Figure 2.12 (c) by setting the rate of leaving an open state $a$ to $k_i^+ c_s$ instead of $k_i^+ c_s$ as in ordinary kinetic equations.

Almost all transition rates in the scheme (Figure 2.12 (c)) are obtained from the original DYK rates. Simulations by Rüdiger [2014a] showed that most of the reactions ($k_a^-$, $k_i^+$ and $k_i^-$) in

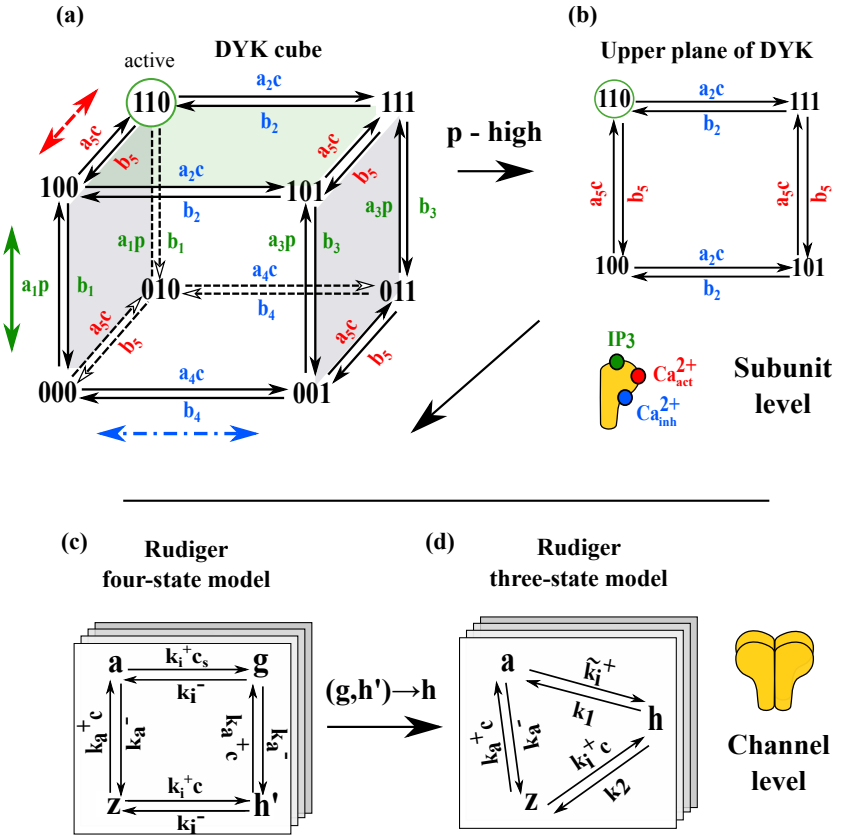


FIGURE 2.12: (a) Schematic diagram of the DYK eight-state gating model of the activation of a single subunit of an $IP_3R$ channel. (b) When $p$ is high, most of the transitions take place in the upper plane of the DYK cube. (c) The scheme of the four-state model Rüdiger [2014a] for high $p$ at the channel level indicated by the 4 sheets. The states of the channels are marked as $a, g, z, h'$ instead of $110, 111, 100, 101$ that are typically used for subunits. The transition rates between channel states are $k^{\pm}_{a,i}$. (d) The final three-state model includes a compound state $h$ formed from the states $g$ and $h'$ with the effective rates $k_{1,2}$.

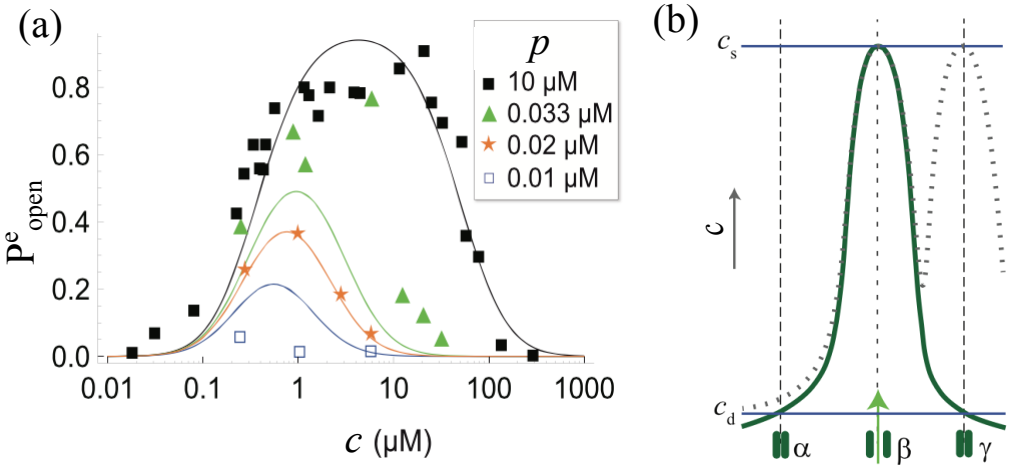


FIGURE 2.13: (a) Open probability $P^e_{\mathrm{act}}$ of $IP_3R$ channel for different cytosolic $Ca^{2+}$ and $IP_3$ concentrations. The experimental data is adapted from Mak et al. [1998]. (b) $Ca^{2+}$ distribution after an opening of a channel adapted from the model by Rüdiger et al. [2012].

TABLE 2.3: Parameters used in the three-state model [Rüdiger, 2014a].

| Parameter | Value | Description |
|---|---|---|
| $a_5$ | $100\,(\mu\mathrm{M}\cdot\mathrm{s})^{-1}$ | $Ca^{2+}$ activation binding rate |
| $(b_5, k_a^-)$ | $20\,\mathrm{s}^{-1}$ | Activation unbinding rate |
| $(a_2, k_i^+)$ | $0.1\,(\mu\mathrm{M}\cdot\mathrm{s})^{-1}$ | $Ca^{2+}$ inhibition binding rate |
| $(b_2, k_i^-)$ | $1.7\,\mathrm{s}^{-1}$ | Inhibition unbinding rate |
| $c_s$ | $300\,\mu\mathrm{M}$ | Local $[Ca^{2+}]$ at opened channel |
| $c_0$ | $0.025\,\mu\mathrm{M}$ | Rest level of $[Ca^{2+}]$ |
| $\alpha$ | $0.74\,\mu\mathrm{M}$ | Channels coupling constant |
| $\lambda$ | $10^3\,\mathrm{s}^{-1}$ | Equilibration rate |
| $\epsilon$ | 0.1 | Characteristic of the step |

the four-state model by construction are $b_5$, $a_2$ and $b_2$, respectively. All the transition rates used in this study are different from the ones accepted in original DYK model. It happened because the bell-shaped curve $P_{\mathrm{act}}^{\mathrm{e}}$, described by Equation (2.20) and shown in Figure 2.6, does not reproduce the experimental patch-clamp data measured under high $[IP_3]$ loads very well. Thus, the adapted transition rates $a_i$, $b_i$ and, thus, $k_a^-$, $k_i^+$ and $k_i^-$ have been obtained by fitting the curve (2.20) to the measurements depicted in Figure 2.13 (a), Rüdiger et al. [2012]. All the parameters used in the Rüdiger model, and their values, are presented in Table 2.3.

In contrast to the rates introduced in the previous paragraph, $k_a^+$ has been constructed from the condition of channel opening (at least three subunits should be active). The probability of the single subunit activated is $P_{\mathrm{act}} = a_5 c/(a_5 c + b_5)$. This is the effective rate derived from the detailed balance condition of the single subunit activation. To account for subsequent activation of subunits leading to the channel opening we derive the binomial probabilities. According to the binomial distributions, the probability of none of the subunits is active is $P_0 = (1-P_{\mathrm{act}})^4$. If only one of four subunits is active, and all remaining ones are inactive, $P_1 = 4P_{\mathrm{act}}(1-P_{\mathrm{act}})^3$. There are $C_4^2 = \frac{4!}{2!2!} = 6$ ways for two of four subunits to be activated, thus, $P_2 = 6P_{\mathrm{act}}^2(1-P_{\mathrm{act}})^2$. Therefore, the transition to this state is possible only after the activation of two subunits. The probability that two subunits are active under the condition that the channel is closed is $P(2|\{0,1,2\}) = P_2/(P_0+P_1+P_2)$.

We calculate $k_a^+$ as a transition rate from a closed channel with two active subunits and one in the state 100 to an opened channel where at least three subunits are active, thus in the state 110. The transition rate for the channel to become open, thus, is postulated to be the rate of the third subunit to become active, scaled by the conditional probability $P(2|\{0,1,2\})$ of the previous activation of the two subunits. The scaler comes from the availability of 2 remaining inactive subunits to make the final transition. Thus, we obtain

$$k_a^+ = 2a_5 P(2|\{0,1,2\}). \tag{2.72}$$

Similarly to the derivation of $k_a^+$, we derive $C_{\mathrm{ch}}^{\mathrm{up}}$ which requires four subunits to bind $IP_3$ [Taylor and Konieczny, 2016]

$$C_{\mathrm{ch}}^{\mathrm{up}} = C^{\mathrm{up}} P_{\mathrm{IP}}(3|\{0,1,2,3\}), \tag{2.73}$$

where $C^{\mathrm{up}}$ is given by Equation (2.64),

$$P_{\mathrm{IP}}(3|\{0,1,2,3\}) = \frac{P_3^{\mathrm{IP}}}{P_0^{\mathrm{IP}} + P_1^{\mathrm{IP}} + P_2^{\mathrm{IP}} + P_3^{\mathrm{IP}}}, \tag{2.74}$$

similarly

$$\begin{aligned} P_{\mathrm{act}}^{\mathrm{IP}} &= \frac{C^{\mathrm{up}}}{C^{\mathrm{down}} + C^{\mathrm{up}}}, & (2.75)\\ P_0^{\mathrm{IP}} &= (1 - P_{\mathrm{act}}^{\mathrm{IP}})^4, & (2.76)\\ P_1^{\mathrm{IP}} &= 4P_{\mathrm{act}}^{\mathrm{IP}}(1 - P_{\mathrm{act}}^{\mathrm{IP}})^3 & (2.77)\\ P_2^{\mathrm{IP}} &= 6(P_{\mathrm{act}}^{\mathrm{IP}})^2(1 - P_{\mathrm{act}}^{\mathrm{IP}})^2 & (2.78)\\ P_3^{\mathrm{IP}} &= 4(P_{\mathrm{act}}^{\mathrm{IP}})^3(1 - P_{\mathrm{act}}^{\mathrm{IP}}). & (2.79) \end{aligned}$$

In order to reduce the number of variables, Rüdiger introduces a compound state $h$ which contains $g$ and $h'$. The effective rates of transitions to this state are obtained from a detailed balance between $g$ and $h'$. We introduce the fraction of channels in the compound state as the sum of components $h = g + h'$, where from detailed balance

$$\begin{aligned} h &= \frac{k_a^-}{k_a^+ c} g + g = \frac{k_a^+ c + k_a^-}{k_a^+ c} g, & (2.80)\\ h &= h' + \frac{k_a^+}{k_a^- c} h' = \frac{k_a^+ c + k_a^-}{k_a^-} h'. & (2.81) \end{aligned}$$

Considering that the rates of transition to the compound state are

$$\begin{aligned} k_1 &= k_i^- \frac{k_a^+ c}{k_a^+ c + k_a^-} = k_i^- g_0, & (2.82)\\ k_2 &= k_i^- \frac{k_a^-}{k_a^+ c + k_a^-} = k_i^- (1 - g_0), & (2.83) \end{aligned}$$

where $g_0 = k_a^+ c/(k_a^+ c + k_a^-)$, the formulation of the three-state model is mathematically expressed via

$$\begin{aligned} \frac{\mathrm{d}a}{\mathrm{d}t} &= k_a^+ cz - k_a^- a + k_1 h - k_i^+ c_s a, & (2.84)\\ \frac{\mathrm{d}h}{\mathrm{d}t} &= k_i^+ cz - k_1 h - k_2 h + k_i^+ c_s a, & (2.85) \end{aligned}$$

where $z = 1 - a - h$ as the sum of fractions to unity.

One of the big challenges of $Ca^{2+}$ modelling nowadays is in building an adequate link between the dynamics of the subunit states and $Ca^{2+}$ concentration. The description of the behaviour of clusters containing a few channels using mass action kinetics is problematic [Rüdiger, 2014b]. To overcome this, we draw from the approach by Rüdiger [2014a] and make a principal assumption about the connection between the continuous variable $a$ (fraction of the open channels in a cluster) and $[Ca^{2+}]$ which is described in detail further. We also assume the relaxation of the cytosolic $[Ca^{2+}]$ to the quasi-steady-state level $c_d$, which is discussed later as well:

$$\frac{\mathrm{d}c}{\mathrm{d}t} = \lambda(c_d(a) - c), \tag{2.86}$$

where $\lambda$ is a parameter which characterises a rate of equilibration, which scales with the reciprocal of the relaxation time.

In the Equation (2.86) $c$ is the actual cytosolic $[Ca^{2+}]$. The concentration level $c_d$ is the quasi-steady state level of $Ca^{2+}$. It enters the dynamics after Rüdiger [2014a] separated several concentration levels schematically presented in Figure 2.14 (a). At the open channel $Ca^{2+}$ concentration, denoted by $c_s$, is high ($\sim 100\,\mu$M), it causes relatively high binding to the receptor. At any closed channel, the 'coupling' $Ca^{2+}$ concentration, denoted by $c_d$, is low ($\sim 1\,\mu$M). However, it nonlinearly depends on the number of open channels in a cluster due to CICR. Roughly, $[Ca^{2+}]$ in a cluster can be replaced by an average concentration, which is independent of the location of channels in a cluster. All these concentrations are sketched in Figure 2.13 (b). Including small rest $Ca^{2+}$ concentration $c_0$ present in the cytosol, one can obtain the average $Ca^{2+}$ concentration within the cluster:

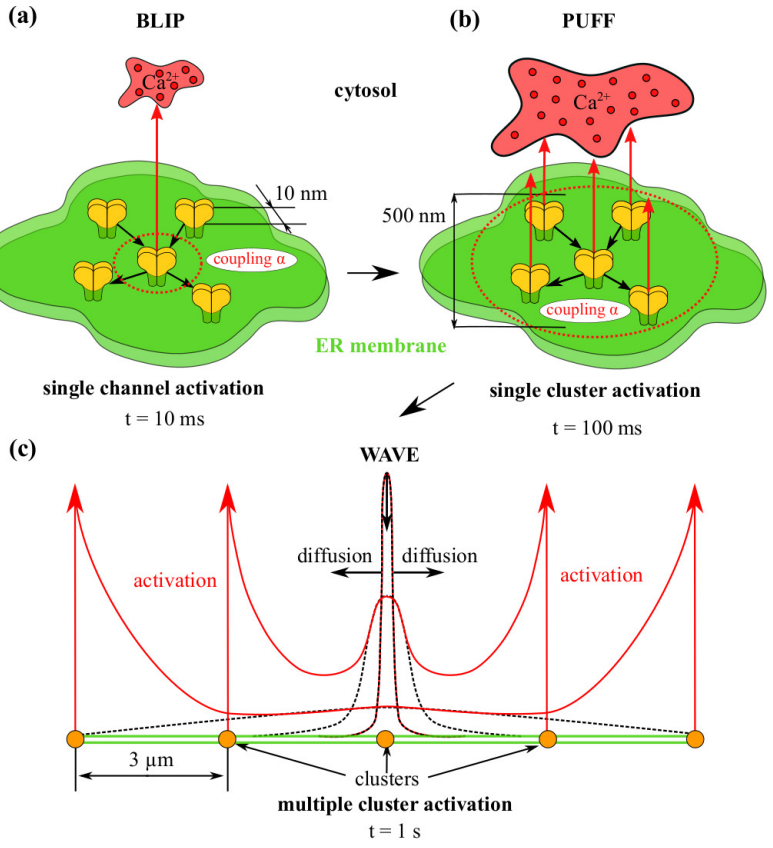


FIGURE 2.14: (a) Schematic representation of a $Ca^{2+}$ blip, its dimensions in space and average duration. The green plane represents a part of the ER membrane, the red arrow indicates $Ca^{2+}$ release from the activated channel indicated by the dotted circle. The coupling between channels (marked by black arrows) is defined by the constant $\alpha$ in the nonlinear dependence (2.87). (b) A puff is represented by multiple $Ca^{2+}$ blips occurring in a single cluster of channels. (c) The wave propagation as a sequence of puffs (red lines) caused by raised levels of $[Ca^{2+}]$. The activation of neighbouring clusters is caused by $Ca^{2+}$ diffusion from the initial $Ca^{2+}$ release localized in the centre (black dotted lines).

$$c_d(a) = c_0 + \frac{1}{2}\alpha N a\left\{1 + \tanh\left[\frac{Na-1}{\epsilon}\right]\right\}, \tag{2.87}$$

where $c_0$ is a rest level of $Ca^{2+}$ concentration, $\alpha$ is a coupling constant, $N$ is a number of activatable channels in a cluster. Thus, $Na$ is the number of active channels in a cluster,

since $a$ is the fraction of active channels. The nonlinear function in Equation (2.87) is plotted in (Figure 2.15) and has been chosen arbitrarily to provide a smooth transition between $Na = 0$ and $Na = 1$ to ensure the resistance of the system to small perturbations. Parameter $\epsilon$ characterises a sharpness of this transition in the functional form.

Interestingly, the main finding of the study by Dickinson et al. [2012] is that the probability of triggering $Ca^{2+}$ puffs is almost a linear function of the number of activatable $IP_3R$ channel channels in the cluster. However, Rüdiger [2014a] introduces the step shown in Figure 2.15 to avoid an increase in cytosolic concentration in a cluster when all channels are closed.

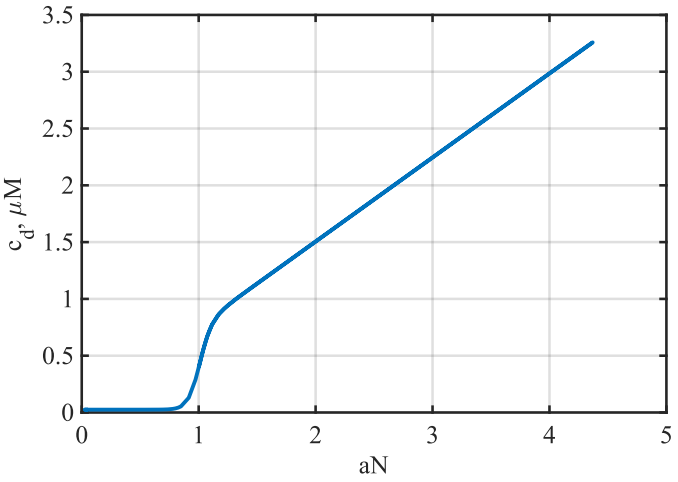


FIGURE 2.15: The value of steady-state $[Ca^{2+}]$ $c_d$ plotted as the function of $Na$. The number of activated channels in the cluster, the step between $Na = 0$ and $Na = 1$ introduced with the sharpness controlled by $\epsilon = 0.1$ (reproduced from Rüdiger [2014a]).

The three-state simplified DYK model is developed to show the formation of $Ca^{2+}$ puffs from $Ca^{2+}$ blips. In Figure 2.14 (a) the smallest $Ca^{2+}$ blip is sketched schematically. Due to the coupling mechanism represented by the second term in equation (2.87), $Ca^{2+}$ blips trigger $Ca^{2+}$ puff shown in Figure 2.14 (b). In the next chapter, we develop a model for the third hierarchical level which corresponds to $Ca^{2+}$ waves (Figure 2.14 (c)).

The assumption of equilibration to steady-state level smooths the high-value $c_s$ of $[Ca^{2+}]$ corresponding to $Ca^{2+}$ blips within the clusters. Here, and further in the thesis, we assume the value $c_s = 300\,\mu$M to be constant. For the value of $\lambda = 10^3\,s^{-1}$ chosen from Rüdiger [2014a], it takes $\sim 1 - 10$ ms to $Ca^{2+}$ levels to reach cytosolic concentrations in the $10 - 10^3$ nM range. In what follows, we introduce a diffusion term to enable $Ca^{2+}$ to activate inactive clusters by CICR thereby having $Ca^{2+}$ blips combine to form puffs as shown in Figure 2.14 (b).

The two-dimensional system studied by Rüdiger [2014a] is formulated in terms of the standard theory developed for dynamical systems. The system exhibits excitability similar to that typical of FitzHugh-Nagumo model shown in Figure 2.3. This property is shown from the solution of equations (2.84), (2.85) using a quasistationary approximation for $[Ca^{2+}]$. In quasistationary state cytosolic $Ca^{2+}$ concentration $c = c_d$, where the $c_d$ is described by equation (2.87). The solution of the system of three nonlinear equations is numerically obtained in Rüdiger [2014a] using the Runge-Kutta method–the nonlinearity arises from the $cz$ term in equations (2.84) and (2.85), which is coupled with the dynamics of $c$ given by equation (2.87), in which the state

variable $a$ enters via the function $c_d(a)$. The results for two different values of the number of activatable channels $N$ are shown in Figure 2.16, as reproduced from Rüdiger [2014a]. The black solid line corresponds to an exemplary trajectory for initial values $a = 0.12$, $h = 0.1$, the green dashed and red solid lines are $a$- and $h$-nullclines, respectively. The nullclines and trajectory corresponding to excitable behaviour of puff dynamics are shown in Figure 2.16 (a) for a small number of channels in the cluster. Whereas there is only one intersection of the nullclines present in this figure, the system has only one stable fixed point (marked by an 'X') very close to the origin. Therefore, sufficiently large perturbation away from the fixed point (marked by the dotted arrow, see the bottom left corner of the two figures near the lower fixed point) is needed to initiate a puff (marked by solid arrows), the trajectory of which follows back into the fixed point.

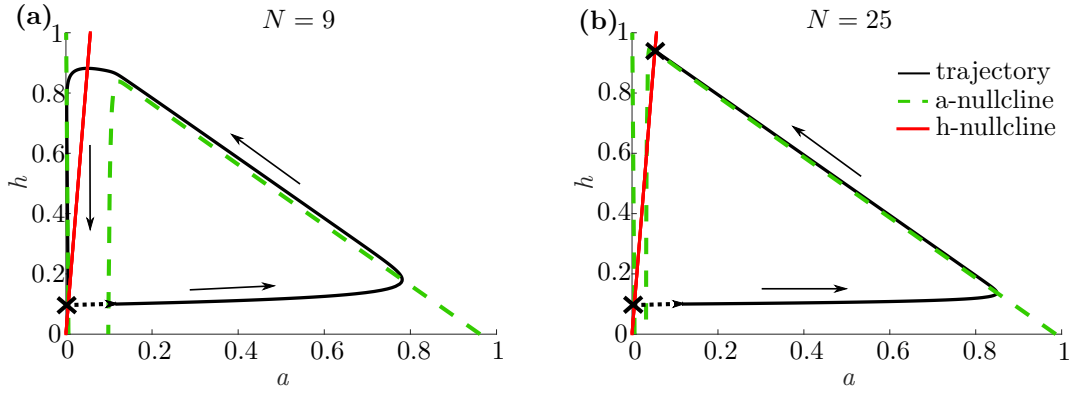


FIGURE 2.16: Nullclines and trajectories in two regimes of the three-state model for (a) excitable $N = 9$ and (b) bistable $N = 25$, initial conditions $a_0 = 0.12$, $h_0 = 0.1$ (reproduced from Rüdiger [2014a]).

Rüdiger [2014a] proposed the transition between excitable (single fixed point) and bistable (two stable fixed points and single unstable one) state by shifting $h$-nullcline to the left or $a$-nullcline to the right. This shift might be performed through the change in the characteristics of clusters. The most physiologically plausible change is the variation in the number of activatable channels in a cluster $N$. For example, in Figure 2.16 (b) the position of the unstable (middle) branch of the green dashed a-nullcline shifts with the change in $N$. This causes the transition from excitable regime in Figure 2.16 (b) *left* to the bistable one in Figure 2.16 (b) *right*). In the two-variable system (2.84), (2.85) such shifting of the nullclines also can be performed either by decreasing one of the parameters $c_s$, $\alpha$, and $k_i^+$, or by increasing $N$. However, which mechanisms of cell regulation are involved in these processes, is an open issue.

Rückl et al. [2015] interpret $N$ as the total number of activatable channels in a cluster, which could be connected with $[IP_3]$. It can be considered as an instrument for the transition of the system from excitable to bistable behaviour. Further, we develop a model based on this approach which represents $Ca^{2+}$ waves and oscillations observed in many electrically non-excitable systems.

# Chapter 3

# Calcium Dynamics at the Scale of a Single Cluster

Despite a long history of $Ca^{2+}$ modelling, many important questions remain unanswered. For example, the role of $IP_3R$ clustering in the formation of $Ca^{2+}$ patterns remains unclear. Our research is focused on the qualitative understanding of the physical mechanisms driving the occurrence of $Ca^{2+}$ oscillations from the interplay of the $Ca^{2+}$ releases at clustered $IP_3R$ channels. We aim to establish the interrelations between characteristics of membrane for which $Ca^{2+}$ oscillations can be observed.

In this chapter, we apply the three-state model to a case of high $[IP_3]$ and corroborate the existence of a transition from excitable to bistable behaviour in a cluster of channels previously studied by Rüdiger [2014a]. We reveal the existence of two Hopf bifurcations in a cluster of channels observed by continuously varying the rest $Ca^{2+}$ concentration parameter $c_0$. This illustrates the possibility of a single cluster exhibiting oscillations as channel activity and homeostatic mechanisms could regulate the state of the system to undergo dynamical regime shifts.

## 3.1 Regimes of a single cluster behaviour

We study the three-state model described by Equations (2.84)–(2.85) including the parameters shown in Table 3.1. We treat the following as control parameters for the bifurcation analysis. Parameter $N$ is the number of channels in a cluster and $c_0$ is the rest concentration of $Ca^{2+}$ ions for all channels being closed. The latter parameter varies in the interval $(0.025\,\mu\text{M} \leq c_0 \leq 0.6)\,\mu\text{M}$ which might seem excessive at the first glance. We explain the reasoning of such variation in the end of this chapter. Transition rates $k_i^+ = 0.02\,(\mu\text{M} \times \text{s})^{-1}$ and $k_i^- = 1.56\,\text{s}^{-1}$ were determined from the patch-clamp data containing the probability distribution for channel opening typical for *Xenopus* oocytes at high $[IP_3]$ from Rückl et al. [2015]. This has implications for the number of channels to be opened within each cluster and shapes how we build the model followed by an impact on the results discussed further. We assume that cytosolic $[Ca^{2+}]$ equilibrates to the steady-state value $c_d$ very fast, which is reflected by $\lambda = 10^3\,\text{s}^{-1}$ in Equation (2.86). Therefore, we study the model of a single cluster dynamics given by Equations (2.84)-(2.85) and obtain the solutions numerically using the standard Runge-Kutta method. We plot the solutions on the

TABLE 3.1: The parameters used in the cluster-based model.

| Parameter | Value | Description | Source |
|---|---|---|---|
| $a_5$ | $100\,(\mu\text{M}\times\text{s})^{-1}$ | $Ca^{2+}$ activation binding rate | Rüdiger [2014a] Rückl et al. [2015] |
| $(b_5, k_a^-)$ | $20\,\text{s}^{-1}$ | Activation unbinding rate | Rüdiger [2014a] |
| $(a_2, k_i^+)$ | $0.02\,(\mu\text{M}\times\text{s})^{-1}$ | $Ca^{2+}$ inhibition binding rate | Rückl et al. [2015] |
| $(b_2, k_i^-)$ | $1.56\,\text{s}^{-1}$ | Inhibition unbinding rate | Rückl et al. [2015] |
| $c_s$ | $300\,\mu\text{M}$ | Local $[Ca^{2+}]$ at opened channel | Rüdiger [2014a] |
| $c_0$ | $0.025$–$0.6\,\mu\text{M}$ | Rest level of $[Ca^{2+}]$ | Braichenko et al. [2018] |
| $\alpha$ | $0.74\,\mu\text{M}$ | Channels coupling constant | Rüdiger [2014a] |
| $\lambda$ | $10^3\,\text{s}^{-1}$ | Equilibration rate | Rüdiger [2014a] |
| $\epsilon$ | 0.1 | Characteristic of the step | Rüdiger [2014a] |
| $N$ | 5, 6 | Number of channels in a cluster | Braichenko et al. [2018] |

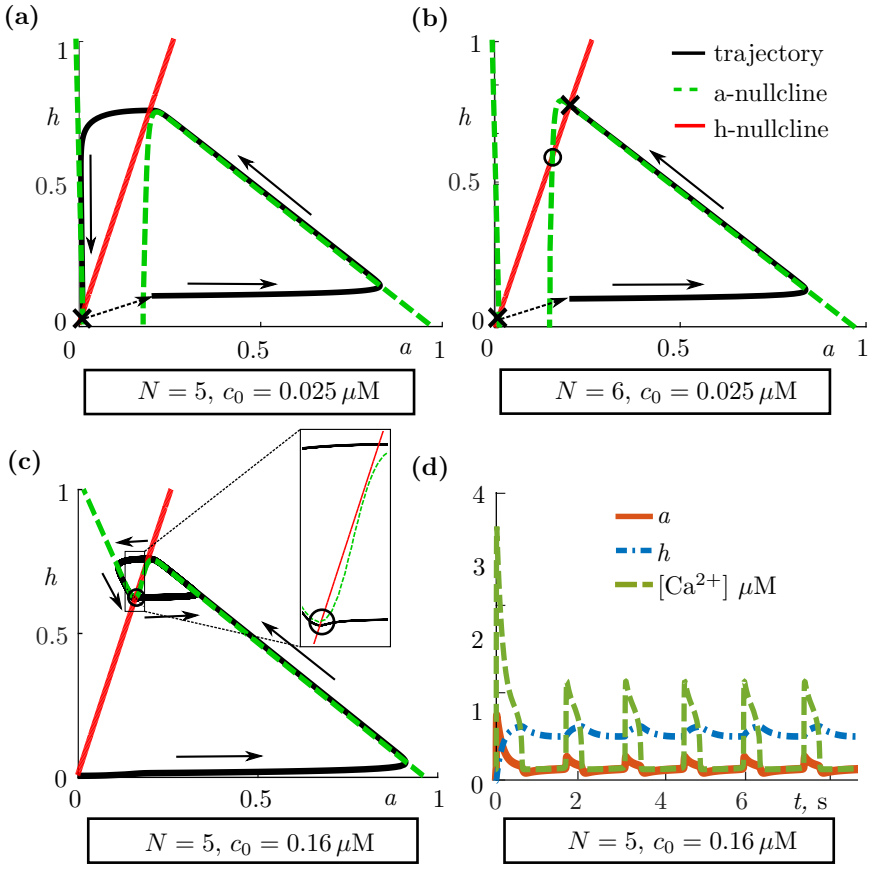


FIGURE 3.1: Three different regimes of $Ca^{2+}$ release obtained from the three-state model (2.84)–(2.85) assuming $c = c_d$ given by Equation (2.87) as proposed by Rüdiger [2014a]. **(a)** The phase diagram in ($h$, $a$) space, calculated for the excitable cluster ($N = 5$). The *red solid line* is the $h$-nullcline (inhibition), the *green dashed line* is the $a$-nullcline (for opened channel with at least three active $Ca^{2+}$ bound), the *black solid line* is the system's trajectory that starts from $a = 0.2$, $h = 0.1$ and evolves as indicated by *black arrows* arriving at the stable fixed point (*black cross*). **(b)** The phase diagram of the bistable cluster ($N = 6$). It contains two stable fixed points. The trajectory starts at $a = 0.2$, $h = 0.1$ and arrives at the upper fixed point. **(c)** Oscillations in the three-state model observed for $N = 5$ and $c_0 = 0.16\,\mu$M. A single unstable fixed point is marked as the *open circle* in the zoomed subplot. **(d)** Oscillations in cytosolic $[Ca^{2+}]$ associated with oscillations in $a$ (fraction of channels in open state) and $h$ (fraction of closed channels) for $N = 5$ and $c_0 = 0.16\,\mu$M.

($a$, $h$) phase plane as shown in Figures 3.1 (a), (b), and (c). Note that $\lambda$ will be reduced in the following chapters, and the corresponding fast-slow decoupling will no longer be valid.

Figure 3.1 (a) and Figure 3.1 (b) show the system behaviour as determined by the orientation and position of the nullclines $\dot{a} = f(a,h) = 0$ (*green dashed line*) and $\dot{h} = g(a,h) = 0$ (*red solid line*) in the ($a$, $h$) phase planes. We mark points where nullclines intersect with 'X' as stable fixed points. The *dashed arrows* coming from the black crosses indicate the perturbation away from the stable fixed point for the system to start evolving along the trajectory as shown with *black arrows*. The trajectory of system's evolution is guided by the nullclines shown with *green dashed* and *red solid lines*. In Figure 3.1 (a) we see that the system is perturbed enough to lend on the starting point of the trajectory which lies to the right of the second vertical dashed line. Therefore, the system does not simply settle back into the stable point but evolves following a more complex trajectory (*black curve*) and then returns to the fixed point. In Figure 3.1 (a) the trajectory comes back to the same fixed point and demonstrates that the monostable state is an excitable one. At the same time, in Figure 3.1 (b), we see that the trajectory terminates in another fixed point which corresponds to the higher values of $(a,h)$ – a bistable state. The excitable dynamics leads to a short-lasting puff when the $Ca^{2+}$ concentration is pulse-like. In contrast, the bistable cluster dynamics ensures that the $Ca^{2+}$ concentration does not return to a base level but stays elevated for longer. This behaviour is associated with a long-lasting puff. The termination of such a long-lasting puff attributes to $IP_3$ unbinding which is discussed in the next chapter. Also, later we will study the possible role of the intra-cluster, inter-channel coupling represented by $\alpha$ in Equation (2.87) in accounting for termination of puffs.

Figure 3.1 (a) and Figure 3.1 (b) confirm the transition from monostable excitable to bistable behaviour previously reported by Rüdiger [2014a]. However, our further analysis based on parameters adapted from Rückl et al. [2015], reveals that another type of behaviour – bistable dynamics – exists in a cluster. We report that it occurs when the number of channels is $N \geq 6$, which is smaller than $N \geq 9$ considered by Rüdiger [2014a]. The studies of clusters with $N = 5$ and $N = 6$ channels are important since such channels were considered when the triggering of calcium waves as a function of increasing $IP_3$ was reported from the hybrid reaction-diffusion simulation by Rückl et al. [2015]. In the next section, we explain the results shown in Figure 3.1 in more detail and study the transitions between three cluster states with bifurcation analysis.

## 3.2 Bifurcation analysis of a single cluster of IP$_3$R channels

In this section, we study how the behaviour of an excitable cluster containing $N = 5$ channels under cytosolic concentration $c_0 = 0.025\,\mu$M, as the reference system, changes with an increase in $N$ or $c_0$. We study the transition between different kinds of behaviour and perform a bifurcation analysis of the dynamical system (2.84)–(2.86). Starting with the key features of the stability analysis, we write the general system compactly in quasistationary approximation

$$\frac{\mathrm{d}a}{\mathrm{d}t} = f(a,h,c), \tag{3.1}$$

$$\frac{\mathrm{d}h}{\mathrm{d}t} = g(a,h,c), \tag{3.2}$$

where

$$c = c_d = c_0 + \frac{1}{2}\alpha N a \left\{ 1 + \tanh\left[\frac{Na-1}{\epsilon}\right]\right\}, \tag{3.3}$$

and $f(a,h,c)$ and $g(a,h,c)$ are right-hand sides of (2.84) and (2.85), respectively. Also, note that $k_a$, $k_1$, and $k_2$ are the functions of $c$ and other parameters given by (2.72), (2.82) and (2.83), respectively. Values of all the other parameters used are presented in Table 3.1.

A cluster typically rests at the excitable fixed point characterised by low fractions of channels $a$, $h$, and concentration $c$. The stability of the two-variable system at the excitable fixed point ($a = a_f$, $h = h_f$) can be studied by introducing a small perturbation in the dynamical variables. Therefore, a new state of the system is $a = a_f + \tilde{a}$, $h = h_f + \tilde{h}$, where $(\tilde{a}, \tilde{h}) \to 0$. We expand the system in Taylor series around $a = a_f$, $h = h_f$ taking into account all previous assumptions. The function in the right-hand side of (3.1) is expanded as

$$\begin{aligned} f(a,h) =& f(a_f + \tilde{a}, h_f + \tilde{h}) = f(a_f, h_f) + \\ &+ \left.\frac{\partial f(a,h)}{\partial a}\right|_{(a,h)=(a_f,h_f)} \tilde{a} + \left.\frac{\partial f(a,h)}{\partial h}\right|_{(a,h)=(a_f,h_f)} \tilde{h} + \mathcal{O}(\tilde{a}^2, \tilde{h}^2). \end{aligned} \tag{3.4}$$

The similar expression is derived for the function $g(a,h,c)$ that appears on the right-hand side of (3.2). Because at fixed points $\mathrm{d}a_f/\,\mathrm{d}t = 0$, $\mathrm{d}h_f/\,\mathrm{d}t = 0$, we write $f(a_f, h_f) = 0$, $g(a_f, h_f) = 0$ from (3.1) and (3.2). Neglecting high-order terms $\mathcal{O}(\tilde{a}^2, \tilde{h}^2)$, we express the nonlinear system of coupled ordinary differential equations in a linearised form as

$$\frac{\mathrm{d}\mathbf{x}}{\mathrm{d}t} = \mathbf{J}\mathbf{x}, \tag{3.5}$$

where matrix $\mathbf{J}$ is the Jacobian of the system calculated at the fixed point and vector $\mathbf{x} = \{\tilde{a}, \tilde{h}\}$. The Jacobian is given by

$$\mathbf{J} = \begin{pmatrix} \frac{\partial f}{\partial a} & \frac{\partial f}{\partial h} \\ \frac{\partial g}{\partial a} & \frac{\partial g}{\partial h} \end{pmatrix}_{(a,h)=(a_f,h_f)}. \tag{3.6}$$

The local stability of the system (3.1)–(3.2) in the vicinity of the fixed point can be determined by the eigenvalues $\lambda_1$, $\lambda_2$ of the matrix $\mathbf{J}$. The time evolution of the perturbations can be expressed as the following exponentials that contain the eigenvalues of the Jacobian

$$\begin{pmatrix} \tilde{a}(t) \\ \tilde{h}(t) \end{pmatrix} = A e^{\lambda_1 t}\vec{v}_1 + H e^{\lambda_2 t}\vec{v}_2, \tag{3.7}$$

where $A$, $H$ are constants and $\vec{v}_1$, $\vec{v}_2$ are the eigenvectors of the Jacobian.

Depending on the values of $\lambda_i$, where $i = 1, 2$, the stability of the fixed point changes (see Strogatz [2014]). Thus, coming back to the ER membrane, for $c_0 = 0.025\,\mu M$ we obtain $\lambda_1 = -26\ \mathrm{s}^{-1}$, $\lambda_2 = -2\ \mathrm{s}^{-1}$ i.e. $\lambda_i < 0$ at fixed point ($a_f \approx 0$, $h_f \approx 0$). This means that the point is stable for small perturbations. This is because perturbations decay exponentially according to (3.7) for negative real parts of eigenvalues. Figure 3.1 (a) and (b) corresponds to a large enough perturbation of the system which allows leaving the fixed point. In this case, it is possible to

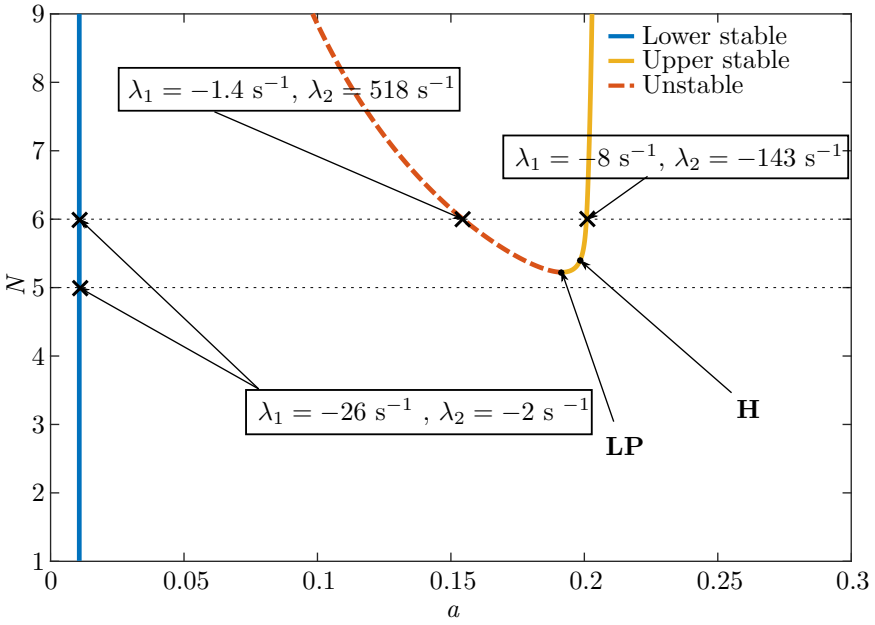


FIGURE 3.2: The bifurcation diagram of the three-state system depending on the number of activatable channels in the cluster $N$. The lower stable branch (*blue solid* line) corresponds to the position of a lower stable fixed point in Figures 3.1(a) and (b). The eigenvalues of the Jacobian on this branch are always real and negative ($\lambda_1 = -26$, $\lambda_2 = -2$). The upper stable (*yellow solid* line) and unstable (*red dashed* line) branches occur as the consequence of the saddle-node (limit point) bifurcation marked by LP. Also, subcritical Hopf bifurcation occurs on a stable branch (marked by H). The positions of fixed points for $N = 6$ correspond to the fixed points in Figure 3.1(b). The stability of the branches are defined by the eigenvalues shown in Figure 3.3 (for $N = 6$ eigenvalues $\lambda_1 = -8$, $\lambda_2 = -143$ correspond to stable fixed point and $\lambda_1 = -1.4$, $\lambda_2 = 518$ correspond to unstable saddle point).

observe puff trajectories (black lines). Small perturbations dissipate according to Equation (3.7) taking the states back to the initial fixed point without following puff trajectories.

Firstly, we study how the behaviour of the system is affected by the increase in the number of activatable channels. The continuation analysis of the three-state system (3.1)–(3.2) has been performed to study the stability of the cluster depending on the number of activatable channels. We plot the bifurcation diagram of the system in Figure 3.2. Three distinctive stability branches corresponding to the three fixed points in Figure 3.1 are shown in Figure 3.2.

Let us study Figure 3.2 in detail. Only the stable branch of the solution exists for the clusters with $N = 5$ and fewer channels on the blue curve. For $N = 5$, the solution corresponds to the stable fixed point in Figure 3.1(a). Note, that the position of the fixed point on the *blue solid* branch for $N \leq 5$ does not depend on $a$. In this case, the eigenvalues of the Jacobian are always negative. However, as $N$ increases passed $N = 5$, a saddle-node bifurcation (or limit point marked by LP) appears. Thus, for $N = 6$ we observe three fixed points as shown in Figure 3.1 (b). Notably, the eigenvalues are negative on the stable branch (shown using *yellow solid* line) and have opposite signs on unstable branch (*red dashed* line). In Figure 3.3 (a) and (b) the eigenvalues of unstable and upper stable branches are plotted as functions of the number of activatable channels $N$ in the cluster. LP is characterised by $\mathrm{Re}(\lambda_1) = 0$ and the two values of $\mathrm{Re}(\lambda_2)$ from the two distinctive branches shown in the top subplots in Figures 3.3 (a) and (b). Also, the imaginary part of both eigenvalues at LP should be zero (as depicted in Figure 3.3 (a) and (b) in bottom subplots). Sub-critical Hopf bifurcation point (H) is associated

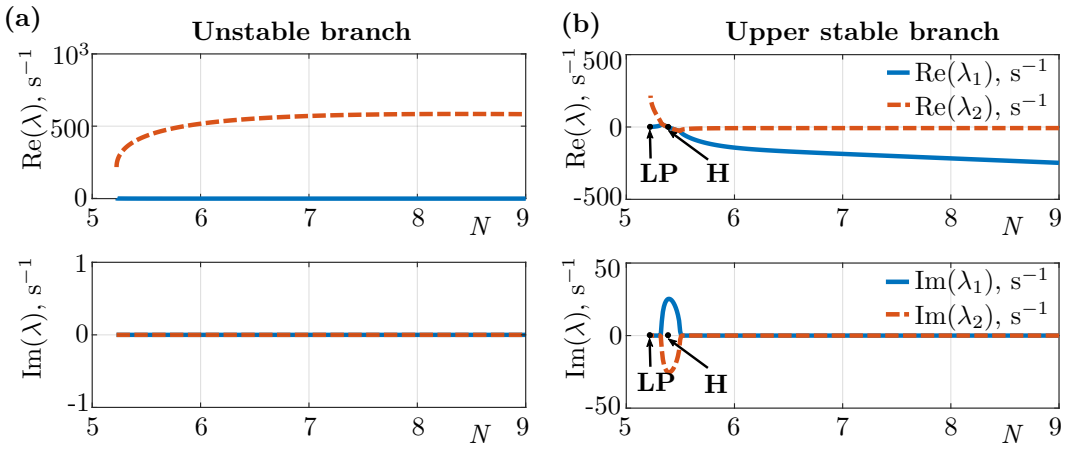


FIGURE 3.3: The eigenvalues corresponding to the bifurcation diagram where $N$ is a control parameter. (a) The real (*top*) and imaginary (*bottom*) parts of the eigenvalues corresponding to the unstable branch in Figure 3.2. (b) The real (*top*) and imaginary (*bottom*) parts of the eigenvalues corresponding to the upper stable branch in Figure 3.2.

with $\mathrm{Re}(\lambda_1) = 0$ and $\mathrm{Re}(\lambda_2) = 0$ and non-zero imaginary parts. We discuss the stability of Hopf points in more details further in this section.

We have confirmed that the change in the number of activatable channels alters the dynamics. As seen in Figures 3.1 (a) and (b), the rest concentration of $Ca^{2+}$ ions was assumed to be $c_0 = 0.025\,\mu$M. Now we study the stability of the lower fixed point in the phase plane, upon changes in $c_0$ parameter. Hence, we vary $c_0$ continuously within the range $(0.025 \leq c_0 \leq 0.6)\,\mu$M to probe qualitative shifts in the system dynamics. For this purpose, we use the MatCont [Dhooge et al., 2008] package for Matlab and report the results of the bifurcation and the continuation analysis. We track how a continuous change in parameters such as $c_0$ alters the fixed point from its location shown in Figure 3.1 (a) to the one shown in Figure 3.1 (c). We supplement our analysis with the study of how the eigenvalues of the Jacobian change as well.

The bifurcation diagram revealing how the location of the fixed point changed with the parameter $c_0$ is shown in Figure 3.4. The real and the imaginary parts of the eigenvalues ($\lambda_{1,2}$) of the Jacobian of the system are plotted in Figure 3.5 (a) and (b). We report two Hopf bifurcation points ($\mathrm{Re}(\lambda_1,\ \lambda_2) = 0$ and $\mathrm{Im}(\lambda_1,\ \lambda_2) \neq 0$) in the range of $c_0$ that determine the stability of the limit cycles in a cluster. The limit cycles are marked by the thin blue horizontal lines scattered in the range between the Hopf points (denoted $\mathrm{H_U}$ and $\mathrm{H_L}$). In particular, we are judging whether the Hopf point is stable based on the Lyapunov coefficient $l_1$ (see Kuznetsov [2000]) derived from the normal form of the system of Equations (2.84)–(2.85). We apply this procedure for each Hopf point assuming $c = c_d$ as in Equation (2.87). If $l_1$ is positive (negative), the Hopf bifurcation is subcritical (supercritical), and the limit cycle is unstable (stable).

Figure 3.6 illustrates in more detail the outcomes of the continuation analysis performed using MatCont. Unlike in Figure 3.4, the phase space here is defined in three variables $c_0$, $a$, $h$, and contains the continuation of the stable limit cycle into a wider range of $c_0$ (blue curves). In our case, the first Lyapunov coefficient is $l_1 = -2.9 \times 10^2$ at $\mathrm{H_U}$ which is the upper point in Figure 3.6. At this point, a stable limit cycle emerges via a supercritical Hopf bifurcation. The first Lyapunov factor is $l_1 = 5.32 \times 10^4$ at a lower Hopf bifurcation point $\mathrm{H_L}$ (this can be seen from the zoomed subplot in Figure 3.6).

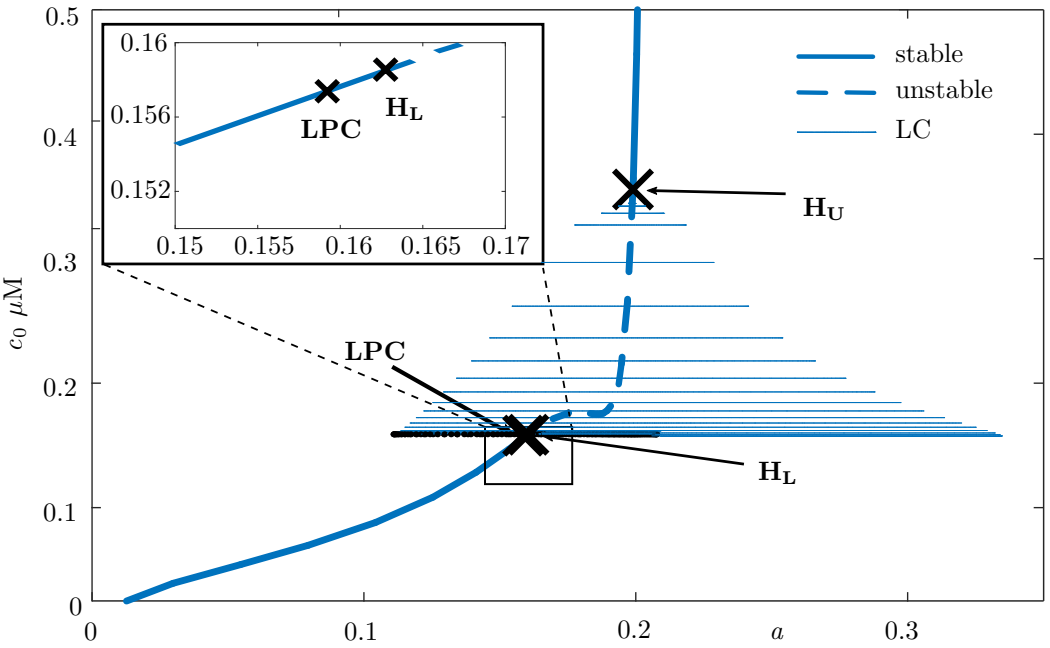


FIGURE 3.4: Bifurcation diagram of the two-dimensional system at $N = 5$ plotted versus control parameter $c_0$, *black crosses* labelled by $H_L$ and $H_U$ correspond to Hopf bifurcation points ($\mathrm{Re}(\lambda) = 0$, $\mathrm{Im}(\lambda) \neq 0$), the limit cycle (LC) solutions are marked by multiple *narrow blue lines*, LPC corresponds to the value of $c_0$ where the fold bifurcation of two limit cycles occurs marked by the line formed from multiple *black dots*. The stable branches shown with the *solid line* while the unstable branch marked with *dashed line*. The difference between the LPC and $H_L$ points is shown in the inset.

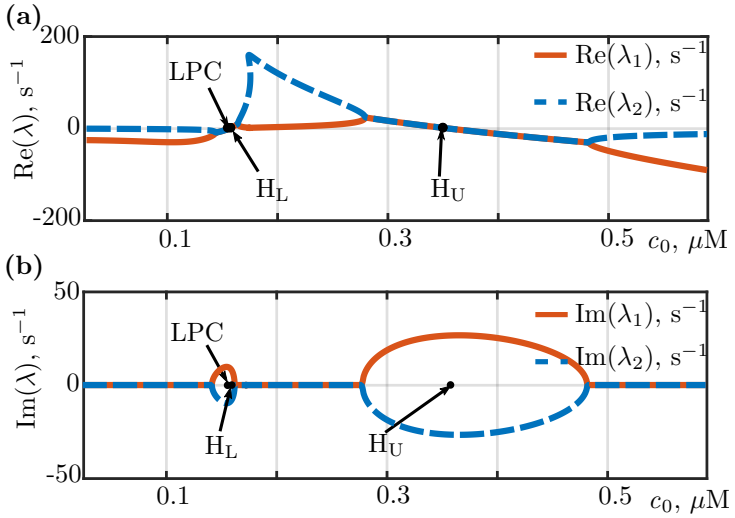


FIGURE 3.5: The real parts of the first two eigenvalues of the system as functions of $c_0$ are shown in (a). The zeros of these functions correspond to Hopf points. The imaginary parts of the eigenvalues of the system as functions of $c_0$ are shown in (b). These functions are non-zero at Hopf points. Two saddle-node bifurcation points are also present in the diagram at $c_0 \approx 0.18\,\mu$M. However, we do not show them in the plot as these points are not relevant to the analysis below and will no longer be discussed.

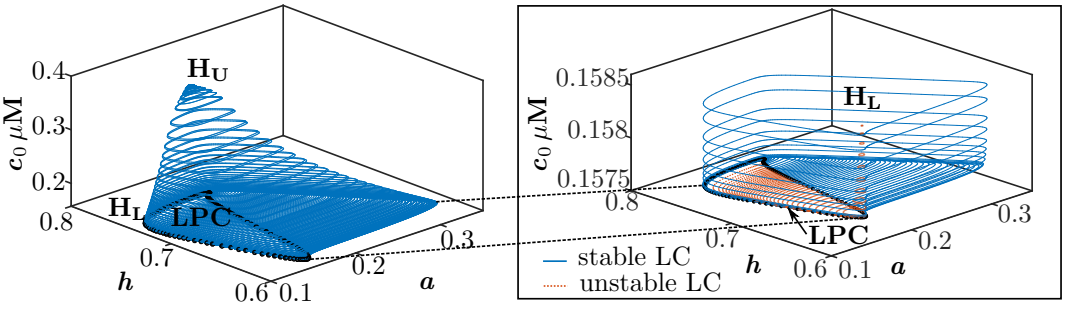


FIGURE 3.6: The stable limit cycle emerges at a supercritical Hopf point labelled as $H_U$. The continuation of the stable limit cycle shown by *blue solid lines*. With the decrease in $c_0$, the unstable limit cycle occurs from subcritical $H_L$ point as indicated by *red dashed lines* of small amplitude in zoomed view. *Black dotted line* corresponds to the fold (limit point) bifurcation of two limit cycles marked as LPC.

Note that the considered range of $c_0$ appears to be larger than the physiologically plausible bounds for the rest concentration of $Ca^{2+}$-ions. Therefore, $c_0$ parameter is considered not to be just a rest value of $[Ca^{2+}]$ but can be attributed to the external influx of $Ca^{2+}$, thus explaining the higher values of $c_0$. We then model $c_0$ to appear within an extended range by the system dynamics. Therefore, now $c_0$ is no longer to be understood as the rest level of $Ca^{2+}$ but is a part of the cytosolic $[Ca^{2+}]$ brought to the cluster by an external source.

Consider the continuation of the stable limit cycle shown in Figure 3.6 in detail. At the maximum value of $c_0 = 0.5\,\mu$M, the fixed point is stable (top of the *blue curve* in Figure 3.4), as supported by the negative real parts and zero imaginary parts of the eigenvalues of the Jacobian plotted in 3.5 (a)-(b). Upon decreasing $c_0$, we reach $H_U$ point for which $c_0 = 0.34\,\mu$M (see Figure 3.6). Here, the stable limit cycle emerges. As we continue decreasing $c_0$, we observe limit cycles with increasing amplitude as shown with the *blue cyclic trajectories* in Figure 3.6. The cyclic trajectory for a chosen intermediate value of $c_0 = 0.16\,\mu$M is shown in Figure 3.1 (c). As we reach $H_L$ point for which $c_0 = 0.1585\,\mu$M, the unstable limit cycle (invisible in the plot) occurs around LPC point. The two limit cycles (unstable and stable) collide near $c_0 = 0.158\,\mu$M. This fold bifurcation of limit cycles is labelled as LPC (marked by *black dotted trajectory*). The limit cycle solution ceases to exist for values of $c_0$ smaller than the LPC point. Thus, we conclude that the stable limit cycle solutions exist in a narrow range of $[Ca^{2+}]$ concentrations between $H_U$ and LPC points.

The bifurcation diagrams obtained from the models by De Young and Keizer [1992] and by Li and Rinzel [1994] are different from the ones studied here. The difference is due to the assumptions about the speed of dynamical variables and different reduction schemes employed. In De Young and Keizer [1992] and Li and Rinzel [1994] $[Ca^{2+}]$ is dynamical and $[IP_3]$ is a parameter changing in a certain range, whereas we keep $[IP_3]$ at a constant high level. Moreover, the earlier models assume a well-mixed membrane and do not account for the clustering of channels that was introduced in Rüdiger [2014a]. We further study the different $Ca^{2+}$ dynamics associated with $IP_3R$ clusters and physiological parameters for which the transitions for different kinds of behaviour may occur.

## 3.3 Conclusions

In the current chapter, we show three different regimes of cluster behaviour in *Xenopus* oocytes, i.e. excitable, bistable and oscillatory. These regimes are observed under different physiological conditions such as the number of activatable channels in a cluster, or the level of rest $Ca^{2+}$ concentration. The transitions between the observed regimes are studied employing dynamical systems theory. We apply continuation analysis to study bifurcation diagrams, analyse the real and the imaginary parts of eigenvalues of the Jacobian to investigate the stability of fixed points under changing parameters. Furthermore, we predict the existence of the stable limit cycle occurring at the upper supercritical Hopf point and report that it collides with the unstable limit cycle occurring at the lower subcritical Hopf point. The latter is an indicator of the most curious regime of cluster dynamics – oscillations.

The reported results demonstrate the possibility of $Ca^{2+}$ oscillations in a cytosolic $[Ca^{2+}]$ within a single cluster containing $N = 5$ channels. The amplitudes of oscillations lie within a physiologically plausible range and their periods are similar to those of oscillations found in several cell types by Callamaras et al. [1998]. The oscillatory regime returned by the proposed three-state model relates to autonomous oscillations of $[Ca^{2+}]$ within a single cluster of $IP_3R$ channels in *Xenopus* oocytes. This suggests that cells may have evolved to ensure certain conditions on the ER membrane, such as significantly increased levels of the rest cytosolic concentration, to trigger regulation via $Ca^{2+}$ oscillations. Certainly, the concentrations required to enter the oscillatory regime ($c_0 > 0.16\,\mu$M) are too high to be achieved only by the random fluctuations in $Ca^{2+}$ levels.

High levels of $[Ca^{2+}]$ may be caused either by the external stimulus (coming from outside of the cell) or by the activation of the neighbouring clusters. We will study the second mechanism in detail in the next few chapters. Various studies [Skupin et al., 2008, Thurley et al., 2011] indicate that $Ca^{2+}$ oscillations are collective events, and emerge when multiple clusters are involved. Inspired by this, we will study the role of coupling between the neighbouring clusters in the emergence of the synchronous oscillations. We will further demonstrate that if the coupling between the clusters is removed, the oscillations of the neighbouring clusters become asynchronous.

# Chapter 4

# A Cluster-based One-dimensional Model of Calcium Waves & Oscillations

---

The present chapter contains several modelling approaches devoted to the study of $Ca^{2+}$ waves and oscillations. We extend the single-cluster approach described in the previous chapter to a chain of coupled clusters. A chain of clusters enables us to incorporate a spatial variation of the system states as field variables, and also introduce the diffusive transport. Instead of letting $c_0$ to be a fixed external control parameter that sets the level of $Ca^{2+}$ ions in the appropriate range for oscillatory behaviour in the bifurcation analysis, we allow $Ca^{2+}$ levels to be dynamically set by diffusion. In this case, the effective diffusion constant $D$ is the control parameter that sets the $Ca^{2+}$ levels locally and affects the physiological output. To ascertain whether altering the $Ca^{2+}$ levels between a cluster primed for bistability and the one which is excitably monostable, we set up in Section 4.2 a two-cluster model to study its phase diagram by bifurcation analysis. Once again, we find the existence of two Hopf bifurcation points as $D$ is altered and obtain the corresponding limit cycle trajectories. We associate these trajectories with the emergence of $Ca^{2+}$ oscillations in a chain of coupled clusters.

The structure of this chapter is as follows. The discrete model for the dynamics of a single cluster is extended to a spatial model in the first section. In Section 4.3, we apply our cluster-based model to study $Ca^{2+}$ release from a domain in the ER membrane with clusters containing different numbers of channels. We demonstrate how the interplay between excitable and bistable clusters is a mechanism for the emergence of $Ca^{2+}$ oscillations within the ER membrane. We also show that the cluster-based model, endowed with spatial diffusion, is capable of exhibiting $Ca^{2+}$ waves that propagate throughout the membrane.

## 4.1 Spatial extension of the single-cluster model

In this section, we lay down the assumptions employed in the development of a spatially distributed model for a phenomenological representation of $Ca^{2+}$ waves viewed as a set of sequential $Ca^{2+}$ releases from clusters (recall Figure 2.14 (c)). We also incorporate carefully chosen features of earlier models from the literature (Atri et al. [1993], Dawson et al. [1999], De Young

and Keizer [1992], Li and Rinzel [1994], Rückl et al. [2015], Rüdiger [2014a]). An examination of the dynamical regimes of individual cluster-level reductions that account for the blip to puff phenomena enables us to propose a model of diffusively coupled clusters in the ER membrane where $Ca^{2+}$ release occurs. We have analysed the clusters separately using dynamical systems theory and confirmed the existence of two qualitatively different types of behaviour in clusters with the different number of channels – excitable (puff regime) and bistable (wave regime) as in Rüdiger [2014a]. We shall probe whether introducing diffusive coupling and linear relaxation (as in equation (2.86)), that can subsume effects such as buffering (see Duffy et al. [1998]) or other modes of reducing spatial gradients, can facilitate the occurrence of oscillating $Ca^{2+}$ releases in the ER membrane.

Incorporating $Ca^{2+}$ buffering into the model requires the following reaction scheme

$$\mathrm{Ca^{2+}} + \mathrm{B} \underset{\mathrm{k^-}}{\overset{\mathrm{k^+}}{\rightleftharpoons}} \mathrm{CaB},$$

where B is a buffer, CaB is a $Ca^{2+}$–buffer complex, $k^{\pm}$ are kinetic rates.

For example, the model by Duffy et al. [1998] in a compact notation denoting [CaB] as $b$, [$Ca^{2+}$] as $c$ and the total amount of buffer as $b_t$=[B]+[CaB], employing the described reaction scheme can be written as

$$\frac{\partial c}{\partial t} = D_c \frac{\partial^2 c}{\partial x^2} + f(c) + k^- b - k^+ c(b_t - b), \tag{4.1}$$

$$\frac{\partial b}{\partial t} = D_b \frac{\partial^2 b}{\partial x^2} - k^- b + k^+ c(b_t - b), \tag{4.2}$$

where only one spatial dimension $x$ is considered, $D_c$, $D_b$ are diffusion constants of $Ca^{2+}$ and CaB, respectively. Here the Fick-type term accounts for spatial diffusion and the non-linear function $f(c)$ is given by

$$f(c) = J_{\mathrm{act}} + J_{\mathrm{leak}} + J_{\mathrm{pump}} = c_1(\nu_1 P^e_{\mathrm{open}} + \nu_2)(c_{ER} - c) - \frac{\nu_3 c^2}{c^2 + k_3^2}, \tag{4.3}$$

analogous to Equation (2.21) in DYK. In the case of fast buffering, the equations can be significantly simplified. We assume quasistationary state for $b$ thus, the forward reaction is equal to a reverse one $k^- b = k^+ c(b_t - b)$, so

$$b = \frac{b_t c}{K + c}, K = \frac{k^-}{k^+}. \tag{4.4}$$

Therefore, using (4.4) and assuming $b_t$ as constant we get

$$\frac{\partial c}{\partial t} + \frac{\partial b}{\partial t} = \frac{\partial c}{\partial t} + \frac{\mathrm{d}b}{\mathrm{d}c}\frac{\partial c}{\partial t} = (1 + b_t V)\frac{\partial c}{\partial t}, \tag{4.5}$$

where the factor before $\frac{\partial c}{\partial t}$ is obtained from the derivative of Equation (4.4) and

$$V = \frac{K}{(K + c)^2}. \tag{4.6}$$

Substituting (4.1) and (4.2) in (4.5) and assuming quasistationary state we obtain

$$\begin{aligned}\frac{\partial c}{\partial t} &= \left(\frac{D_c}{1+b_tV}\right)\frac{\partial^2 c}{\partial x^2} + \left(\frac{D_b b_t}{1+b_tV}\right)\frac{\partial^2}{\partial x^2}\left(\frac{c}{K+c}\right) + \frac{f(c)}{1+b_tV} \\ &= \left(\frac{D_c + D_b b_t V}{1+b_tV}\right)\frac{\partial^2 c}{\partial x^2} - \frac{2D_b b_t V}{(K+c)(1+b_tV)}\left(\frac{\partial c}{\partial x}\right)^2 + \frac{f(c)}{1+b_tV}.\end{aligned} \tag{4.7}$$

This result is reported by Duffy et al. [1998] as the diffusion-advection equation, which represents the transport of $Ca^{2+}$ by fast buffering. The simplified models normally introduce the effective diffusion coefficient $D$, which effectively accounts for $Ca^{2+}$ buffering. For simplicity, we account for all kinds of buffers in such a way by adapting the value of effective coefficient $D$. It allows us to qualitatively account for $Ca^{2+}$ buffering. Thus, we simplify the equation for $Ca^{2+}$ dynamics, including advection term into an effective diffusion coefficient. The result is a continuum differential equation of Fick's type, with a nonlinear source/sink-type term $f(c)$ in it

$$\frac{\partial c}{\partial t} = D\frac{\partial^2 c}{\partial x^2} + \beta f(c), \tag{4.8}$$

where $\beta = 1/(1+b_tV)$. We use the simplified version of equation (4.8) in the following manner. Our model employs the approach proposed by Rüdiger [2014a], which is valid for a single cluster containing $N$ activatable channels. We extend this approach to larger scales by introducing a diffusion term in Equation (2.86) and using $J_{\text{act}} = H(r_{cl} - |x - x_i|)\lambda(c_d - c)$ as an approximation for the activation term in $\alpha f(c)$, which has nonzero values only at the clusters of channels. The small rest level of $Ca^{2+}$ concentration $c_0$ is brought into the model by the leak term $J_{\text{leak}}$. Since the timescales of pumps ($\sim 1 - 10$ s) are slower than those considered here, we incorporate the linearised terms corresponding to $J_{\text{pump}}$ into the model. We account for different pump strengths effectively by varying the coefficient $\lambda$ responsible for the reaction term. All the previous assumptions are incorporated into the model by modifying the equilibration Equation (2.86), and by introducing a one-dimensional diffusive transport term, which results in the following field equation

$$\frac{\partial c}{\partial t} = D\frac{\partial^2 c}{\partial x^2} - \lambda\sum_i H(r_{cl} - |x - x_i|)\left(c - c_d(a_i)\right), \tag{4.9}$$

where $c_d(a_i)$ is given by (Equation (2.87)), $D$ is an effective diffusion constant, $x$ is a spatial coordinate, $H(x)$ is the Heaviside step-function ensuring that calcium release into the cytoplasm occurs only at the clusters located at $x_i$, $i = \overline{1, L}$, and $r_{cl}$ is the cluster radius. The Heaviside function is the step function given by

$$H(x) = \begin{cases} 1, & \text{if } x \geq 0, \\ 0, & \text{otherwise.} \end{cases} \tag{4.10}$$

For the convenience of notation, we shall assume that the $i$ dependence within $a_i$ is implicit hereafter.

The model proposed in the current chapter is of the fire-diffuse-fire type, studied before by Dawson et al. [1999]. Unlike previous studies, we propose a direct link between the $Ca^{2+}$ level $c$ and the proportion of opened channels $a$ through nonlinear function within Equation (2.87). This also

helps us to associate cellular behaviour of $Ca^{2+}$ release on a spatial scale larger than the cluster size $r_{cl}$ to microscopic channel characteristics found by De Young and Keizer [1992].

The system of equations (2.84)–(2.85) together with Equation (4.9) is a reaction-diffusion system. The first term on the right side of Equation (4.9) corresponds to the smoothing of a $Ca^{2+}$ front and the spreading of $[Ca^{2+}]$ from the active clusters to the neighbouring ones as sketched in Figure 2.14 (c). The second term on the right side is the reaction term, in which $c_d$ (2.87) is a function of the number of opened channels and accounts for the opening of $IP_3R$ channels in the clusters. The equilibration of cytosolic $Ca^{2+}$ to $c_d$ at the rate $\lambda$ is a linear homeostatic reaction term that subsumes the action of pumps, leaks, and buffers, which drives the cytosolic $[Ca^{2+}]$ to the quasi-steady-state value $c_d$. We explore next how the proposed model can generate waves and oscillations and characterize them in terms of the model parameters.

## 4.2 Discrete cluster-based model

Here we study the dynamics of a chain of clusters coupled by diffusing $Ca^{2+}$ ions. The interactions between the clusters via diffusive fluxes $J_{ij}$ are schematically shown in Figure 4.1. We study a simple example to illustrate the effect of coupling between neighbouring clusters. Consider $L$ number of clusters coupled with by diffusion term in Equation (4.9). The discrete form of Equation (4.9) is specified for the $i^{th}$ cluster in terms of the local $Ca^{2+}$ concentration $c_i$, whose rate of change is proportional to the spatial gradient of the diffusive flux $J_i$ for $i = 1, \ldots, L$

$$\frac{\partial c_i}{\partial t} = \frac{1}{\ell}(J_i - J_{i-1}) = \frac{1}{\ell}\left[D\left(\frac{c_{i-1} - c_i}{\ell}\right) - D\left(\frac{c_i - c_{i+1}}{\ell}\right)\right]. \tag{4.11}$$

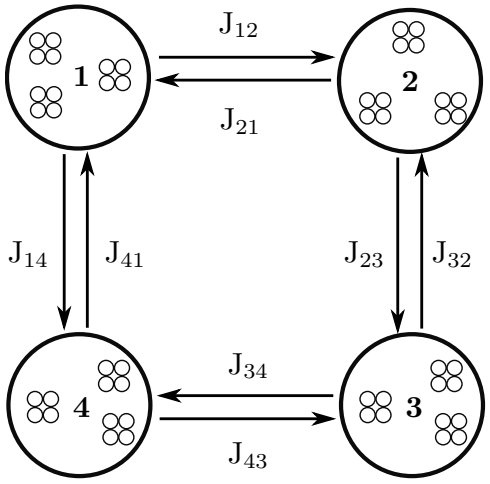


FIGURE 4.1: The scheme of diffusive fluxes $J_{ij}$ between $L = 4$ number of clusters coupled in a ring topology.

For the modelling case, we specify the characteristic distance between clusters $\ell \approx 1.3\,\mu$m. The effective diffusion constant for $Ca^{2+}$ ions is taken to be $D = 30\ \mu m^2/s^{-1}$ according to Allbritton et al. [1992]. As per Figure 4.1, we assume the clusters to be coupled following ring topology with the periodic condition $c_{i+L} = c_i$.

The system (2.84)–(2.85) for clusters coupled by diffusion (4.9) is rewritten considering that the diffusion term is given by Equation (4.11), which for $L$ clusters results in

$$\frac{\mathrm{d}a_j}{\mathrm{d}t} = k^+_{a_j} c_j(1 - a_j - h_j) - k^-_{a_j} a_j + k_{1j} h_j - k^+_i c_s a_j, \tag{4.12}$$

$$\frac{\mathrm{d}h_j}{\mathrm{d}t} = k^+_i c_j(1 - a_j - h_j) - k_{1j} h_j - k_{2j} h_j + k^+_i c_s a_j, \tag{4.13}$$

$$\frac{\mathrm{d}c_j}{\mathrm{d}t} = D\frac{\partial^2 c_j}{\partial x^2} + \lambda(c^d_j(N_j a_j) - c_j), \tag{4.14}$$

where $j = 1, .., L$. Variable $a_j$ is the fraction of the number of activated channels and $h_j$ is the function of the number of inhibited channels in the $j^{th}$ cluster, while $c^d_j = c_0 + 0.5\alpha N_j a_j(1 + \tanh((N_j a_j - 1)/\epsilon))$ is the steady-state $[Ca^{2+}]$ and $N_j$ is a number of actavatable channels in the $j^{th}$ cluster.

We numerically solve the system (4.12)–(4.14) for $\ell \approx 1.3\,\mu$m and $D = 30\ \mu\mathrm{m}^2/\mathrm{s}^{-1}$ as well as for cluster parameters as specified in the previous section. Only the equilibration rate is modified for these simulations and set to $\lambda = 230\,\mathrm{s}^{-1}$, instead of $\lambda = 10^3\,\mathrm{s}^{-1}$ that was used earlier. We modify the coefficient $\lambda$ to make the transition from puff regime to propagating wave regime similarly as reported by Rüdiger et al. [2012]. The variability in $\lambda$ may be explained by the influence of the various processes which are accounted for effectively in the model, e. g. pumps, leak, etc. The main target of the current chapter is to demonstrate the occurrence of various curious effects observed in the system of coupled clusters. Thus, we choose the values of parameters $D$, $\lambda$ and $\ell$ and then look at how the variability in those characteristics affects the results.

The formation of travelling $Ca^{2+}$ waves in the chain of clusters obtained from our model is depicted in Figure 4.2 for a chain of three clusters consisting of $N = 5$ channels each. At the

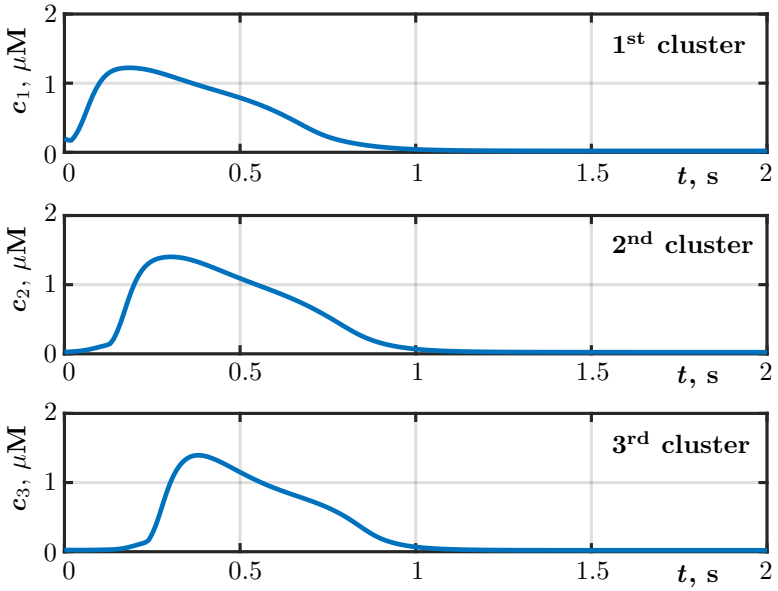


FIGURE 4.2: The emergence of a travelling $Ca^{2+}$ wave in the second and third clusters triggered by the initial $[Ca^{2+}]$ rise at the first cluster. The numbers of channels in each cluster are the same and equal to $N = 5$.

first step of the simulation, an initial rise in the local concentration $[Ca^{2+}]$ in the first cluster is triggered by a stimulus arriving from the surroundings. The excitation of the first cluster

activates a travelling wave in the clusters two and three as shown in Figure 4.2 with the $[Ca^{2+}]$ profiles plotted versus time for each of the three clusters. The time traces of the concentration profiles approximately show a form $F(x - vt)$, where $F$ is the travelling waveform, and $v$ some wave speed. The slight changes in the shape of the waveform suggest a dispersive character of the travelling wave, in addition to nonlinearity within the system. The coupling due to diffusion enables the spatial propagation of the initial excitation to the neighbouring cluster. This mechanism illustrates the emergence of train-like $Ca^{2+}$ waves. Similar travelling fronts have been observed in previous phenomenological models by Duffy et al. [1998] and Timofeeva [2003]. The prolonged durations of puffs here $\sim 1$ s, unlike $\sim 100$ ms in the previous chapter, may be explained by the transition from puff to wave regime. In the previous chapters, we looked at the isolated cluster level, while here we consider a chain of the coupled clusters. Interestingly, the equilibration rate $\lambda$ may serve as the additional degree of freedom to regulate the release durations.

In this study, we account for a discrete array of clusters with the emphasis on studying the influence of the number of activatable $IP_3R$ channels in a cluster on the $Ca^{2+}$ dynamics. This allows us not only to obtain the travelling wave behaviour but also to study the dependence of such waves on physiological characteristics of clusters.

To understand the effect of cluster parameters on the emergence of $Ca^{2+}$ waves, consider a unit cell of a discrete chain of clusters – a system of $L = 2$ clusters coupled by diffusion. The model parameters for both clusters are the same apart from the activatable numbers of channels. These are equal to $N = 9$ ($N = 5$) in the first (second) cluster. The dynamics of the two coupled clusters in our model is described by

$$\frac{\mathrm{d}a_i}{\mathrm{d}t} = f(a_i, h_i, c_i),\ i = 1, 2 \tag{4.15}$$

$$\frac{\mathrm{d}h_i}{\mathrm{d}t} = g(a_i, h_i, c_i),\ i = 1, 2 \tag{4.16}$$

$$\frac{\mathrm{d}c_1}{\mathrm{d}t} = -\lambda[c_1 - c_d(a_1)] - \frac{2D}{\ell^2}(c_1 - c_2), \tag{4.17}$$

$$\frac{\mathrm{d}c_2}{\mathrm{d}t} = -\lambda[c_2 - c_d(a_2)] - \frac{2D}{\ell^2}(c_2 - c_1). \tag{4.18}$$

The results obtained from numerical integration of the above equations are presented for $L = 2$ model in Figure 4.3. Note, that this unit cell case is a particular example of a chain of clusters of arbitrary length $L$. We use the discrete chain approximation to illustrate the behaviour of the clusters in a "one-dimensional membrane". Unlike in the single-cluster analysis, calcium concentration $c$ in the cytosol is now explicitly added to the model; the equilibration rate $\lambda$ is reduced and the diffusion term is introduced in (4.17)–(4.18). The assumption that $c$ is driven to $c_d$ very quickly is inapplicable as we need to account for a separate dynamics of $Ca^{2+}$ cytosolic concentration away from the steady-state value $c_d$.

Even though cluster 1 is bistable and cluster 2 is excitable in the isolated case when the coupling is on the system of clusters shown in Figure 4.3 turns oscillatory. The oscillations are observed from the dynamical analysis of cluster 1 as per Figure 4.3 (a) and of cluster 2 as per Figure 4.3 (b); oscillations being attributed to the diffusive interaction between the clusters. Notably, the concentration of $Ca^{2+}$ at cluster 1 exhibits small amplitude oscillations (as apparent from Figure 4.3 (c)) around the fixed point with high $c_1$. The influx from cluster 1 causes

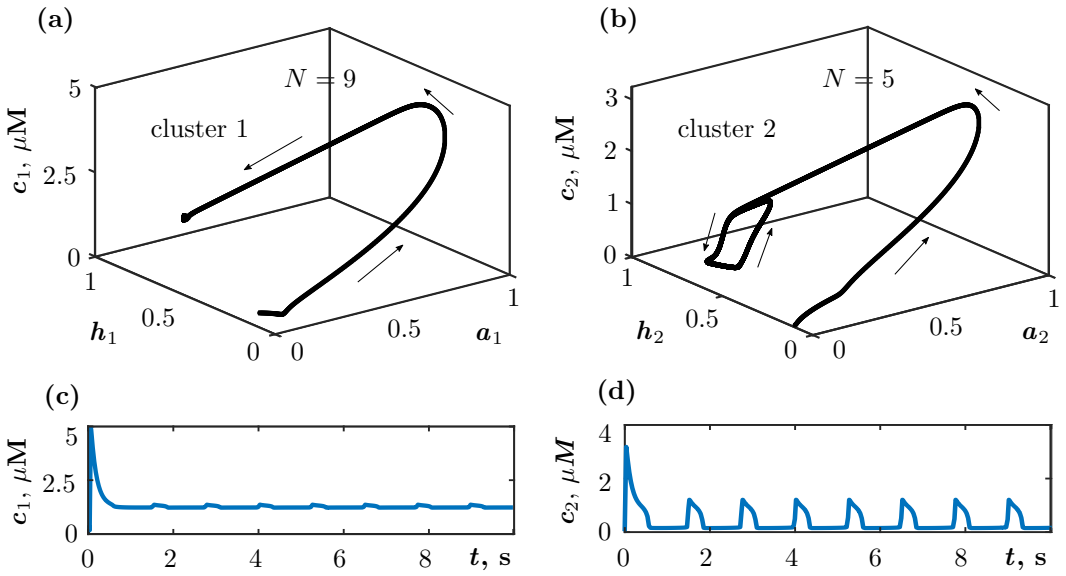


FIGURE 4.3: The initiation of $Ca^{2+}$ oscillations in the array of two clusters $D = 30\,\mu m^2/s$, $\lambda = 230\,s^{-1}$. **(a)** The trajectory in cluster 1 with $N = 9$ channels. **(b)** The oscillatory trajectory in cluster 2 ($N = 5$) triggered by the diffusion from the first cluster. **(c)**, **(d)** Oscillating $Ca^{2+}$ profiles in each cluster respectively.

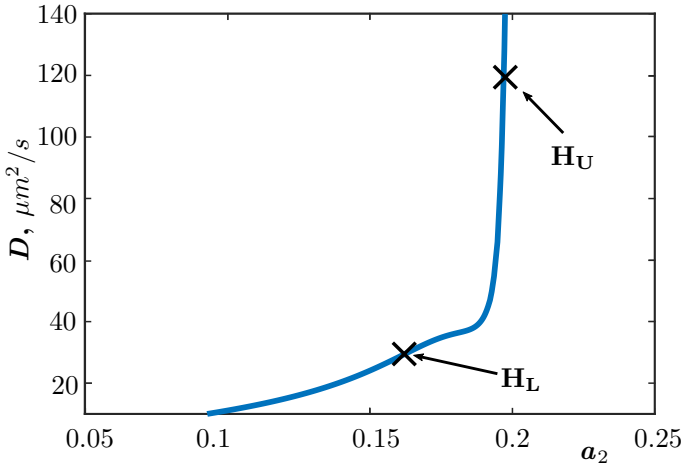


FIGURE 4.4: Bifurcation diagram for varying fraction of the open channels in the cluster 2 denoted $a_2$ plotted versus diffusion coefficient $D$. The points $H_L$ and $H_U$ represent Hopf bifurcation points ($\mathrm{Re}(\lambda) = 0$, $\mathrm{Im}(\lambda) \neq 0$).

the emergence of $Ca^{2+}$ oscillations in cluster 2 as apparent from Figure 4.3 (d). To study this effect, we perform the continuation analysis of the system of two coupled clusters given by Equations (4.15)–(4.18) using an approach similar to that for a single cluster described earlier. The number of dimensions of the system used in the bifurcation analysis is 6, but we represent the results on two three-dimensional plots to depict the governing dynamics at each cluster. The bifurcation diagram is shown in Figure 4.4 showing the dependence of the control parameter $D$ on the magnitude of $a_2$ corresponding to the fixed point. The effect of $Ca^{2+}$ flux from cluster 1 to cluster 2 is proportional to $D$, which controls the strength of coupling. We determine two Hopf points $H_U$ and $H_L$ from the plots of the real and the imaginary parts of the eigenvalues of the Jacobian matrix $\mathbf{J}$ shown in Figure 4.5. These points correspond to the stable and unstable limit

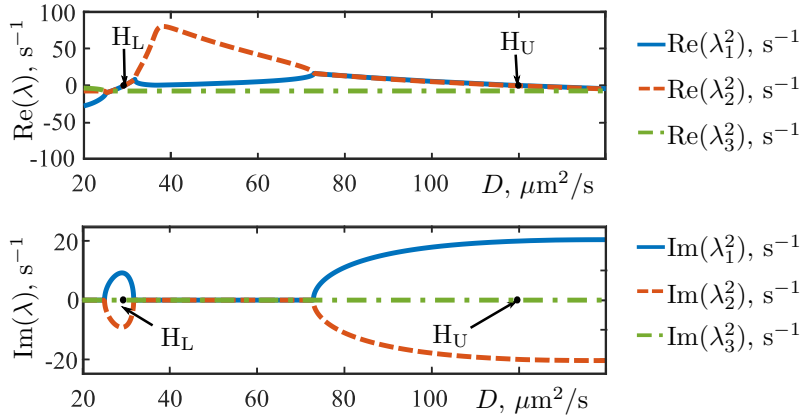


FIGURE 4.5: Eigenvalues of the Jacobian of Equations (4.15)–(4.18) in the cluster 2 denoted by $\lambda_i^2$, $i = \overline{1,3}$. (a) The real parts of the eigenvalues in the cluster 2, which are zeros at Hopf points. (b) The imaginary parts of the eigenvalues in the cluster are non-zeros at Hopf points.

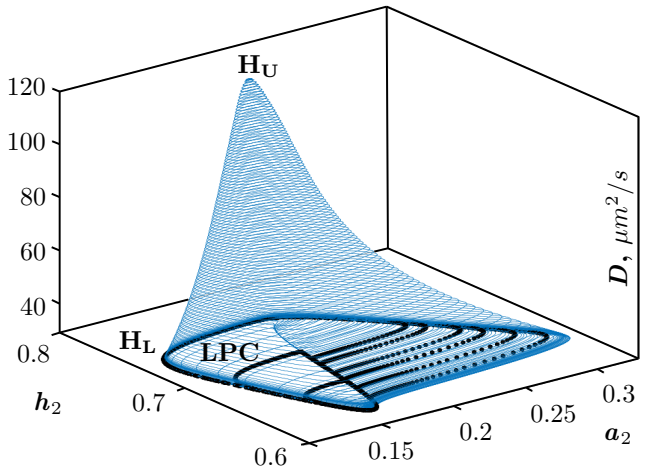


FIGURE 4.6: The continuation of a limit cycle (blue lines) performed by analogy to Figure 3.4 varying $D$. Similarly, the black markers correspond to the fold bifurcation of limit cycles (LPC).

cycles, respectively. The continuation analysis of the stable limit cycle at $H_U$ visualised in Figure 4.6, shows that the periodic solutions in cluster 2 exist in the range $(29 \leq D \leq 120)\,\mu m^2/s$. This brings the range of concentrations of $Ca^{2+}$ to the one shown in Figure 3.4 for the same $\lambda$. Thus, we conclude that the emergence of oscillations in the second cluster depends on the concentration influx from cluster 1 to cluster 2 which raises the level of concentration in cluster 2 to a range that drives oscillations in the single cluster model. Note, that if the numbers of channels in both clusters are the same, the behaviour in the system would be similar to Figure 4.2.

In the more general case of 3 clusters shown in Figure 4.7, we observe the similar behaviour as before in Figure 4.3. This implies the existence of a similar effect in the larger systems consisting of three clusters and more. The only condition on the occurrence of the oscillations lies on the numbers of channels in the connected clusters. Note, that the transition from excitable to bistable behaviour in the isolated cluster in our case occurs between $N = 5$ and $N = 6$ channels. To become oscillatory, one of the clusters must be in the bistable regime if isolated, thus consisting more than $N = 6$ channels ($N = 9$ here is enough to establish the oscillatory regime). The rest of the clusters are at the edge of excitability consisting of $N = 5$ activatable channels.

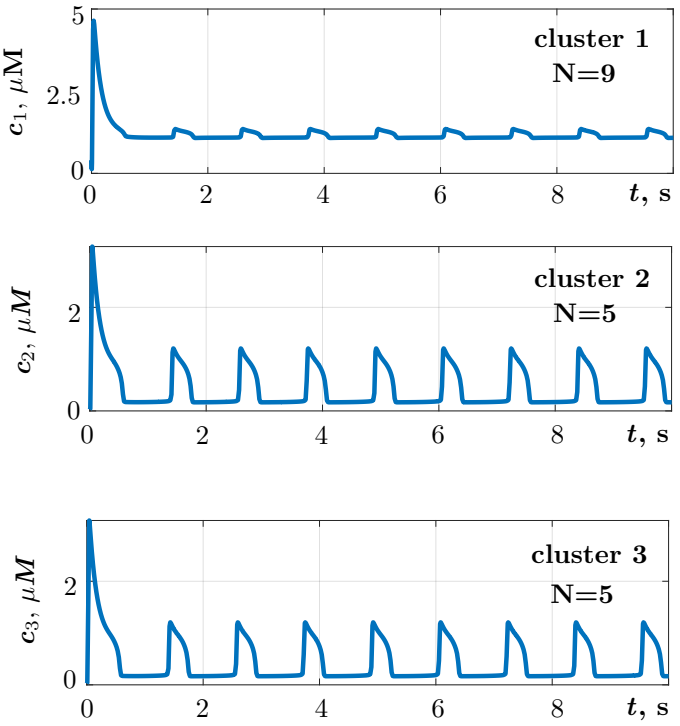


FIGURE 4.7: The emergence of the oscillations in 3 coupled clusters. The first one contains $N = 9$ activatable channels, both clusters 2 and 3 contain $N = 5$ channels.

Interestingly, the boundaries of the oscillatory effect are defined by the ratio $D/(\ell^2\lambda)$. We fix values of $\ell$ to the ones observed experimentally, equilibration rate $\lambda$ is heuristically defined to accommodate various effects (pumps, leak), the diffusion coefficient $D$ also varies when accounting for various buffers. This serves as the cause for variability in these parameters in the further sections. Having accounted for the ability of diffusive couplings to bring about oscillations in a coupled-cluster system when the individual clusters exhibit non-oscillatory dynamics on their own, we extend the model to one with continuum description. In the next subsection, we apply this mechanism to a domain of the membrane to qualitatively demonstrate the emergence of $Ca^{2+}$ waves and oscillations in the ER membrane.

## 4.3 Calcium waves and oscillations

We have shown that the behaviour of the three-state model for a single cluster depends on the number of channels $N$ in a cluster that are $IP_3$ bound and may be activated or deactivated by $Ca^{2+}$. While the ER membrane would typically contain clusters with various numbers of channels, we study the simplest heterogeneous scenario with one bistable cluster with $N = 9$ and the multiple excitable clusters with $N = 5$. Here and onward, we refer to a cluster with $N = 9$ as bistable, and to a cluster with $N = 5$ as excitable, as per their behaviour in the isolated single cluster case even though it is the entire system whose stability matters. The choice of the specific activatable numbers of channels is based on the study by Rückl et al. [2015], in which the average number of activatable channels in *Xenopus* oocytes tends to $N = 5$ with the increase in $[IP_3]$. The distribution of the reported numbers of channels appears to be very close

to a Poisson distribution [Rückl et al., 2015, Taufiq-Ur-Rahman et al., 2009]. We will discuss the fitted distributions of numbers of channels in Chapter 6. We chose these numbers to be consistent with Rückl et al. [2015] and propose the modelling of more complex heterogeneous systems in the following chapters. In the chosen situation, the excitable behaviour may be associated with short-lasting puffs, while the bistable behaviour may be associated with waves or long-lasting puffs, where the exit from the long-lasting puffs that is thought to be driven by dissociation of $IP_3$, or other mechanisms which are discussed in Chapter 5. The exit from the long elevated high $Ca^{2+}$ concentrations might be performed through other mechanisms such as change in coupling strength $\alpha$, maximal $Ca^{2+}$ elevation $c_s$ or transition rate $k_i^+$.

Here, we model a domain of the ER membrane, which is assumed to contain multiple excitable clusters ($N = 5$) and only one bistable ($N = 9$) cluster to study the interplay between excitable and bistable clusters. We demonstrate the emergence of oscillations and quantify the characteristics of wave propagation, such as the front velocity and its period. The proposed domain is modelled by solving the following reaction-diffusion system

$$\frac{\partial a}{\partial t} = k_a^+ c(1-a-h) - k_a^- a + k_1 h - k_i^+ c_s a, \tag{4.19}$$

$$\frac{\partial h}{\partial t} = k_i^+ c(1-a-h) - k_1 h - k_2 h + k_i^+ c_s a, \tag{4.20}$$

$$\frac{\partial c}{\partial t} = D\frac{\partial^2 c}{\partial x^2} - \lambda \sum_i H(r_{cl} - |x - x_i|)\left(c - c_d(a_i)\right), \tag{4.21}$$

$$c_d = c_0 + \frac{1}{2}\alpha N a \left\{ 1 + \tanh\left[\frac{Na-1}{\epsilon}\right]\right\}, \tag{4.22}$$

where $a = a(x,t)$, $h = h(x,t)$ and $c = c(x,t)$ are the mean field variables, which now are functions of space and time.

The reaction mechanism can be explained with a simple example. Consider a non-diffusive case $D = 0$ and assume that the nonlinear term at a single cluster (4.22) is $c_d = c_d(a(t)) = c_d(t)$, which is a function of time. Then, equation (4.21) reads

$$\frac{\mathrm{d}c}{\mathrm{d}t} = \lambda(c_d(t) - c). \tag{4.23}$$

The solution of this equation

$$c = A\mathrm{e}^{-\lambda t} + \lambda \mathrm{e}^{-\lambda t}\int_1^t \mathrm{e}^{\lambda\tau} c_d(\tau) d\tau, \tag{4.24}$$

is written in terms of a constant $A$ and a dummy variable $\tau$. The exponential part quickly dissipates with time and the part given by the integral drives the solution to a value which is defined by $c_d$. From the above, $c_d$ contains the activation part $a(t)$, thus, the reaction term yields activation. At the same time, the full reaction-diffusion system follows a combination of two processes, i.e., diffusion which leads to spreading of the $Ca^{2+}$ concentration along the membrane, and reaction, which results in subsequent activation of each cluster and a release of $Ca^{2+}$.

Consider the following modelling assumptions. We set the cluster size $r_{\mathrm{cl}}$ (100 nm) to be equal to the step of integration $\mathrm{d}x$ to simplify the modelling approach. Such consideration is consistent

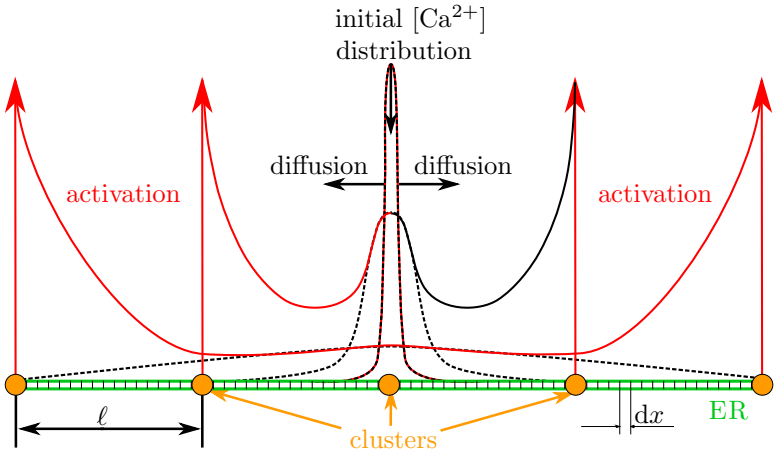


FIGURE 4.8: The schematic representation of reaction and the diffusion in spatial model. The black concentration profiles represent a diffusion of an initial $Ca^{2+}$ distribution when $\lambda = 0$. The red lines correspond to the exemplary profiles, where the reaction part is included, which corresponds to the activation of each cluster. The distance between clusters $\ell$ and computational step $dx$ are shown in the scheme.

with the experimental findings of cluster sizes in *Xenopus* oocytes reviewed by Rüdiger [2014b]. The step of space integration $\mathrm{d}x$ is chosen to be small enough compared to the distance between clusters. This ensures the convergence of the method, however, restricts the choice of the cluster size. Here the cluster size has to be independent of the number of channels for the sake of simplicity. We assume activation and inhibition variables ($a$ and $h$) to be non-zero only at points corresponding to clusters (indicated by orange markers in Figure 4.8).

We apply an explicit finite difference method for space discretisation in application to Equation (4.21) and a standard explicit Euler scheme for time marching in application to Equations (4.19)–(4.20). Such an approach is stable if $\beta = D\,\mathrm{d}t/\,\mathrm{d}x^2 \leq 0.5$ [Iserles, 2012]. Therefore, we should adjust the time and space steps accordingly. The typical effective diffusion coefficient is usually taken equal $D = 30\,\mu\mathrm{m}^2/\mathrm{s}$ in ER membranes. By substituting this value into the convergence condition, we obtain an approximate value for the space step $\mathrm{d}x = 0.1\,\mu\mathrm{m}$ (Figure 4.8), and for the time step $\mathrm{d}t = 10^{-4}$ s. Note, that the scheme is very sensitive to space step variation. Even if the condition $\beta \leq 0.5$ is satisfied, the method gives a significant numerical error, if $\mathrm{d}x \geqslant 0.2$ for a given $D$ and $\mathrm{d}t$. Therefore, apart from satisfying the numerical stability condition, the space step should be chosen to be smaller than 0.2. We select values for space and time steps by validating the scheme against the analytical solution for pure diffusion given by Equation (4.21) after setting $\lambda = 0$. Such a discretisation scheme keeps computational cost at a reasonable level while giving satisfactory accuracy for the full reaction-diffusion system.

We have also tested an advanced discretisation approach by applying the classical Runge-Kutta method to Equations (4.19)–(4.20), and the Crank-Nicholson method to Equation (4.21). The test confirmed that a more computationally expensive technique that is supposed to have better accuracy converged to the same results. Therefore, we have concluded that complex discretisation techniques would overcomplicate the simulations without giving any significant gain in accuracy. Taking this into account, further in this section, we apply the explicit Euler scheme and a standard finite difference method.

The solution of Equations (4.19)–(4.22) in the chosen one-dimensional domain (the multi-dimensional approach is taken up later in Section 5.2) is proposed with the open boundaries and Neumann boundary conditions $\frac{\partial c}{\partial x}(x = 0, L, t) = 0$. Let us assume the part of ER membrane with the initial distribution of cytosolic $[Ca^{2+}]$: $c(x, 0) = c_0 + A \exp\{-[x^2/(2\sigma^2)]\}$, where $A = 2\,\mu$M, $\sigma = 0.1\,\mu$m, which travels from the left part of a membrane as shown in Figure 4.9 (a). Calcium release upon activation occurs only at the $i$-th cluster in Equation (4.9) via $c_d(a)$ and cytosolic concentration of $Ca^{2+}$ is raised above basal level $c_0$ by diffusion between clusters a constant distance $\ell = 3.5\,\mu$m apart. The results depicted in Figure 4.9 are obtained for equilibration rate $\lambda = 230\,s^{-1}$. The effect of changing the values of $D$, $\lambda$, and $\ell$ upon qualitatively differing $Ca^{2+}$ release response is discussed further in this section.

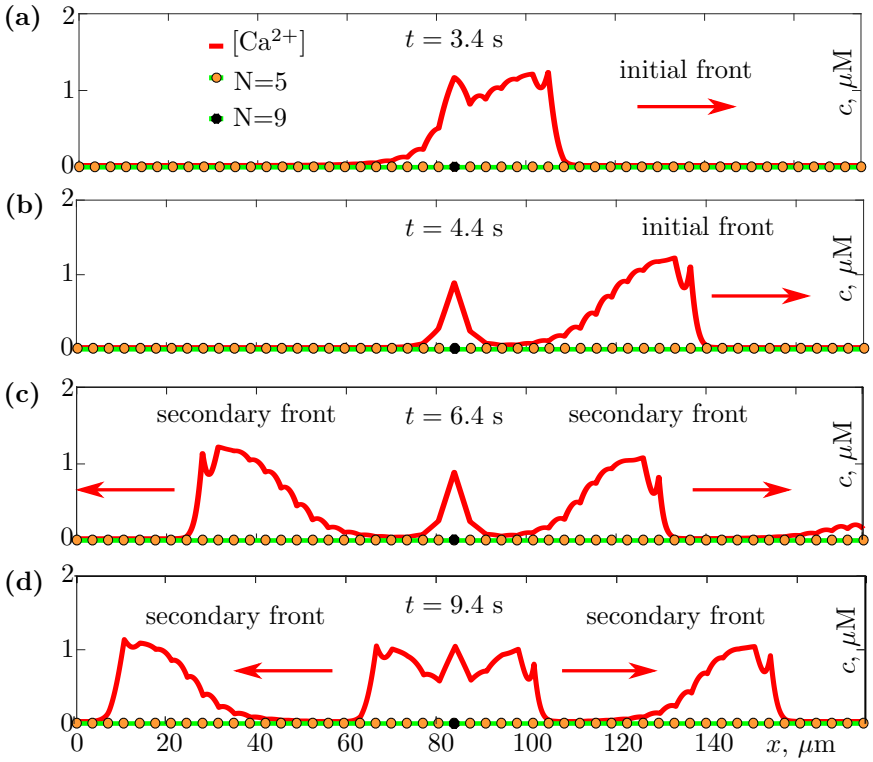


FIGURE 4.9: $Ca^{2+}$ front propagation from the spatial model for two types of clusters and for $D = 30\,\mu m^2/s$, $\lambda = 230\,s^{-1}$. The *orange dots* label excitable clusters with $N = 5$ channels, the *large black dot* corresponds to a bistable cluster with $N = 9$ channels. **(a)** The propagation of a front caused by the raised initial $[Ca^{2+}]$ near $x = 0$. **(b)** The $Ca^{2+}$ peak occurs from the bistable cluster as the wave passes it. **(c)** The diffusion from the peak initiates a secondary wave. **(d)** Oscillating waves initiated from the bistable cluster.

TABLE 4.1: Parameters used in the cluster-based reaction-diffusion model.

| Parameter | Value | Description |
|---|---|---|
| $c_0$ | $0.025\,\mu$M | Rest level of $[Ca^{2+}]$ |
| $N$ | 5 or 9 | Number of activatable channels in a cluster ($IP_3$ bound) |
| $\lambda$ | $230\,s^{-1}$ | Equilibration rate |
| $D$ | $30\,\mu m^2/s$ | Diffusion coefficient |
| $\ell$ | $3.5\,\mu$m | Inter-cluster distance |
| $r_{cl}$ | $0.1\,\mu$m | Cluster radius |

In Figures 4.9 (c) and (d) we observe the emergence of $Ca^{2+}$ oscillations from the bistable cluster (*black dot*) triggered by the initial front. The front starts from an initial $Ca^{2+}$ stimulus near $x = 0\,\mu$m and propagates throughout the membrane. In this simulation, the initiation event is specified by an initial condition in our deterministic model. In an actual membrane, however, the behaviour can be triggered by an initial peak either due to an internal or an external stimulus or by a stochastic fluctuation of $Ca^{2+}$ levels. As the wave-front passes the bistable cluster, it raises the ambient $Ca^{2+}$ concentration around it to the value $c$ (upper fixed point) and activates the bistable regime in Figure 4.3 (a). Physiologically this can be interpreted as a long-lasting state of continuous $Ca^{2+}$ release which is terminated by the unbinding of $IP_3$. We discuss this behaviour in detail later. At this point, we report that due to bistability, a residual peak of $Ca^{2+}$ concentration remains at cluster with $N = 9$ even after the from has passed as shown in Figure 4.9 (b). The ions of $Ca^{2+}$ spread due to diffusion raising ambient $Ca^{2+}$ concentrations in the neighbouring clusters driving them to an oscillatory regime, similarly as in Figure 4.7 but for the larger number of clusters ($n = 3$), which results in the subsequent secondary waves that occur periodically in a deterministic setting. The secondary wave profiles are shown in Figure 4.9 (c)-(d).

Further, we look at the oscillations in coordinate-time representation to observe the evolution of the fronts in space and time more clearly. We assume the distance between clusters to be significantly smaller, i. e. $\ell = 1\,\mu m$ and $\lambda = 90\,s^{-1}$. Figure 4.10 depicts the travelling waves as $Ca^{2+}$ concentration profiles plotted in space $x$ versus time $t$ coordinates. The value of the

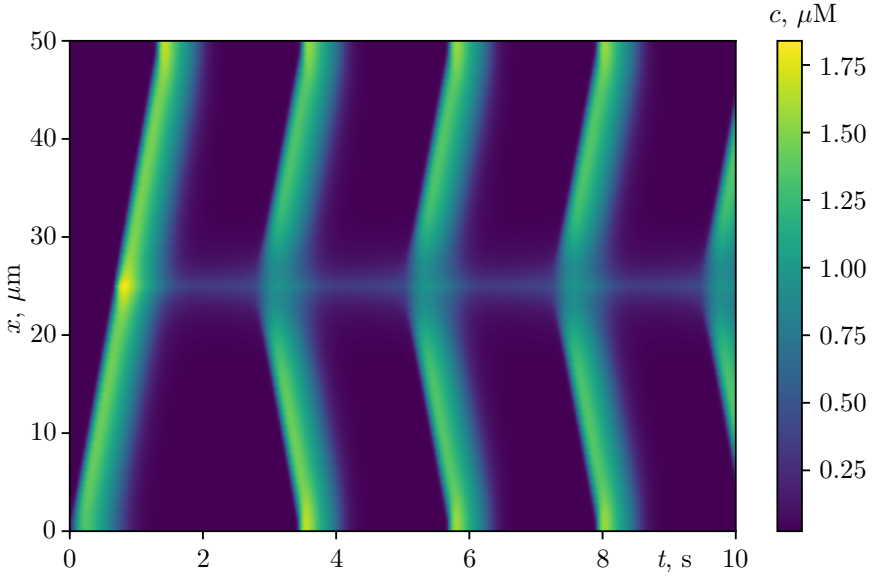


FIGURE 4.10: The emergence of $Ca^{2+}$ oscillations for inhomogeneous numbers of activatable channels in clusters ($\ell = 1\,\mu$m, $\lambda = 90\,s^{-1}$). The yellow spot corresponds to the position of the bistable cluster in the membrane. A value of risen $[Ca^{2+}]$ in the bistable cluster causes the emergence of $Ca^{2+}$ oscillations.

average time calculated between two subsequent $Ca^{2+}$ releases is the wave period and is one of the key characteristics of the behaviour. Therefore, we illustrate the rich dynamics via a phase diagram specified in $\lambda$–$D$ coordinates with wave periods labelled by colour as shown in Figure 4.11 (a). Notice that wave periods appear to be almost constant throughout the whole range of physiological values of $\lambda$ and $D$. Behaviour-wise, the dark regions on the phase diagram correspond to a non-oscillatory dynamics, while oscillations occur within the purple

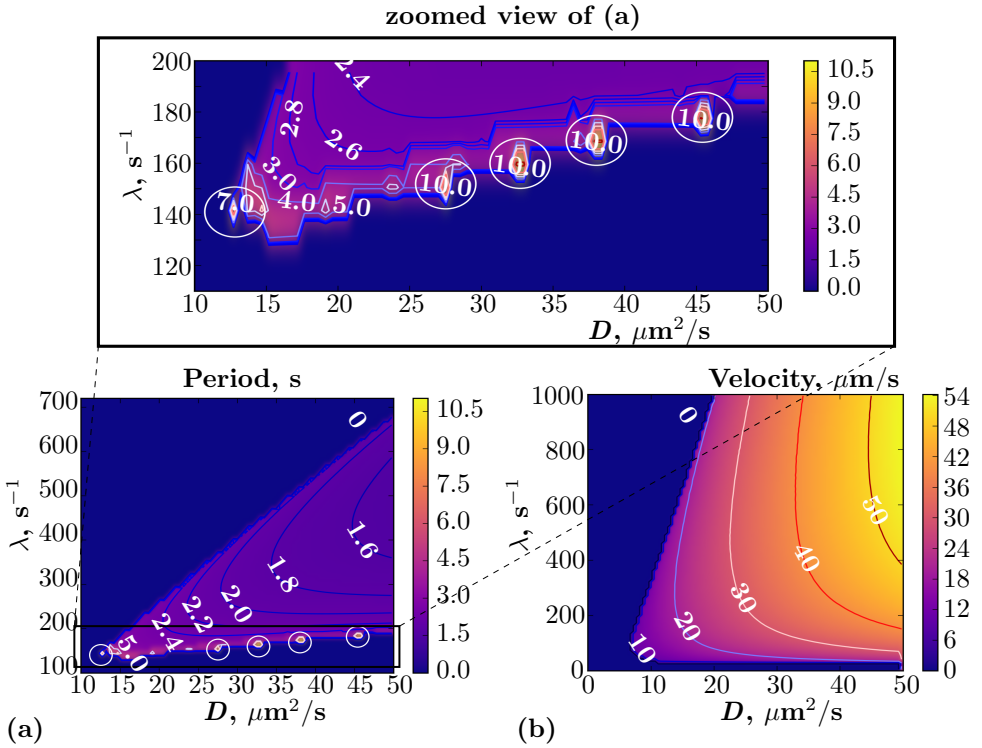


FIGURE 4.11: **(a)** The phase diagram which represents different kinds of $Ca^{2+}$ dynamics such as puffs, waves, and oscillations. The domain with zero periods [*dark-blue zone* in (a)] contains both puffs and waves in a co-existing manner. The *triangular light-blue domain* with non-zero periods contains oscillatory behaviour of the system. The *white circles* indicate the regions with $Ca^{2+}$ alternans (Figure 4.12). **(b)** The phase diagram representing two regimes of $Ca^{2+}$ dynamics such as puffs and waves in the case when all the clusters are excitable. Zero velocity domain in *dark-blue* corresponds to puffs and abortive waves, while the non-zero-velocity domain (shown in *blue* to *red* colours) represents waves.

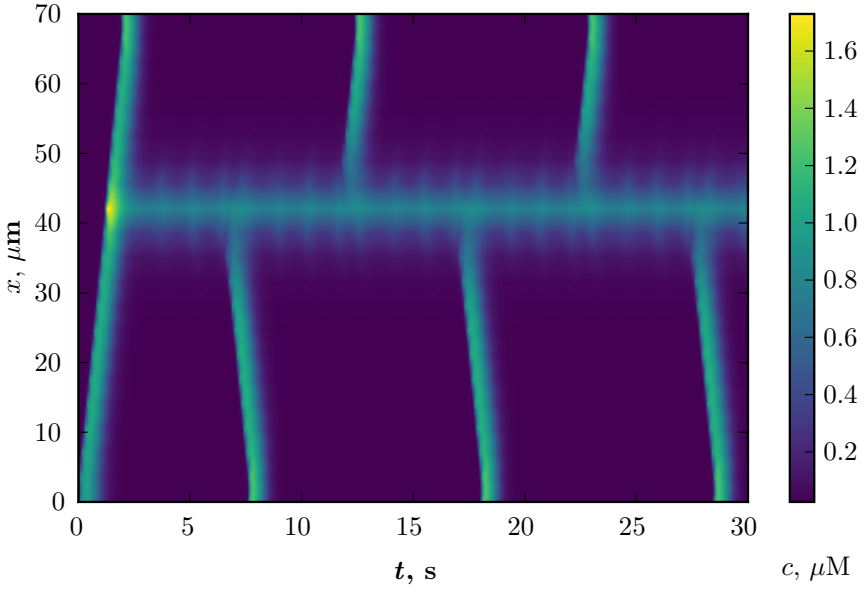


FIGURE 4.12: The alternate oscillations emerging from the bistable cluster at $D = 38.5\,\mu\text{m}^2/\text{s}$, $\lambda = 170\,\text{s}^{-1}$, $\ell = 3.5\,\mu\text{m}$.

triangular zone. A curious effect is observed at the lower edge of the triangle in the range $(100 \leq \lambda \leq 200)\,\mathrm{s}^{-1}$. The light spots within white circles correspond to oscillations with periods $\approx 10$ s and are characterised by $Ca^{2+}$ alternans – a type of travelling wave when a pulse travels alternately to the right, followed by another to the left and so on as depicted in Figure 4.12. This effect can be explained by the asymmetric initial conditions. Asymmetry is imposed because the wavefront is initiated at the left boundary and propagates to the right (Figure 4.10 (a)), while, at the same time, there is no pulse at the right boundary at $t = 0$. Therefore, the residual concentration diffusing from the bistable cluster after the initial front has passed is sufficient to excite a neighbouring cluster only from one side at a time. Thus, we observe oscillations occurring on alternate sides of the bistable cluster sequentially.

A similar phase diagram but for velocities of wave-fronts in $\lambda$-$D$ coordinates is depicted in Figure 4.11 (b). We calculate the velocities of $Ca^{2+}$ waves in the membrane containing only excitable clusters by studying the time required for a pulse to reach from a chosen cluster to the neighbouring one. The dark regions in the velocity map correspond to abortive waves or puffs while the light trapezium corresponds to propagating $Ca^{2+}$ waves.

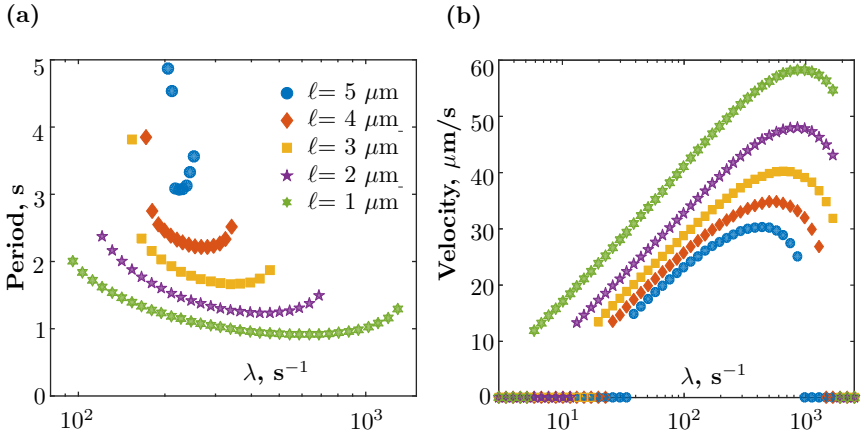


FIGURE 4.13: The dependence of velocity and period on the inter-cluster distances for fixed $D = 30\,\mu\mathrm{m}^2/\mathrm{s}$. (a) The dependence of period on $\lambda$ for different inter-cluster distances. (b) The dependence of velocity on $\lambda$, the distances, and the diffusion coefficient are the same as in (a).

The distance between clusters in the various cell types lies in the range $1 - 7\,\mu$m as reviewed by Rüdiger [2014b]. Figure 4.13 shows the dependence of the periods and the velocities on $\lambda$ for different values of the separation $\ell$ between the clusters. In both graphs, we consider the effective diffusion constant to be fixed at a typical value of $D = 30\,\mu\mathrm{m}^2/\mathrm{s}$. The period of the oscillations shown in Figure 4.13 (a) generally reaches larger values for larger separation between clusters. This can be explained by the fact that the front travels a longer distance in order to reach neighbouring clusters. Interestingly, the oscillatory behaviour exists for wider ranges of $\lambda$ for smaller distances between the clusters as shown in Figure 4.13 (a); oscillations are more robust to the equilibration process if the distances between clusters are smaller. The same processes define the velocities in Figure 4.13 (b); these are higher for shorter distances because a front reaches a neighbouring cluster faster and can trigger a response there. The data for comparatively large periods $\approx 4 - 5$ s for $\ell = 5\,\mu$m, $\ell = 4\,\mu$m and $\ell = 3\,\mu$m in Figure 4.13 (a) correspond the non-regular alternans emerging similarly as in Figure 4.11 (a).

Interestingly, the curves representing the period/velocity of travelling waves exhibit minima/maxima for some fixed values of $\lambda$. This means that a certain set of optimal parameters exists in the model leading to the smallest refractory period and fastest front velocity. Also, the shapes of the curves prompt scaling relations in the model. The analysis of these phenomena is a curious task, however, it lies out of the scope of our study and subject to future research.

## 4.4 Conclusions

The main contribution of the current study is the introduction of coupling between the $IP_3R$ clusters in the three-state-model. This helps us to study the oscillatory regime reported in Chapter 3 in the setting of a two-cluster system (one cluster in the regime corresponding to excitable behaviour and the other to the bistable one) for various coupling strengths between the clusters. Curiously, the limit cycle continuation diagram for a single cluster (Figure 3.6) with altering rest level of $Ca^{2+}$ is almost identical to the one for the excitable cluster in the two-cluster case (Figure 4.6) with varying coupling strength. In the two-cluster case, the bistable cluster is sustained at the high $[Ca^{2+}]$ level and serves as the source of $[Ca^{2+}]$ for the second one. The coupling strength regulates the level of the concentration brought from the bistable cluster to an excitable one. This level of concentration brought from the bistable cluster may effectively serve as the "external" $[Ca^{2+}]$ for the excitable cluster. This means that the mechanism of triggering the oscillations in both cases (single cluster and two coupled clusters) has the same nature. Also, this reasoning may serve as the explanation of the coupled nature of $[Ca^{2+}]$ oscillations at the $IP_3R$ clusters under sustained high levels of $IP_3$ concentration.

The reaction-diffusion model of the $IP_3R$ clusters in the one-dimensional ER was developed based on the insight from the interaction between two clusters. The proposed model results in the observation of $Ca^{2+}$ oscillations in the specific setup characterised by a chain of excitable clusters with a single bistable cluster positioned approximately in the middle. Such a model yields a reach and complex behaviour which we summarise using maps of the periods of oscillations and the velocities of the wave-fronts specified on the plane of two parameters – diffusion coefficient and equilibration rate. The dynamics of a chain of clusters presented within the maps are consistent with the experimental observations for high $[IP_3]$ by [Marchant et al., 1999] exhibiting velocities in range $10-50\,\mu m^2/s$. Due to the fixed high level of $[IP_3]$ assumed, our model exhibits periods of oscillations lower than the wide range found in typical experimental studies [Marchant and Parker, 2001]. Although the high $[IP_3]$ assumption narrows the range of periods observed, it helps us to study the main characteristics of waves and oscillations phenomenologically. The extended analysis with variable $[IP_3]$ and stochastic effects exhibiting a full range of durations is presented further in this thesis. We also observe a curious spatially alternating wave pattern in a regime of parameter space that is reminiscent of the occurrence of intracellular spatially organized $Ca^{2+}$ alternans.

# Chapter 5

# An $IP_3$-dependent Cluster-based Model in 2D-membranes

We extend a chain of coupled clusters to a two-dimensional case of ER membrane to study the spatial effects of $Ca^{2+}$ signalling. Unlike the previous chapter, here we account for effective $IP_3$ rebinding to $IP_3R$ channels. Section 5.1 contains a study of the decay of $Ca^{2+}$ oscillations for diffusing $[IP_3]$ after stimulus termination while Section 5.2 contain an extension of our model to the two-dimensional case where the spatio-temporal propagation is in a plane. We study the emergence of $Ca^{2+}$ fronts and oscillations under high $[IP_3]$ for randomly positioned $IP_3R$ clusters in the 2D ER membrane. A membrane is naturally a two-dimensional structure, which justifies the choice of the spatial modelling domain.

## 5.1 $IP_3$ dynamics leading to termination of $Ca^{2+}$ release

We have shown that the assumption of high levels of $IP_3$ results in the existence of a bistable state of a cluster of $IP_3R$ channels, leading to a sustained $Ca^{2+}$ release from the cluster. Here we aim to link the termination of this event with the change in the $[IP_3]$ levels which will be shown later on.

In Figure 5.1 we present a schematic diagram of an extension of the three-state model implemented by releasing the constraint on high $[IP_3]$ and introducing effective rates for the transitions between the upper and the lower planes in the DYK cube. The detailed derivation of the effective rates is given in Section 2.5. In the case of two coupled clusters the $IP_3$ dependent model (4.15)–(4.16) reads

$$\frac{\mathrm{d}a_i}{\mathrm{d}t} = k_a^+(c_i)c_i(1-a_i-h_i-y_i) - k_a^- a_i + k_1(c_i)h_i - k_i^+ c_s a_i, \tag{5.1}$$

$$\frac{\mathrm{d}h_i}{\mathrm{d}t} = k_i^+(c_i)c_i(1-a_i-h_i-y_i) - k_1(c_i)h_i - k_2(c_i)h_i + k_i^+ c_s a_i, \tag{5.2}$$

$$\frac{\mathrm{d}y_i}{\mathrm{d}t} = C^{\mathrm{down}}(c_i)(1-y_i) - C_{\mathrm{ch}}^{\mathrm{up}}(c_i,p)y_i, \tag{5.3}$$

where $C^{\mathrm{down}}$ and $C_{\mathrm{ch}}^{\mathrm{up}}$ are given in Equations (2.63) and (2.73), respectively and $i = 1, 2$ refers to the numbering of 2 clusters. $Ca^{2+}$ dynamics is governed by Equations (4.17) and (4.18).

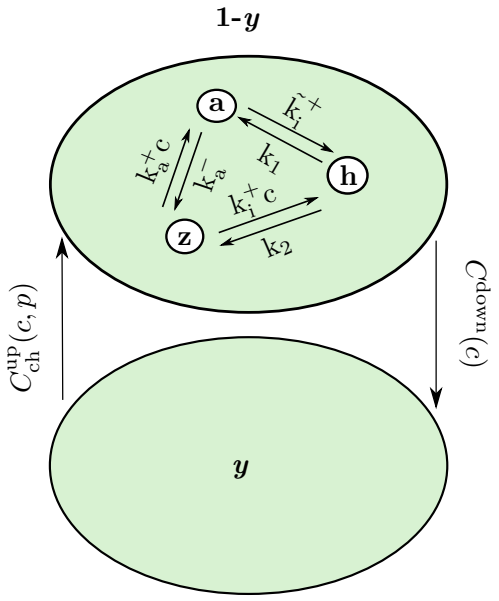


FIGURE 5.1: The scheme of an extension of the three-state model introduced in Figure 2.12 (d). The transitions between the upper and the lower plane of the DYK cube are governed by the steady-state rates $C^{\text{down}}$ and $C_{\text{ch}}^{\text{up}}$.

We estimate the timescale of the [IP$_3$] change by solving the diffusion equation in the infinite 2D domain, as shown in Figure 5.2. The initial shape of the IP$_3$ excitation (*blue line* in Figure 5.2) is assumed as Gaussian with axial symmetry

$$p(x,y,0) = p_a \, \mathrm{e}^{\frac{-x^2-y^2}{2\sigma_0^2}}, \tag{5.4}$$

where the amplitude is $p_a = 4.6\,\mu$M (the high concentrations of several $\mu$M are commonly used in wave experiments [Marchant et al., 1999]) and variance $\sigma_0^2 = 1\,\mu\text{m}^2$ is a measure of the spread of the initial shape.

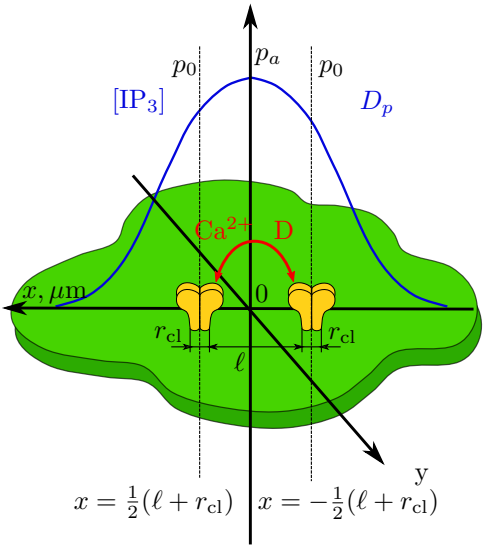


FIGURE 5.2: The schematic representation of the IP$_3$ diffusion in the infinite 2D domain containing two channels.

The solution of the diffusion equation in the infinite 2D domain is

$$p(x,y,t) = \int_{-\infty}^{+\infty}\int_{-\infty}^{+\infty} p(\xi,\zeta,0)G(x-\xi,y-\zeta,t)\,\mathrm{d}\xi\,\mathrm{d}\zeta, \tag{5.5}$$

where the Green's function is

$$G(x-\xi,y-\zeta,t) = \frac{1}{4\pi D_p t}\,\mathrm{e}^{-\frac{(x-\xi)^2+(y-\zeta)^2}{4D_p t}}, \tag{5.6}$$

where $\xi$ and $\zeta$ are dummy spatial variables. The integration of Equation (5.5) is carried out analytically leading to

$$p(x,y,t) = \frac{p_a\sigma_0^2}{\sigma_0^2+2D_p t}\,\mathrm{e}^{\frac{-x^2-y^2}{4D_p t+2\sigma_0^2}}, \tag{5.7}$$

where $D_p = 10\,\mu\mathrm{m}^2/\mathrm{s}$ [Dickinson et al., 2016]. Considering the clusters in Figure 5.2 to be located at $x = \pm\frac{1}{2}(\ell + r_{cl})$, $y = 0$, where the distance between clusters $\ell = 1.4\,\mu\mathrm{m}$ and cluster radius $r_{cl} = 0.1\,\mu\mathrm{m}$, the $[IP_3]$ trace for each cluster appears as indicated with *red dashed lines* in Figure 5.3 (c) and (d).

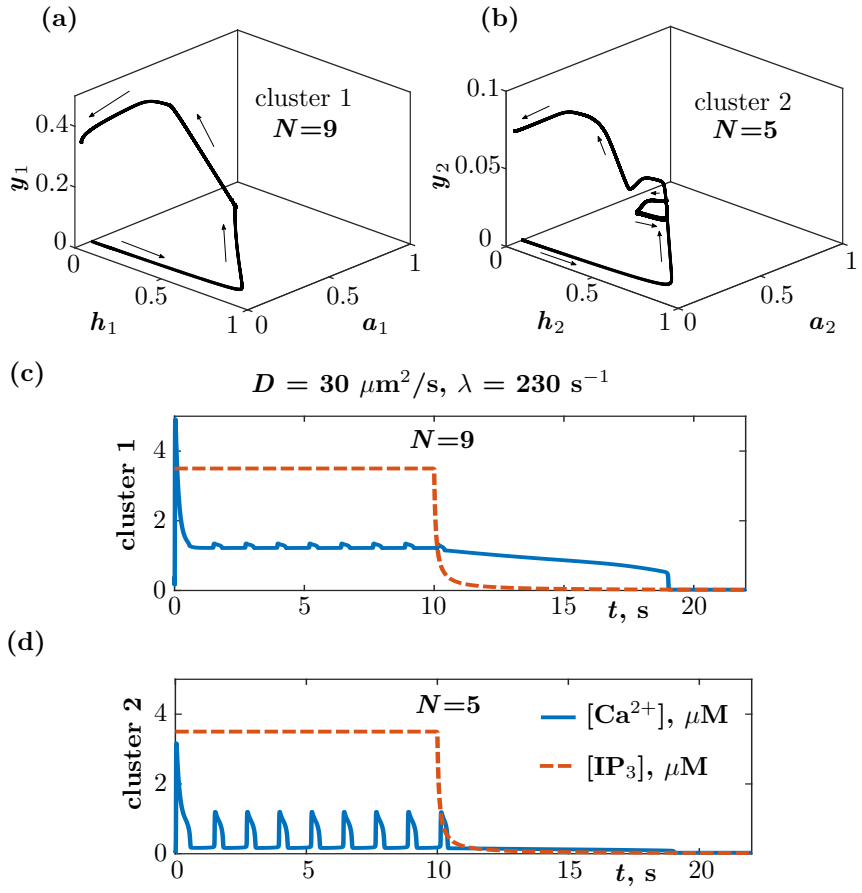


FIGURE 5.3: The $IP_3$ dependent model for two coupled clusters with variable $[IP_3]$. **(a)**, **(b)** The trajectories in the $(a,h,y)$ phase space, where $y$ corresponds to the fraction of the channels in a cluster occupying the lower plane of the DYK cube, $N$ is the number of activatable channels in a cluster. **(c)**, **(d)** The oscillatory regime corresponding to Figure 4.3 (*blue solid lines*) for high $[IP_3]$ is terminated due to the decrease in the $[IP_3]$ (*red dashed lines*).

We consider [IP$_3$] to be constant during the stimulus and then diffuse after the stimulus terminates with a rate characterised by the diffusion coefficient $D_p = 10\,\mu\text{m}^2/\text{s}$ according to Dickinson et al. [2016]. Therefore, we can write the spatial-temporal change in [IP$_3$] as

$$p(t) = \begin{cases} p_0, & \text{if } t \leq t_{\text{dur}}, \\ \frac{p_a \sigma_0^2}{\sigma_0^2 + 2D_p t}\, \mathrm{e}^{\frac{-x^2-y^2}{4D_p t + 2\sigma_0^2}}, & \text{otherwise}, \end{cases} \tag{5.8}$$

where the initial value of [IP$_3$] at a cluster $p_0 = 3.5\,\mu\text{M}$ may be calculated from the initial Gaussian with the amplitude $p_a = 4.6\,\mu\text{M}$, the duration of the IP$_3$ stimulus is $t_{\text{dur}} = 10\,\text{s}$.

TABLE 5.1: Parameters used in the two-clusters model dependent on IP$_3$ [Rückl and Rüdiger, 2016].

| Parameter | Value | Description |
|---|---|---|
| $a_1$ | $2\,(\mu\text{M} \times \text{s})^{-1}$ | IP$_3$ binding rate |
| $b_1$ | $2 \times 10^{-3}\,\text{s}^{-1}$ | IP$_3$ unbinding rate |
| $d_1$ | $10^{-3}\,\mu\text{M}$ | IP$_3$ activation dissociation constant |
| $(a_2, k_i^+)$ | $0.02\,(\mu\text{M} \times \text{s})^{-1}$ | $Ca^{2+}$ inhibition binding rate |
| $(b_2, k_i^-)$ | $1.56\,\text{s}^{-1}$ | $Ca^{2+}$ inhibition binding rate |
| $d_2$ | $78\ \mu\text{M}$ | $Ca^{2+}$ inhibition dissociation constant |
| $a_3$ | $4\,(\mu\text{M} \times \text{s})^{-1}$ | IP$_3$ binding rate |
| $b_3$ | $8\,\text{s}^{-1}$ | IP$_3$ unbinding rate |
| $d_3$ | $2\,\mu\text{M}$ | IP$_3$ inhibition dissociation constant |
| $a_4$ | $0.1\,(\mu\text{M} \times \text{s})^{-1}$ | $Ca^{2+}$ inhibition binding rate |
| $b_4$ | $3.9 \times 10^{-3}\,\text{s}^{-1}$ | $Ca^{2+}$ inhibition unbinding rate |
| $d_4$ | $3.9 \times 10^{-2}\,\mu\text{M}$ | $Ca^{2+}$ inhibition dissociation constant |
| $a_5$ | $100\,(\mu\text{M} \times \text{s})^{-1}$ | $Ca^{2+}$ activation binding rate |
| $(b_5, k_a^-)$ | $20\,\text{s}^{-1}$ | $Ca^{2+}$ activation unbinding rate |
| $d_5$ | $0.2\,\mu\text{M}$ | $Ca^{2+}$ activation dissociation constant |

The trajectories in $(a, h, y)$ phase space for the two clusters are exhibited in Figures 5.3 (a) and (b), respectively. The global oscillations occur in our model for the level of [IP$_3$]$\approx 3 - 4\,\mu\text{M}$, which is compatible with the levels considered by Marchant et al. [1999]. The termination of the oscillations (solid blue lines in Figures 5.3 (c) and (d)) at both clusters is caused by the decrease in [IP$_3$] under a level of several tens of nM, which is typically taken as the rest value of the [IP$_3$], as in [Rückl et al., 2015]. It might be useful to reconsider the influence of the calcium pumps in the termination process as we argued that their effects are subsumed in a linearised equilibration rate $\lambda$. We have checked that the effect of introducing an explicit pump term [De Young and Keizer, 1992] on the wave termination behaviour can be accommodated by adjusting $\lambda$. We incorporate these terms in 2D-membrane in the next section.

## 5.2 Two dimensional IP$_3$-dependent Model

In this section, we extend the results obtained in Section 4.3 to the case of two-dimensional ER membrane under fixed IP$_3$ load. To approach realistic $Ca^{2+}$ behaviour, we revisit several assumptions applied to the one-dimensional model. Here we consider the pump term as in Equation (4.3). The leak term estimated similarly to Rückl and Rüdiger [2016] as the base level of [$Ca^{2+}$] $c_0$ is brought to the cytosol by pumps $P_l = P_p \frac{c_0^2}{c_0^2 + K_d}$. Revising the system (4.19)–(4.22),

TABLE 5.2: Parameters used in the two-dimensional model dependent on $IP_3$.

| Parameter | Value | Description |
|---|---|---|
| $D$ | $30\,\mu m^2/\mathrm{s}$ | diffusion coefficient |
| $\lambda$ | $4000\,\mathrm{s}^{-1}$ | equilibration rate |
| $P_p$ | $0.9\,\mu\mathrm{M/s}$ | Pump strength |
| $K_p$ | $0.1\,\mu\mathrm{M}$ | Pump dissociation constant |
| $P_l$ | $5.6\times10^{-3}\,\mu\mathrm{M}/s$ | Leak term |

we have the following set of four coupled ODEs describing the dynamics

$$\frac{\partial a}{\partial t} = k_a^+ c(1-a-h-y) - k_a^- a + k_1 h - k_i^+ c_s a, \tag{5.9}$$

$$\frac{\partial h}{\partial t} = k_i^+ c(1-a-h-y) - k_1 h - k_2 h + k_i^+ c_s a, \tag{5.10}$$

$$\frac{\partial y}{\partial t} = C^{\mathrm{down}}(1-y) - C_{\mathrm{ch}}^{\mathrm{up}} y, \tag{5.11}$$

$$\frac{\partial c}{\partial t} = D\vec{\nabla}^2 c - \lambda \sum_i \sum_j H(r_{cl} - |\vec{r} - \vec{r}_{ij}|)\left(c - c_d(a_{ij})\right) - P_p \frac{c^2}{c^2 + K_p^2} + P_l, \tag{5.12}$$

$$c_d = c_0 + \frac{1}{2}\alpha N a \left\{1 + \tanh\left[\frac{Na-1}{\epsilon}\right]\right\}, \tag{5.13}$$

where $\vec{\nabla}^2 = \left(\frac{\partial^2}{\partial x_1^2}, \frac{\partial^2}{\partial x_2^2}\right)$ is a diffusion operator in Cartesian coordinates, $\vec{r} = (x_1, x_2)$ is a radius vector. Note, that unlike functions $a = a(\vec{r}, t)$, $h = h(\vec{r}, t)$, $y = y(\vec{r}, t)$ which are non-zero only at the clusters, $c = c(\vec{r}, t)$ may be non-zero at every point of space due to the diffusion term. A slightly different notation is used in Equation (5.12), where $a_{ij}$, $i = \overline{1,n}$, $j = \overline{1,n}$ denote fractions of active channels located at every cluster with coordinate $\vec{r}_{ij}$. All the DYK parameters are provided in Table 5.1, $C^{\mathrm{down}}$ and $C_{\mathrm{ch}}^{\mathrm{up}}$ are given in Equations (2.63) and (2.73). All the new parameters and those adapted from previous models are given in Table 5.2.

The formation of $Ca^{2+}$ patterns in living cells is strongly affected by the levels of $[IP_3]$ in the cytoplasm. Even though in order to enable $Ca^{2+}$ release, each channel must bind four $IP_3$ molecules [Alzayady et al., 2016], low enough $[IP_3]$ (around 10 nM) may open the channel. Normally, the intermediate levels of $[IP_3]$ $(10 - 100$ nM) considered in the case of $Ca^{2+}$ puff (or in some cases $Ca^{2+}$ spike) regime [Dickinson et al., 2016]. In the present chapter, we consider saturation levels of $[IP_3]$ to be $3.5\,\mu$M to ensure the established $Ca^{2+}$ wave regime, as shown in the experiment by Marchant et al. [1999].

In Figure 5.4, we present snapshots of the cytosolic $Ca^{2+}$ concentration under $p = 3.5\,\mu$M. The integration of coupled Equations (5.9)–(5.12) is performed using explicit Euler scheme similarly to Section 4.3. The only difference is in using 2D spatial grid for finite difference scheme in Equation (5.12). The placement of the clusters in the membrane is random (*orange and black dots*). Similarly to Section 4.3, we consider two types of clusters: bistable ($N = 25$) represented by two *black dots* and excitable ($N = 5$) shown as multiple *orange dots*. Note, that the results of the simulations are similar to those shown in Section 4.3 if we include two major differences in our assumptions. Firstly, in order to produce oscillations in two dimensions, the residual peak formed at the bistable cluster must be significantly higher. Thus, we simulate a much larger bistable cluster containing $N = 25$ channels. Secondly, here we consider much higher equilibration rate ($\lambda = 4 \times 10^3$ s$^{-1}$ in contrast with $\lambda = 230$ s$^{-1}$ in the 1D case) in order to

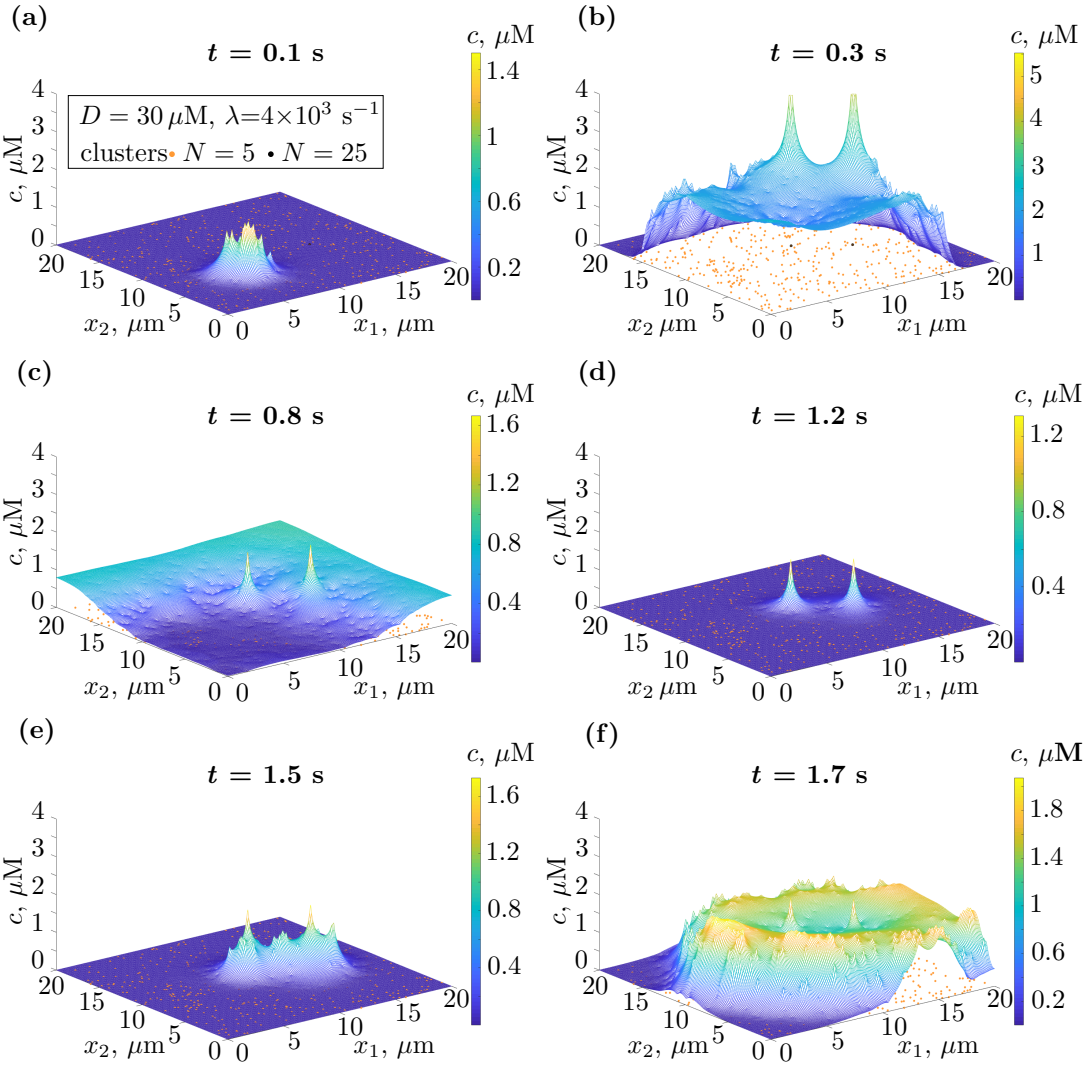


FIGURE 5.4: The IP$_3$ evolution in the two-dimensional ER membrane under $p = 3.5\,\mu$M, $D = 30\,\mu m/s$, $\lambda = 4 \times 10^3$ s$^{-1}$. (a) The evolution of the initial [Ca$^{2+}$] release evoked by the stimulus. (b) The initial Ca$^{2+}$ excitation propagates throughout the ER membrane. (c) After the initial Ca$^{2+}$ front passes, the bistable clusters ($N = 25$ *two black dots*) form two residual peaks.(d) The residual peaks stay elevated on the timescales driven by high IP$_3$ levels. (e) The secondary oscillatory waves occur from the residual peaks. The effect of the collision of secondary waves is observed. (f) The waves emerging from the residual peaks propagate in oscillatory manner.

account for the adjustment of the effective impact of the various phenomena (pumps, leak) in two-dimensional case. Here these adjustments are merely heuristic and based on the search for the values of $N$ at the bistable cluster and $\lambda$ for which the oscillations are observed. In the future, the nature of the parameter change and the occurrence of the behaviour should be studied as well as the behaviour in the three-dimensional case.

In contrast to the one-dimensional case, here we consider two bistable clusters in the membrane domain which form two residual peaks to observe the interaction between two waves generated in Figure 5.4 (e). Thus, we can observe the effect of wave collision found experimentally [Falcke, 2003b].

## 5.3 Conclusions

In the present chapter, we extend the cluster-based model from Chapter 4 to describe $Ca^{2+}$ signals in the realistic ER membrane. The changing levels of $[IP_3]$, leak and pump terms were incorporated as well. The termination of $Ca^{2+}$ oscillations was observed in the two-coupled-clusters case. The effect of colliding waves is present in the 2D-membrane.

In general, $Ca^{2+}$ evolution on the two-dimensional membrane with random cluster positioning and considering leak and pump terms reproduces the effect given by the simpler model in one dimension described in Section 4.3. Thus, we may conclude that the mechanism of initiation of $Ca^{2+}$ oscillations proposed in the current study is robust even for more complex deterministic approaches. Further, we propose the stochastic model based on our approach to study the properties of stochastic $Ca^{2+}$ signals.

# Chapter 6

# Spatio-temporal Stochastic Dynamics in ER Membrane

Conformational states of receptor profiles are subject to fluctuations in the thermal environment of the cell. State transition, such as those described in the DYK model, are probabilistic in nature. The ODE models we have employed previously, are descriptions of the deterministic evolution of the averaged state variables. When describing transients of the dynamical evolution of the system away from and subsequent return to a steady state, appropriate initial conditions were chosen away from the fixed point. In a stochastic description, random fluctuations of protein conformations generate deviations from the steady state for the dynamic evolution to generate the excitable trajectories. Here we implement previously discussed three-state-model to calculate the deterministic trajectories and complement it with a stochastic term to comprise the Langevin model.

There is an ongoing argument about the applicability of Langevin dynamics in the systems containing few components. The obvious benefit of this method is computational efficiency since unlike Gillespie simulations [Gillespie, 2007], for example, it allows obtaining fairly accurate $Ca^{2+}$ dynamics without accounting for each subunit state separately. The Langevin approach is proven to be beneficial for modelling ER membranes containing a few tens of channels [Rüdiger, 2014b]. Furthermore, there also are various modifications of the method focused on improved accuracy [Shuai and Jung, 2003a]. Nevertheless, the accuracy of this approach in case of clusters having under 10 channels may be reduced [Shuai and Jung, 2003a]. We employ the Langevin dynamics for clusters with few channels considering its possible limitations. To ensure the accuracy of the computations, we further validate the approach against a detailed DYK model-based stochastic simulations of a single cluster [Rückl et al., 2015]. The proposed phenomenological model is defined in terms of mean properties of channels, such as averaged transition rates and fractions of channels in open or closed states. This assumption presents a coarse-grain view of the behaviour of multiple clusters alleviating the need for explicit modelling of their structure. As a result, we calculate inter-puff intervals (IPI) for a single cluster and correlations between $Ca^{2+}$ release events in multiple clusters on a membrane that we hypothesise to facilitate large-scale spatial events such as waves.

The proposed Langevin model shows a significant boost in computational efficiency compared to more complex procedures such as the one by Rückl et al. [2015]. Yet, our model does not

compromise on the complexity of behaviour as we effectively account for a vast spatial hierarchy from the level of a single subunit to the level of a cluster. The simplification is made in the dynamics of the channel but keeping the actual distributions of numbers of channels in clusters [Rückl et al., 2015, Taufiq-Ur-Rahman et al., 2009], linear relationship between $[Ca^{2+}]$ and the probability of puffs [Dickinson et al., 2012], etc.

A boost in computational efficiency even at a cost of a compromise in complexity allowed us to compute the single cluster statistics using just an ordinary PC. Furthermore, we were able to study the stochastic dynamics of the large-scale $Ca^{2+}$ release events at a level of the membrane with hundreds of channels within a temporal frame of dozens of seconds. The latter study was performed on IRIDIS – a high-performance computing facility at the University of Southampton. This study provides with a crucial insight into the main membrane characteristics, such as the threshold value of $IP_3$ triggering global calcium release ($Ca^{2+}$ spikes or $Ca^{2+}$ waves) and the characteristics of wave propagation. These characteristics are occasionally addressed in the literature [Calabrese et al., 2010, Coombes and Timofeeva, 2003].

## 6.1 Langevin model of a single cluster of $IP_3R$ channels under fixed $[IP_3]$

We propose a stochastic cluster-based approach by introducing the Langevin model of $Ca^{2+}$ release at a single cluster level. We start by introducing a noise term into the model (2.84), (2.85) for the simplest case of saturating $IP_3$ to account for the stochastic nature of channel behaviour. This results in the following set of Stochastic Differential Equations (SDEs)

$$\mathrm{d}a = f(a,h,c)\,\mathrm{d}t + As_a\,\mathrm{d}W, \tag{6.1}$$

$$\mathrm{d}h = g(a,h,c)\,\mathrm{d}t + As_h\,\mathrm{d}W, \tag{6.2}$$

where $\mathrm{d}W$ is a Wiener increment distributed as a normal Gaussian with mean 0 and variance 1 [Øksendal, 2003], $s_a$ and $s_h$ are functions of the states of a cluster in the general case of multiplicative noise with amplitude $A$.

We carry out Ito integration [Øksendal, 2003] with the Euler-Maruyama method using the custom-built MATLAB toolbox [Horchler, 2013] to obtain the solution of the system (6.1), (6.2) under the assumption of the fast equilibration of $[Ca^{2+}]$ to the steady-state level $c = c_d$ (Equation (2.87)). Performing the computations, we observed that the standard Euler-Murayama method often returns negative values of $a$ and $h$ which are non-physical. To overcome this issue, the method is often modified [Rüdiger, 2014b] by discarding the values of $\mathrm{d}W$ generated by the Monte-Carlo algorithm leading to the negative $a$ and, as a result, negative $Ca^{2+}$ concentrations.

Here, we initialise the model (6.1), (6.2) with the set of parameters presented in the last column of Table 2.3 but replacing the number of activatable channels with $N = 7$. We consider $s_a = s_h = 1$ which corresponds to the case of additive noise. The specified amplitude $A = 0.37$ is selected to be large enough to overcome the threshold of excitability of the cluster. We will discuss this important requirement further down in this section bringing in the rationale from the theory of dynamical systems.

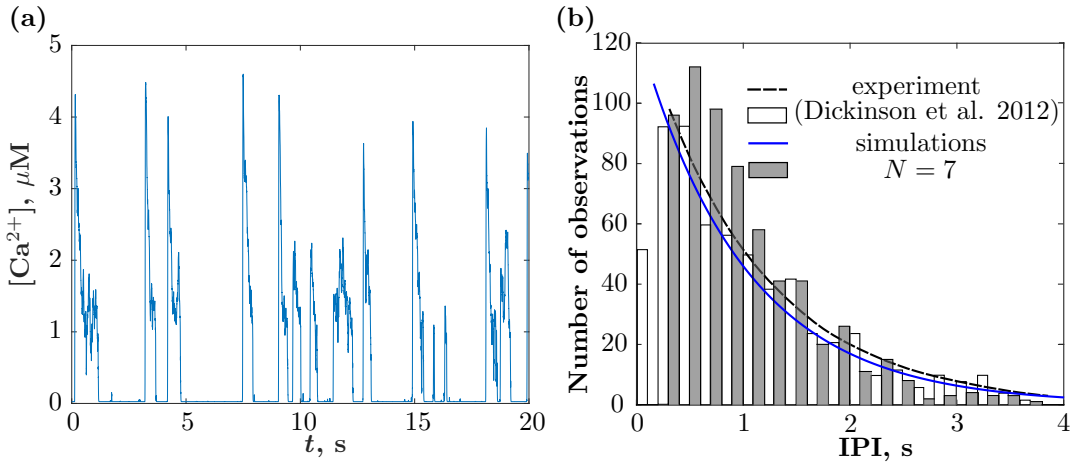


FIGURE 6.1: (a) [$Ca^{2+}$] traces in the stochastic single-cluster model (6.1), (6.2), (2.86) containing $N = 7$ channels with additive Wiener noise. (b) Inter-puff intervals calculated from the statistical series of the traces similar to (a). *Grey bars* are fitted with the *blue solid* curve and represent the distribution of IPIs obtained from the modelling of 622 puffs. *White bars* with *black dashed* fit are reproduced from the experiments reported in Dickinson et al. [2012].

Consider the short time frame (20 s) of changes in [$Ca^{2+}$] levels at a single cluster shown in Figure 6.1 (a) computed using the Langevin model. We use a longer stochastic single-cluster traces ($\sim 10^3$ s containing 622 puffs) returned by our simulations to compute the statistics of IPIs which is presented in Figure 6.1 (b) by a histogram with grey bars fitted with an exponential distribution – solid blue curve. We use the exponential fit which is a particular case of the Poisson distribution because of the independence between puffs. The simulation results are seen to agree with the experimental measurements of IPIs presented as a histogram with white bars fitted by a dashed black line in Figure 6.1 (b).

As puffs are short-term high rises in [$Ca^{2+}$] followed by small fluctuations near the rest level concentration, the IPIs are easily calculated as distances along the time axis between the end of the current puff and the beginning of the next one (see Figure 6.1 (a)). The rest level fluctuations do not surpass 0.1 $\mu$M. Therefore we assume the higher [$Ca^{2+}$] values to correspond to a puff and associate the lower [$Ca^{2+}$] values with the cluster being at rest.

Now we seek to understand how the dynamics of a single cluster depends on IP$_3$. To better anticipate and explain the results of stochastic simulations with Langevin model that are carried out further in this chapter, we study the same problem applying the deterministic model described by Equations (5.1)–(5.3).

Consider the phase portraits of a single cluster dynamics derived from the deterministic model for a case of no [IP$_3$] (Figure 6.2 (a)), small [IP$_3$] (Figure 6.2 (b)), moderate [IP$_3$] (Figure 6.2 (c)) and saturating [IP$_3$] (Figure 6.2 (d)). The phase portraits are defined here in three variables ($a$, $h$, $y$) in contrast to Chapter 3 defined in ($a$, $h$) phase space. The variable $y$ stands for the fraction of channels within a cluster that occupy the lower plane of the DYK cube (Figure 2.5). The velocity vector-fields are superposed on each phase portrait – the length of the arrows is proportional to the magnitude of the time derivative vector, whereas the direction denotes their inclination. The velocity vector field characterises the direction and the velocity of the system's evolution. It is apparent from Figure 6.2 that velocity vector fields are mostly similar for all

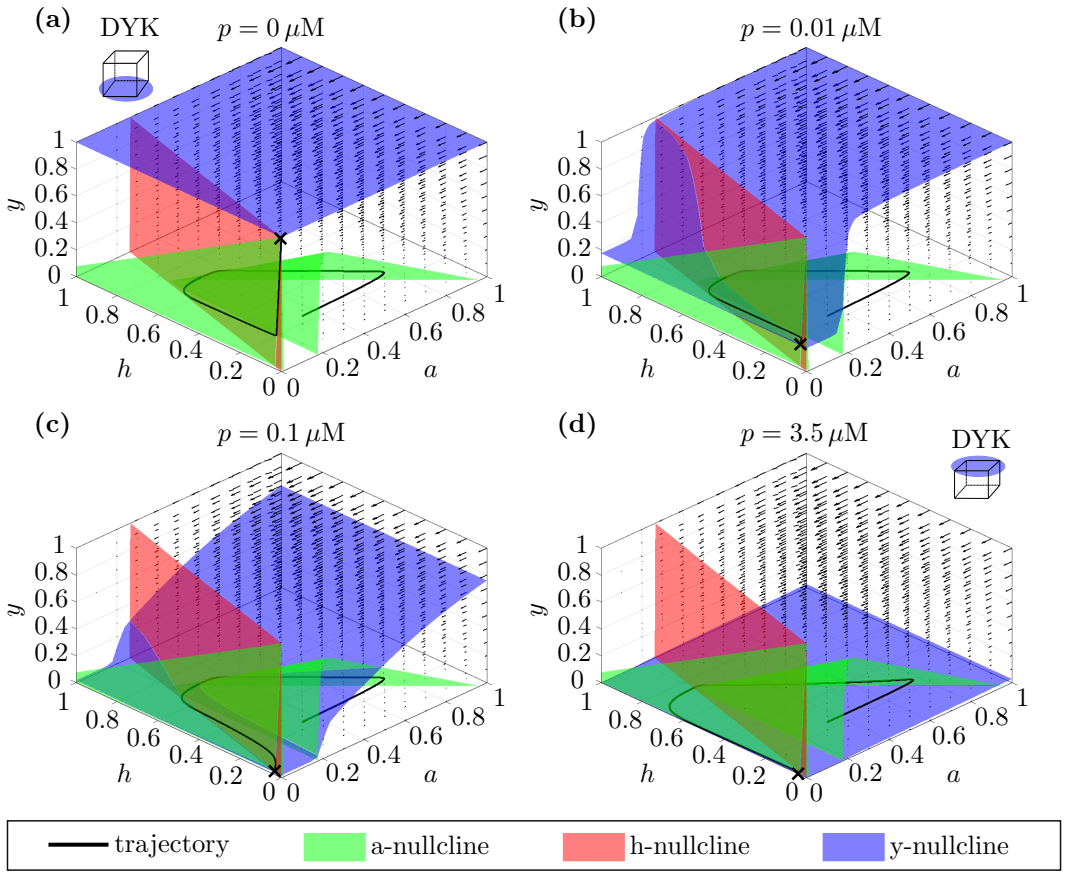


FIGURE 6.2: The $(a, h, y)$ phase space containing typical trajectories (*black lines*), nullclines (*green plane* – $a$-nullcline, *red plane* – $h$-nullcline and *blue plane* – $y$-nullcline,) and velocity fields (marked by tiny *black arrows* which are proportional to the magnitude of the time derivative vector at each point of $(a, h, y)$ space). The trajectories start at $(0.2, 0.1, 0.2)$ and finish at the fixed points with low $a$ and $h$ components, the $y$ components of these fixed points depend on $IP_3$ concentration $p$. Where (a) $p = 0\,\mu$M , (b) $p = 0.01\,\mu$M, (c) $p = 0.1\,\mu$M and saturating (d) $p = 3.5\,\mu$M.

values of $[IP_3]$. When a system appears at any state within $(a, h, y)$ phase space, it is being driven unidirectionally towards $a = 0$. The strength of the drive depends on how closely a given state is to the one given by $a = 1$ and $y = 1$, for which the drive is the strongest. Thus, we conclude that the system leaves states of high $a$ much faster than states of high $y$ or $h$.

The cluster dynamics in the two limiting cases of no $[IP_3]$ ($p = 0\,\mu$M) and saturating $[IP_3]$ ($p = 3.5\,\mu$M) are presented in Figure 6.2 (a) and Figure 6.2 (d). In the case of $p = 0\,\mu$M, the *blue nullcline* at $y = 1$ in Figure 6.2 (a) corresponds to the states of the channels in the cluster that occupy the lower plane of the DYK cube (Figure 2.5). The intersection of nullclines $a$, $h$ and $y$ gives a fixed point at $a = 0$, $h = 0$ and $y = 1$. It is apparent from the system's trajectory that in the case of absent $[IP_3]$ ($p = 0\,\mu$M), the cluster is in low-firing mode meaning that the excitable trajectory is not realisable unless we start from the point with $y < 0.5$. In contrast, the case of saturating $[IP_3]$ ($p = 3.5\,\mu$M) is characterised by all the channels occupying the upper DYK plane (all subunits has $IP_3$ bound) as reflected by the $y$-nullcline. The fixed point, in this case, is at $a = 0$, $h = 0$ and $y = 0$ which corresponds to the high-firing mode. Notice that the alternating position of the fixed point between each of the four cases is affected by the shape and position of $y$-nullcline.

In the intermediate cases in Figure 6.2 (b) and (c), the shape of the $y$-nullcline is defined by the interplay between $d_1$, $d_2$ and $d_3$ (given in Table 5.1). The $y$ coordinate of the fixed point is the fraction of the channels occupying lower DYK plane. The low values of the $y$ at $p \geq 0.01\,\mu$M indicate that the channel is at high-firing mode even if [IP$_3$] is very low. The $y$ component of the fixed point decreases further with an increase in [IP$_3$] load making excitations in the cluster even more favourable.

Let us proceed to the derivation of Chemical Langevin Equation (CLE) for an IP$_3$R cluster. The stochastic vector $\mathbf{X}(t) = \mathbf{x} = \big[a(t), h(t), y(t)\big]$ defines the state of the system at time $t$. $M$ is the number of the types of reactions $R_j$, where $j = \overline{1, M}$. These reactions may occur in the system according to the transitions between the different states in the reduced three-state model as shown in Figure 5.1 meaning un/binding of IP$_3$ or $Ca^{2+}$ molecules to the subunits, where $M$ represents the number of arrows (transitions or reactions) pointing towards or from each vertex (state of a channel). The number of the reactions $R_j$ occurring in the system in some time interval $[t, t+\tau)$, where $\tau > 0$ is a random variable $K_j(\mathbf{x}, \tau)$. Each of those reactions will increase the numbers of channels in corresponding states by $\nu_{ji}$, thus the state of the system is changed according to

$$X_i(t+\tau) = X_i(t) + \sum_{j=1}^{M} K_j(\mathbf{x}, \tau)\nu_{ji}, \tag{6.3}$$

where $i = \overline{1, 3}$ denoting each component of the vector $\mathbf{X}(t)$ corresponding to $a(t)$, $h(t)$ or $y(t)$.

In the classic literature on the stochastic simulations, the reaction rates are often called propensities of the reactions and denoted as $\mathfrak{a}_j(\mathbf{x})$, where $j = \overline{1, M}$. Gillespie [2000] defines $\mathfrak{a}_j(\mathbf{x})\,\mathrm{d}t$ as the probability that $R_j$ reaction occurs in a small volume in infinitesimal time interval $[t, t+\mathrm{d}t)$.

Generally, the random increment $K_j(\mathbf{x}, \tau)$ in Equation (6.3) is difficult to compute without any assumptions. The first feasible assumption is in imposing $\tau$ to be small enough that the propensities of the reactions do not change. Gillespie [2000] acknowledges that this condition is always satisfied if all reactant molecule populations are sufficiently larger than 1. This assumption leads to the independence between the reactions, thus, Equation (6.3) transforms to

$$X_i(t+\tau) = X_i(t) + \sum_{j=1}^{M} \mathcal{P}_j(\mathfrak{a}_j(\mathbf{x}), \tau)\nu_{ji}, \tag{6.4}$$

where $\mathcal{P}_j(\mathfrak{a}_j(\mathbf{x}), \tau)$ is a Poisson random variable.

The second assumption is that $\tau$ is large enough for the expected number of occurrences of each reaction $R_j$ in $[t, t+\tau)$ to be much larger than 1, i. e.

$$\langle \mathcal{P}_j(\mathfrak{a}_j(\mathbf{x}), \tau) \rangle = \mathfrak{a}_j(\mathbf{x})\tau \gg 1, \forall j \in [1, M]. \tag{6.5}$$

As shown by Gillespie [2000], under condition (6.5) the Poisson random variable $\mathcal{P}_j(\mathfrak{a}_j(\mathbf{x}), \tau)$ may be approximated by a normal random variable $\mathcal{N}_j(\mathfrak{a}_j(\mathbf{x})\tau, \mathfrak{a}_j(\mathbf{x})\tau)$. According to linear combination theorem

$$\mathcal{N}(m,\sigma^2) = m + \sigma\mathcal{N}(0,1) \tag{6.6}$$

where the normal Gaussian $\mathcal{N}(m,\sigma^2)$ is presented trough mean $m$, variance $\sigma^2$ and a normal zero-mean Gaussian $\mathcal{N}(0,1)$.

Taking into account all previous assumptions Equation (6.4) becomes

$$X_i(t+\tau) = X_i(t) + \sum_{j=1}^{M} \mathfrak{a}_j(\mathbf{x})\tau\nu_{ji} + \sum_{j=1}^{M} [\mathfrak{a}_j(\mathbf{x})\tau]^{\frac{1}{2}}\nu_{ji}\mathcal{N}_j(0,1), \tag{6.7}$$

where the second sum corresponds to the deterministic component same as in the rate equations representing the averaged behaviour, while the stochastic part is introduced in the third sum which includes scalers of a standard deviation and a normal random variable $\mathcal{N}_j(0,1)$, $j = \overline{1,M}$. All normal random variables at different $j$ are independent for all species because of the initial assumption of the independence between the reactions.

Taking into account all the assumptions, the resulting CLE for $IP_3R$ clusters may be derived from the Equation (6.7) leading to the following set of equations:

$$\begin{aligned}
\frac{\mathrm{d}a}{\mathrm{d}t} &= f(a,h,c) + A\Big(\sqrt{k_a^+(c)c(1-a-h-y)} + \sqrt{k_a^- a} + \sqrt{k_1(c)h} \\
&+ \sqrt{k_i^+ ca}\Big)\,\mathrm{d}W, \qquad (6.8)\\
\frac{\mathrm{d}h}{\mathrm{d}t} &= g(a,h,c) + A\Big(\sqrt{k_i^+(c)c(1-a-h-y)} + \sqrt{k_1(c)h} + \sqrt{k_2(c)h} \\
&+ \sqrt{k_i^+ ca}\Big)\,\mathrm{d}W, \qquad (6.9)\\
\frac{\mathrm{d}y}{\mathrm{d}t} &= C^{\mathrm{down}}(c)(1-y) - C_{\mathrm{ch}}^{\mathrm{up}}(c,p)y + A\Big(\sqrt{C^{\mathrm{down}}(c)(1-y)} \\
&+ \sqrt{C_{\mathrm{ch}}^{\mathrm{up}}(c,p)y}\Big)\,\mathrm{d}W, \qquad (6.10)
\end{aligned}$$

where $f = k_a^+(c)c(1-a-h-y) + k_a^- a + k_1(c)h + k_i^+ ca$ and $g = k_i^+(c)c(1-a-h-y) + k_1(c)h + k_2(c)h + k_i^+ ca$ are the same as in (2.84) and (2.85). The parameters $(k_i^+, k_a^-)$ are given in Table 5.1; $k_a^+$, $k_1$, $k_2$, $C^{\mathrm{down}}(c)$ and $C_{\mathrm{ch}}^{\mathrm{up}}(c,p)$ are given by (2.72), (2.82), (2.83), (2.63) and (2.73), respectively. We define $[Ca^{2+}]$ as $c = c_d = c_0 + 0.5\alpha Na\{1+\tanh[(Na-1)/\epsilon]\}$ with $N = 7$ channels. $\mathrm{d}W$ is a Wiener noise with the amplitude $A = \frac{0.27}{\sqrt{N}}$.

To explain the scaling factor $\sqrt{N}$ in the noise amplitude $A$, let a fraction of activatable channels as a deterministic variable $\bar{a} = \bar{n}_a/N$, where $\bar{n}_a$ is a deterministic count of the number of active channels and $N$ is the total number of channels. If $n_a$ is a Poisson variable with mean $\bar{n}_a$, $\bar{a} = \bar{n}_a/N$; $a$ as stochastic variable is

$$a \sim \bar{a} \pm \sigma_a = \frac{\bar{n}_a}{N} \pm \frac{\sqrt{\bar{n}_a}}{N} = \frac{\bar{n}_a}{N} \pm \frac{1}{\sqrt{N}}\sqrt{\frac{\bar{n}_a}{N}} = \bar{a} \pm \frac{1}{\sqrt{N}}\sqrt{\bar{a}}, \tag{6.11}$$

taking into account the fact that for Poisson random variable $\sigma_a = \sqrt{\bar{n}_a}$. A similar approach is also applicable to the stochastic variables $h$ and $y$ leading to the same noise amplitude $A$ in all the equations in the model (6.8) – (6.10).

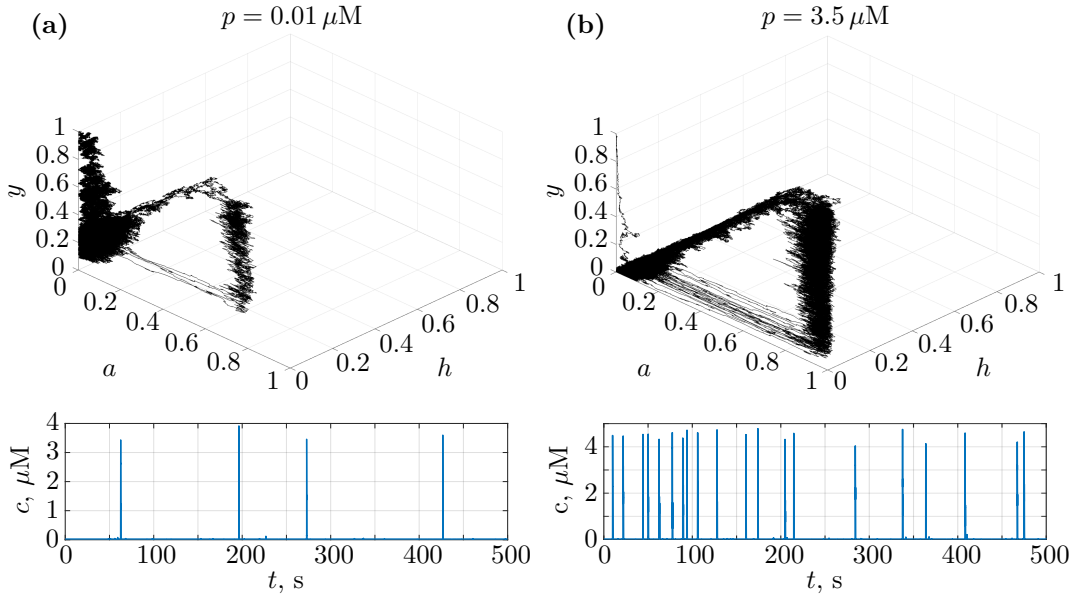


FIGURE 6.3: Stochastic trajectories in the $(a, h, y)$ phase plane (starting at $(0, 0, 1)$) in the *top* and $[Ca^{2+}]$ traces in a cluster containing $N = 7$ IP$_3$R channels in the *bottom* under (a) [IP$_3$] $= 0.01\,\mu$M and (b) [IP$_3$] $= 3.5\,\mu$M.

In Figure 6.3, we show the stochastic trajectories in the ($a$, $h$, $y$) phase plane (Figure 6.3 *top*) and corresponding $[Ca^{2+}]$ traces (Figure 6.3 *bottom*) obtained from Equations (6.8)–(6.10) under $p = 0.01\,\mu$M (Figure 6.3 (a)) and $p = 3.5\,\mu$M (Figure 6.3 (b)). The stochastic trajectories start at $(0, 0, 1)$, recalling Figure 6.2 (b) and (d), we can see that the significant parts of the trajectories are concentrated around the fixed points excluding individual firing events. These events manifest in excitable trajectories (Figure 6.3 (top)) and correspond to $Ca^{2+}$ puffs (Figure 6.3 (bottom)) which are possible when the amplitude of noise is sufficient to cross the excitability threshold (between fixed point (0, 0, $y_{\text{st}}$) and the unstable middle branch of the green $a$-nullcline in Figure 6.2). Thus, the choice of the amplitude $A$ is linked to the size of the excitable threshold in the deterministic case. Comparing the two cases in Figure 6.3 (a) under [IP$_3$] $= 0.01\,\mu$M and in Figure 6.3 (b) under [IP$_3$] $= 3.5\,\mu$M, we observe much fewer crossings for lower $p$. This leads to a decrease in IPIs for stochastic simulations with an increase in [IP$_3$] discovered theoretically and experimentally [Rückl et al., 2015]. Following the position of the $y$-nullcline (the *blue plane* in Figure 6.2), in the higher [IP$_3$] case, the trajectory is restricted to the $y = 0$ plane (all channels are IP$_3$ bound) which leads to much higher firing rate and thus shorter IPIs. In contrast, under low [IP$_3$] loads, $y$ serves as an additional degree of freedom. Thus, the trajectory in Figure 6.3 (a) features multiple 'walks' towards $y = 1$ where none of the channels has IP$_3$ bound to them and the firing regime is possible only for low values of $y$ where the majority of channels are IP$_3$ bound.

Even though the multiplicative noise is believed to possess more accurate behaviour of the system, the stochastic trajectories in the additive (only Wiener increments considered) and multiplicative (the Wiener increments are scaled by the system state) represent the similar statistics at high [IP$_3$].

We simulate puffs from a single cluster within a time frame of 1000 s. Some simulations were performed varying the number of activatable channels and [IP$_3$] levels in a cluster. Selected regions (500 s) of two complete traces of $[Ca^{2+}]$ are depicted under the respective trajectories

in Figure 6.3 (a) and (b). We compute IPIs from each trace using a previously discussed approach which results in a statistics of the magnitudes of IPIs for each trace characterised by the mean value (mean IPI) and the standard deviation. The mean IPI is calculated as

$$\mathrm{IPI} = \frac{1}{n}\sum_{i=1}^{n}\mathrm{IPI}_i, \tag{6.12}$$

where $n$ is a number of puffs within a single modelling trace, $\mathrm{IPI}_i$ is an interval between $i^{\mathrm{th}}$ and $(i+1)^{\mathrm{th}}$ puff. The standard deviation of IPI is defined as

$$\mathrm{SD} = \sqrt{\frac{1}{n-1}\sum_{i=1}^{n}|\mathrm{IPI}-\mathrm{IPI}_i|^2}. \tag{6.13}$$

Therefore, each trace is effectively described by two numbers – mean IPI and its standard deviation, and we now show that they play a key role in characterising the behaviour of a cluster.

The detailed dependence of average IPI on $p$ in a single cluster is shown in Figure 6.4 (a). The trends of IPIs as a function of $p$ for various numbers of activatable channels are indicated with the markers of respective colour and shape. We observe that IPI moderately reduces with $[IP_3]$. Similar behaviour is reported by Rückl et al. [2015] and is also reproduced by us as shown with (*blue open circles* in Figure 6.4 (a)) in addition to our results. Good qualitative agreement between our approach and modelling by Rückl et al. [2015] in similar trends of the curves is apparent from the figure.

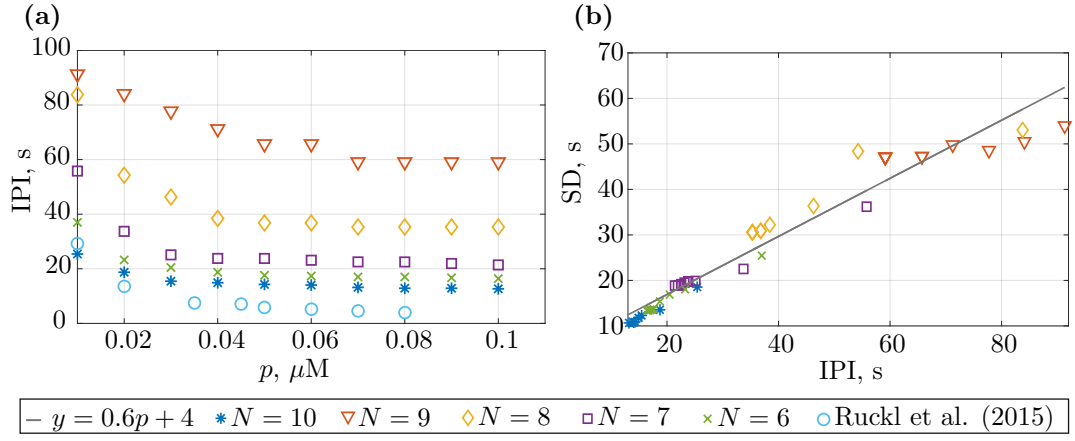


FIGURE 6.4: (a) The dependence of IPIs on $[IP_3]$ in clusters containing $6-10$ $IP_3R$ channels comparing to simulations by Rückl et al. [2015] (*blue open circles*). (b) The linear dependence of IPIs on the standard deviation of $Ca^{2+}$ puffs.

Figure 6.4 (b) contains scatter plots of the values of the standard deviation of IPIs versus the mean values of IPIs. Same as before, the markers of the same shape and colour correspond to the same number of activatable channels, while the spread in the values with the same markers is due to $[IP_3]$ effect. It is apparent from the figure that all the computed dots fall into the same line $y = 0.6p + 4$, which is the line of best-fit to the standard deviation data. In general, this simplified model is able to qualitatively reproduce the results of the detailed single-cluster model proposed by [Rückl et al., 2015] featuring the linear dependence of IPIs on the standard

deviation of the $Ca^{2+}$ signals which is robust against microscopic characteristics of clusters such as numbers of channels or $[IP_3]$ loads.

The recent findings by Thurley et al. [2014] suggest that the $Ca^{2+}$ release events taking place at the highest hierarchical level – spikes – are essential for the transmission of information within the cell in a way that the cell is able to encode information via inter-spike intervals (ISIs). The authors reported a linear dependence between the standard deviation of ISIs and the average ISIs similarly to Cao et al. [2017], Thurley et al. [2011, 2014]. The properties of IPIs, studied by us here, are tightly connected to the distributions of inter-spike intervals (ISIs) in cells [Thurley and Falcke, 2011]. Curiously, the trend of the standard deviation of IPIs versus average IPIs appears to be linear as well. It may be that puffs and spikes are somehow encoded similarly, but we reserve this question for the future study. Instead, we further study the $Ca^{2+}$ waves by extending our reasoning to the membrane level, incorporating hundreds of clusters and building a Langevin framework for spatial $Ca^{2+}$ signalling.

## 6.2 Membrane level simulations

In the previous chapters, we carried out deterministic modelling of the $Ca^{2+}$ wave propagation and extended it to the 2D-membrane case, with random positioning of clusters. However, the question of the realistic distribution of the numbers of channels in the clusters has not been clearly addressed in this study so far. [Rückl et al., 2015, Taufiq-Ur-Rahman et al., 2009] suggest the distribution of the number of channels in clusters to be Poissonian. This implies an independence in the number of channels forming distinct clusters. In Figure 6.5 we use coloured histograms for multiple $[IP_3]$ loads to reproduce the results of detailed simulations reported by Rückl et al. [2015]. These distributions are obtained from a single cluster containing 16 $IP_3R$ channels, each of them modelled by a collection of DYK cubes (Figure 2.5). The histograms in Figure 6.5 are obtained from calculating the numbers of activatable channels at the beginning of each release event. It means that the authors calculate the numbers of channels out of 16 which have at least 3 subunits to occupy the upper plane of the DYK cube. Also in Figure 6.5, we present our fitting of the data using Poisson distributions. The visual appearance of the fit is consistent, especially for the highest values of $[IP_3]$ (Figure 6.5 (b) and (c)). Note, that we recreate the data for the fitting by generating a synthetic data which leads to the same histograms as in Rückl et al. [2015]. This may be the reason for the large deviation of the distribution fit from the actual histogram for small $IP_3R$ in Figure 6.5. This observation also agrees with the experimental findings by Taufiq-Ur-Rahman et al. [2009]. The use of the pre-defined Poissonian distributions of numbers of activatable channels in clusters leads to a significant simplification of the analysis without compromising on accuracy.

Langevin Equations (6.8)–(6.10) in combination with the deterministic reaction-diffusion Equation (5.12) leads us to a hybrid approach to the modelling of $Ca^{2+}$ signals. Figure 6.6 shows snapshots of $Ca^{2+}$ wave occurrence and propagation (under saturating $[IP_3] = 3.5\,\mu M$) within the uniformly distributed clusters throughout a 2D-membrane. The distances between the clusters are $d_{\text{mean}} = 1\,\mu m$ [Rüdiger, 2014b]. We model the numbers of activatable channels in a cluster using Poisson distribution with the mean $N_{\text{mean}} = 5$ [Rückl et al., 2015]. The initial condition of all channel subunits to be $IP_3$ bound $y(t, x_1, x_2) = 0$ facilitates the fast occurrence of the

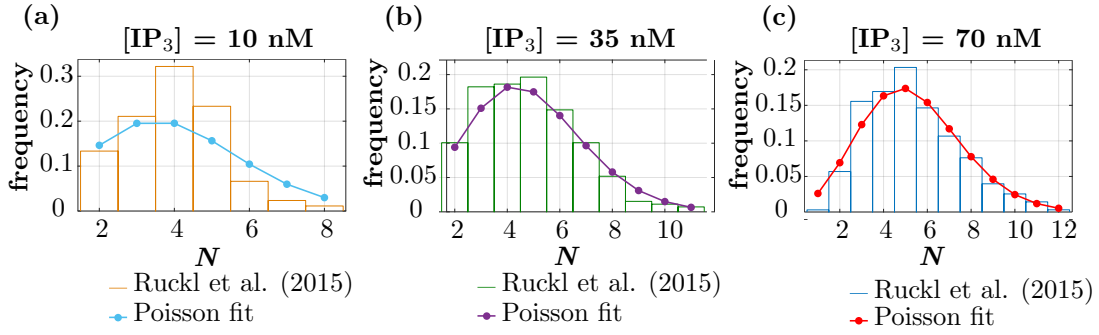


FIGURE 6.5: The Poisson fitting of the distributions of the numbers of activatable channels for various $[IP_3]$ loads. (a) $[IP_3] = 10$ nM. (b) $[IP_3] = 35$ nM. (c) $[IP_3] = 70$ nM (adapted from Rückl et al. [2015]).

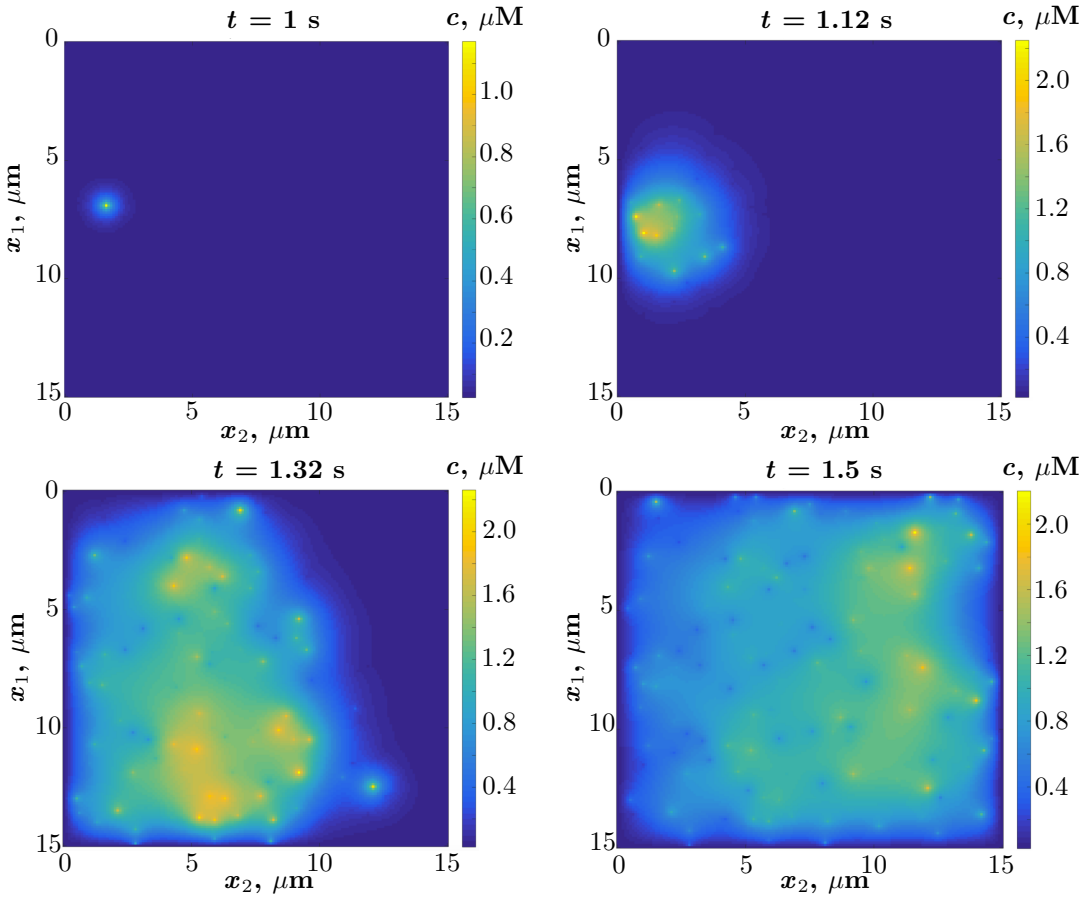


FIGURE 6.6: The $IP_3$ stochastic $Ca^{2+}$ front initiation and propagation in the two-dimensional ER membrane under $p = 3.5\,\mu$M, $D = 30\,\mu\text{m}^2/\text{s}$, $\lambda = 4 \times 10^3$ s$^{-1}$, starting from $y(t = 0, x_1, x_2) = 1$ (all subunits have $IP_3$ bound). Distances between the cluster are uniformly distributed with $d_{\text{mean}} = 1\,\mu$m, the distribution of the numbers of channels in the clusters is Poissonian with $N_{\text{mean}} = 5$.

wave (after 1 s). The reasoning behind choosing the diffusion coefficient $D = 30\,\mu\text{m}^2/\text{s}$ and the equilibration rate $\lambda = 4 \times 10^3$ s$^{-1}$ are discussed earlier in Chapter 4 and Chapter 5. The snapshots in Figure 6.6 represent a modelled travelling wave propagation.

To simplify the analysis, we use the system of cluster labelling depicted in Figure 6.7. Further, we will analyse the concentrations only at the $IP_3R$ clusters as the most relevant ones. For the representation of the results, we will use only the information about the cluster number (as

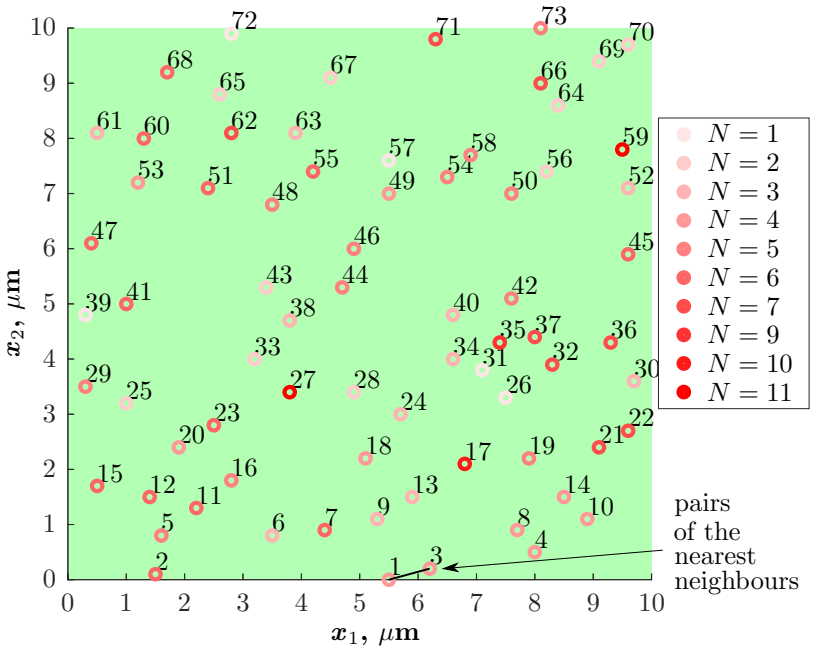


FIGURE 6.7: The labelling of the clusters within the 2D-membrane, numbers of activatable channels in clusters are highlighted by the shades of *red*.

labelled in Figure 6.7) in the membrane and respective $Ca^{2+}$ trace in time. Different numbers of activatable channels in clusters are highlighted by different shades of *red* as displayed in the legend. Typically, clusters with the largest numbers (highlighted by the bright *red* in Figure 6.7) are more likely to release $Ca^{2+}$ and normally feature longer release events. Clusters with low numbers of channels (highlighted by the light *red* in Figure 6.7) are less likely to participate in the release events and typically exhibit shorter durations being rather orchestrating players in the global $Ca^{2+}$ excitations.

We calculate the correlation coefficients between the $[Ca^{2+}]$ traces from the nearest clusters (for example, 1 and 3 as shown in Figure 6.7) depending on various levels of $[IP_3]$ and plot them as a function of the sequential number of each cluster in Figure 6.8. At first, we calculate the correlation between $[Ca^{2+}]$ at nearest neighbours and then calculate the average over all clusters to represent the whole membrane behaviour. The correlation coefficient $k_{ij}$ between the nearest clusters $i$ and $j$ is calculated as

$$k_{ij} = \frac{1}{N-1} \sum_{k=1}^{N} \left( \frac{c_i^k - \mu_i}{\sigma_i} \right) \left( \frac{c_j^k - \mu_j}{\sigma_j} \right), \tag{6.14}$$

where $c_i$ and $c_j$ are $[Ca^{2+}]$ traces captured at the $i^{\text{th}}$ and the $j^{\text{th}}$ clusters, respectively. Each trace contains $Ca^{2+}$ concentrations for discrete times $t_k$, $k = 1, \ldots, N$ within 40 s interval; $\mu_{i,j}$ are averages of $c_i$ and $c_j$ respectively, while $\sigma_{i,j}$ are the respective standard deviations. We look at the correlations between the nearest neighbours only to distinguish puffs (only one cluster involved) from spikes or waves (more than one cluster involved).

These correlations are displayed in Figure 6.8. Note, that the first plot (for $p = 0.014\,\mu$M) does not contain any data points, the second plot (for $p = 0.021\,\mu$M) contains few points and starting from $p = 0.031\,\mu$M onwards, the correlation coefficients are tightly spaced between 0.5 and 1.0

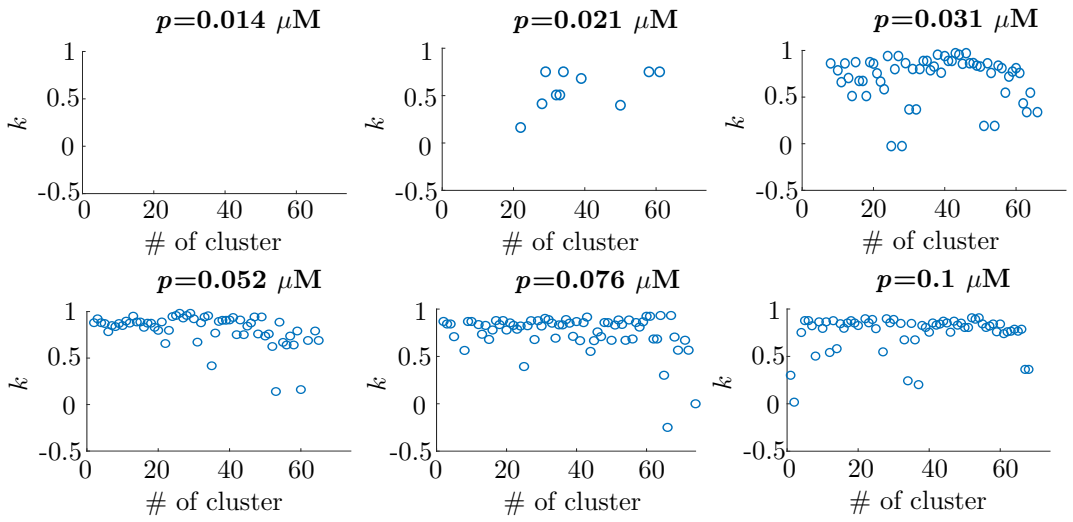


FIGURE 6.8: The correlation coefficients of $[Ca^{2+}]$ traces between the pairs of nearest neighbouring clusters exhibiting the threshold value of $[IP_3]$.

and tend to 1.0 as $p$ increases. However, some points persist to appear between 0.0 and 0.5 and others that persist to be close to 1.0 for a wide range of $p$.

The value of the threshold between non-correlated and correlated cases was checked for concentrations recorded over 20 s and 40 s. The value of the threshold differs between two durations for $< 0.005\,\mu$M. When $p < 0.014\,\mu$M, the following two types of behaviour are observed, neither of which makes the calculation of correlation between clusters relevant. The first type is associated with neighbouring clusters fluctuating around the rest cytosolic $[Ca^{2+}]$ level. In this case, the clusters are highly correlated but no release events occur. The second type is characterised by a release event from one cluster of a pair, while the other one stays closed – the clusters are uncorrelated. This scenario is also irrelevant for our analysis as we are concerned with the large-scale releases, e.g., release from multiple correlated clusters. Here we detect the large-scale events by calculating correlations between the pairs of neighbours and, considering large numbers of pairs connected in Figure 6.7, we assume that the release event featured by a high correlation coefficient takes place on the scales much larger than 1 or 2 clusters.

When $p > 0.014\,\mu$M, we start observing correlated release events and discuss here how the correlation between the nearest clusters affects the behaviour. The clusters with the highest number of channels tend to release $Ca^{2+}$ more frequently. If these clusters appear close to each other, they synchronise, which corresponds to correlation coefficients near 1.0 persisting for a range of $p > 0.014\,\mu$M. On the other hand, the correlations that are low for most values of $p$ correspond to clusters with the small number of channels or the clusters being far from their neighbours and barely participating in the release events. A majority of average clusters tend to develop a higher level of synchronisation between the nearest neighbours as $p$ increases – this leads to a high density of correlation coefficients near 1.0. In such a way, the higher $p$ is, the more synchronised the neighbouring clusters are on the membrane and the easier it is for an event involving more than one cluster to occur.

It is more informative to study a single average correlation coefficient for all the nearest neighbouring clusters on the membrane. Such a coefficient is calculated as an average over all points

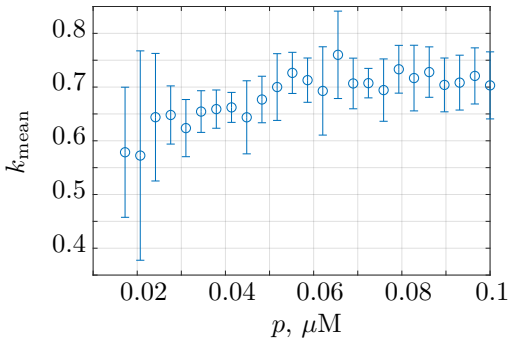


FIGURE 6.9: The averaged over whole membrane correlation coefficients of $[Ca^{2+}]$ traces at clusters within the ER membrane. The circles and error bars correspond to the mean and the standard deviation of the average correlation coefficient over five simulation rounds with distinct uniformly distributed positions of clusters.

on each subplot in Figure 6.8 for a range $0\,\mu\text{M} < p < 0.1\,\mu\text{M}$. The calculated values of the average correlation coefficient for the membrane are plotted as a function of $p$ in Figure 6.9. One more averaging was performed over five batches of simulations within the same range of $[IP_3]$ featuring different positions of the clusters on the membrane. All the positions were drawn from the uniform distribution. The corresponding standard deviation between the different configurations of the membrane is also shown in Figure 6.9. From the plot, it is apparent that the average correlation coefficient approaches $\approx 0.7$ when $p$ traverses a threshold of $p \approx 0.05\,\mu\text{M}$. For $p < 0.05\,\mu\text{M}$, the average correlation decreases indicating less synchrony between the neighbouring clusters which results in a smaller likelihood of release events involving more than one cluster. For $p > 0.05\,\mu\text{M}$, the release events involving a bunch of clusters – possibly $Ca^{2+}$ spikes or waves – become most likely and are independent of a further increase in $p$ (saturation).

The threshold value of $[IP_3]$ serves as the boundary between the localised and the propagating $Ca^{2+}$ release events in the ER membrane. Our cluster-based approach allows us to estimate the main trigger of the transition between those two regimes. Although we model many complex physiological factors (e. g. leak, pump-action, buffers, etc.) in a simplified manner, our analysis results in a reasonably accurate prediction of the transition from the localised to the propagating releases on a membrane consistent with Rückl et al. [2015].

## 6.3 Conclusions

In this chapter, we have introduced a cluster-based Langevin reaction-diffusion model. As the model is based on a set of Stochastic Differential Equations determined from a simplification of the kinetic DYK model (in contrast to the full DYK-based model by [Rückl et al., 2015]), it captures the single cluster dynamics while being efficient enough for modelling at large spatial scales. Therefore, at a single cluster level, we report realistic distributions of IPIs (which match experiments by Dickinson et al. [2012]). We also report a decrease in IPIs with $[IP_3]$ [Rückl et al., 2015] and a decrease in IPIs with the number of activatable channels in a cluster [Thurley and Falcke, 2011]. Furthermore, the model is capable of displaying the linear IPI-standard deviation relation previously observed in [Thurley et al., 2011]. This demonstrates the capacity of the model to capture essential dynamics at a single cluster level.

A simplified formulation allows for studying complex spatial dynamics at large scales. We also reduce the complexity of the modelling by imposing the discretisation of cluster sizes to follow a Poisson distribution as suggested by detailed simulations of a cluster Rückl et al. [2015] and experimental observations Taufiq-Ur-Rahman et al. [2009]. Having incorporated the stochastic aspects of $Ca^{2+}$ signalling, we acquire an insight into the cooperation between neighbouring clusters on a membrane to facilitate the occurrence of the propagating release events, such as $Ca^{2+}$ waves. It appears that clusters tend to synchronise their releases in time with the increase in $[IP_3]$ which facilitates spatial propagation of waves. We have identified a threshold value of $[IP_3]$ that separates two regimes – the domination of the localised release evens and domination of the propagating release events. Further, we apply the cluster-based Langevin reaction-diffusion model to study the effects of $IP_3R$ clustering on $Ca^{2+}$ releases experimentally observed by Taufiq-Ur-Rahman et al. [2009] for DT40 cells.

# Chapter 7

# Sensitivity and Coupling Effects in $IP_3R$ Clusters

In the previous chapters, we have proposed an extensive theoretical framework of $Ca^{2+}$ signalling incorporating deterministic dynamics and the stochasticity of $Ca^{2+}$ releases from clusters of $IP_3R$ channels. However, very little attention was given to the problem of $IP_3R$ clustering itself and the way it affects $Ca^{2+}$ signalling. The channels forming $IP_3$ clusters are reported to exhibit a 2-fold decrease in the open probability under low $[Ca^{2+}]$ ($0.2\,\mu$M) comparing to a single channel [Taufiq-Ur-Rahman et al., 2009]. We study this effect in detail here. We suggest it might be connected to the existence of excitability in the coupled $IP_3R$ clusters while non-excitable behaviour is manifest in the case of a single channel as it will be shown in this chapter. We perform extensive sensitivity analysis to build a coarse-graining approach and to identify the main triggers of the $Ca^{2+}$ dynamics in the parameter space of both DYK model and cluster-based $IP_3$ dependent model presented in Chapter 5. Further, we model the dynamics of the clusters incorporating the negative cooperativity via parametric study and analyse how it affects $Ca^{2+}$ signalling.

## 7.1 Sensitivity analysis of the DYK model

We derive a slightly modified version of the stationary open probability of the channel in the DYK that was shown in Section 2.3. The revised open probability equation accounts for the probabilities of activation of three or four subunits (instead of just three as in the DYK) for a channel to be activated. Thus, the stationary open probability of a single subunit from Equation (2.20) is

$$P_{\text{act}} = \frac{cpd_2}{(cp + pd_2 + d_1d_2 + cd_3)(c + d_5)}, \tag{7.1}$$

where $c = [Ca^{2+}]$ , $p = [IP_3]$ and $d_4 = \frac{d_1d_2}{d_3}$, the last is derived from the detailed balance condition. The open probability is the sum of the probabilities of three or four subunits being active:

$$P_{\text{open}} = 4(P_{\text{act}})^3(1 - P_{\text{act}}) + (P_{\text{act}})^4. \tag{7.2}$$

Equation (7.2) together with Equation (7.1) gives a function of multiple DYK dissociation rates $P_{\text{open}} = f(d_1, d_2, d_3, d_5)$. We fit the patch-clamp open probability data by Taufiq-Ur-Rahman et al. [2009] reproduced in Figure 7.1 (dots with error bars) with the open probability function

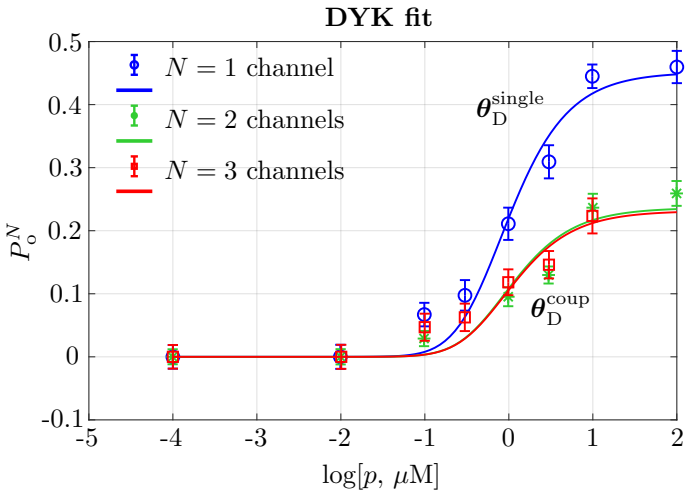


FIGURE 7.1: Steady-state open probability data $P_{\mathrm{o}}^{N}$ calculated from the openings of $N = 1$ (*blue points*), $N = 2$ (*red points*) and $N = 3$ (*green points*) channels in a cluster and fitted by the single channel DYK model given by Equation (7.2) under $[\mathrm{Ca}^{2+}] = 0.2\,\mu$M. Set of parameters satisfying the single channel fit $\boldsymbol{\theta}_{\mathrm{D}}^{\mathrm{single}}$ are given in Table 7.1 (*blue line*), while for 2 (*red line*) and 3 channels (*green line*) all parameters $\boldsymbol{\theta}_{\mathrm{D}}^{\mathrm{coup}}$ are the same apart from $d_5 = 0.2509\,\mathrm{s}^{-1}$ and $d_5 = 0.2471\,\mathrm{s}^{-1}$, respectively (reproduced from Taufiq-Ur-Rahman et al. [2009]).

given by Equation (7.2). The fitting is performed using the method based on least-squares from the standard MATLAB fitting toolbox. Here we need to reconsider the state transition rates $\boldsymbol{\theta} = (d_1, d_2, d_3, d_5)$ used in the previous chapters. In the earlier models, the fitting of the open probability data was performed in Purkinje cells of the cerebellum, resulting in the best parameter fit $\boldsymbol{\theta}_{\mathrm{P}}$, and *Xenopus* oocytes $\boldsymbol{\theta}_{\mathrm{O}}$ [Bezprozvanny et al., 1991, Mak et al., 1998]. In the current chapter, however, we fit the data from a different cell type – DT40 cells and we refer to the set of best-fit parameters in this case as $\boldsymbol{\theta}_{\mathrm{D}}$ [Taufiq-Ur-Rahman et al., 2009].

Three best fits of the expression in Equation (7.2) are shown in Figure 7.1 to the data from Taufiq-Ur-Rahman et al. [2009]. In the case of a single channel $N = 1$, the fit is indicated with *blue line* and characterised by a set of parameters $\boldsymbol{\theta}_{\mathrm{D}}^{\mathrm{single}}$. In the case of coupled channels, two fits are present – for $N = 2$ (*green line* characterised by $\boldsymbol{\theta}_{\mathrm{D}}^{\mathrm{coup}}$) and for $N = 3$ (*red line* characterised by the same $\boldsymbol{\theta}_{\mathrm{D}}^{\mathrm{coup}}$). We discuss the precise values of $\boldsymbol{\theta}_{\mathrm{D}}^{\mathrm{single}}$ and $\boldsymbol{\theta}_{\mathrm{D}}^{\mathrm{coup}}$ later in this section.

It appears counter-intuitive that the open probability in the case of $N = 2$ and $N = 3$ should be much smaller than the one in the case of $N = 1$. We focus on explaining this by studying whether we can fit the data for $N = 2$ and $N = 3$ with the open probability function for $N = 1$, given by Equation (7.2). In such a way we expect to identify which parameters affect the two-fold difference between $N = 1$ and $N = 2$, $N = 3$. Interestingly, we observe that the difference between the best fits for all the cases depends only on a single parameter $d_5$. By increasing $d_5$ by a factor of 2 ($d_5 = 0.2509\,\mathrm{s}^{-1}$ for 2 channels (*red line*), $d_5 = 0.2471\,\mathrm{s}^{-1}$ for 3 channels (*green line*)) and retaining all other parameters unchanged, we can get the best fit. This means that the DYK model in the given situation appears to be sensitive to $d_5$ only and insensitive to the rest of the parameters. To scrutinize this observation we formally perform a sensitivity analysis of the DYK model for the open probability $P_{\mathrm{open}}$.

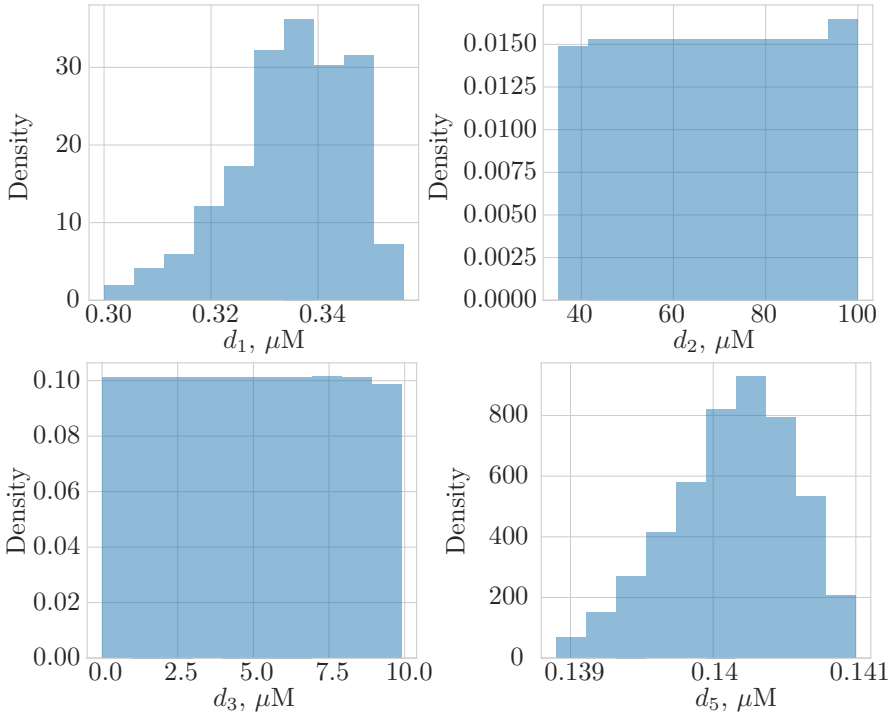


FIGURE 7.2: The ABC rejection sampling distributions obtained from the regression of the DYK model to the single-channel data presented in Figure 7.1.

We study the sensitivity of the DYK model in more detail using two approaches: non-linear regression using the Approximate Bayesian Computation (ABC) method with a rejection sampling algorithm [Beaumont, 2010] and sloppy parameter sensitivity analysis [Gutenkunst et al., 2007].

Both approaches are based on the study of the loss function of the single-channel or coupled data by Taufiq-Ur-Rahman et al. [2009] fitted by the sets $\boldsymbol{\theta}_{\mathrm{D}}^{\mathrm{single}}$ or $\boldsymbol{\theta}_{\mathrm{D}}^{\mathrm{coup}}$, respectively. We use Equation (7.2), which gives us an expression for the loss function as

$$L = \sum_{i=1}^{N} \left(P_{\mathrm{open}} - P_i\right)^2, \tag{7.3}$$

where $P_i$, $i = \overline{1, N}$, are the data points for the single channel shown in blue in Figure 7.1.

From the first method, we generate the distributions of parameters ($d_1$, $d_2$, $d_3$ and $d_5$) satisfying the least square loss function criterion $L < \bar{\epsilon}$ with the given accuracy $\bar{\epsilon} = 0.03029$ which is the mean error for all data points. The distributions of the parameters satisfying the best fit are plotted in Figure 7.2. We can conclude from the shapes of these distributions that the model is more sensitive to $d_5$ and $d_1$ (narrow distributions) rather than to $d_2$ and $d_3$ (flat distributions). It is apparent from the figure that the scales of the distributions are very different. We also shift the distributions by their mean values to obtain $\mu = \bar{\boldsymbol{\theta}}_j = 0$ in the new dataset for convenience of further analysis

$$\boldsymbol{\theta}_j = \tilde{\boldsymbol{\theta}}_j - \bar{\boldsymbol{\theta}}, \tag{7.4}$$

where $\tilde{\boldsymbol{\theta}}_j = (d_1^j,\, d_2^j,\, d_3^j,\, d_5^j)$, $j = \overline{1, D}$, are $4D$ data points generated by the regression sampling algorithm ($D$ is a sample size), $\bar{\boldsymbol{\theta}}$ is the mean of the original dataset.

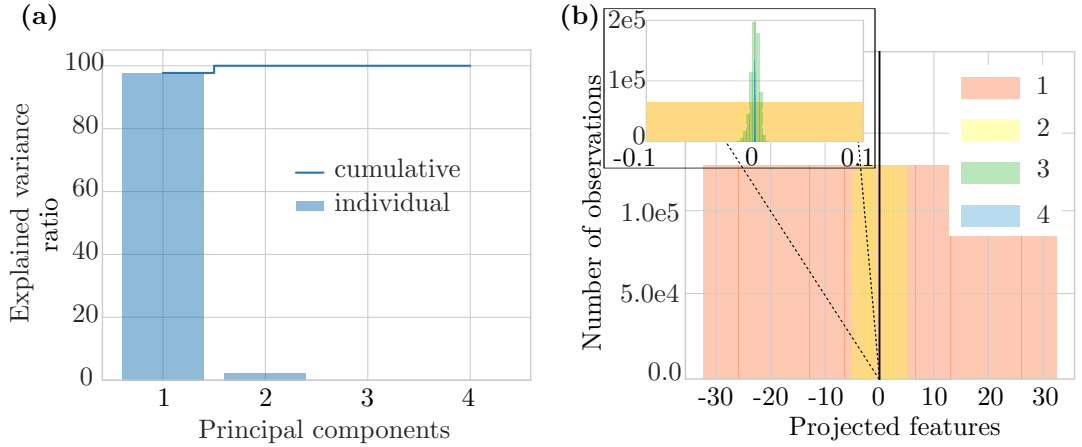


FIGURE 7.3: (a) The explained variance ratios calculated from the eigenvalues of the covariance matrix representing the principal components of the distributions shown in Figure 7.2. (b) The distributions of the projected data onto the new feature space defined by the eigenvectors of the covariance matrix with zoomed components 3 and 4 due to different scales.

To quantify the observed sensitivity, we perform the eigendecomposition of the distributions in the spirit of Principal Component Analysis (PCA) by calculating the eigenvectors and eigenvalues of the $4\times4$ covariance matrix, because in our case there are 4 features (parameters). The elements of the matrix are covariances between the pairs of averaged features

$$\sigma_{jk} = \frac{1}{D-1}\sum_{i=1}^{D}\left(\theta_{ij}-\bar{\theta}_j\right)\left(\theta_{ik}-\bar{\theta}_k\right), \tag{7.5}$$

where $\theta_{ij} = d_i^j$ are points generated by rejection-sampling algorithm, $i = 1, 2, 3$ or 5, $j = \overline{1,4}$, and $\bar{\theta}_j = \frac{1}{D}\sum_{k=1}^{D}\theta_{jk}$ is an average over sample corresponding to feature $j$.

Further, we proceed with the calculation of the principal components. The principal components of the dataset are the ones corresponding to the highest eigenvalues and whose eigenvectors denote directions in parameter space with the largest variance. The idea behind the feature space reduction is in dismissing the lowest eigenvalues which bear the least information about the distribution of the data. The principal components are chosen from the explained variance ratio $\sigma_i^{\text{exp}} = \frac{\lambda_i}{\sum_{i=1}^{4}\lambda_i}$. From Figure 7.3 (a) we observe that the first principal component bears information about 97.72% of the variance of the dataset. In Figure 7.3 (b) we show the projections of the distributions onto the eigenvectors of the covariance matrix $\mathbf{V}_i$, $i = \overline{1,4}$

$$\boldsymbol{\theta}^{\text{proj}}{}_i = \boldsymbol{\theta}_i\mathbf{V}_i \tag{7.6}$$

where $\boldsymbol{\theta}^{\text{proj}}{}_i$ correspond to the distributions plotted in Figure 7.3 (b). The figure clearly indicates the high sensitivity of the model to the fourth principal component shown as thin blue distribution in the inset with the smallest variance. From the figure, we see that the pair of features (highlighted with *red* and *yellow*) have much larger variances than the rest (highlighted with *green* and *blue*). The components of the eigenvectors (Equation (A.1)) define which directions in the $\boldsymbol{\theta}_{\text{D}} = (d_1, d_2, d_3, d_5)$ are affecting the loss function Equation (7.3) in the most significant way. Thus, we proceed to the second method to find the correspondence between the principal components and sensitivity of the model to parameters $d_1$, $d_2$, $d_3$ and $d_5$.

To further analyse the sensitivity of the model, we perform the Hessian analysis used to study the "sloppy models" presented by Gutenkunst et al. [2007]. Those models are characterised by high sensitivity to certain parameters which are normally called "stiff". On the other hand, the changes in "sloppy" parameters do not affect the model behaviour significantly. This technique is very handy for biological problems as it defines the parameters which allow errors in the measurements (sloppy) or the ones which have to be defined very accurately (stiff). According to Sethna [2008] such systems are met in multiple models in biology, mathematics and physics (e.g. hormones response model, Quantum Monte Carlo method, some regression problems).

To define the sensitivity of the model, we will study the derivatives of the residuals given by the loss function Equation (7.3). Let

$$r_i = \frac{P_{\text{open}} - P_i}{\epsilon_i}, \tag{7.7}$$

where error $\epsilon_i = 1$. The gradients and the curvatures of the loss function hyper surface can be calculated as

$$L = \sum_i r_i^2, \tag{7.8}$$

$$\frac{\partial L}{\partial d_\alpha} = \sum_i 2 r_i \frac{\partial r_i}{\partial d_\alpha}, \tag{7.9}$$

$$\frac{\partial^2 L}{\partial d_\alpha \partial d_\beta} = 2 \sum_i \left( \frac{\partial r_i}{\partial d_\alpha} \frac{\partial r_i}{\partial d_\beta} + r_i \frac{\partial^2 r_i}{\partial d_\alpha \partial d_\beta} \right). \tag{7.10}$$

At the best-fit point $L(\boldsymbol{\theta}_{\text{D}})$ (presented in Table 7.1 for the DYK model) is minimal and for small $\boldsymbol{\epsilon}$

$$L(\boldsymbol{\theta}^* + \boldsymbol{\epsilon}) = L(\boldsymbol{\theta}^*) + \boldsymbol{\epsilon}^\top \, 2 \sum_i (r_i \boldsymbol{\nabla}_{\boldsymbol{\theta}} r_i) \Big|_{\theta=\theta^*} + \boldsymbol{\epsilon}^\top \sum_i \left( \boldsymbol{\nabla}_{\boldsymbol{\theta}}{}^\top r_i \boldsymbol{\nabla}_{\boldsymbol{\theta}} r_i + r_i \boldsymbol{\nabla}_{\boldsymbol{\theta}}{}^2 r_i \right) \Big|_{\theta=\theta^*} \boldsymbol{\epsilon} + \ldots \tag{7.11}$$

where $\boldsymbol{\theta}^* = (d_1^*, d_2^*, d_3^*, d_5^*)$ is the vector composed of the best fit parameters. The second term vanishes at the best-fit point because the gradient $\boldsymbol{\nabla}_{\boldsymbol{\theta}} r_i$ is zero, then we are left with

$$L(\boldsymbol{\theta}^* + \boldsymbol{\epsilon}) = L(\boldsymbol{\theta}^*) + \boldsymbol{\epsilon}^\top \sum_i \left( \boldsymbol{\nabla}_{\boldsymbol{\theta}}{}^\top r_i \boldsymbol{\nabla}_{\boldsymbol{\theta}} r_i \right) \Big|_{\theta=\theta^*} \boldsymbol{\epsilon}. \tag{7.12}$$

The derivative of the residuals is purely model driven

$$\boldsymbol{\nabla}_{\boldsymbol{\theta}} r_i = \boldsymbol{\nabla}_{\boldsymbol{\theta}} P_{\text{open}}, \tag{7.13}$$

thus, the sensitivity of the model may be described by the Hessian matrix. Which can be written explicitly as

$$H = \begin{pmatrix} \frac{\partial^2 L}{\partial d_1^2} & \frac{\partial^2 L}{\partial d_1 \partial d_2} & \frac{\partial^2 L}{\partial d_1 \partial d_3} & \frac{\partial^2 L}{\partial d_1 \partial d_5} \\ \frac{\partial^2 L}{\partial d_2 \partial d_1} & \frac{\partial^2 L}{\partial d_2^2} & \frac{\partial^2 L}{\partial d_2 \partial d_3} & \frac{\partial^2 L}{\partial d_2 \partial d_5} \\ \frac{\partial^2 L}{\partial d_3 \partial d_1} & \frac{\partial^2 L}{\partial d_3 \partial d_2} & \frac{\partial^2 L}{\partial d_3^2} & \frac{\partial^2 L}{\partial d_3 \partial d_5} \\ \frac{\partial^2 L}{\partial d_5 \partial d_1} & \frac{\partial^2 L}{\partial d_5 \partial d_2} & \frac{\partial^2 L}{\partial d_5 \partial d_3} & \frac{\partial^2 L}{\partial d_5^2} \end{pmatrix}_{\boldsymbol{\theta}^* = \boldsymbol{\theta}_{\text{D}}}, \tag{7.14}$$

where $\boldsymbol{\theta}^*$ is the best model fit for single-channel ($\boldsymbol{\theta}^{\text{single}}$) or coupled channels ($\boldsymbol{\theta}^{\text{coup}}$) data [Taufiq-Ur-Rahman et al., 2009] which is presented in Table 7.1.

TABLE 7.1: The best fit of the DYK model to the single-channel data.

| Parameter $\boldsymbol{\theta}_{\text{D}}^{\text{single}}$ or $\boldsymbol{\theta}_{\text{D}}^{\text{coup}}$ | Best fit, $\mu$M |
|---|---|
| $d_1^{\text{single/coup}}$ | 0.3425 |
| $d_2^{\text{single/coup}}$ | 76.3 |
| $d_3^{\text{single/coup}}$ | 3.291 |
| $d_5^{\text{single}}$ | 0.1403 |
| $d_5^{\text{coup}}$ | 0.2509 |

The sensitivity of the loss function is studied by performing the eigendecomposition of the Hessian matrix. The eigenvalues of the Hessian are $\lambda_1^H = 0.29$, $\lambda_2^H = 10^{-3}$, $\lambda_3^H = 10^{-3}$, $\lambda_4^H = 50.47$. Judging by the scales of the eigenvalues, one can define the impact of the change in the corresponding parameter on the model behaviour around the best fit point. The corresponding eigenvectors are used to define the directions of the greatest sensitivities of the loss function in the multi-dimensional spaces. The direction of the sharpest change is defined by the eigenvectors of the stiffest parameters.

The projection of the Hessian onto the eigenvector space is

$$H^{\text{Pr}} = (\boldsymbol{\theta} - \boldsymbol{\theta}_{\text{D}})^\top \mathbf{V}^\top \mathbf{H} \mathbf{V} (\boldsymbol{\theta} - \boldsymbol{\theta}_{\text{D}}) \tag{7.15}$$

where $\mathbf{V}$ is the matrix composed of eigenvectors given in Equation (A.6) which can be used to interpret the stiffness of the model. $H^{\text{Pr}}|_{d_2=d_2^{\text{D}}, d_3=d_3^{\text{D}}}$ is depicted in Figure 7.4 (a) in $(d_1, d_5)$ coordinates. The stiffest component of the model $d_5$ corresponds to the smallest axis of the ellipse which is defined by the eigenvalue of $H$ as $a = \frac{1}{\sqrt{\lambda_4^{\text{H}}}}$. Thus, we estimate that $d_5$ is $\sqrt{\frac{\lambda_4^{\text{H}}}{\lambda_1^{\text{H}}}} \approx 13$ times stiffer than $d_1$, whereas around 417 times stiffer than $d_2$ or $d_3$ (as shown in Figure 7.4 (b) and (c)).

From this analysis we conclude that the stiffest components $d_5$ and $d_1$ are defined by the largest components of the eigenvectors which correspond to the highest eigenvalues of the Hessian matrix. Comparison of the eigenvalues and the eigenvectors of the covariance matrix used in the Principal Component Analysis (Equation (A.1)) with those of the Hessian matrix (Equation (A.6)) results in the clearer distinction of the stiff parameters in the later. The loss function of the $\boldsymbol{\theta}_{\text{D}}$ fit is introduced in Equation (7.3) and plotted against the stiffest parameters $d_1$ and $d_5$ in Figure 7.5. There is a global minimum of the loss function corresponding to the best fit of data (presented in Table 7.1). The slope of the function change in the $d_2$ or $d_3$ directions is much lower comparing to $d_1$ and $d_5$.

Coming back to the original DYK model, $d_5 = b_5/a_5$ is the dissociation constant responsible for $Ca^{2+}$ binding/unbinding in the DYK cube (Figure 2.5). It affects the rates of $Ca^{2+}$ binding and unbinding to a subunit and, thus, plays a crucial role in $Ca^{2+}$ dynamics. In conclusion, $d_5$ is the sensitivity trigger of the stationary open probability in the DYK model. This makes it a suitable driver of the coupling effects as even small changes in $d_5$ ($\approx 2$ times) may lead to the reduction of the open probability triggered by IP$_3$ binding [Taufiq-Ur-Rahman et al., 2009]. Further, we

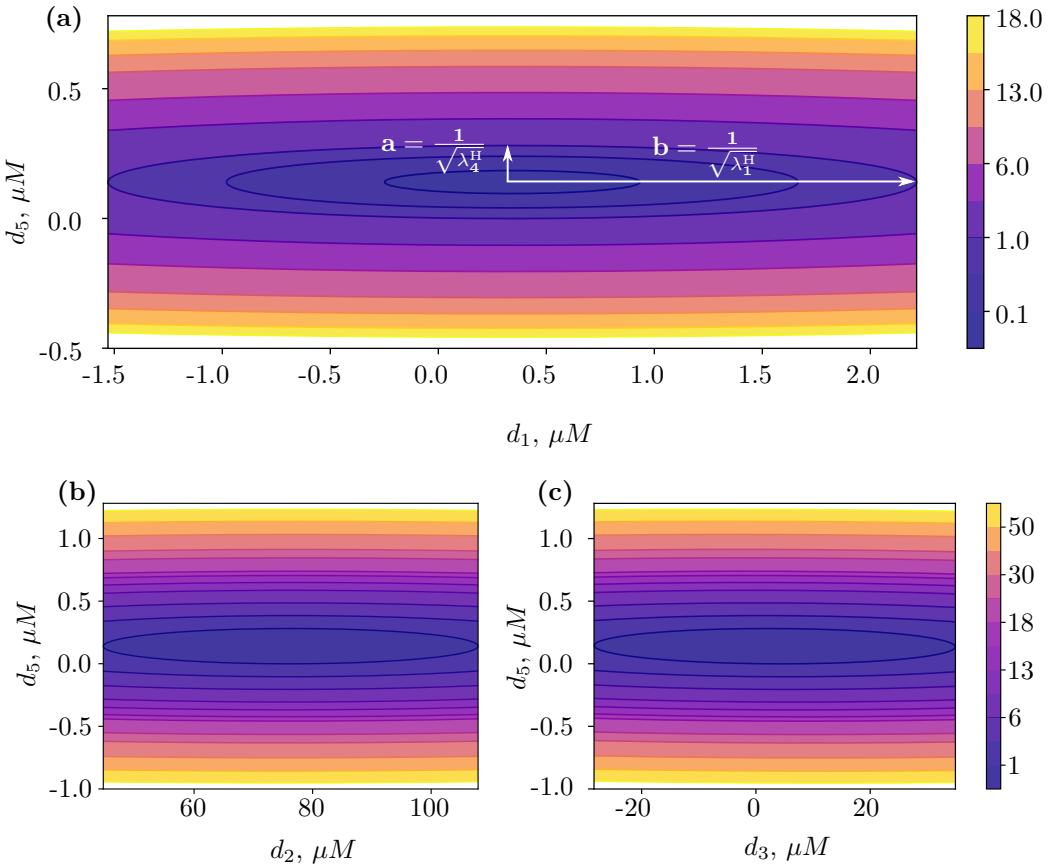


FIGURE 7.4: The Hessian projection plots representing the stiffness of model parameters. (a) The ($d_1$, $d_5$) contour plot exhibiting $d_5$ as a stiff parameter (small ellipse axis $a = 1/\sqrt{\lambda_4^H}$) and $d_1$ as a sloppy parameter (large ellipse axis $b = 1/\sqrt{\lambda_1^H}$). (b) and (c) The Hessian contours ($d_2$,$d_5$) and ($d_3$,$d_5$), respectively, representing $d_2$ and $d_3$ as sloppy parameters.

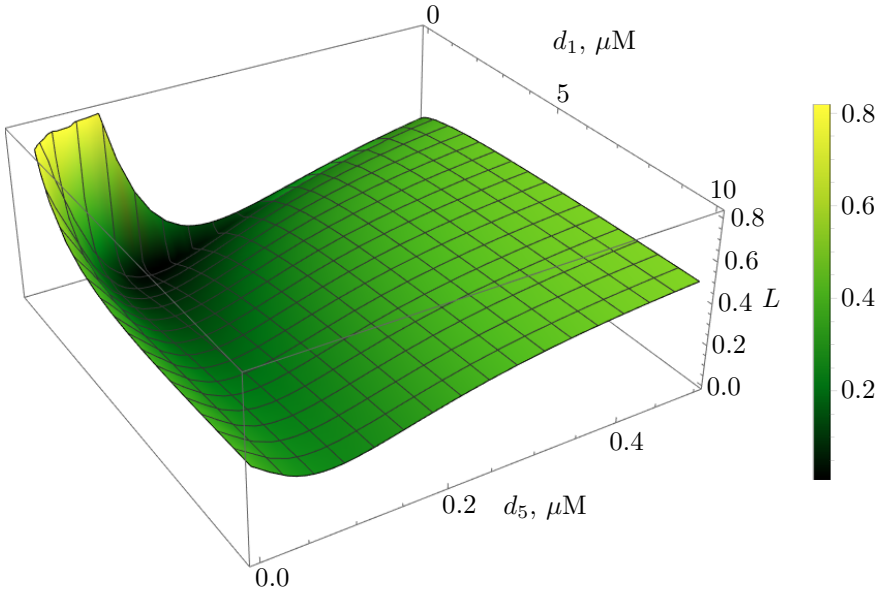


FIGURE 7.5: The loss function of the single-channel data fit calculated from Equation (7.3) where the "sloppy" parameters are fixed ($d_2 = d_2^D$, $d_3 = d_3^D$). The colours represent the magnitude of the projection of Hessian Equation (7.15).

would like to incorporate the effect of change in $d_5$ into the model of $Ca^{2+}$ dynamics to study the effects brought by the negative cooperativity of IP$_3$R channels to the $Ca^{2+}$ signalling. Thus, we come back to the IP$_3$ dependent cluster-based model introduced in Chapter 5 to study the $Ca^{2+}$ dynamics in clusters, and the way how the effect discovered by Taufiq-Ur-Rahman et al. [2009] influences the dynamics.

## 7.2 The IP$_3$R model with effects of clustering

### 7.2.1 Steady-state open probability fit

We start with rewriting the model (5.1)–(5.3) for the single cluster of channels for case of reference

$$\frac{\mathrm{d}a}{\mathrm{d}t} = k_a^+(c)c(1-a-h-y) - k_a^- a + k_1(c)h - k_i^+ ca, \tag{7.16}$$

$$\frac{\mathrm{d}h}{\mathrm{d}t} = k_i^+(c)c(1-a-h-y) - k_1(c)h - k_2(c)h + k_i^+ ca, \tag{7.17}$$

$$\frac{\mathrm{d}y}{\mathrm{d}t} = C^{\mathrm{down}}(c)(1-y) - C_{\mathrm{ch}}^{\mathrm{up}}(c,p)y, \tag{7.18}$$

where $C_{\mathrm{ch}}^{\mathrm{up}}$ is given by Equation (2.73) which we derived previously. The transition rate $C_{\mathrm{ch}}^{\mathrm{up}}$ incorporates the idea that all 4 subunits have to bind IP$_3$ for a channel to open. This is done through accounting for probabilities of subsequent binding of IP$_3$ to all subunits as explained earlier in Chapter 2 resulting in Equation (2.73). The experimental evidence supporting the suggestion that the opening of a channel requires all four subunits to bind IP$_3$ was brought by [Alzayady et al., 2016]. The transition rate that reflects this idea – $C_{\mathrm{ch}}^{\mathrm{up}}$ is introduced here for the first time.

Previously, in order to model the transient puffs, the transitions away from the active state, controlled by $k_i^+$, were taken to be $c_s = 300\,\mu$M. This argument was adopted from the study by Rüdiger et al. [2010a] to account for large $[Ca^{2+}]$ at channels after opening. This assumption eliminates the detailed balance in the model. Rüdiger et al. [2010a] also study an alternative approach keeping the detailed balance but considering high concentration gradients in the equation for $Ca^{2+}$ dynamics. The author also shows that both ways lead to similar dynamics. The advantage of the second approach is in the possibility to perform the fitting of the stationary open probability to the data. Here, in (7.16)–(7.18) we stick to the second approach taking the terms $k_i^+ ca$ to be dynamical in $c$. For the stationary open probability fitting we define the transition rates which characterise IP$_3$R channels from patch-clamp open probability measurements [Mak et al., 1998, Taufiq-Ur-Rahman et al., 2009] obtained from the openings of channels averaged over long a time. Further, we show that the open probability curve can be obtained from the long $[Ca^{2+}]$ traces in the transient regime.

We obtain the stationary open probability by solving the system (7.16)–(7.18) with preserved detailed balance ($c_s = c$) in the steady-state case. Thus, the open probability is calculated from the system $\dot{a} = 0$, $\dot{h} = 0$, $\dot{y} = 0$ as the fraction of the active channels in the cluster

$$P_{\mathrm{open}}^{\mathrm{IP}} = a_{\mathrm{st}} = \frac{12c^3 C_{\mathrm{ch}}^{\mathrm{up}} d_2}{\left(12c^3 + 6c^2 d_5 + 4cd_5^2 + d_5^3\right)\left(\left(C_{\mathrm{ch}}^{\mathrm{up}} + a_1 d_1\right) + c\left(C_{\mathrm{ch}}^{\mathrm{up}} + a_3 d_3\right)\right)}. \tag{7.19}$$

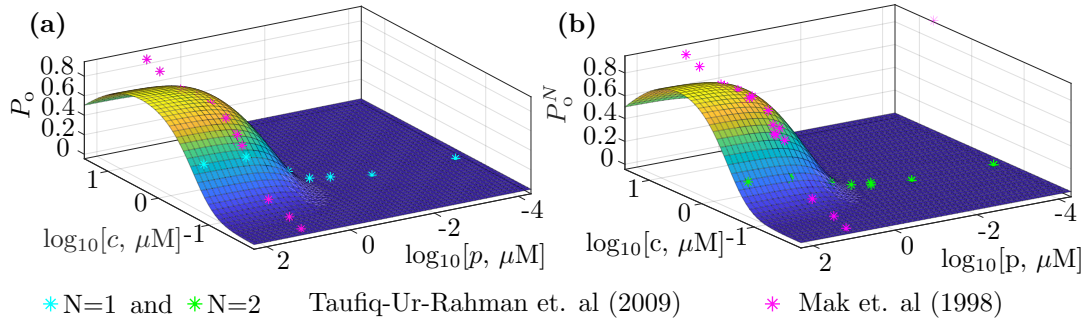


FIGURE 7.6: The regression of the open probability data in range of [IP$_3$] [Taufiq-Ur-Rahman et al., 2009] for a single channel $P_o$ (a) and coupled channels $P_o^N$ (b) the parameters of both fits are given in Table 7.2, $Ca^{2+}$-dependent data [Mak et al., 1998] is given for reference.

After substituting $C_{ch}^{up}$ from Equation (2.73), we get the detailed expression for the open probability which is given in Equation (A.10). In the final form, the dependence of $P_{open}^{IP}$ on $a_1$ and $a_3$ cancels out and we get the expression defined by 4 parameters ($d_1$, $d_2$, $d_3$, $d_5$). In the previous section, Equation (7.2) was used to fit the data obtained from DT40 cells [Taufiq-Ur-Rahman et al., 2009] with the set of parameters $\boldsymbol{\theta}_D$. In contrast, here, we use a new expression from Equation (7.19) to fit the same data with the different set of parameters $\boldsymbol{\theta}_{IP}$. The best fit for a single channel (characterised by $\boldsymbol{\theta}_{IP}^{single}$) is shown in Figure 7.6 (a) and the best fit for coupled channels (characterised by $\boldsymbol{\theta}_{IP}^{coup}$) is shown in Figure 7.6 (b). The best-fitting values of parameters are shown in Table 7.2. We fit the IP$_3$ dependent data from Taufiq-Ur-Rahman et al. [2009] and display the measurements for various $Ca^{2+}$ loads by Mak et al. [1998] (*Xenopus* oocyte) for reference. The results of the fitting are presented in the range of $[Ca^{2+}]$ consistent with cell physiology($10^{-4}$–100 $\mu$M). We can disregard the increasing error for high $[Ca^{2+}]$ as the maximum value of cytosolic $Ca^{2+}$ we consider in our model is $< 10\,\mu$M.

The Hessian of the cluster-based model with its numerical values, corresponding to the chosen parameters, appears in Equation (A.15) for a single-channel case and in Equation (A.20) for coupled channels. The calculated eigenvalues and eigenvectors (in Equations (A.16) and (A.21), respectively) of both matrices suggest that in both cases model is most sensitive to $d_1$ and $d_5$. The directions of the eigenvectors corresponding to the greatest eigenvalue define the stiffest components. From the eigenvectors, we see that the components corresponding to $d_5$ are at least one order of magnitude larger than the other directions. Thus, we conclude that the $d_5$ has the most significant impact on the open probability similarly to the DYK fitting for $\boldsymbol{\theta}_D$.

TABLE 7.2: The best fit of the cluster-based IP$_3$ model to the single vs coupled channels data together with the other parameters defined in the model.

| Parameters defining $P_0$ | Best fit | Parameters not included in $P_0$ | Value |
|---|---|---|---|
| $d_1^{IP}$ | 0.5 $\mu$M | $a_1$ | $2\,(\mu M \times s)^{-1}$ |
| $d_2^{IP}$ | 30 $\mu$M | $(k_i^+, a_2)$ | $0.02\,(\mu M \times s)^{-1}$ |
| $d_3^{IP}$ | 0.1 $\mu$M | $a_3$ | $4\,(\mu M \times s)^{-1}$ |
| $d_{5\,single}^{IP}$ | 0.2441 $\mu$M | $a_5$ | $15\,(\mu M \times s)^{-1}$ |
| $d_{5\,coup}^{IP}$ | 0.4315 $\mu$M | $c_s$ | 300 $\mu$M |
| $b_i = d_i a_i$ | | $c_0$ | 0.02 $\mu$M |
| | | $\alpha$ | 0.74 $\mu$M |

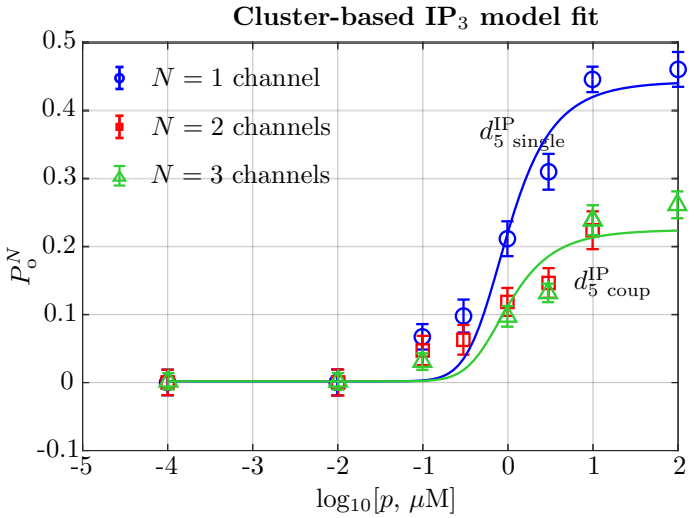


FIGURE 7.7: The regression of the open probability data $P_o^N$ [Taufiq-Ur-Rahman et al., 2009] for single (blue circles) vs coupled ($N = 2$ red squares and $N = 3$ light-green triangles) channels distinct values of $d_5$ under $[Ca^{2+}] = 0.2\mu$M.

In conclusion, we performed two fits – $\boldsymbol{\theta}_{\mathrm{D}}$ and $\boldsymbol{\theta}_{\mathrm{IP}}$. The first one comes from the DYK model, while the second one is obtained from the cluster-based model. The fitting of the same data was carried out by the two models independently. The fit with the DYK model resulted in a set of parameters $d_1$, $d_2$ and $d_3$ that satisfy both case of $N = 1$ and $N = 2, 3$. The parameter $d_5$ appeared to be two times smaller for $N = 1$ than the same parameter $d_5$ for the case of $N = 2, 3$. In the same way, the fit by the cluster-based model resulted in a different set of parameters $d_1$, $d_2$ and $d_3$, all of these satisfying the case of $N = 1$ and $N = 2, 3$. Similarly, the difference between the fits by the cluster-based model between the two cases ($N = 1$ and $N = 2, 3$) is attributed to the difference in $d_5$ alone.

Taufiq-Ur-Rahman et al. [2009] report 2-fold decrease in the dissociation rate connecting open and closed state of channel in their own 3-state model to explain the effect of change in the open probability. Thus, this effect seems to be intrinsic to the channel as it is independent on the modelling approach.

### 7.2.2 Dynamical system analysis

The dynamical behaviour of the system of Equations (7.16)–(7.18) in transient regime (containing terms $k_i^+ c_s a$) is shown in Figure 7.8. We take into account the values of the fitted parameters and select the rest of the components ($3^{rd}$ and $4^{th}$ columns in Table 7.2) of the model to comply with the durations of events (governed by $a_2$) and position of $h$-nullcline (governed by $d_2$) and the excitability threshold (governed by $a_5$). The rest of the parameters ($a_1$, $a_3$, $c_0$ and $\alpha$) are adopted from the previous chapters and the response of the model is insensitive to the most of these parameters. The value of $c_s$ is also taken from the previous models to establish the transient regime for puffs, where an excitable trajectory is possible. The excitability quasi-threshold (magnified in the inset of Figure 7.8 (a) and projected to $(a, h)$ plane in Figure 7.9) is the line in the phase space which separates the trajectories falling to the origin and those following the long excursions to form the puff (light grey lines in Figure 7.9). The existence of the threshold is an intrinsic feature of excitable models.

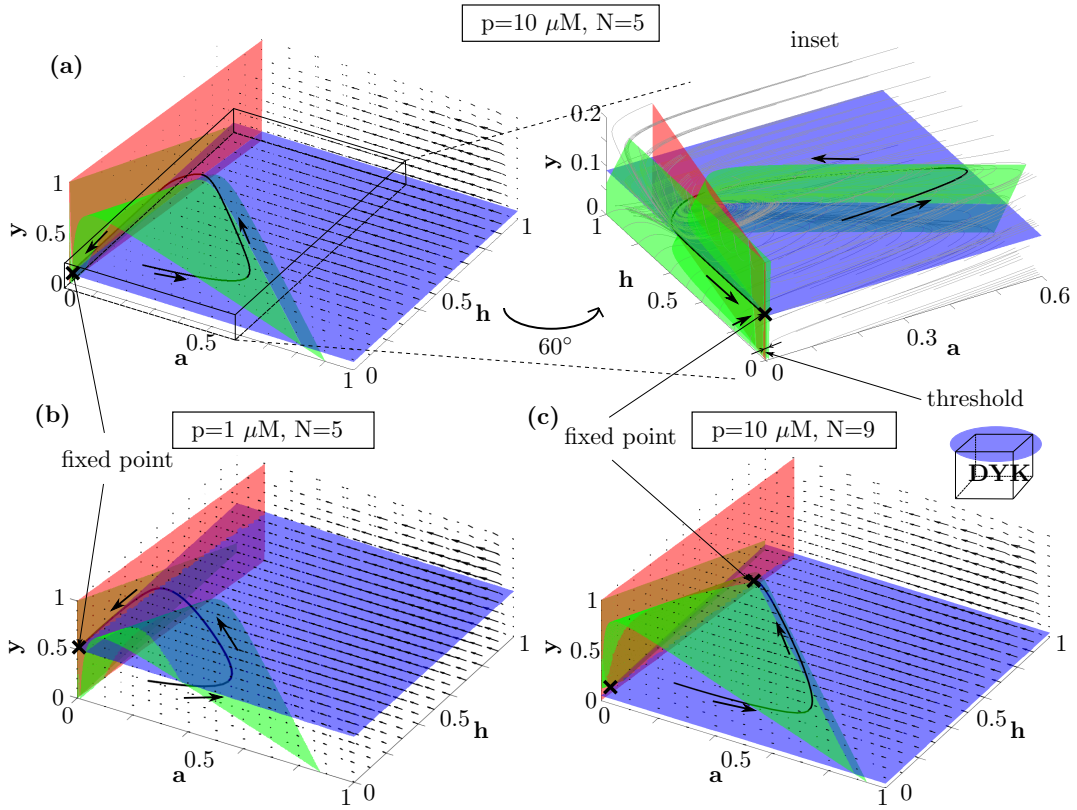


FIGURE 7.8: Three-dimensional phase space representing various kinds of behaviour in the cluster-based IP$_3$ model. **(a)** The nullclines and exemplary puff trajectory at $p = 10\,\mu$M at the cluster containing 5 channels. The different angle of view in the inset shows separatrix (excitability quasi-threshold). **(b)** Under $p = 1\,\mu$M the position of the fixed point corresponds to $y \approx 0.5$ (nearly half of channels has IP$_3$ bound). The excitable trajectory is possible only for the nullcline at $y < 0.6$ and with a further decrease in IP$_3$ no excitations are observed (the position of blue nullcline tends to $y = 1$). **(c)** The bistable behaviour for $p = 10\,\mu$M and $N = 9$ channels similar to the one described in previous chapters.

The main details of the model presented later in this section are:

1. We compare the existence of the threshold for both $d_{5\ \mathrm{single}}^{\mathrm{IP}}$ and $d_{5\ \mathrm{coup}}^{\mathrm{IP}}$ (illustrated later in Figure 7.9).

2. We incorporate the linear dependence of $[\mathrm{Ca}^{2+}]$ on the fraction of activated channels $c = c_0 + \alpha N a$ as taking for $d_{5\ \mathrm{coup}}^{\mathrm{IP}}$ is enough for observing the excitability threshold (no introduction of non-linearity needed in $c(a)$ unlike in the previous chapters).

3. Also, an additional level of freedom in the model corresponding to $y$ dynamics in Equation (7.18) gives us the puff trajectories for decreasing $[\mathrm{IP}_3]$ with the transition to the non-excitable regime for $p \to 0$ and as the consequence $y \to 1$ (shown later in Figure 7.8 (b)) corresponding to all channels occupying lower DYK plane.

The position of the blue nullcline in Figure 7.8 (b) for $p = 1\,\mu$M is at $y \approx 0.5$ allows puff trajectories. The excitable trajectories are observed only if the $y$-nullcline is at $y < 0.6$ (the green nullcline intersects the blue one). With a further decrease in IP$_3$ $y \to 1$ there are no puffs observed.

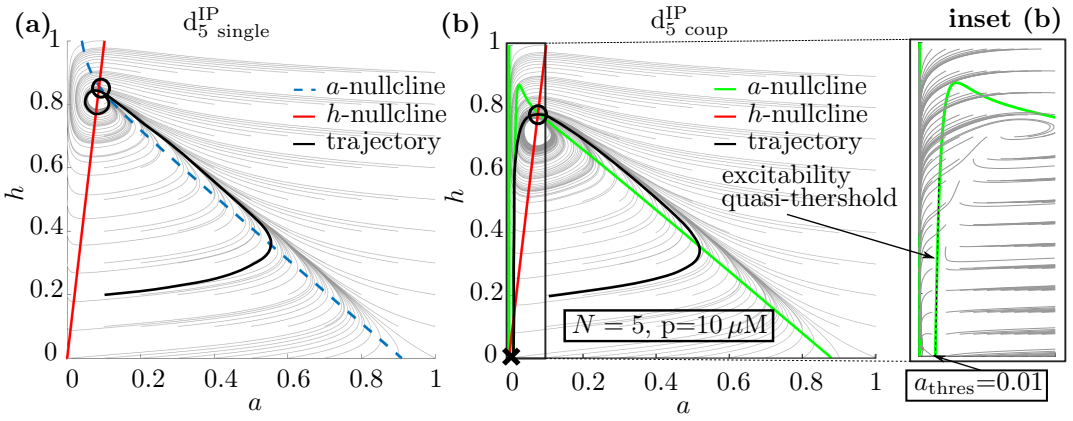


FIGURE 7.9: Projection of the nullclines onto $(a, h)$ phase space for $y = 0$ shown with the typical trajectories (*black lines*) and streamlines (*grey lines*). **(a)** In a cluster with $N = 5$ under $p = 10\,\mu$M considering $d_5 = d_{5\ \mathrm{single}}^{\mathrm{IP}}$ there is only one fixed point (*black open circle*) and no excitability threshold. **(b)** For $d_5 = d_{5\ \mathrm{coup}}^{\mathrm{IP}}$ the lower stable fixed point (*black cross*) occurs as well as excitability quasi-threshold (shown in the inset).

The main finding of the current model is that the bell-shaped curve incorporating $d_{5\ \mathrm{coup}}^{\mathrm{IP}}$ exhibits a much steeper increase of the open probability curve for low $[Ca^{2+}]$ (Figure 7.6 (b)) while for high $[Ca^{2+}]$ the difference between the two cases is negligible (which is consistent with the measurements by Taufiq-Ur-Rahman et al. [2009] for $[Ca^{2+}] = 1\,\mu$M). Note that this is different from a fit of the data for a single-channel (Figure 7.6 (a)). This effect appears to play a crucial role in the dynamics of a cluster within our cluster-based framework when we determine whether $Ca^{2+}$ puffs are generated, or not. Specifically, $Ca^{2+}$ puffs, shown as *black line* in Figure 7.9 (b), are explained by the existence of a threshold for excitability for $d_5$ set to $d_{5\ \mathrm{coup}}^{\mathrm{IP}}$ (as shown in the inset in Figure 7.9 (b) for the $a$-nullcline). The inability of, the model to generate puffs for $d_5$ set to $d_{5\ \mathrm{single}}^{\mathrm{IP}}$ is due to the lack of a stable fixed point at the origin and the non-existence of a threshold, as seen from the *blue dashed* $a$-nullcline in Figure 7.9 (a). These two regimes characterise the two modes of IP$_3$R signalling – single channels which are silent and coupled clusters generating signals. Such a distinction was first reported in the experiment by Smith et al. [2014] and will be discussed further in conclusion.

In the earlier model by Rüdiger [2014a], the linear dependence of $[Ca^{2+}]$ on the active fraction of clusters led to non-separable excitations that could not be interpreted as distinct puffs (excitable trajectories) because of the absence of a threshold shown in Figure 7.8 (a) and the inset (b). This issue was resolved by introducing an "artificial" non-linearity in the $c(Na)$ dependence described by Equation (2.87). In our case, incorporating the rates obtained from the measurements of the coupled channels is an alternative to the effect of non-linearity. This suggests that the reduction of the open probability in clustered channels and the existence of an excitable threshold are related mechanisms.

### 7.2.3 Characterisation of the transient dynamics

A cluster-based model is a unique tool allowing us to interpret various observed phenomena in phase space. It provides us with useful insights about the following

- how various puff morphologies (smooth, stepwise, square and re-openings according to Wiltgen et al. [2014])) are interpreted in $(a, h)$ phase space.
- the puff statistics, e. g. distributions of puff durations and IPIs;
- how numbers of channels in clusters and [IP$_3$] affect durations of puffs and IPIs;

In Chapter 6, we introduced the inclusion of the multiplicative noise in Equations (7.16)–(7.18) which leads to the Langevin model as follows

$$\begin{aligned}
\frac{\mathrm{d}a}{\mathrm{d}t} &= f(a,h,c) + A\Big(\sqrt{k_a^+(c)c(1-a-h-y)} + \sqrt{k_a^- a} + \sqrt{k_1(c)h} \\
&+ \sqrt{k_i^+ ca}\Big)\,\mathrm{d}W, \qquad (7.20)\\
\frac{\mathrm{d}h}{\mathrm{d}t} &= g(a,h,c) + A\Big(\sqrt{k_i^+(c)c(1-a-h-y)} + \sqrt{k_1(c)h} + \sqrt{k_2(c)h} \\
&+ \sqrt{k_i^+ ca}\Big)\,\mathrm{d}W, \qquad (7.21)\\
\frac{\mathrm{d}y}{\mathrm{d}t} &= C^{\mathrm{down}}(c)(1-y) - C_{\mathrm{ch}}^{\mathrm{up}}(c,p)y + A\Big(\sqrt{C^{\mathrm{down}}(c)(1-y)} \\
&+ \sqrt{C_{\mathrm{ch}}^{\mathrm{up}}(c,p)y}\Big)\,\mathrm{d}W, \qquad (7.22)
\end{aligned}$$

where $f(a,h,c)$ and $g(a,h,c)$ are right hand sides of Equations (7.16) and (7.17) and $c = c_0 + \alpha N a$. The amplitude of the noise term is $A = \frac{1}{4\sqrt{N}}$ according to Equation (6.11). All other parameters are given in Table 7.2 (coupled case) or defined in the earlier models.

We confirm the validity of the fitting we have performed within the steady-state approach. We calculate the open probability from the Langevin model by generating solutions by integration and then calculating the fraction of time when a cluster is open (the total durations of release events greater than $[Ca^{2+}] = 0.1\,\mu$M which approximately corresponds to the threshold value)

$$P_{\mathrm{o}}^N = \sum_{i=1}^{n} \frac{T_i}{T}, \qquad (7.23)$$

where $T_i$, $i = \overline{1,n}$ are durations of individual release events and $n$ is the total number of release events taking place at the cluster over $T = 1000$ s. The open probabilities calculated from our model shown in Figure 7.10 for $N_{\mathrm{tot}} = 3$ (*dark-green asterisks*), 4 (*blue crosses*) and 5 (*black diamonds*) The number of activatable channels is recalculated from the dynamics of the fraction of channels in a cluster occupying the lower ([IP$_3$]-unbound) plane of the DYK cube as

$$N = N_{\mathrm{tot}}(1-y) \qquad (7.24)$$

where the calculations for $N_{\mathrm{tot}} = 3$ were repeated 5 times to show the deviation between the data points which displays the effect of the noise term in the open probability calculation. In Chapters 2 – 4 the total number of channels $N_{\mathrm{tot}}$ was always equivalent the to number of activatable channels $N$ because of $y = 0$. Imposing variability in $y$ makes the distinction between $N$ and $N_{\mathrm{tot}}$ a necessary step. However, all previous analysis same as the derivation of the simplified model is made in terms of $N = N_{\mathrm{tot}}$ which was constant. In general, the calculated data from our stochastic model shown in Figure 7.10 is consistent with the experimental measurements. There are discrepancies between the points due to the inaccuracies in the method to calculate the

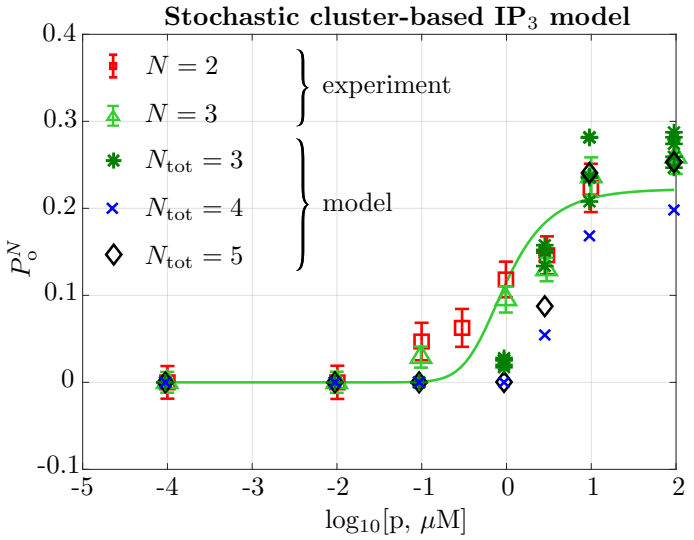


FIGURE 7.10: The open probability calculated from Langevin model using Equation (7.23) for $N_{\text{tot}} = 3$ (over 5 traces marked by *dark-green asterisks*), 4 (*blue crosses*) and 5 (*black diamonds*), the number of activatable channels in a cluster is given by Equation (7.24).

open probabilities from the simulations. We choose the threshold $[Ca^{2+}]$= 0.1 $\mu$M to distinguish the occurrence of a release event as suggested in the literature [Rüdiger, 2014b]. However, there is ambiguity in choosing this threshold which may lead to a bias.

There is also mismatch between the simulations and experiments for $N_{\text{tot}} = 2$ where we obtain too few excitations. We think that this is due to the restriction of the Langevin approach to a large number of members in the system. If the number of channels is small we get the negative values of variables from the Langevin which are discarded by the algorithm.

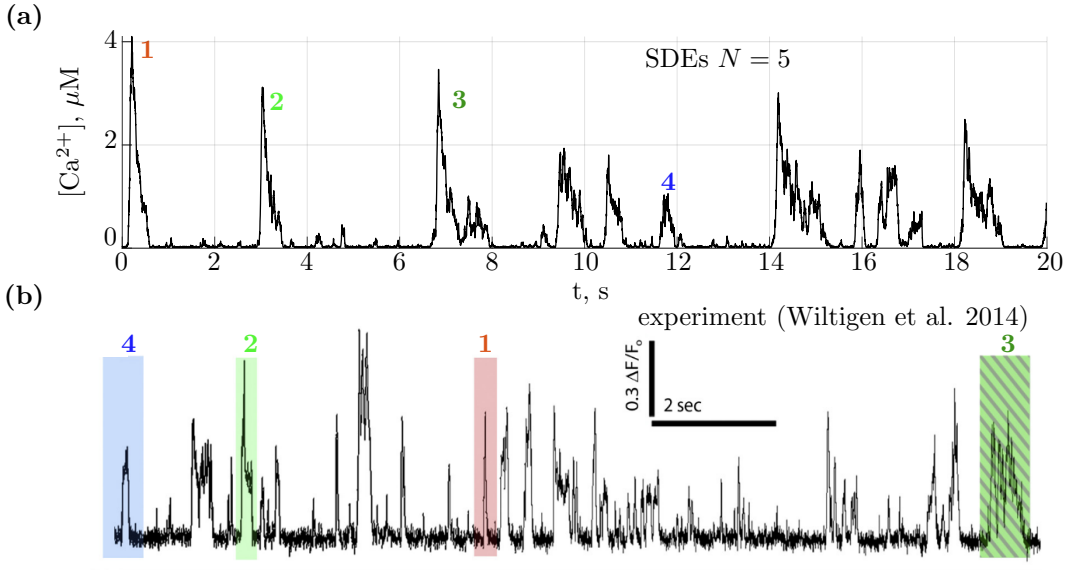


FIGURE 7.11: $[Ca^{2+}]$ traces obtained from the Langevin model (under $[IP_3] = 10\,\mu$M) incorporating clustering effects for a cluster of IP$_3$R with 5 channels **(a)** in comparison with the experimental results **(b)** by Wiltgen et al. [2014].

Figure 7.11 (a) shows $[Ca^{2+}]$ trace for larger cluster containing $N_{tot} = N = 7$ channels (here the number of activatable channels equals to the total number of channels due to high $[IP_3] = 10\,\mu M$ and therefore $y = 0$). The numbered puffs in the trace correspond to 4 distinct puff types:

1. smoothly decaying puffs (*red*),
2. stepwise decaying puffs (*light green*),
3. re-openings (*dark green*),
4. square puffs (*blue*).

The colours and numbers in Figure 7.11 (a) show the corresponding event types observed experimentally by Wiltgen et al. [2014] (Figure 7.11 (b)). Please note the timescales in both figures are similar.

To discuss the mechanisms governing various puff initiations and terminations, and, also, a possible failure of termination, we refer to the phase space $(a, h)$. Recalling that $a$ is the fraction of channels in a cluster in the active state and $h$ – in the inhibited state, the remaining channels are in the rest state $z = 1 - a - h$. The nullclines are as shown in Figure 7.8 (a). In Figure 7.12 the behaviour of corresponding modelled puffs in Figure 7.11 (a) is highlighted.

1. Smoothly decaying puffs (*red*) are ordinary puff trajectories originating near the lower fixed point $(0, 0)$ and terminating close to the origin.
2. Stepwise puffs (*light green*) are initiated close to the origin and perform multiple "walks" away from the a-nullcline as they approach to the point where the fraction of inhibited channels is the highest.
3. Re-openings (*dark green*) caused by multiple re-entering the trajectory close to the highest inhibition.
4. Square puffs (*blue*) start with high $h$ and resemble "walks" around the higher fixed point.

Wiltgen et al. [2014] connect the existence of prolonged square puffs (up to 15 s) with the phenomenon of puff termination failure, which might be toxic to a cell. In the phase space dynamics, this phenomenon can be linked to the trajectory continuously "walking" around the upper fixed point. This is further indicated by the high density of grey streamlines in Figure 7.9 (b) in the deterministic case. The duration of such events in $IP_3R$ clusters is determined by the tails of the exponential distributions as seen from Figure 7.13. In large clusters which contain more than 15 activatable channels, these events may become up to 8 s long (see Figure 7.13 (c)). This behaviour may be associated with the transition of the deterministic system to the bistable state (Figure 7.8 (c)). Our model displays the tendency of the increase in the maximal durations of events (Figure 7.13 *top*) and the decrease in the IPIs (Figure 7.13 *bottom*) with $N$.

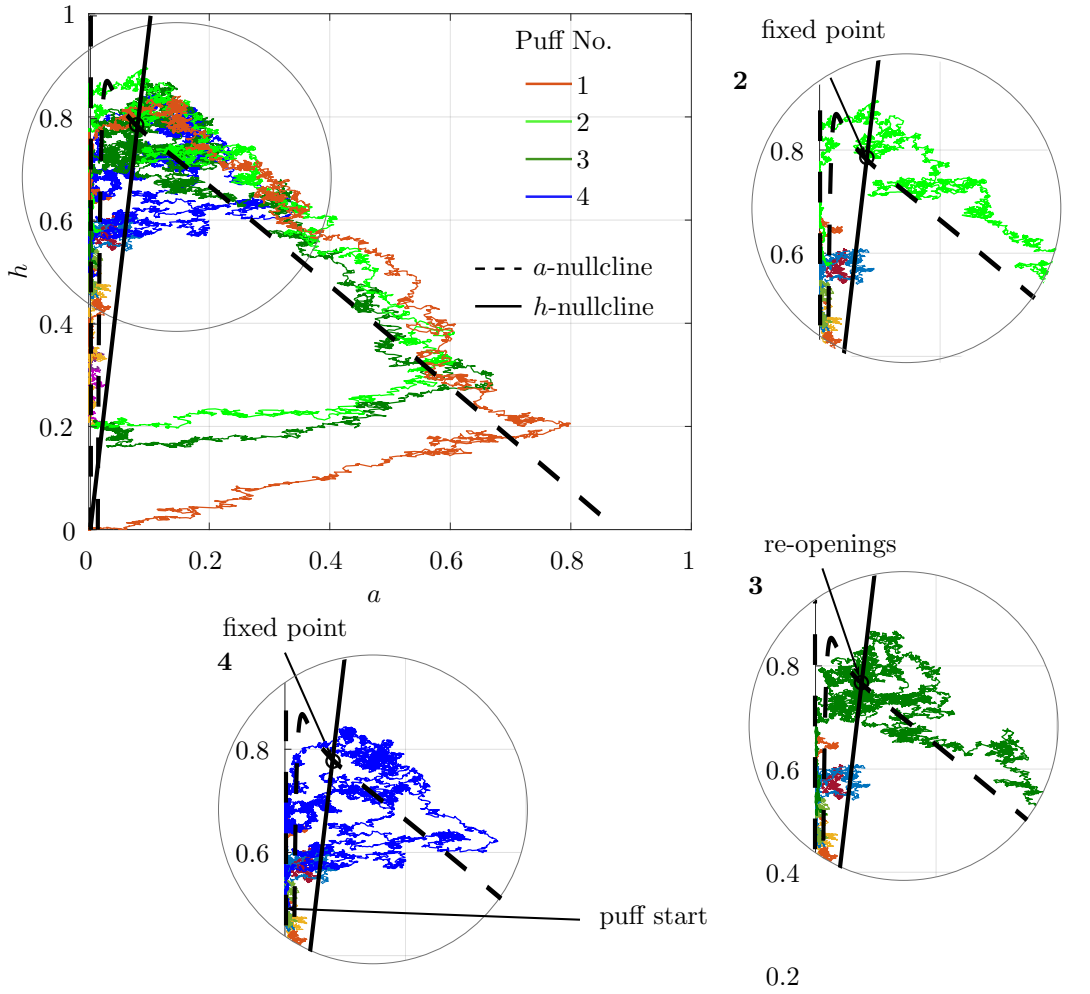


FIGURE 7.12: The trajectories of 5 puffs in $(a, h)$ phase plane displaying the dynamics of the cluster the numbers correspond to puffs shown in Figure 7.11.

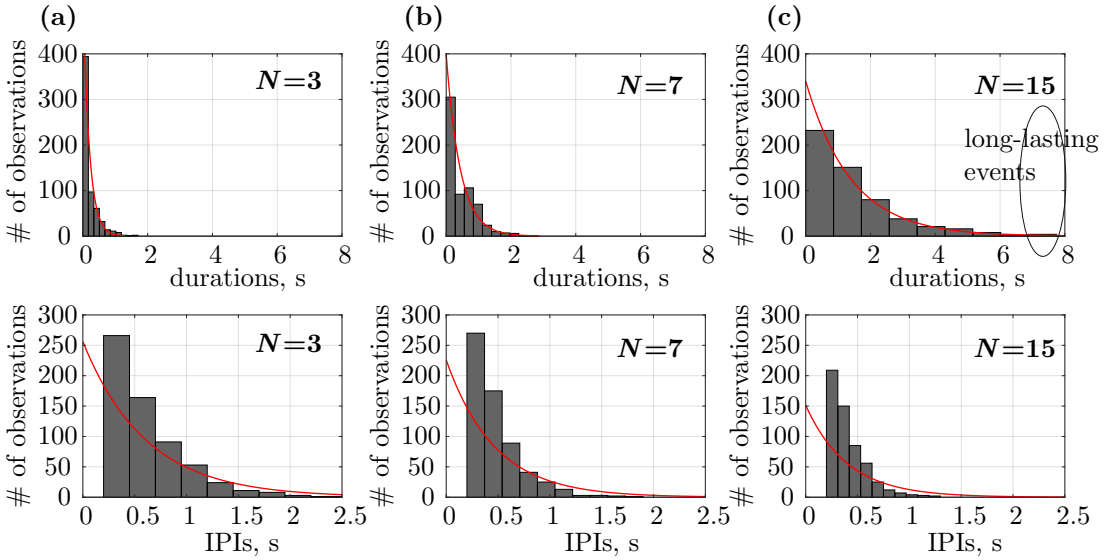


FIGURE 7.13: Durations and IPIs of $Ca^{2+}$ puffs for increasing $N$ in IP$_3$R clusters under [IP$_3$] $= 10\,\mu$M.

## 7.3 Conclusions

The novel approach of modelling DT40 cells is presented in this chapter incorporating the effect of clustering on lowering the open probability of a channel. The model suggests a connection between the reduction of the open probability of a channel and the existence of a threshold that is essential for the generation of excitable dynamics. Existence of the excitable dynamics for coupled channels and non-excitability for single channels suggests two separate modes of $Ca^{2+}$ signalling. The two modes of signalling – silent for single channels and responsive for coupled clusters is experimentally observed by Smith et al. [2014].

Our results confirmed the reproducibility of the stationary open probability generated by the cluster-based model. Also, the model gives us useful insight into the stochastic nature of $Ca^{2+}$ puffs being significantly consistent with the puff experiments by Wiltgen et al. [2014]. We use the phase space interpretation to observe the formation of different puff types and explain the formation of long-lasting events observed experimentally [Wiltgen et al., 2014].

# Chapter 8

# Ising Modelling of $IP_3R$ Clusters

When modelling the opening/closing of *coupled* $IP_3R$ channels, in this chapter, we are inspired by an approach frequently used to study the physics of spins of atoms in the magnetic field interacting with each other. The simplest approach to study magnetic interaction between atoms is to account for the two main factors, e.g., the coupling between members and the external field which is the basis of Ising model [Baxter, 1985]. The Ising model is a prominent but simple approach which allows using it in different disciplines, and even in computational biology [Endres, 2013, Maltsev et al., 2017]. As the states (open/closed) of individual channels within each cluster are affected by coupling between respective channels and by external concentrations of ligands, they can be studied using the Ising model. Thus, in this chapter, we exploit an analogy between atoms and channels with the focus on formulating Ising model for a cluster of channels under external concentrations ($[Ca^{2+}]$ and $[IP_3]$).

## 8.1 Open probabilities and connectivities in the Ising $IP_3$ model

The sensitivity analysis of the DYK and cluster-based $IP_3$ models (see Chapter 7) suggests that the $Ca^{2+}$ behaviour in the steady-state is mostly controlled by the single parameter $d_5$ which is responsible for $Ca^{2+}$ dependent activation in DYK model. In the previous chapter, we have also shown that $d_5$ may model the coupling effect in the clusters brought by $[IP_3]$ [Taufiq-Ur-Rahman et al., 2009]. Thus, a coarse-grained approach to $Ca^{2+}$ modelling may be developed.

We start building the model from the simplest case of two coupled $IP_3R$ channels. We introduce the Ising model using the original parameters – $J$ to represent coupling between channels and $h_{\text{ext}}$ to correspond to the external field of the influence of $[IP_3]$ and $[Ca^{2+}]$ on the channel opening. We later explain the physical contexts of $J$ and $h_{\text{ext}}$ in terms of $IP_3R$ channels. Figure 8.1 schematically represents the model for two $IP_3R$ channels. As previously discussed (Section 2.3), the channel is considered open if at least three out of four subunits are active ($\uparrow$). Following are the possible sequences of subunit states that correspond to the open channel: $\{(\uparrow\uparrow\uparrow\uparrow), (\downarrow\uparrow\uparrow\uparrow), (\uparrow\downarrow\uparrow\uparrow), (\uparrow\uparrow\downarrow\uparrow), (\uparrow\uparrow\uparrow\downarrow)\}$. All other combinations correspond to a closed channel. In Figure 8.1, $\sigma_j = 1$ (active) or $\sigma_j = -1$ (inactive) identify the states of each subunit. $S_i = 1$ (open) or $S_i = -1$ (closed) are identified as the states of each channel. Either of the combinations of $\sigma_j$ within the braces labelled with $S_i = 1$ ($S_i = -1$) defines the open (closed) channel. The labels $\sigma_j$

are not further used in the derivations but are discussed here for the sake of clarity. In contrast, $S_i$ is an essential parameter of our model.

It may seem that such definition brings a large bias into the Ising dynamics as the open state of the channel $S_j = 1$ contains only 5 states of subunits ($\sigma_1$, $\sigma_2$, $\sigma_3$, $\sigma_4$). In contrast, the closed one $S_j = -1$ contains $4! - 5 = 19$ states. However, the action of the external field $h_{\text{ext}}$ containing effectively [$Ca^{2+}$] and [$IP_3$] has much larger control over channel dynamics eliminating the possible bias.

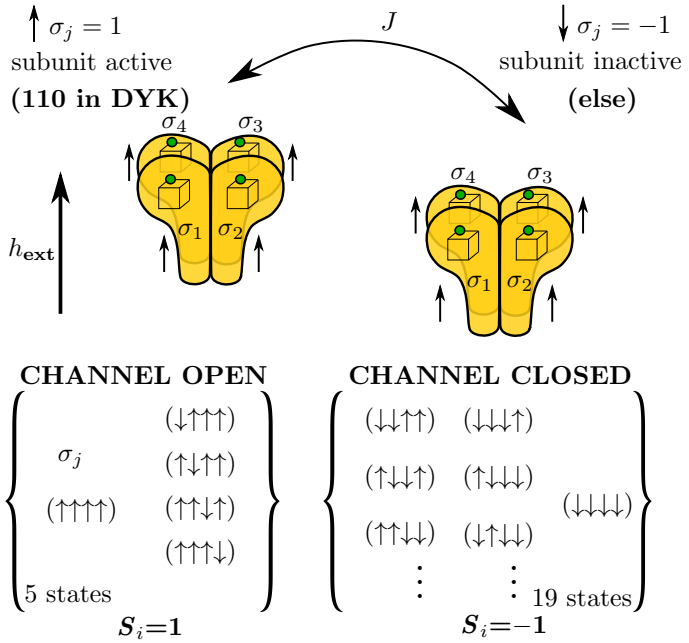


FIGURE 8.1: Ising model for two IP$_3$R channels. Here we show the case when both channels are open. $\sigma_i = \pm 1$ represents states of subunits, $S_i = \pm 1$ represents states of channels. Combination of states of the subunits {(↑↑↑↑),(↓↑↑↑),(↑↓↑↑),(↑↑↓↑),(↑↑↑↓)} correspond to the open channel. All the rest of the combinations form the closed channel state.

From the results of the previous chapter, we conclude that there are limited features of IP$_3$R channels affecting the steady-state open probability in the entire cluster. Firstly, the clustering may affect the open probability in certain cases. Secondly, the external concentrations [$Ca^{2+}$] and [$IP_3$] affect the averaged behaviour of a cluster. Thus, given the huge complexity of the transient dynamics of $Ca^{2+}$ signalling, the steady-state behaviour of a cluster seems to be driven by a few features. In the simplest two-parameter representation for $N$ channels in a cluster, the Hamiltonian of the system using Ising formulation is

$$H(\{S_i\}) = -J \sum_{\langle i,j \rangle} S_i S_j - h_{\text{ext}} \sum_{i=1}^{N} S_i, \tag{8.1}$$

where $\{S_i\}$ is the whole set of the states of channels in a cluster, $\langle i, j \rangle$ represents the sum over the nearest neighbours. Here we perform the analysis using the nearest neighbours approximation. However, further in the chapter, we will work with the various assumptions of the connectivity in a cluster. The coupling strength $J$ effectively accommodates all the changes in the open-probability brought by clustering. The external field $h_{\text{ext}}$ contains the effect of external concentrations of $Ca^{2+}$ and $IP_3$, leading to opening/closing of channels.

Using canonical ensemble representation, one can calculate the probabilities of the different states of a cluster as

$$P(\{S_i\}) = \frac{1}{Z} \mathrm{e}^{\beta H(\{S_i\})}, \tag{8.2}$$

where $Z = \sum_{\{S_i\}} \exp(-\beta H(\{S_i\}))$ is the partition function, $\beta = \frac{1}{k_{\mathrm{B}} T}$ in the standard thermodynamic representation.

For $N = 2$, the Hamiltonians for all combinations of system realisations are obtained from Equation (8.1)

$$H(\pm, \pm) = -J \mp 2h_{\mathrm{ext}}, \tag{8.3}$$

$$H(\pm, \mp) = J, \tag{8.4}$$

the partition function in this case is

$$Z = \mathrm{e}^{-\beta H(+1,+1)} + \mathrm{e}^{-\beta H(+1,-1)} + \mathrm{e}^{-\beta H(-1,+1)} + \mathrm{e}^{-\beta H(-1,-1)} = 2\mathrm{e}^{\tilde{J}} \left( \cosh 2\tilde{h} + \mathrm{e}^{-2\tilde{J}} \right), \tag{8.5}$$

where $\tilde{J} = \beta J$ and $\tilde{h} = \beta h_{\mathrm{ext}}$.

The probabilities, in this case, are as follows

$$P(\pm 1, \pm 1) = \frac{e^{\pm 2\tilde{h}}}{2\left( \cosh 2\tilde{h} + e^{-2\tilde{J}} \right)}, \tag{8.6}$$

$$P(\pm 1, \mp 1) = \frac{1}{2\left( e^{2\tilde{J}} \cosh 2\tilde{h} + 1 \right)}, \tag{8.7}$$

where the coupling strength $\tilde{J}$ and external parameter $\tilde{h}$ are intrinsic characteristics of the $IP_3R$ clusters (scaled by a constant $\beta$). Later in this chapter, we discuss how to extract those characteristics from the open probability data [Taufiq-Ur-Rahman et al., 2009] for clustered $IP_3R$ channels.

Consider the connectivities between $IP_3R$ channels in the Ising model. Although there are several works in the literature [Mak and Foskett, 1997, Taufiq-Ur-Rahman et al., 2009] pointing to the evidence that $IP_3R$ channels are densely packed in clusters, the actual topology of the connections between the channels is mostly unknown. The existing modelling approaches consider all-to-all connectivity in the clusters [Thurley and Falcke, 2011, Thurley et al., 2011, 2012]. In our model, we start with all-to-all connectivity assumption and then adopt various other cases (circle, chain, see Appendix B) as we seek to understand the effect of different configurations of connectivity on the open probability of a single cluster.

A scheme of all-to-all connectivity between channels in a cluster of $N = 3$ and $N = 4$ channels is depicted in Figure 8.2. Here, $N$ is the total number of channels in a cluster, $0 \leq n \leq N$ is the number of open channels in the given state of a cluster. Each cluster state can be defined by several equally probable realisations. For example, consider a cluster within the rectangle in Figure 8.2. It has $N = 3$ channels and a single channel ($n = 1$) may be open. We label the open channels with *black circles* and the closed channels with *white circles*. The open probability of a cluster is independent of which particular channel is open (black) – only the number $n$ of open channels matters. Thus, there are three equally probable realisations of having a single

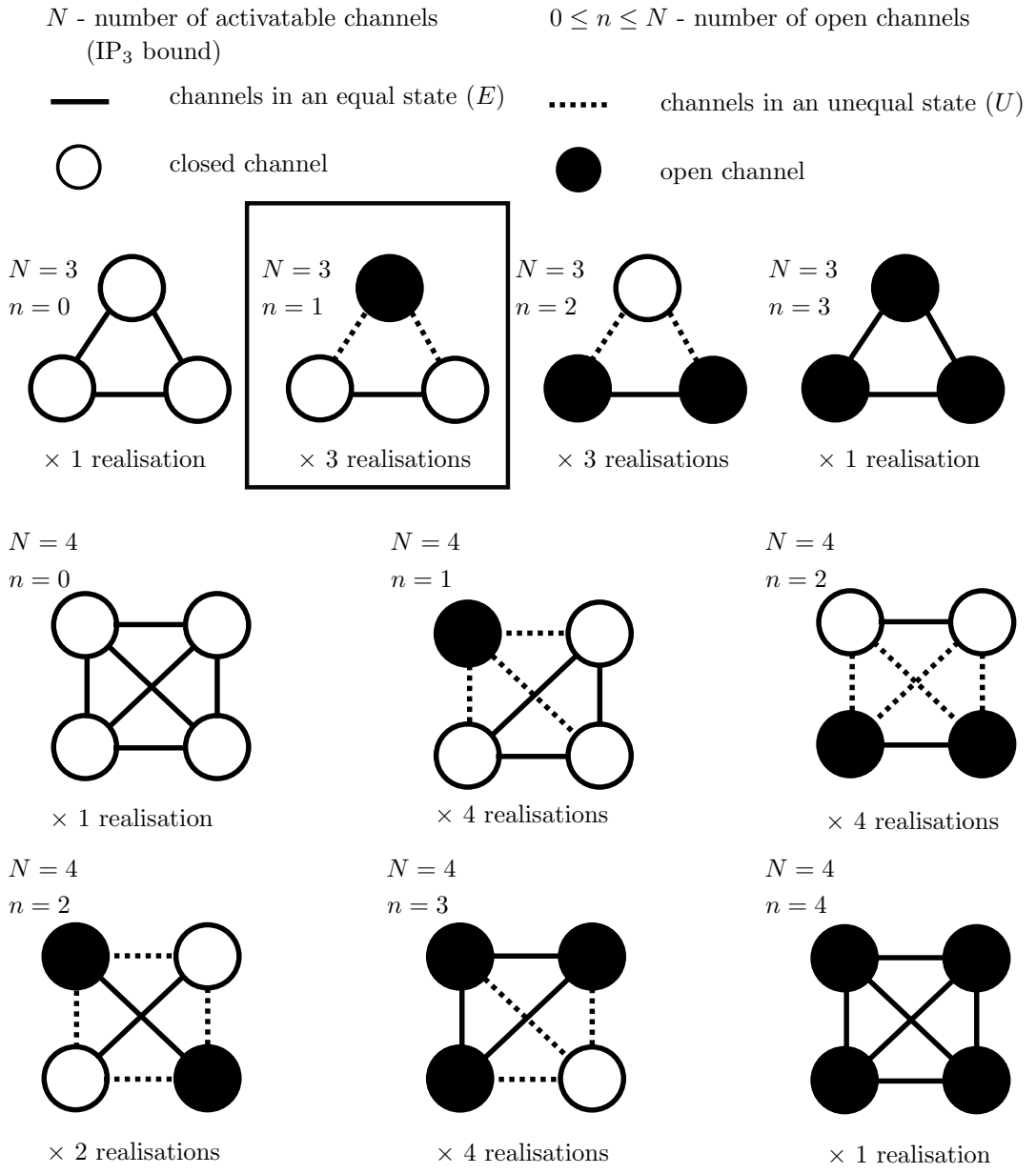


FIGURE 8.2: The connections between channels in clusters with $N = 3$ and $N = 4$. *White circles* correspond to closed channels and the *black circles* to the open ones. The connections between the channels in equal states are marked by *solid lines* and unequal ones by *dashed lines*.

channel open out of three. We introduce two types of connections between channels. The connections labelled with dashed lines are between channels in opposite states (open/closed) – unequal connections, while connections between channels in the same states are indicated with solid lines – equal connections. The number of equal (unequal) connections is $E$ ($U$). The total number of pairs of channels (connections) $\frac{N(N-1)}{2}$ is calculated using the binomial coefficient.

Proceed to study the generic open probability of $n$ channels out of $N$ in a cluster. Following Equation (8.1) and Equation (8.2) we get:

$$P_N^n = \frac{N!}{n!(N-n)!} \frac{\mathrm{e}^{\tilde{J}[(+1)E+(-1)U]+\tilde{h}[(+1)n+(-1)(N-n)]}}{Z}, \tag{8.8}$$

where $N-n$ is a number of closed channels, the factor is the binomial coefficient for choosing $n$ (number of realisations) out of $N$ channels, $Z$ is a partition function which includes contributions from all realisations of the system ($n \in \overline{0,N}$)

$$Z = \sum_{n=0}^{N} \frac{N!}{n!(N-n)!} \mathrm{e}^{\tilde{J}(E-U)+\tilde{h}(2n-N)}. \tag{8.9}$$

Generalising the cases shown in Figure 8.2 for arbitrary $n$ out of $N$, we write the number of equal connections

$$E = \frac{1}{2}n(n-1) + \frac{1}{2}(N-n)(N-n-1), \tag{8.10}$$

where $\frac{n(n-1)}{2}$ is the number of pairs of open channels and $\frac{(N-n)(N-n-1)}{2}$ is the number of pairs of closed ones. At the same time, the number of unequal connections is the total number of pairs subtract $E$:

$$U = \frac{N(N-1)}{2} - E = \frac{1}{2}[N(N-1) - n(n-1) - (N-n)(N-n-1)]. \tag{8.11}$$

We shall define and use the open probability of a cluster containing $N$ channels. In probabilistic theory, the expectation value of discrete variable $A$ is defined as

$$\langle A \rangle = \sum_{i} A_i P(A), \tag{8.12}$$

where $A_i$ characterises actual system states and $P(A)$ is a probability function of $A$. The average number of channel openings, scaled by $N$ to retain the probability between 0 and 1, is

$$P_{\mathrm{o}}^{N} = \frac{1}{N} \sum_{n=1}^{N} n P_N^n, \tag{8.13}$$

where $P_N^n$ is given by Equation (8.8).

Equation (8.13) is used for the definition of $\tilde{J}$ and $\tilde{h}$ by matching the calculated open probabilities to those experimentally found [Taufiq-Ur-Rahman et al., 2009]. This helps us to get an insight into the dependence of these parameters on $N$, [$IP_3$] and even different connectivities between the channels in clusters.

## 8.2 Calculation of Ising model parameters from the open probability data

In the previous section, we have derived the expression for the steady-state probability in the cluster containing $N$ channels. However, the role of the governing parameters $\tilde{J}$ and $\tilde{h}$ of the Ising-like approach in the $IP_3$ model remains unclear. Therefore, we fit the open probability data for a cluster with $1-5$ channels [Taufiq-Ur-Rahman et al., 2009] and determine the parameters. There are two types of open probability data available: [$IP_3$] dependent data ($P_{\mathrm{o}}^{N}$) in the range $0-100\,\mu$M for a cluster with $1-3$ channels (Figure 7.1) and the scaled probability data for

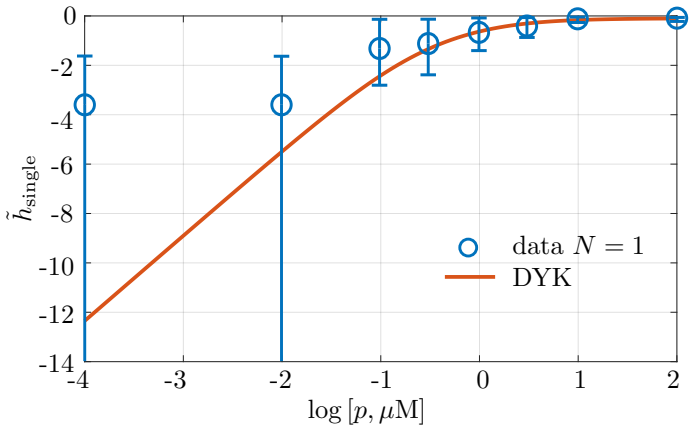


FIGURE 8.3: The dependence of the external field parameter $\tilde{h}_{\text{single}}$ as a function of $p = [\text{IP}_3]$ for single cluster obtained from the single-channel data with corresponding error bars (*blue circles*), from the DYK fit in Figure 7.1 (*red curve* obtained from Equation (8.15)).

fixed $[\text{IP}_3] = 10\,\mu\text{M}$ ($NP_{\text{o}}^N$) in case of clusters containing $1-5$ channels (Figure 8.7 (a)). We start with the $[\text{IP}_3]$ dependent data for a regime of fixed $[\text{Ca}^{2+}] = 0.2\,\mu\text{M}$ which shows that the open probability for a single cluster is roughly two times the open probability of the clustered channels. We suggest that there are two qualitatively different regimes of IP$_3$R activation – coupled and uncoupled (single channel), where coupled regime implies that the channels reduce their open probability via coupling, while the single-channel regime implies that a channel is not in a cluster. From the perspective of Ising framework, we may think of the uncoupled activation as that characterised by $\tilde{J} = 0$ while the coupled activation is characterised by $\tilde{J} \neq 0$.

Blue data points in Figure 7.1 are measured open probabilities ($P_{\text{open}}$) of a single channel plotted against $[\text{IP}_3]$ which are mapped to the blue points in Figure 8.3 according to the following logic. Here we assume a specific case of a cluster consisting of a single channel ($N = 1$). We substitute $\tilde{J} = 0$ (no coupling case) and $N = 1$ into the expression for the open probability of a cluster derived from the Ising model and given by Equation (8.13) and obtain

$$P_{\text{o}}^1 = \frac{\mathrm{e}^{\tilde{h}}}{\mathrm{e}^{\tilde{h}} + \mathrm{e}^{-\tilde{h}}} = \frac{1}{1 + \mathrm{e}^{-2\tilde{h}}}, \tag{8.14}$$

where $\tilde{h}$ is the external field. At the same time, the open probability for a cluster with a single channel predicted by the Ising model ($P_{\text{o}}^1$) should be equal to the measured open probability of a single cluster $P_{\text{open}}$. Equating the two, we express the strength of the external field $\tilde{h}$ in terms of the measured open probability $P_{\text{open}}$ as

$$\tilde{h}_{\text{single}} = -\frac{1}{2} \ln \frac{1 - P_{\text{open}}}{P_{\text{open}}}. \tag{8.15}$$

In such a way, the blue points in Figure 8.3 correspond to the strengths of the external field in Ising model for each measured open probability ($P_{\text{open}}$) plotted as a function of $[\text{IP}_3]$ for a specific cluster with a single channel. The error bars in $\tilde{h}$ correspond to the errors in measurements of $P_{\text{open}}$ via Equation (8.15). Finally, the red curve in Figure 8.3 is obtained when the DYK fit of the measured $P_{\text{open}}$ (solid blue curve in Figure 7.1) is plugged into Equation (8.15) instead of $P_{\text{open}}$.

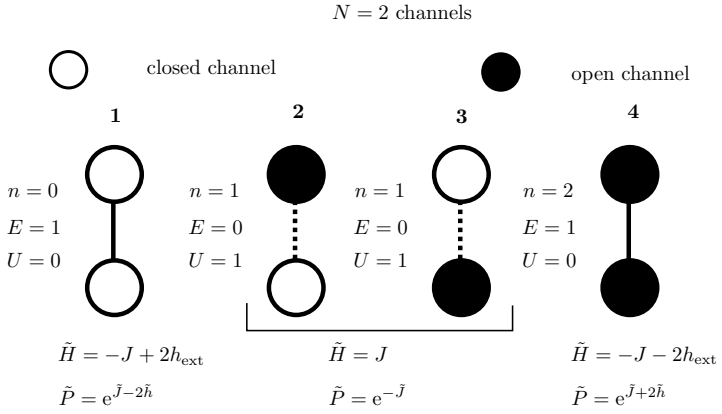


FIGURE 8.4: Different openings of $n$ channels in $IP_3R$ cluster with the total number $N = 2$. *White circles* correspond to closed channels and the *black circles* to the open ones. There are $E$ connections between the channels in equal states (*solid lines*) and $U$ between the unequal ones (*dashed lines*). $\tilde{H}$ and $\tilde{P}$ stand for the contribution of given configuration into Hamiltonian $H$ and open probability $P_{\text{o}}^2$.

Note, that there is a range of $[IP_3]$ ($[IP_3] \leq 10^{-2}\,\mu$M) for which the error bars in Figure 8.3 appear to be large. In fact, the lowest uncertainty bounds tend to $-\infty$ as can be seen from Equation (8.15) as this uncertain region corresponds to $P_{\text{open}} \to 0$. Identification of $\tilde{h}$ within such a region is impractical due to high uncertainty, hence, we will not take it further. Nevertheless, we managed to identify $\tilde{h}$ for a wide range of $[IP_3]$ values.

Let us derive both $\tilde{h}$ and $\tilde{J}$ (for coupled channels $\tilde{J} \neq 0$) for the case of the experimentally measured open probabilities in a cluster with $N = 2$ and $N = 3$ channels shown with red and green dots respectively along with the associated DYK fits in Figure 7.1. Since we now have two parameters to identify, we need two equations. The logic for the further derivation is accompanied by a schematic diagram in Figure 8.4. A cluster with $N = 2$ channels has four possible states. *State 1* is characterised by both channels being closed which implies one equal connection (closed–closed) $E = 1$, no unequal connections $U = 0$ and is shown by two linked white circles in Figure 8.4. In this case, the contribution to Hamiltonian (see Equation (8.1)) is $\tilde{H} = -J + 2h_{\text{ext}}$ and the contribution to open probability (see Equation (8.2)) is $\tilde{P} = \mathrm{e}^{\tilde{J}-2\tilde{h}}$. *State 2* and *State 3* are similar and characterised by one channel being open (black circle) while anther one – closed (white circle) which implies one unequal connection $U = 1$ and no equal connections $E = 0$. The contribution to the Hamiltonian is thus $\tilde{H} = J$ and the contribution to the probability $\tilde{P} = \mathrm{e}^{-\tilde{J}}$. Finally, *State 4* is characterised by both channels being open, a single equal connection $E = 1$ and no unequal connections $U = 0$. Here, the contribution to Hamiltonian is $\tilde{H} = -J - 2h_{\text{ext}}$ and the contribution to the probability is $\tilde{P} = \mathrm{e}^{\tilde{J}+2\tilde{h}}$.

Taking the contributions from each of the four states to Hamiltonian and probability and substituting them into Equation (8.13), we obtain an expression for the open probability of a cluster with two channels

$$P_{\text{o}}^2 = \frac{1}{2}\frac{\mathrm{e}^{-\tilde{J}} + 2\mathrm{e}^{\tilde{J}+2\tilde{h}}}{\mathrm{e}^{\tilde{J}-2\tilde{h}} + 2\mathrm{e}^{-\tilde{J}} + \mathrm{e}^{\tilde{J}+2\tilde{h}}}. \tag{8.16}$$

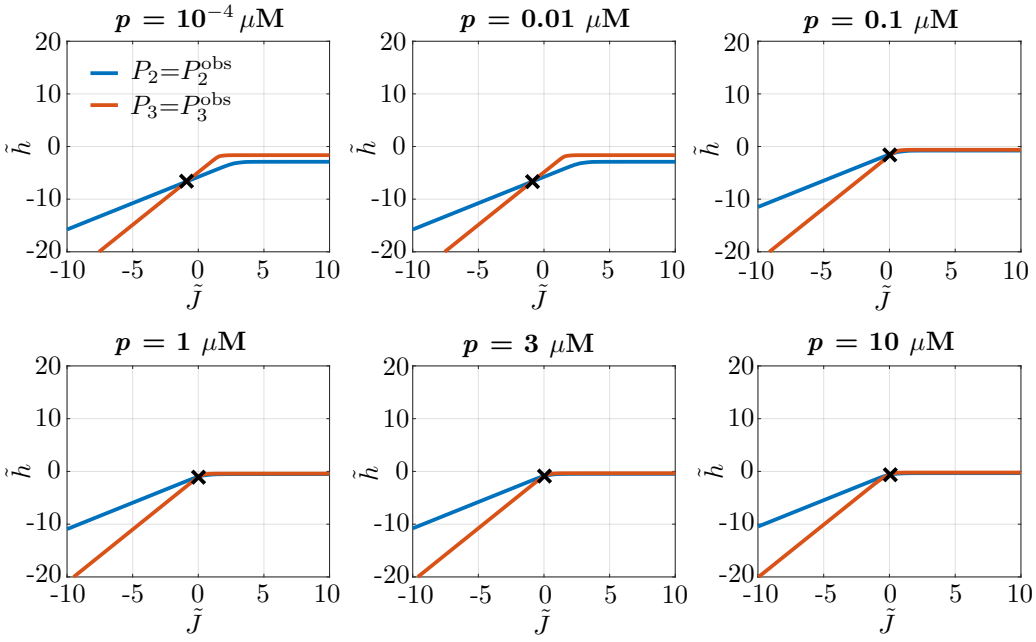


FIGURE 8.5: The values of coupling coefficient $\tilde{J}$ and external parameter $\tilde{h}$ calculated from the Ising probabilities for 2 (*blue curve* obtained from Equation (8.16)) and 3 (*red curve* obtained from Equation (8.17)) channels under $[Ca^{2+}] = 0.2\,\mu$M (Figure 7.1).

Following the same logic and considering Figure 8.2 for $N = 3$, we derive the expression for the open probability of a cluster with three channels

$$P_o^3 = \frac{e^{-\tilde{J}-\tilde{h}} + 2e^{-\tilde{J}+\tilde{h}} + e^{3\tilde{J}+3\tilde{h}}}{e^{-\tilde{J}-3\tilde{h}} + 3e^{-\tilde{J}-\tilde{h}} + 3e^{-\tilde{J}+\tilde{h}} + e^{3\tilde{J}+3\tilde{h}}}. \tag{8.17}$$

Having defined the open probabilities of a cluster with two ($P_o^2$) and three ($P_o^3$) channels using Ising model, we will equate those probabilities to the measured open probabilities $P_{open}$ for $N = 2$ and $N = 3$ respectively. Therefore, we can write a system of equations

$$P_o^2 = P_2^{obs}, \tag{8.18}$$
$$P_o^3 = P_3^{obs}, \tag{8.19}$$

in terms of $\tilde{J}$ and $\tilde{h}$. We solve the first equation numerically for several [IP$_3$] values and plot the solutions as blue curves on $\tilde{h}$–$\tilde{J}$ planes as shown in Figure 8.5. Then, we solve the second equation for the same [IP$_3$] values and plot its solutions as red curves on the same planes. Since experimental data suggests that the open probabilities should be equal for $N = 2$ and $N = 3$, the intersection of the red and the blue curves on each subplot in Figure 8.5 gives us a unique combination of parameters of Ising model, for which this is the case. We extract the identified pairs of $\tilde{h}$ and $\tilde{J}$ and plot them versus [IP$_3$] in Figure 8.6 where blue dots correspond to $\tilde{J}$ and red dots correspond to $\tilde{h}$.

From Figure 8.6 we observe that $\tilde{J}$ impacts the open probability of the cluster much less compared to $\tilde{h}$ as $\tilde{J}$ is near zero for the whole [IP$_3$] range. Note, the dependence of $\tilde{h}$ on [IP$_3$] for a single-cluster case shown in Figure 8.3 is different from the one obtained for $N > 1$ case in Figure 8.6. Thus, we can conclude that the parameter $\tilde{h}$ contains the effects of $\tilde{J}$ on a cluster effectively

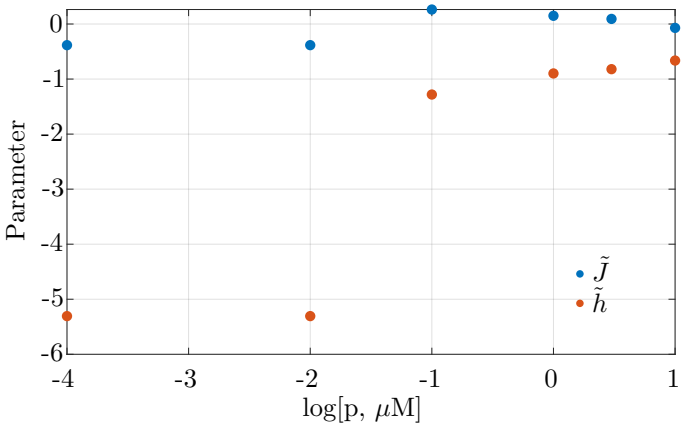


FIGURE 8.6: The values of coupling coefficient $\tilde{J}$ (*blue markers*) and external parameter $\tilde{h}$ (*red markers*) calculated from the Ising probabilities in Equations (8.18), (8.19).

leading to mean-field dynamics. We present the derivation of the mean-field approach and argue about its application in our case in the next sections.

To build stronger evidence for the observed effect, we perform a more detailed analysis of the different experimental data [Taufiq-Ur-Rahman et al., 2009] obtained for clusters with various numbers of channels $N \in \{2, .., 5\}$. The data is plotted in Figure 8.7 (a) for the constant values

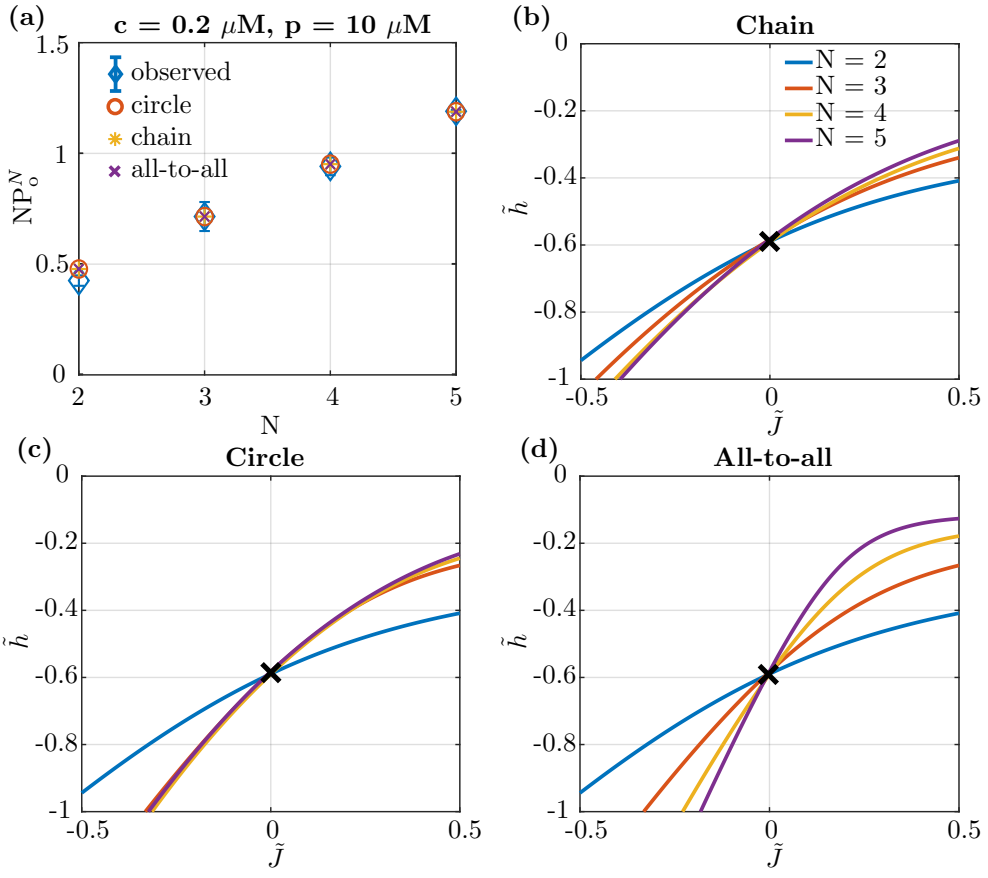


FIGURE 8.7: The $\tilde{J}$ and $\tilde{h}$ derived from the data by Taufiq-Ur-Rahman et al. [2009] for various cluster sizes under $[Ca^{2+}] = 0.2\,\mu M$, $[IP_3] = 10\,\mu M$ and calculated from the Ising probabilities in Equation (B.4).

of $[Ca^{2+}] = 0.2\,\mu$M and $[IP_3] = 10\,\mu$M with the blue dots with error bars.

We also want to understand the effect of the different topologies of connectivity between the channels. Therefore, we plug the experimental data points into the numerical routine of calculating the Ising parameters for clusters with $N \leq 5$ (a separate approach given by Equation (B.4) based on corresponding adjacency matrices in Appendix B). The computed points appear to perfectly coincide with the experimental data suggesting that the topology of connectivity between the channels may not affect the open probability of a cluster (see Figure 8.7).

We follow the same approach as in the case of $N = 1, 2, 3$ channels, but now for $N = 2, 3, 4, 5$ and assuming $[IP_3] = 10\,\mu$M to be fixed. Figure 8.7 (b)–(d) contains curves that correspond to the predicted open probability being equal to the experimentally measured one for $N = 2$ (blue), $N = 3$ (red), $N = 4$ (orange) and $N = 5$ channels for various topologies. As the experimental data suggests that open probability is independent of $N$, we find $\tilde{h}$ and $\tilde{J}$ values on $\tilde{h}$–$\tilde{J}$ planes in Figure 8.7 (b)-(d) that correspond to this case. For all topologies, we obtain $\tilde{J} \approx 0$ and $\tilde{h} \approx -0.66$ which are consistent with results in Figure 8.6 at $[IP_3] = 10\,\mu$M and independent on the connectivities of the channels in a cluster.

Therefore, we conclude that based on the experimental observations, the channels appear to open or close in a mean-field manner, which, effectively is characterised by the effective field created by coupled channels $\tilde{J}$. It also becomes apparent that the topology of channel connectivity does not affect the probability of channels to be opened or closed. These conclusions are aligned with the notion of mean-field behaviour in the Ising-like model. Therefore, it is natural to reduce our approach using mean-field and then to study cluster dynamics under this assumption.

## 8.3 The mean-field behaviour in IP$_3$R clusters

We introduce a single variable $m$ to characterise the state of $N$ channels in a cluster in an averaged sense

$$m = \sum_{i=1}^{N} S_i P(S_i), \tag{8.20}$$

where $P(S_i)$ is the probability of the state $S_i$ calculated from the Ising model.

We have defined $S_i = \pm 1$ as one of the two possible states of a channel. If we use the equivalent choice of the variables, $\tilde{S}_i = 0$ if the channel is closed and $\tilde{S}_i = 1$ if it is open, the mean-field variable $m$ represents the fraction of open channels in a cluster $a$ as only $\tilde{S}_i = 1$ contribute to the sum in (8.20). The transition from the variable $m$ changing in the range $-1 \leq m \leq 1$ to $a$ ranging $0 \leq a \leq 1$ may be performed by a simple shift of the coordinates and rescaling the range of the variable $m = (a + 1)/2$.

The main assumption standing behind the mean-field theory is the independence of the system of the fluctuations $\delta S_i = S_i - m$. In the mean-field approximation, the Hamiltonian of the system Equation (8.1) is

$$
\begin{aligned}
H &= -J \sum_{\langle i,j \rangle} (m + (S_i - m))(m + (S_j - m)) - h_{\text{ext}} \sum_i S_i \\
&= -J \sum_{\langle i,j \rangle} \Big( m^2 + m(S_i - m) + m(S_j - m) + \delta S_i \delta S_j \Big) - h_{\text{ext}} \sum_i S_i,
\end{aligned} \tag{8.21}
$$

where in the mean-field approximation $\delta S_i \delta S_j \ll 1$, so the last summand in $\langle i,j \rangle$ in negligibly small and

$$
\begin{aligned}
H &\approx -J \sum_{\langle i,j \rangle} (m^2 + m(S_i - m) + m(S_j - m) - h_{\text{ext}} \sum_i S_i = \\
&= -J \sum_{\langle i,j \rangle} (-m^2 + m(S_i + S_j)) - h_{\text{ext}} \sum_i S_i = \\
&= Jm^2 \sum_{\langle i,j \rangle} 1 - Jm \sum_{\langle i,j \rangle} (S_i + S_j) - h_{\text{ext}} \sum_i S_i.
\end{aligned} \tag{8.22}
$$

To simplify this expression we substitute the sum over pairs $\langle i,j \rangle$ by the number of bonds at each given site $z$ (coordination number) as each bond appears only once in the sum, it gives the multiplier of $z/2$, then

$$
H = Jm^2 N \frac{z}{2} - Jmz \sum_i S_i - h_{\text{ext}} \sum S_i = Jm^2 N \frac{z}{2} - (Jmz + h_{\text{ext}}) \sum_i S_i, \tag{8.23}
$$

where the factor in the power of exponent $(Jmz + h_{\text{ext}})$ serves as a new effective field containing the contributions from the coupling between the channels.

Then the partition functions as in Equation (8.2) is

$$
Z = \sum_{\{S_i\}} \mathrm{e}^{-\beta H} = \mathrm{e}^{-\tilde{J} m^2 N \frac{z}{2}} \sum_{\{S_i\}} \mathrm{e}^{h_{\text{eff}} \sum_i S_i}, \tag{8.24}
$$

where $h_{\text{eff}} = \tilde{J} z m + \tilde{h}$. Given that $\{S_i\}$ are the combinations of all states in the cluster, the pairs $S_i = 1$ and $S_i = -1$ in the sum leading to pairs of exponents $\mathrm{e}^{h_{\text{eff}}} + \mathrm{e}^{-h_{\text{eff}}} = 2 \cosh h_{\text{eff}}$. The resulting partition function is

$$
Z = \mathrm{e}^{-\tilde{J} m^2 N \frac{z}{2}} \left( 2 \cosh h_{\text{eff}} \right)^N. \tag{8.25}
$$

The free energy in the canonical ensemble is

$$
F = -\frac{1}{\beta} \ln Z = NJm^2 \frac{z}{2} - \frac{N}{\beta} \ln \left( 2 \cosh h_{\text{eff}} \right). \tag{8.26}
$$

From the minimum of free energy

$$
0 = \frac{\partial F}{\partial m} = NJzm - NJz \tanh h_{\text{eff}} \tag{8.27}
$$

we obtain the equation from which the mean-field variable is defined

$$
m = \tanh \left( \tilde{J} m z + \tilde{h} \right), \tag{8.28}
$$

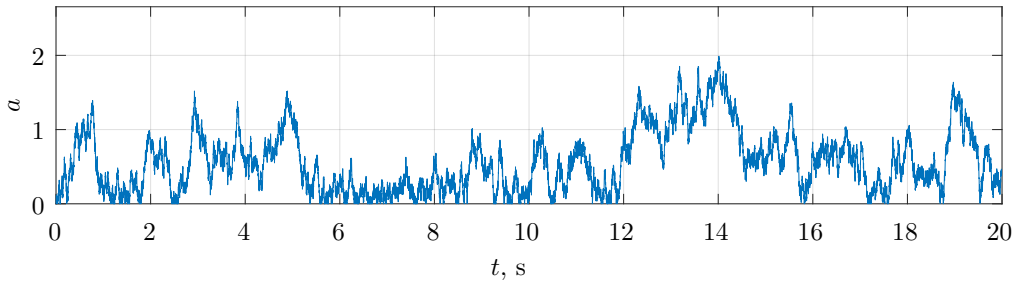


FIGURE 8.8: The simulations of a fraction of open channels in a cluster $a$ for the Langevin model in the Ising mean-field approximation with $\tilde{h} = -0.66$, $\tilde{J} = 0$.

where $\tilde{J} = \beta J$ and $\tilde{h} = \beta h_{\text{ext}}$. This expression is well known in magnetism as it leads to the occurrence of magnetisation when the external field $h_{\text{ext}}$ is non-zero. In the context of the IP$_3$ Ising model, the variable $m$ is the averaged state of a cluster combined of a collection of open or closed states describing the steady-state open probability of a cluster.

From the general perspective, we can bring the findings from the cluster-based three-state model (Chapter 7) to a two-state (open or closed) Ising model in a mean-field approximation. Several kinds of models with two states where proposed in the literature (e.g. Li and Rinzel [1994]), however, reduced models are capable to capture only limited kinds of phenomena due to their simplicity. More complex approaches must be developed in order to capture the diverse dynamics of $Ca^{2+}$. We build our reasoning on the findings from the previous detailed modelling. We incorporate the findings into the simplest two-state model to study the dynamics of a mean-field variable fluctuating around the steady-state value:

$$\frac{\mathrm{d}m}{\mathrm{d}t} = \tanh\left(\tilde{J}mz + \tilde{h}\right) - m + A\,\mathrm{d}W, \tag{8.29}$$

where $\mathrm{d}W$ is a Wiener noise and with amplitude $A$. The result of the Langevin simulations is presented in Figure 8.8. The Langevin model shows the threshold dependence of the dynamics on the amplitude of the noise. When the amplitude is small we obtain almost no excitations and when it is large we get a noisy trajectory. In the figure, we use $\tilde{h} = -0.66$ and $\tilde{J} = 0$ as found in Figure 8.6 under $p = 10\,\mu$M and Figure 8.7, respectively.

The Langevin approach appears to be incapable of capturing the real dynamics of the fraction of open channels as the variable $a$ changes in much larger range ($0 \leq a \leq 2$ instead of $0 \leq a \leq 1$) and the releases are too frequent. Thus, our 2-state (open or closed) Ising model results in the one-variable equation Equation (8.29). In the future, we aim to apply Glauber or Kawaski dynamics to the one variable model to explore if the discrete dynamics is capable of giving extra features to the model. Or we will develop an extended approach incorporating inhibition of a cluster to capture the behaviour of in more detail.

## 8.4 Conclusions

Ising model allows us to develop a conceptual understanding of a single cluster. We introduce coupling – a collective term that aggregates the effects of the multitude of complex processes governing the interaction between individual channels and external field – a collective term for

the effects of external $[Ca^{2+}]$ and $[IP_3]$. Therefore, we can study the interaction between all these effects at the abstract level.

The open probability data [Taufiq-Ur-Rahman et al., 2009] suggests the independence of the open probability of a cluster from the number of channels when cluster contains two channels or more. We fit a single cluster data (blue circles in Figure 7.7) with Ising model using Equation (8.15). Since $\tilde{J} = 0$ for a single channel, only $\tilde{h}_{\text{single}}$ is obtained from the fit. At the same time, when fitting data for $N = 2, 3$ channels (Figure 8.5), we obtain $\tilde{J}$ close to zero and $\tilde{h} \neq \tilde{h}_{\text{single}}$. Since $\tilde{h}$ must be the same as $\tilde{h}_{\text{single}}$, the inequality between the two suggests that $\tilde{h}$ consists of $\tilde{h}_{\text{single}}$ plus an extra component. This component corresponds to $\tilde{J}ms$ from the mean-field Equation (8.23). In contrast, decoupling gives $\tilde{J} = 0$ and $\tilde{h} = \tilde{h}_{\text{single}}$. The mean-field theory is derived using the assumption that the fluctuations of the states of channels have little effect on each other, and the cluster with many channels have a similar probability as the one with few channels.

Furthermore, the external field parameter represents the effect opposite to $[IP_3]$, i.e., large negative external field damps the ability of channels to open. In addition to that, we report (see Figure 8.6) that $\tilde{h}$ depends on $[IP_3]$ in a switch-like manner meaning that a threshold in $[IP_3]$ exists. Below the threshold $[IP_3]$, channels are almost always closed (large negative external field) while immediately above the threshold $[IP_3]$, the channels tend to be open (near-zero external field). In future, the refined stochastic model may be developed to capture the mean-field behaviour of a cluster.

# Chapter 9

# Conclusions and Future Work

$Ca^{2+}$ signalling within a cell is an extremely complex multi-scale spatio-temporal process emerging from the collective participation of numerous players such as $Ca^{2+}$ channels, various ligands, pumps, etc., and is far from being completely understood. In this study, we carried out a multi-scale modelling of $Ca^{2+}$ releases from $IP_3R$ channels for several cell types through the lens of the reduction of the detailed dynamics. We bridge the gap between the events on drastically different temporal and length scales and come to the reaction-diffusion system to predict $Ca^{2+}$ concentrations within deterministic and stochastic frameworks as depicted in Figure 9.1. In contrast to other modelling approaches, thanks to the conception of coarse-graining, we view $Ca^{2+}$ releases from the clusters of $IP_3R$ channels as non-linear dynamical systems spatially coupled with diffusion. Simplifying the functioning of each subunit, we came up with a profound conceptualization of the underlying dynamics of $Ca^{2+}$ releases at different levels of an organisation, spanning 3 orders of magnitude in space and two in time. A high-level diagram of the key studies undertaken here on the respective levels of the hierarchy of organisation is presented in Figure 9.1. The thick blue dotted curve schematically shows how our modelling has bridged the gap between the scales.

At a single channel scale, the conformational changes of subunits may occur spontaneously or under a stimulus leading to the opening of the channel and $Ca^{2+}$ release called a $Ca^{2+}$ blip. Many approaches to studying $Ca^{2+}$ release events rely on a detailed modelling of the dynamics of each subunit in a channel with the 8 states connected by transitions, as represented by DYK cube. This allows us to look at larger-scale events – $Ca^{2+}$ puffs as a collection of $Ca^{2+}$ blips. As such approaches are associated with extremely high computational complexity (complete transition lattice with thousands of variables), in Chapter 3 we applied the heuristic reduction of the behaviour of subunits by replacing slow/fast transition rates within the so-called DYK cube with the effective parameters (see 3-state triangle [Rüdiger, 2014a] in Figure 9.1). The adopted simplifications allowed us to formulate a two-variable non-linear system which we studied as a dynamical system. Then, we identified fixed points in the phase space around which the dynamical behaviour of the cluster is wrapped. Using these points as markers and studying bifurcations induced by the changes in physiological parameters (cluster parameters, external $Ca^{2+}$, etc.), we were able to observe and interpret a multitude of different $Ca^{2+}$ release events. In particular, we discovered a stable limit cycle orbits in a single cluster dynamics – $Ca^{2+}$ oscillations (see phase portrait in Figure 9.1). Oscillatory $Ca^{2+}$ releases from clusters are particularly remarkable in *Xenopus* oocytes in a way that these cells use them as means of regulating various protein cascades to activate the fertilized eggs [Kline and Kline, 1992].

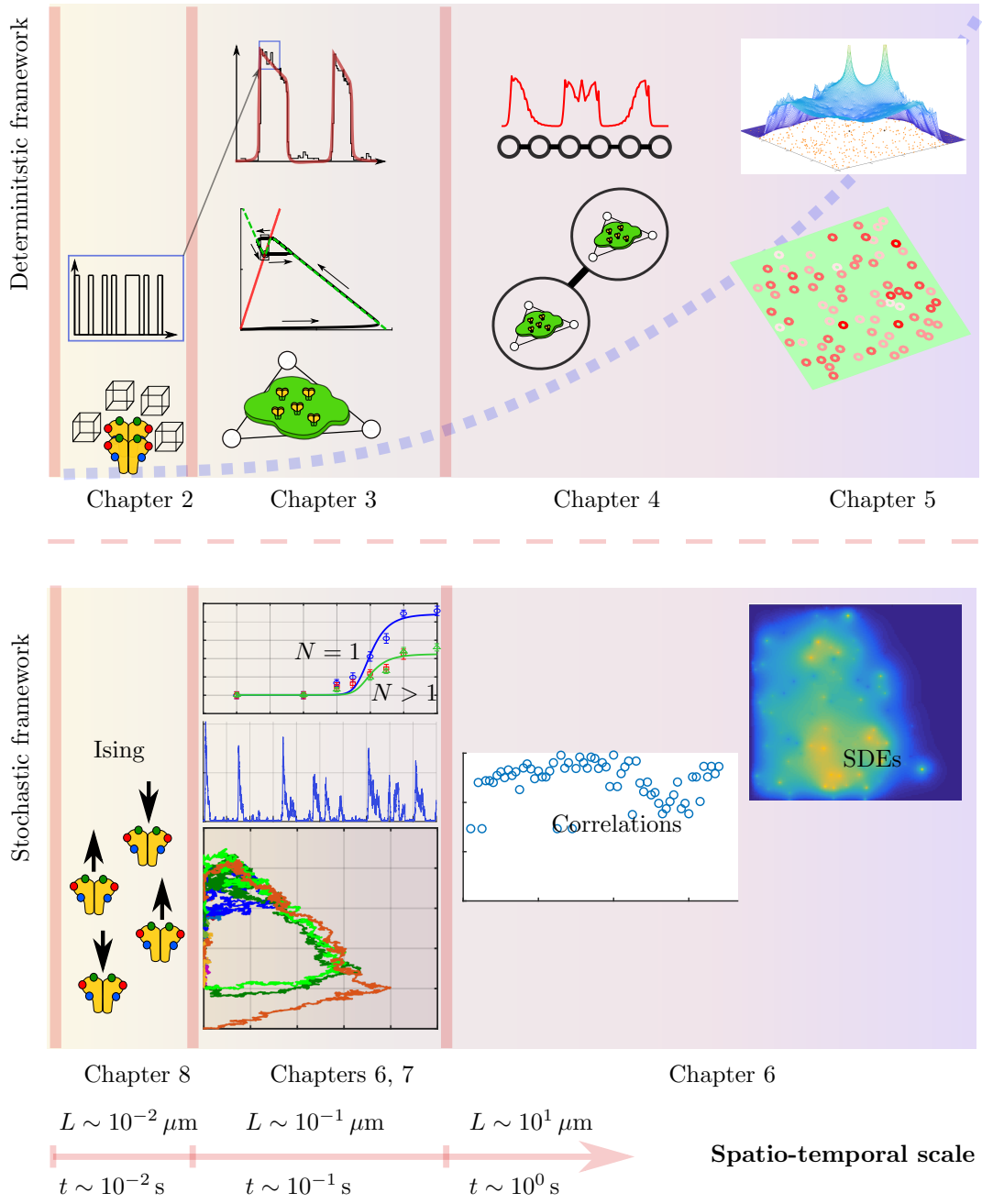


FIGURE 9.1: The map of the main findings of the thesis corresponding to respective chapters.

Oscillations from a cluster appear to be the simplest way of ensuring periodic release events (which are required to encode signals) in contrast to random puffs.

Taking inspiration from the oscillatory regime in a single cluster, in Chapter 4 we investigate whether similar behaviour persists in the case of two coupled clusters. The coupling was introduced via a diffusion term in the previously formulated system of non-linear reaction-diffusion system. Having applied a similar dynamical systems analysis, we report that oscillations occur both at the level of a single cluster and at the level of a group of multiple clusters. Furthermore, we see that the clusters cooperate to create conditions (external $[Ca^{2+}]$) under which oscillations may appear in subsequent clusters and thus travel along the membrane from one cluster to another such as shown in Figure 9.1.

Following the same idea, in Chapter 5 we study $Ca^{2+}$ oscillations from clusters randomly distributed in an idealised 2D-membrane using a reaction-diffusion system (see Figure 9.1). Chapter 4 and Chapter 5 present studies at the highest level of the spatial ($L \sim 10^1\,\mu$m) and temporal ($t \sim 10^0$) s hierarchy. Consider the scheme of the deterministic framework in Figure 9.1. By bridging the gap between the scales using a coarse-graining approach and applying dynamical systems analysis, we can effectively describe global scale events such as oscillations and even travelling $Ca^{2+}$ waves in terms of the dynamics of the events happening at much smaller scales.

In Chapter 6, we extended the deterministic framework to account for spontaneous conformational changes in subunits to study the behaviour of clusters of $IP_3R$ channels on the membrane in a setting close to real-life conditions. These changes are incorporated into our reaction-diffusion model using the Langevin approach leading to Stochastic Differential Equations (SDEs) within the stochastic framework as shown in Figure 9.1. In this setting, we were able to simulate long traces of $Ca^{2+}$ puffs from each cluster and calculate the inter-puff intervals (IPIs). IPIs are one of the key experimentally measurable characteristics of a cluster, hence, we validated the proposed stochastic modelling framework against detailed constitutionally expensive simulations [Rückl et al., 2015]. Furthermore, we studied how the synchronic releases from neighbouring clusters depend on the level of $[IP_3]$ or, in other words, how correlated the releases from neighbouring clusters are in time depending on $[IP_3]$. We observe that the switch-like change in behaviour. For $[IP_3] < 0.05\,\mu$M, clusters appear to be largely uncorrelated and the large scale propagating events, in this case, are very rare. However, as $[IP_3] > 0.05\,\mu$M, the clusters suddenly start synchronising their activity to facilitate the occurrence and propagation of the large scale events. In this case, oscillation and waves are likely to occur. In future, we aim to explore the transition from local to global behaviour by analysing emergent phenomena in $IP_3R$ clusters with a focus of calculating the critical exponents of the correlations between clusters to understand self-organisation in these complex dynamical systems.

In Chapter 7, we fitted open probability data [Taufiq-Ur-Rahman et al., 2009] for a single channel, and clusters with $N = 2$ and $N = 3$ channels with the cluster-based thee-state model. Comparing the fits, we observed that the open probabilities for a single channel and clusters of channels differ by up to two times in case of $[Ca^{2+}] = 0.2\,\mu$M. This indicates that in a big time span a single channel can be open up to two times longer than a cluster of channels for the same $[Ca^{2+}]$ and $[IP_3]$ while the difference in open probabilities between the clusters with $N = 2$ and $N = 3$ channels is negligible. Therefore, we see that there are $[IP_3]$ and $[Ca^{2+}]$ for which the rate of $Ca^{2+}$ dissociation from the channel ($d_5$) depends neither on $[IP_3]$ nor on $[Ca^{2+}]$ and is defined only by whether the channel is single or a part of a cluster. Clusters are shown to have two times larger dissociation rates compared to the individual channels. At first glance, this seems like a disadvantage for $Ca^{2+}$ releases, since smaller open probability may result in less $[Ca^{2+}]$ being released. However, in reality, clusters release more $Ca^{2+}$ than individual channels despite their open probability being smaller which is measured by Taufiq-Ur-Rahman et al. [2009]. We have suggested an explanation for such a decrease. We mapped the dynamic behaviour of a cluster to a phase space for various dissociation constants. We report that an excitable trajectory is absent for smaller dissociation rates characterised by slow $Ca^{2+}$ unbinding ($b_5 = d_5 a_5$) or fast $Ca^{2+}$ biding ($a_5$) in the single-channel case. On the other hand, an excitable trajectory resulting in puffs is present for larger dissociation rates in clustered channels. Therefore, we suggest that clusters may regulate dissociation rates to facilitate puffs.

In Chapter 7, we also used the insight from dynamical systems to explain four different characters of puffs also observed experimentally [Wiltgen et al., 2014]. Finally, we explain recently reported long-lasting release events Wiltgen et al. [2014] by the possible presence of an attracting fixed point for clusters with many activatable channels ($N > 9$). In future work, we plan to also apply the deterministic dynamical system analysis to the case of long-lasting release events to develop a more profound understanding of their dynamics.

Chapter 8 is inspired by the realisation that despite the multiplicity of parameters that affect the transient behaviour of a cluster, only a few of them play a role in the steady-state open probability. We identified that just three parameters, e.g., the coupling between the channels and external $[Ca^{2+}]$ and $[IP_3]$ have the defining contribution. Thus, we constructed an Ising-like model of channels considering the only coupling between them and the effect of $[Ca^{2+}]$ and $[IP_3]$ together as an external field. We fitted the experimental data [Taufiq-Ur-Rahman et al., 2009] with the Ising-like model and showed that the coupling between the channels is captured by the effective external field and the fluctuations or cluster state are very small. Therefore, it is reasonable to assume that channels interact within a cluster in a mean-field manner. We have attempted developing a mean-field Ising model incorporating Langevin dynamics and the reduced one-dimensional phase-space trajectory but faced challenges possibly associated with the reduced flexibility of the model. As part of the future work, we plan to attempt Glauber or Kawasaki [Li, 2011] dynamics instead of the continuous Langevin dynamics to allow our model some extra degree of flexibility.

# Appendix A

# Sensitivity analysis of the DYK and cluster-based $IP_3$ dependent model

---

The eigenvalues sorted by the magnitude and corresponding eigenvectors obtained from the principal component analysis in Section 7.1 are

$$\lambda_1 = 3.56 \times 10^2, V_1 = (1.64 \times 10^{-2}, -2.12 \times 10^{-5}, 5.26 \times 10^{-5}, 1); \tag{A.1}$$

$$\lambda_2 = 8.29, V_2 = (1, -2.32 \times 10^{-4}, 3.21 \times 10^{-3}, 1.64 \times 10^{-2}); \tag{A.2}$$

$$\lambda_3 = 1.45 \times 10^{-5}, V_3 = (3.21 \times 10^{-3}, 1.21 \times 10^{-3}, -1, -1.54 \times 10^{-7}); \tag{A.3}$$

$$\lambda_4 = 5.76 \times 10^{-8}, V_4 = (-2.29 \times 10^{-4}, -1, -1.21 \times 10^{-3}, -1.74 \times 10^{-5}). \tag{A.4}$$

The sensitivity of the DYK model is based on the analysis of the Hessian in given by Equation (7.14). Here we present the quantitative evidence of the $d_5$ prevalence in the model. At the point of best fit ($d_1$, $d_2$, $d_3$, $d_5$) = ($d_1^{\mathrm{D}}$, $d_2^{\mathrm{D}}$, $d_3^{\mathrm{D}}$, $d_5^{\mathrm{D}}$) (see Table 7.1)

$$H|_{\boldsymbol{\theta}^*=\boldsymbol{\theta}_{\mathrm{D}}} = \begin{pmatrix} 0.51 & -9.02 \times 10^{-5} & 1.33 \times 10^{-3} & 3.33 \\ -9.02 \times 10^{-5} & 1 \times 10^{-3} & -1.95 \times 10^{-7} & -9.22 \times 10^{-4} \\ 1.33 \times 10^{-3} & -1.95 \times 10^{-7} & 1. \times 10^{-3} & 8.74 \times 10^{-3} \\ 3.33 & -9.22 \times 10^{-4} & 8.74 \times 10^{-3} & 50.24 \end{pmatrix}, \tag{A.5}$$

where the largest components in the last row represent the most significant influence of $d_5$ on the model sensitivity. Also, the elements in the first row that correspond to $d_1$ are several orders of magnitude larger than the ones corresponding to $d_2$ and $d_3$.

The eigenvalues and eigenvectors of the Hessian given by Equation (A.5) are

$$\lambda_1^H = 0.29, V_1^H = (-0.1, 10^{-4}, -3 \times 10^{-3}, 0.067); \tag{A.6}$$

$$\lambda_2^H = 10^{-3}, V_2^H = (2 \times 10^{-3}, 0.73, -0.68, 8.5 \times 10^{-6}); \tag{A.7}$$

$$\lambda_3^H = 10^{-3}, V_3^H = (10^{-3}, -0.68, -0.73, -8 \times 10^{-6}); \tag{A.8}$$

$$\lambda_4^H = 50.47, V_4^H = (0.067, -10^{-5}, 10^{-4}, 0.1). \tag{A.9}$$

In case of the cluster-based $IP_3$ dependent model (7.16)–(7.18) the detailed expression for the steady-sate open probability simplified from Equation (7.19) is

$$P_{\text{open}}^{\text{IP}} = \frac{48c^3d_2p^4(c+d_2)^3}{A_1(c,d_5)\Big(A_2(p,d_3)+A_3(c,p,d_2,d_3)+A_4(c,p,d_1,d_2,d_3)\Big)}, \tag{A.10}$$

where

$$\begin{aligned}
A_1(c,d_5) &= 12c^3+6c^2d_5+4cd_5^2+d_5^3 && \text{(A.11)}\\
A_2(p,d_3) &= c^4\left(d_3^4+4d_3^3p+6d_3^2p^2+4d_3p^3+4p^4\right) && \text{(A.12)}\\
A_3(c,p,d_2,d_3) &= 4c^3d_2p\left(d_3^3+3d_3^2p+3d_3p^2+4p^3\right)+6c^2d_2^2p^2\left(d_3^2+2d_3p+4p^2\right) && \text{(A.13)}\\
A_4(c,p,d_1,d_2,d_3) &= 4d_1^3d_2^3(c(d_3+p)+d_2p)+6d_1^2d_2^2(c(d_3+p)+d_2p)^2+4d_1d_2(c(d_3+p)+d_2p)^3\\
&+ 4cd_2^3p^3(d_3+4p)+d_1^4d_2^4+4d_2^4p^4 && \text{(A.14)}
\end{aligned}$$

the Hessian evaluated at the best fit points corresponding to a case of a single channel (presented in Table 7.2) is

$$H|_{\mathbf{d}=\mathbf{d}^{\mathbf{IP}}{}_{\mathbf{single}}} = \begin{pmatrix} 0.58 & -2.95\times10^{-3} & 0.02 & 3.17\\ -2.95\times10^{-3} & 0.01 & -2.81\times10^{-3} & -0.01\\ 0.02 & -2.81\times10^{-3} & 0.02 & 0.04\\ 3.17 & -0.01 & 0.04 & 37.89 \end{pmatrix}. \tag{A.15}$$

The corresponding eigenvalues and the eigenvectors are

$$\begin{aligned}
&\lambda_1^H = 38.16, V_1^H = (0.08, -3\times10^{-4}, 0.001, 1), && \text{(A.16)}\\
&\lambda_2^H = 0.31, V_1^H = (-1, 0.008, -0.06, 0.08), && \text{(A.17)}\\
&\lambda_3^H = 0.02, V_1^H = (-0.06, -0.28, 0.96, 0.004), && \text{(A.18)}\\
&\lambda_4^H = 0.01, V_1^H = (0.009, -1, -0.28, -7\times10^{-4}). && \text{(A.19)}
\end{aligned}$$

Hessian for the case of coupled channels (presented in Table 7.2) is

$$H|_{\mathbf{d}=\mathbf{d}^{\mathbf{IP}}{}_{\mathbf{coup}}} = \begin{pmatrix} 0.18 & -2.25\times10^{-3} & 1.73\times10^{-2} & 0.83\\ -2.25\times10^{-3} & 1.15\times10^{-2} & -2.95\times10^{-3} & -6.28\times10^{-3}\\ 1.73\times10^{-2} & -2.95\times10^{-3} & 2.07\times10^{-2} & 2.28\times10^{-2}\\ 0.83 & -6.28\times10^{-3} & 2.28\times10^{-2} & 8.41 \end{pmatrix}, \tag{A.20}$$

whose eigenvalues and eigenvectors are

$$\begin{aligned}
&\lambda_1^H = 8.49, V_1^H = (0.1, -7\times10^{-4}, 0.003, 1), && \text{(A.21)}\\
&\lambda_2^H = 0.1, V_1^H = (-0.98, 0.02, -0.18, 0.1), && \text{(A.22)}\\
&\lambda_3^H = 0.02, V_1^H = (-0.98, 0.02, -0.18, 0.1), && \text{(A.23)}\\
&\lambda_4^H = 0.01, V_1^H = (0.04, -0.94, -0.33, -0.004). && \text{(A.24)}
\end{aligned}$$

In all cases, we observe that the elements of the matrices corresponding to $d_1$ (first rows) and $d_5$ (last rows) are at least one order of magnitude higher than the components corresponding to other parameters. Therefore, we conclude that $d_5$ is the stiffest parameter.

# Appendix B

# Connectivities between channels in $IP_3R$ cluster

There is limited evidence on the interactions of channels within $IP_3R$ clusters. Therefore we study the most general types of connectivity between the channels. We aim to understand how interconnectivity between the channels affects the open probability of a cluster. The types of connectivity we consider are all-to-all, chain and circular (closed chain) as shown in Figure B.1. Each configuration is described mathematically by the adjacency matrix of a certain structure. For example, in the general case of $n$ channels connected as all-to-all [Figure B.1 (a)], all distinct

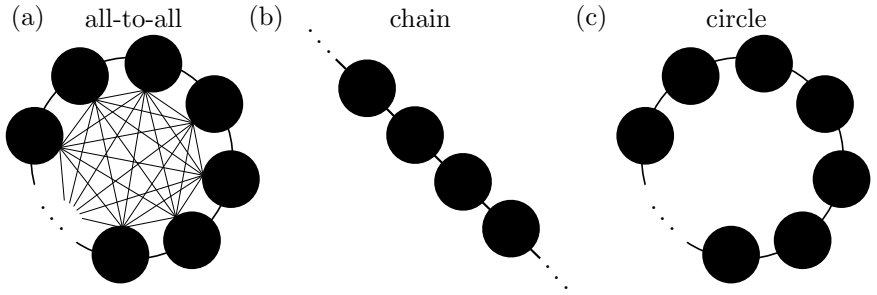


FIGURE B.1

channels are connected which results in the non-diagonal connectivity terms in the matrix being equal 1, apart from self connections which correspond to zero diagonal terms.

$$\mathbf{A}_{\text{all-to-all}} = \begin{pmatrix} 0 & 1 & 1 & 1 & \cdots & \cdots & \cdots & 1 \\ 1 & 0 & 1 & 1 & \ddots & \ddots & \ddots & 1 \\ 1 & 1 & 0 & \ddots & \ddots & \ddots & \ddots & 1 \\ \vdots & \ddots & \ddots & \ddots & \ddots & \ddots & \ddots & \vdots \\ 1 & \ddots & \ddots & 1 & 0 & 1 & \ddots & 1 \\ \vdots & \ddots & \ddots & \ddots & \ddots & \ddots & \ddots & \vdots \\ \vdots & \ddots & \ddots & \ddots & \ddots & \ddots & \ddots & \vdots \\ 1 & \cdots & \cdots & \cdots & \cdots & \cdots & 1 & 0 \end{pmatrix}. \tag{B.1}$$

In the case of chain connectivity between the clusters [Figure B.1 (b)] the channels are connected only to their neighbours (cross-diagonal terms in the matrix are equal to 1)

$$\mathbf{A}_{\text{chain}} = \begin{pmatrix} 0 & 1 & 0 & 0 & \cdots & \cdots & \cdots & 0 \\ 1 & 0 & 1 & 0 & \ddots & \ddots & \ddots & 0 \\ 0 & 1 & 0 & \ddots & \ddots & \ddots & \ddots & 0 \\ \vdots & \ddots & \ddots & \ddots & \ddots & \ddots & \ddots & \vdots \\ 0 & \ddots & \ddots & 1 & 0 & 1 & \ddots & 0 \\ \vdots & \ddots & \ddots & \ddots & \ddots & \ddots & \ddots & \vdots \\ \vdots & \ddots & \ddots & \ddots & \ddots & \ddots & \ddots & \vdots \\ 0 & \cdots & \cdots & \cdots & \cdots & \cdots & 1 & 0 \end{pmatrix}. \tag{B.2}$$

The adjacency matrix in the case of circular connections is very similar to the chain connectivity apart from the boundary terms equal to 1 (closed chain)

$$\mathbf{A}_{\text{circle}} = \begin{pmatrix} 0 & 1 & 0 & 0 & \cdots & \cdots & \cdots & 1 \\ 1 & 0 & 1 & 0 & \ddots & \ddots & \ddots & 0 \\ 0 & 1 & 0 & \ddots & \ddots & \ddots & \ddots & 0 \\ \vdots & \ddots & \ddots & \ddots & \ddots & \ddots & \ddots & \vdots \\ 0 & \ddots & \ddots & 1 & 0 & 1 & \ddots & 0 \\ \vdots & \ddots & \ddots & \ddots & \ddots & \ddots & \ddots & \vdots \\ \vdots & \ddots & \ddots & \ddots & \ddots & \ddots & \ddots & \vdots \\ 1 & \cdots & \cdots & \cdots & \cdots & \cdots & 1 & 0 \end{pmatrix}. \tag{B.3}$$

The open probabilities associated with the respective cluster configurations are calculated as

$$P_{\text{o}}^{N} = \frac{1}{NZ} \sum_{n=1}^{N} n \mathrm{e}^{\frac{\tilde{J}}{2} \mathbf{V}_n^{\top} \mathbf{A} \mathbf{V}_n + \sum_{i=1}^{N} \tilde{h} V_n^i}, \tag{B.4}$$

$$Z = \sum_{n=0}^{N} \mathrm{e}^{\frac{\tilde{J}}{2} \mathbf{V}_n^{\top} \mathbf{A} \mathbf{V}_n + \sum_{i=1}^{N} \tilde{h} V_n^i}, \tag{B.5}$$

where $\mathbf{V}_n = r[S_1, S_2, \ldots, S_N]$, $n = \overline{1, N}$ are the vectors containing $n$ open channels ($S_n = 1$) multiplied by corresponding numbers of realisations $r$. $\mathbf{A}$ may be $\mathbf{A}_{\text{all-to-all}}$, $\mathbf{A}_{\text{chain}}$ or $\mathbf{A}_{\text{circle}}$,

# Bibliography


Xenopus — Definition of Xenopus in English by Oxford Dictionaries, 2019. URL https://en.oxforddictionaries.com/definition/Xenopus.

N. Allbritton, T. Meyer, and L. Stryer. Range of Messenger Action of Calcium Ion and Inositol 1,4,5-Trisphosphate. *Science*, 258(5089):1812–1815, 1992. ISSN 0036-8075. doi:10.1126/science.1465619.

K. J. Alzayady, L. Wang, R. Chandrasekhar, L. E. Wagner, F. Van Petegem, and D. I. Yule. Defining the stoichiometry of inositol 1,4,5-trisphosphate binding required to initiate Ca2+ release. *Science Signaling*, 9(422), 2016. ISSN 19379145. doi:10.1126/scisignal.aad6281.

A. Atri, J. Amundson, D. Clapham, and J. Sneyd. A single-pool model for intracellular calcium oscillations and waves in the Xenopus laevis oocyte. *Biophysical Journal*, 65(4):1727–1739, 1993. ISSN 00063495. doi:10.1016/S0006-3495(93)81191-3.

R. J. Baxter. *Exactly Solved Models in Statistical Mechanics*. Academic Press, Canberra, may 1985. doi:10.1142/9789814415255_0002.

M. A. Beaumont. Approximate Bayesian Computation in Evolution and Ecology. *Annual Review of Ecology, Evolution, and Systematics*, 41(1):379–406, dec 2010. ISSN 1543-592X. doi:10.1146/annurev-ecolsys-102209-144621.

M. J. Berridge. Inositol trisphosphate and calcium oscillations. *Biochemical Society Symposium*, 74(74):1–7, 2007. ISSN 00678694. doi:10.1042/BSS0740001.

M. J. Berridge. Calcium signalling remodelling and disease. *Biochemical Society Transactions*, 40(2):297–309, apr 2012. ISSN 03005127. doi:10.1042/BST20110766.

M. J. Berridge. The Inositol Trisphosphate/Calcium Signaling Pathway in Health and Disease. *Physiological Reviews*, 96(4):1261–1296, 2016. ISSN 0031-9333. doi:10.1152/physrev.00006.2016.

M. J. Berridge, M. D. Bootman, and P. Lipp. Calcium – a life and death signal. *Nature*, 395 (6703):645–8, 1998. ISSN 0028-0836. doi:10.1038/27094.

M. J. Berridge, P. Lipp, and M. D. Bootman. The versatility and universality of calcium signalling. *Nature Reviews Molecular Cell Biology*, 1(1):11–21, oct 2000. ISSN 1471-0072. doi:10.1038/35036035.

I. Bezprozvanny, J. Watras, and B. E. Ehrlich. Bell-shaped calcium-response curves of lns(l,4,5)P3- and calcium-gated channels from endoplasmic reticulum of cerebellum. *Nature*, 351(6329):751–754, jun 1991. ISSN 00280836. doi:10.1038/351751a0.

M. D. Bootman and M. J. Berridge. Subcellular Ca2+ signals underlying waves and graded responses in HeLa cells. *Current Biology*, 6(7):855–865, 1996. ISSN 09609822. doi:10.1016/S0960-9822(02)00609-7.

M. D. Bootman, M. J. Berridge, and P. Lipp. Cooking with calcium: The recipes for composing global signals from elementary events. *Cell*, 91(3):367–373, 1997. ISSN 00928674. doi:10.1016/S0092-8674(00)80420-1.

S. Braichenko, A. Bhaskar, and S. Dasmahapatra. Phenomenological cluster-based model of Ca2+ waves and oscillations for inositol 1,4,5-trisphosphate receptor (IP3R) channels. *Physical Review E*, 98(3):032413, sep 2018. ISSN 2470-0045. doi:10.1103/PhysRevE.98.032413.

A. Calabrese, D. Fraiman, D. Zysman, and S. Ponce Dawson. Stochastic fire-diffuse-fire model with realistic cluster dynamics. *Physical Review E*, 82(3):031910–1–031910–12, 2010. ISSN 15393755. doi:10.1103/PhysRevE.82.031910.

N. Callamaras, J. S. Marchant, X. P. Sun, and I. Parker. Activation and co-ordination of InsP3-mediated elementary Ca2+ events during global Ca2+ signals in Xenopus oocytes. *Journal of Physiology*, 509(1):81–91, may 1998. ISSN 00223751. doi:10.1111/j.1469-7793.1998.081bo.x.

P. Cao, G. Donovan, M. Falcke, and J. Sneyd. A Stochastic Model of Calcium Puffs Based on Single-Channel Data. *Biophysical Journal*, 105(5):1133–1142, 2013. ISSN 00063495. doi:10.1016/j.bpj.2013.07.034.

P. Cao, X. Tan, G. Donovan, M. J. Sanderson, and J. Sneyd. A Deterministic Model Predicts the Properties of Stochastic Calcium Oscillations in Airway Smooth Muscle Cells. *PLoS Computational Biology*, 10(8), 2014. ISSN 15537358. doi:10.1371/journal.pcbi.1003783.

P. Cao, M. Falcke, and J. Sneyd. Mapping Interpuff Interval Distribution to the Properties of Inositol Trisphosphate Receptors. *Biophysical Journal*, 112(10):2138–2146, 2017. ISSN 15420086. doi:10.1016/j.bpj.2017.03.019.

H. Cheng and W. J. Lederer. Calcium Sparks. *Physiological Reviews*, 88(4):1491–1545, oct 2008. ISSN 0031-9333. doi:10.1152/physrev.00030.2007.

S. Coombes and Y. Timofeeva. Sparks and waves in a stochastic fire-diffuse-fire model of Ca2+ release. *Physical Review E*, 68(2):8, 2003. ISSN 1063651X. doi:10.1103/PhysRevE.68.021915.

P. Dandrea and F. Vittur. Spatial and Temporal Ca2+ Signaling in Articular Chondrocytes. *Biochemical and Biophysical Research Communications*, 215(1):129–135, 1995. ISSN 0006291X. doi:10.1006/bbrc.1995.2442.

S. P. Dawson, J. Keizer, and J. E. Pearson. Fire-diffuse-fire model of dynamics of intracellular calcium waves. *Proceedings of the National Academy of Sciences of the United States of America*, 96(11):6060–6063, 1999. ISSN 00278424. doi:10.1073/pnas.96.11.6060.

G. W. De Young and J. Keizer. A single-pool inositol 1,4,5-trisphosphate-receptor-based model for agonist-stimulated oscillations in Ca2+ concentration. *Proceedings of the National Academy of Sciences*, 89(20):9895–9899, oct 1992. ISSN 0027-8424. doi:10.1073/pnas.89.20.9895.

A. Dhooge, W. Govaerts, Y. A. Kuznetsov, H. G. Meijer, and B. Sautois. New features of the software MatCont for bifurcation analysis of dynamical systems. *Mathematical and Computer Modelling of Dynamical Systems*, 14(2):147–175, 2008. ISSN 13873954. doi:10.1080/13873950701742754.

G. D. Dickinson and I. Parker. Factors Determining the Recruitment of Inositol Trisphosphate Receptor Channels During Calcium Puffs. *Biophysical Journal*, 105:2474–2484, 2013. doi:10.1016/j.bpj.2013.10.028.

G. D. Dickinson, D. Swaminathan, and I. Parker. The probability of triggering calcium puffs is linearly related to the number of inositol trisphosphate receptors in a cluster. *Biophysical Journal*, 102(8):1826–1836, apr 2012. ISSN 00063495. doi:10.1016/j.bpj.2012.03.029.

G. D. Dickinson, K. L. Ellefsen, S. P. Dawson, J. E. Pearson, and I. Parker. Hindered cytoplasmic diffusion of inositol trisphosphate restricts its cellular range of action. *Science Signaling*, 9 (453):ra108, 2016. ISSN 19379145. doi:10.1126/scisignal.aag1625.

A. Duffy, J. Sneyd, and P. D. Dale. Traveling Waves in Buffered Systems: Applications to Calcium Waves. *SIAM Journal on Applied Mathematics*, 58(4):1178–1192, 1998. ISSN 0036-1399. doi:10.1137/s0036139996305074.

G. Dupont and A. Goldbeter. One-pool model for Ca2+ oscillations involving Ca2+ and inositol 1,4,5-trisphosphate as co-agonists for Ca2+ release. *Cell Calcium*, 14(4):311–322, 1993. ISSN 01434160. doi:10.1016/0143-4160(93)90052-8.

G. Dupont and A. Goldbeter. Properties of intracellular Ca2+ waves generated by a model based on (Ca2+)-induced Ca2+ release. *Biophysical Journal*, 67(6):2191–2204, 1994. ISSN 00063495. doi:10.1016/S0006-3495(94)80705-2.

G. Dupont, M. Falcke, V. Kirk, and J. Sneyd. *Models of Calcium Signalling*, volume 43 of *Interdisciplinary Applied Mathematics*. Springer International Publishing, Cham, 2016. ISBN 978-3-319-29645-6. doi:10.1007/978-3-319-29647-0.

R. G. Endres. *Physical Principles in Sensing and Signaling: With an Introduction to Modeling in Biology*. Oxford University Press, 2013. ISBN 978-0-19-960063-2.

M. Estrada, P. Uhlen, and B. E. Ehrlich. Ca2+ oscillations induced by testosterone enhance neurite outgrowth. *Journal of Cell Science*, 119(4):733–743, 2006. ISSN 00219533. doi:10.1242/jcs.02775.

M. Falcke. On the role of stochastic channel behavior in intracellular Ca2+ dynamics. *Biophysical Journal*, 84(1):42–56, 2003a. ISSN 00063495. doi:10.1016/S0006-3495(03)74831-0.

M. Falcke. Deterministic and stochastic models of intracellular Ca2+ waves. *New Journal of Physics*, 5:96–96, jul 2003b. ISSN 1367-2630. doi:10.1088/1367-2630/5/1/396.

M. Falcke. Reading the patterns in living cells –the physics of ca2+ signaling. *Advances in Physics*, 53(3):255–440, 2004. ISSN 0001-8732. doi:10.1080/00018730410001703159.

M. Falcke, M. Moein, A. Tilunaite, R. Thul, and A. Skupin. On the phase space structure of IP3 induced Ca2+ signalling and concepts for predictive modeling. *Chaos*, 28(4):045115, apr 2018. ISSN 10541500. doi:10.1063/1.5021073.

O. A. Fedorenko, E. Popugaeva, M. Enomoto, P. B. Stathopulos, M. Ikura, and I. Bezprozvanny. Intracellular calcium channels: Inositol-1,4,5-trisphosphate receptors. *European Journal of Pharmacology*, 739(C):39–48, sep 2014. ISSN 18790712. doi:10.1016/j.ejphar.2013.10.074.

R. A. Fisher. The Wave of Advance of Advantageous Genes. *Annals of Human Genetics*, 7: 355–369, 1937. ISSN 1469-1809. doi:10.1111/j.1469-1809.1937.tb02153.x.

R. FitzHugh. Impulses and Physiological States in Theoretical Models of Nerve Membrane. *Biophysical Journal*, 1(6):445–466, 1961. ISSN 00063495. doi:10.1016/S0006-3495(61)86902-6.

D. T. Gillespie. The chemical Langevin equation Approximate simulation of coupled fast and slow reactions for stochastic chemical kinetics The chemical Langevin equation. *The Journal of Chemical Physics*, 113(10):170901–24103, 2000. doi:10.1063/1.2145882.

D. T. Gillespie. Stochastic Simulation of Chemical Kinetics. *Annual Review of Physical Chemistry*, 58(1):35–55, may 2007. ISSN 0066-426X. doi:10.1146/annurev.physchem.58.032806.104637.

J. Guckenheimer and C. Kuehn. Homoclinic orbits of the Fitzhugh-nagumo equation: The singular-limit. *Discrete and Continuous Dynamical Systems - Series S*, 2(4):851–872, 2009. ISSN 19371632. doi:10.3934/dcdss.2009.2.851.

R. N. Gutenkunst, J. J. Waterfall, F. P. Casey, K. S. Brown, C. R. Myers, and J. P. Sethna. Universally sloppy parameter sensitivities in systems biology models. *PLoS Computational Biology*, 3(10):1871–1878, 2007. ISSN 1553734X. doi:10.1371/journal.pcbi.0030189.

J. M. Han, A. Tanimura, V. Kirk, and J. Sneyd. A mathematical model of calcium dynamics in HSY cells. *PLoS Computational Biology*, 13(2):e1005275, feb 2017. ISSN 15537358. doi:10.1371/journal.pcbi.1005275.

E. Hernandez, M. F. Leite, M. T. Guerra, E. A. Kruglov, O. Bruna-Romero, M. A. Rodrigues, D. A. Gomes, F. J. Giordano, J. A. Dranoff, and M. H. Nathanson. The spatial distribution of inositol 1,4,5-trisphosphate receptor isoforms shapes Ca2+ waves. *Journal of Biological Chemistry*, 282(13):10057–10067, mar 2007. ISSN 00219258. doi:10.1074/jbc.M700746200.

A. L. Hodgkin and A. F. Huxley. A quantitative description of membrane current and its application to conduction and excitation in nerve. *The Journal of Physiology*, 117(4):500–544, aug 1952. ISSN 0022-3751. doi:10.1113/jphysiol.1952.sp004764.

A. D. Horchler. Matlab Toolbox for the Numerical Solution of Stochastic Differential Equations (Version 1.2) [Source code]., 2013.

M. Iino. Molecular basis of spatio-temporal dynamics in inositol 1,4,5-trisphosphate-mediated Ca2+ signalling. *Japanese Journal of Pharmacology*, 82(1):15–20, jan 2000. ISSN 00215198. doi:10.1254/jjp.82.15.

L. Ionescu, C. White, K.-H. Cheung, J. Shuai, I. Parker, J. E. Pearson, J. K. Foskett, and D.-O. D. Mak. Mode switching is the major mechanism of ligand regulation of InsP3 receptor calcium release channels. *The Journal of General Physiology*, 130(6):631–645, 2007. ISSN 0022-1295. doi:10.1085/jgp.200709859.

A. Iserles. The diffusion equation. In *A First Course in the Numerical Analysis of Differential Equations*, pages 349–386. 2012. doi:10.1017/cbo9780511995569.019.

M. S. Jafri and J. Keizer. On the roles of Ca2+ diffusion, Ca2+ buffers, and the endoplasmic reticulum in IP3-induced Ca2+ waves. *Biophysical Journal*, 69(5):2139–2153, 1995. ISSN 00063495. doi:10.1016/S0006-3495(95)80088-3.

C. K. R. T. Jones. Stability of the Travelling Wave Solution of the Fitzhugh-Nagumo System. *Transactions of the American Mathematical Society*, 286(2):431, 1984. ISSN 00029947. doi:10.2307/1999806.

J. P. Keener and J. Sneyd. *Mathematical Physiology*, volume 8. Springer-Verlag, 2008. ISBN 9780387793870. doi:10.1007/978-0-387-79388-7.

J. Keizer and G. D. Smith. Spark-to-wave transition: Saltatory transmission of calcium waves in cardiac myocytes. *Biophysical Chemistry*, 72(1-2):87–100, may 1998. ISSN 03014622. doi:10.1016/S0301-4622(98)00125-2.

D. Kline and J. T. Kline. Repetitive calcium transients and the role of calcium in exocytosis and cell cycle activation in the mouse egg. *Developmental Biology*, 149(1):80–89, jan 1992. ISSN 00121606. doi:10.1016/0012-1606(92)90265-I.

R. Kupferman, P. P. Mitra, P. C. Hohenberg, and S. S. Wang. Analytical calculation of intracellular calcium wave characteristics. *Biophysical Journal*, 72(6):2430–2444, 1997. ISSN 00063495. doi:10.1016/S0006-3495(97)78888-X.

Y. A. Kuznetsov. *Elements of Applied Bifurcation Theory*. Springer, 2000. ISBN 0387983821. doi:10.1007/b98848.

J. Lechleiter, S. Girard, E. Peralta, and D. Clapham. Spiral calcium wave propagation and annihilation in Xenopus laevis oocytes. *Science*, 252(5002):123–126, 1991. ISSN 0036-8075. doi:10.1126/science.2011747.

G. Li. *Glauber and Kawasaki dynamics for permanental point process*. PhD thesis, Swansea University, jan 2011. URL https://cronfa.swan.ac.uk/Record/cronfa42886/Details.

Y. X. Li and J. Rinzel. Equations for InsP3 receptor-mediated [Ca2+](i) oscillations derived from a detailed kinetic model: A hodgkin-huxley like formalism. *Journal of Theoretical Biology*, 166(4):461–473, 1994. ISSN 00225193. doi:10.1006/jtbi.1994.1041.

B. Lindner, J. García-Ojalvo, a. Neiman, and L. Schimansky-Geier. Effects of noise in excitable systems. *Physics Reports*, 392(6):321–424, 2004. ISSN 03701573. doi:10.1016/j.physrep.2003.10.015.

D. O. D. Mak and J. K. Foskett. Single-channel kinetics, inactivation, and spatial distribution of inositol trisphosphate (IP3) receptors in Xenopus oocyte nucleus. *Journal of General Physiology*, 109(5):571–587, may 1997. ISSN 00221295. doi:10.1085/jgp.109.5.571.

D.-O. D. Mak, S. McBride, and J. K. Foskett. Inositol 1,4,5-tris-phosphate activation of inositol tris-phosphate receptor Ca2+ channel by ligand tuning of Ca2+ inhibition. *Proceedings of the National Academy of Sciences*, 95(26):15821–15825, dec 1998. ISSN 0027-8424. doi:10.1073/pnas.95.26.15821.

A. V. Maltsev, V. A. Maltsev, and M. D. Stern. Clusters of calcium release channels harness the Ising phase transition to confine their elementary intracellular signals. *Proceedings of the National Academy of Sciences*, 114(29):7525–7530, 2017. ISSN 0027-8424. doi:10.1073/pnas.1701409114.

J. Marchant, N. Callamaras, and I. Parker. Initiation of IP3-mediated Ca2+ waves in Xenopus oocytes. *EMBO Journal*, 18(19):5285–5299, 1999. ISSN 02614189. doi:10.1093/emboj/18.19.5285.

J. S. Marchant and I. Parker. Role of elementary Ca2+ puffs in generating repetitive Ca2+ oscillations. *EMBO Journal*, 20(1-2):65–76, 2001. ISSN 02614189. doi:10.1093/emboj/20.1.65.

M. Martone. Purkinje cell — anatomy — Britannica.com, 2015. URL https://www.britannica.com/science/Purkinje-cellhttp://www.britannica.com/science/Purkinje-cell.

S. Mataragka and C. W. Taylor. All three IP3 receptor subtypes generate Ca2+ puffs, the universal building blocks of IP3-evoked Ca2+ signals. *Journal of Cell Science*, 131(16):jcs220848, aug 2018. ISSN 0021-9533. doi:10.1242/jcs.220848.

K. Mikoshiba. The IP3 receptor/Ca2+ channel and its cellular function. *Biochemical Society symposium*, 74(74):9–22, 2007. ISSN 00678694. doi:10.1042/BSS2007c02.

J. D. Murray. *Mathematical Biology: II. Spatial Models and Biomedical Applications*, volume 18. Springer, 2000. ISBN 0387952233. doi:10.1086/421587.

J. Nagumo, S. Arimoto, and S. Yoshizawa. An Active Pulse Transmission Line Simulating Nerve Axon. *Proceedings of the IRE*, 50(10):2061–2070, oct 1962. ISSN 0096-8390. doi:10.1109/JRPROC.1962.288235. URL http://ieeexplore.ieee.org/document/4066548/.

H. Nakamura, H. Bannai, T. Inoue, T. Michikawa, M. Sano, and K. Mikoshiba. Cooperative and stochastic calcium releases from multiple calcium puff sites generate calcium microdomains in intact HeLa cells. *Journal of Biological Chemistry*, 287(29):24563–24572, jul 2012. ISSN 00219258. doi:10.1074/jbc.M111.311399.

M. H. Nathanson, A. D. Burgstahler, and M. B. Fallon. Multistep mechanism of polarized Ca2+ wave patterns in hepatocytes. *American Journal of Physiology*, 267(3):G338–G349, sep 1994. ISSN 0193-1857. doi:10.1152/ajpgi.1994.267.3.G338.

E. Neher and B. Sakmann. Single-channel currents recorded from membrane of denervated frog muscle fibres. *Nature*, 260(5554):799–802, 1976. ISSN 0028-0836. doi:10.1038/260799a0.

M. Nivala, E. de Lange, R. Rovetti, and Z. Qu. Computational modeling and numerical methods for spatiotemporal calcium cycling in ventricular myocytes. *Frontiers in Physiology*, 3(114): 1–12, 2012. ISSN 1664042X. doi:10.3389/fphys.2012.00114.

B. Øksendal. *Stochastic Differential Equations*. Universitext. Springer Berlin Heidelberg, Berlin, Heidelberg, 6 edition, 2003. ISBN 978-3-540-04758-2. doi:10.1007/978-3-642-14394-6.

I. Parker. The Parker Lab, 2014. URL http://parkerlab.bio.uci.edu/.

I. Parker and I. Ivorra. Localized all-or-none calcium liberation by inositol trisphosphate. *Science*, 250(4983):977–979, 1990. ISSN 0036-8075. doi:10.1126/science.2237441.

A. Politi, L. D. Gaspers, A. P. Thomas, and T. Höfer. Models of IP3 and Ca2+ oscillations: Frequency encoding and identification of underlying feedbacks. *Biophysical Journal*, 90(9): 3120–3133, 2006. ISSN 00063495. doi:10.1529/biophysj.105.072249.

E. B. Ridgway, J. C. Gilkey, and L. F. Jaffe. Free calcium increases explosively in activating medaka eggs. *Proceedings of the National Academy of Sciences of the United States of America*, 74(2):623–627, 1977. ISSN 0027-8424. doi:10.1073/pnas.74.2.623.

M. Rückl and S. Rüdiger. Calcium waves in a grid of clustered channels with synchronous IP 3 binding and unbinding. *European Physical Journal E*, 39(11):1–11, 2016. ISSN 1292895X. doi:10.1140/epje/i2016-16108-4.

M. Rückl, I. Parker, J. S. Marchant, C. Nagaiah, F. W. Johenning, and S. Rüdiger. Modulation of Elementary Calcium Release Mediates a Transition from Puffs to Waves in an IP3R Cluster Model. *PLoS Computational Biology*, 11(1):e1003965, 2015. ISSN 15537358. doi:10.1371/journal.pcbi.1003965.

S. Rüdiger. Excitability in a stochastic differential equation model for calcium puffs. *Physical Review E*, 89(6):062717, jun 2014a. ISSN 1539-3755. doi:10.1103/PhysRevE.89.062717.

S. Rüdiger. Stochastic models of intracellular calcium signals. *Physics Reports*, 534(2):39–87, 2014b. ISSN 03701573. doi:10.1016/j.physrep.2013.09.002.

S. Rüdiger, J. W. Shuai, W. Huisinga, C. Nagaiah, G. Warnecke, I. Parker, and M. Falcke. Hybrid stochastic and deterministic simulations of calcium blips. *Biophysical Journal*, 93(6): 1847–1857, 2007. ISSN 00063495. doi:10.1529/biophysj.106.099879.

S. Rüdiger, C. Nagaiah, G. Warnecke, and J. W. Shuai. Calcium domains around single and clustered IP3 receptors and their modulation by buffers. *Biophysical Journal*, 99(1):3–12, 2010a. ISSN 00063495. doi:10.1016/j.bpj.2010.02.059.

S. Rüdiger, J. W. Shuai, and I. M. Sokolov. Law of mass action, detailed balance, and the modeling of calcium puffs. *Physical Review Letters*, 105(4):048103, 2010b. ISSN 00319007. doi:10.1103/PhysRevLett.105.048103.

S. Rüdiger, P. Jung, and J. W. Shuai. Termination of Ca2+ release for clustered IP3R channels. *PLoS Computational Biology*, 8(5):e1002485, may 2012. ISSN 1553734X. doi:10.1371/journal.pcbi.1002485.

D. Sadava, D. M. Hillis, H. C. Heller, and M. R. Berenbaum. *LIFE, the Science of Biology*. Sinauer Associates, 10th edition, 2011. ISBN 9781319190002.

H. Schmidle. *Waiting Time Distributions for IP3 gated Ca2+ Channels*. PhD thesis, Freie Universität Berlin, 2008. URL http://www.itp.tu-berlin.de/fileadmin/a3233/upload/AG_Klapp/Mitglieder-Details/Schmidle/Heiko_Schmidle_diplomarbeit.pdf.

J. P. Sethna. What are Sloppy Models?, 2008. URL http://www.lassp.cornell.edu/sethna/Sloppy/WhatAreSloppyModels.html.

J. Shuai and P. Jung. Langevin Modeling of Intracellular Calcium Dynamics. pages 231–252. Springer, Berlin, Heidelberg, nov 2003a. doi:10.1007/978-3-540-44878-5_12. URL http://link.springer.com/10.1007/978-3-540-44878-5{_}12.

J. Shuai, H. J. Rose, and I. Parker. The number and spatial distribution of IP3 receptors underlying calcium puffs in Xenopus oocytes. *Biophysical Journal*, 91(11):4033–4044, 2006. ISSN 00063495. doi:10.1529/biophysj.106.088880.

J. Shuai, J. E. Pearson, and I. Parker. Modeling Ca2+ feedback on a single inositol 1,4,5-trisphosphate receptor and its modulation by Ca2+ buffers. *Biophysical Journal*, 95(8):3738–3752, 2008. ISSN 15420086. doi:10.1529/biophysj.108.137182.

J. W. Shuai and P. Jung. Optimal ion channel clustering for intracellular calcium signaling. *Proceedings of the National Academy of Sciences of the United States of America*, 100(2): 506–510, 2003b. ISSN 00278424. doi:10.1073/pnas.0236032100.

I. Siekmann, L. E. Wagner, D. Yule, E. J. Crampin, and J. Sneyd. A kinetic model for type i and II IP3R accounting for mode changes. *Biophysical Journal*, 103(4):658–668, aug 2012. ISSN 00063495. doi:10.1016/j.bpj.2012.07.016.

A. Skupin, H. Kettenmann, U. Winkler, M. Wartenberg, H. Sauer, S. C. Tovey, C. W. Taylor, and M. Falcke. How does intracellular Ca2+ oscillate: By chance or by the clock? *Biophysical Journal*, 94(6):2404–2411, 2008. ISSN 15420086. doi:10.1529/biophysj.107.119495.

E. Smedler and P. Uhlén. Frequency decoding of calcium oscillations. *Biochimica et Biophysica Acta - General Subjects*, 1840(3):964–969, 2014. ISSN 03044165. doi:10.1016/j.bbagen.2013.11.015.

I. F. Smith, S. M. Wiltgen, and I. Parker. Localization of puff sites adjacent to the plasma membrane: Functional and spatial characterization of Ca2+ signaling in SH-SY5Y cells utilizing membrane-permeant caged IP3. *Cell Calcium*, 45(1):65–76, 2009. ISSN 01434160. doi:10.1016/j.ceca.2008.06.001.

I. F. Smith, D. Swaminathan, G. D. Dickinson, and I. Parker. Single-molecule tracking of inositol trisphosphate receptors reveals different motilities and distributions. *Biophysical Journal*, 107 (4):834–845, aug 2014. ISSN 15420086. doi:10.1016/j.bpj.2014.05.051.

J. Sneyd and J. Sherratt. On the propagation of calcium waves in an inhomogeneous medium. *SIAM Journal on Applied Mathematics*, 57(1):73–94, 1997. ISSN 00361399. doi:10.1137/S0036139995286035.

J. Sneyd, S. Means, D. Zhu, J. Rugis, J. H. Won, and D. I. Yule. Modeling calcium waves in an anatomically accurate three-dimensional parotid acinar cell. *Journal of Theoretical Biology*, 419:383–393, apr 2017. ISSN 0022-5193. doi:10.1016/J.JTBI.2016.04.030.

S. H. Strogatz. *Nonlinear dynamics and chaos: with applications to physics, biology, chemistry, and engineering*. Westview Press, second edition, 2014. ISBN 9780813349107.

Taufiq-Ur-Rahman, A. Skupin, M. Falcke, and C. W. Taylor. Clustering of InsP3 receptors by InsP3 retunes their regulation by InsP3 and Ca2+. *Nature*, 458(7238):655–659, 2009. ISSN 0028-0836. doi:10.1038/nature07763.

C. W. Taylor and V. Konieczny. IP3 receptors: take four IP3 to open. *Science Signaling*, 9(422): 1–9, 2016. doi:10.1126/scisignal.aaf6029.IP.

J. D. Thatcher. The inositol trisphosphate (IP3) signal transduction pathway. *Science Signaling*, 3(119):tr3, apr 2010. ISSN 19450877. doi:10.1126/scisignal.3119tr3.

R. Thul and M. Falcke. Stability of membrane bound. *Physical Review Letters*, 93(18):188103–1–4, 2004a. ISSN 00319007. doi:10.1103/PhysRevLett.93.188103.

R. Thul and M. Falcke. Release Currents of IP3 Receptor Channel Clusters and Concentration Profiles. *Biophysical Journal*, 86(5):2660–2673, may 2004b. ISSN 00063495. doi:10.1016/S0006-3495(04)74322-2.

R. Thul and M. Falcke. Frequency of elemental events of intracellular Ca2+ dynamics. *Physical Review E*, 73(6):061923, 2006. ISSN 1539-3755. doi:10.1103/PhysRevE.73.061923.

R. Thul, S. Coombes, and G. D. Smith. Sensitisation waves in a bidomain fire-diffuse-fire model of intracellular Ca2+ dynamics. *Physica D: Nonlinear Phenomena*, 238(21):2142–2152, nov 2009. ISSN 01672789. doi:10.1016/j.physd.2009.08.011.

R. Thul, S. Coombes, H. L. Roderick, and M. D. Bootman. Subcellular calcium dynamics in a whole-cell model of an atrial myocyte. *Proceedings of the National Academy of Sciences*, 109 (6):2150–2155, feb 2012. ISSN 0027-8424. doi:10.1073/pnas.1115855109.

K. Thurley and M. Falcke. Derivation of Ca2+ signals from puff properties reveals that pathway function is robust against cell variability but sensitive for control. *Proceedings of the National Academy of Sciences of the United States of America*, 108(1):427–432, jan 2011. ISSN 0027-8424. doi:10.1073/pnas.1008435108.

K. Thurley, I. F. Smith, S. C. Tovey, C. W. Taylor, I. Parker, and M. Falcke. Timescales of IP3-evoked Ca2+ spikes emerge from Ca2+ puffs only at the cellular level. *Biophysical Journal*, 101(11):2638–2644, 2011. ISSN 00063495. doi:10.1016/j.bpj.2011.10.030.

K. Thurley, A. Skupin, R. Thul, and M. Falcke. Fundamental properties of Ca2+ signals. *Biochimica et Biophysica Acta - General Subjects*, 1820(8):1185–1194, 2012. ISSN 03044165. doi:10.1016/j.bbagen.2011.10.007.

K. Thurley, S. C. Tovey, G. Moenke, V. L. Prince, A. Meena, A. P. Thomas, A. Skupin, C. W. Taylor, and M. Falcke. Reliable encoding of stimulus intensities within random sequences of intracellular Ca2+ spikes. *Science Signaling*, 7(331):ra59, jun 2014. ISSN 19379145. doi:10.1126/scisignal.2005237.

Y. Timofeeva. *Oscillations and Waves in Single and Multi-cellular Systems with Free Calcium*. PhD thesis, Loughborough University, 2003. URL https://dspace.lboro.ac.uk/dspace-jspui/bitstream/2134/33829/1/Thesis-2003-Timofeeva.pdf.

A. M. Turing. The chemical basis of morphogenesis. *Philosophical Transactions of the Royal Society of London. Series B, Biological Sciences*, 237(641):37–72, aug 1952. ISSN 2054-0280. doi:10.1098/rstb.1952.0012. URL http://www.royalsocietypublishing.org/doi/10.1098/rstb.1952.0012.

G. Ullah, I. Parker, D.-O. D. Mak, and J. E. Pearson. Multi-scale data-driven modeling and observation of calcium puffs. *Cell Calcium*, 52(2):152–160, 2012. ISSN 1532-1991. doi:10.1016/j.ceca.2012.04.018.

J. Watras, I. Bezprozvanny, and B. Ehrlich. Inositol 1,4,5-trisphosphate-gated channels in cerebellum: presence of multiple conductance states. *The Journal of Neuroscience*, 11(10):3239–3245, oct 1991. ISSN 0270-6474. doi:10.1523/JNEUROSCI.11-10-03239.1991.

S. H. Weinberg and G. D. Smith. The influence of Ca2+ buffers on free [Ca2+] fluctuations and the effective volume of Ca2+ microdomains. *Biophysical Journal*, 106(12):2693–2709, jun 2014. ISSN 15420086. doi:10.1016/j.bpj.2014.04.045.

S. M. Wiltgen, G. D. Dickinson, D. Swaminathan, and I. Parker. Termination of calcium puffs and coupled closings of inositol trisphosphate receptor channels. *Cell Calcium*, 56(3):157–168, 2014. ISSN 01434160. doi:10.1016/j.ceca.2014.06.005.

P. Winding and M. W. Berchtold. The chicken B cell line DT40: A novel tool for gene disruption experiments. *Journal of Immunological Methods*, 249(1-2):1–16, mar 2001. ISSN 00221759. doi:10.1016/S0022-1759(00)00333-1.

E. Wiseman, L. Bates, A. Dubé, and D. J. Carroll. *Marine Organisms as Model Systems in Biology and Medicine*, volume 65 of *Results and Problems in Cell Differentiation*. Springer International Publishing, Cham, 2018. ISBN 978-3-319-92485-4. doi:10.1007/978-3-319-92486-1.